Mathematical Neuroscience: From Neural Fields to Neuroimaging

James Ross

A thesis presented for the degree of

Doctor of Philosophy

School of Mathematical Sciences

University of Nottingham

Abstract

Modern non-invasive techniques for probing human brain activity, such as magnetoencephalography (MEG), offer high temporal resolution and continuously improving spatial resolution, providing an increasingly detailed view of brain function. These advancements enable the development of sophisticated mathematical models to better understand the mechanisms underlying spatio-temporal neuroimaging signals. This thesis enhances the biological accuracy of neural mass, field, and network models by incorporating a variety of key biological features, improving their utility in understanding brain function. We make use of various neural models, including mean-field models derived from networks of single neurons, which allow for tracking neuronal synchrony and incorporating biological features such as gap junctions at the cellular level. A model incorporating dendritic depth allows more direct measures of local field potentials (LFP) and electroencephalography (EEG) signals. Furthermore, models integrating gap-junctions and extracellular ion concentrations are developed, providing insights into the relationship between extracellular activity and neuronal dynamics—a subject particularly relevant to epilepsy research. An optimisation algorithm is also developed and utilised to fit these models to real data.

PUBLICATIONS

- Brain-wave equation incorporating axodendritic connectivity by J.Ross, M. Margetts, I. Bojak, R. Nicks, D. Avitabile, and S. Coombes. Physical Review E 101, 022411, 2020.
- Next Generation Neural Mass and Field Modelling by Á. Byrne, R. O'Dea, M. Forrester, J. Ross and S. Coombes. The Journal of Neurophysiology 123, 726-742, 2020.
- Mean-Field Models for EEG/MEG: From Oscillations to Waves by Á. Byrne, J. Ross, R. Nicks and S. Coombes. Brain Topography 35, 36–53, 2022.

PAPERS IN PREPARATION

- Using a Genetic Algorithm to Fit a Stochastic Neural Mass Model to MEG Beta-Burst Data by J. Ross, R. Nicks and S. Coombes.
- Coupling a Neural Activity Model to Extracellular Space by J. Ross, R. Nicks and S. Coombes.

CONTENTS

CHAPTER 1

INTRODUCTION

In this thesis, we explore a variety of mathematical models of brain activity and discuss their potential applications in the fields of mathematical neuroscience and neuroimaging. The models we investigate range from a Wilson-Cowan-based neural field model with axo-dendritic connections to next-generation neural mass and field models that include gap-junction coupling and extracellular ion concentrations. We use various tools to investigate these neural activity models, such as linear stability analysis, computational simulation, and heuristic optimisation.

The structure of this thesis, beyond this introductory preface, consists of one background chapter, four research chapters, and one discussion chapter. A brief summary of the main chapters of this thesis is now presented.

Chapter 2

In this chapter, we cover some of the background for this thesis. Since this thesis discusses multiple variations of different neural models, we use this chapter to introduce

some of the fundamental models that we build upon and improve in the main chapters. We also provide motivation for how and why mathematical models can benefit neuroscience as a whole and discuss the specific improvements to current models that we aim to address in the research chapters.

Chapter 3

Here, we introduce a model that extends the Wilson-Cowan neural field model. We enhance the classic Wilson-Cowan model by incorporating passive dendritic processing and axo-dendritic connectivity patterns. While synaptic processing is often included in neural models, dendritic filtering is frequently neglected. To address this, we develop a neural field model that includes both synaptic processing and dendritic filtering, as well as axonal delays.

Using this integro-differential model, we derive a brain-wave PDE formulation, which is computationally more feasible than directly simulating delay-differential equations. We first investigate the wave behaviour of a single-population model before analysing a two-population model, composed of excitatory and inhibitory neuronal populations, where more complex patterns may emerge.

The work in this chapter is based on *Brain-Wave Equation Incorporating Axodendritic Connectivity* by J. Ross, M. Margetts, I. Bojak, R. Nicks, D. Avitabile, and S. Coombes, published in *Physical Review E* in 2020 [1]. Julia code for the simulation and analysis of the model discussed in this chapter is available at https://github.com/Jamesafross/Thesis_Code/tree/main/Axo_Dendritic_Paper.

Chapter 4

In this chapter, we move away from sigmoidal firing rate models and explore next-generation neural models derived directly from an underlying network of quadratic integrate-and-fire neurons. We introduce a neural mass model that incorporates both gap-junction coupling and chemical synaptic coupling.

We perform a bifurcation analysis of this model, demonstrating how increasing and decreasing gap-junction coupling can induce synchrony in neuronal populations. We then extend this neural mass model to a neural field model and conduct a Turing instability analysis to investigate the model's spatiotemporal behaviour across various parameter regimes. Additionally, we examine how varying gap-junction coupling influences synchrony and the emergent patterns in the neural field model.

This chapter is based on *Mean-Field Models for EEG/MEG: From Oscillations to Waves* by Á. Byrne, J. Ross, R. Nicks, and S. Coombes, published in *Brain Topography* on 15 May 2021 [2]. Julia code for the simulation and instability analysis of all models discussed in this chapter is available at https://github.com/Jamesafross/Neural_Field_with_gaps.

Chapter 5

Here, we develop a genetic algorithm to optimise parameters in a next-generation neural mass model, fitting the model to real MEG beta-bursting data acquired at the Sir Peter Mansfield Imaging Centre at the University of Nottingham.

We use a hidden Markov model to detect beta bursts in a simulated neural activity model, then apply statistics derived from this burst detection method to fit certain statistical properties of the MEG data. Furthermore, we demonstrate the impact of

using the optimised parameter set in a network model based on real brain network data obtained from diffusion tensor imaging.

Julia and MATLAB code for the genetic algorithm used in this chapter is available at https://github.com/Jamesafross/BetaBurstGA, and the code for the hidden Markov model, developed by OHBA, can be found at https://github.com/OHBA-analysis/HMM-MAR.

Chapter 6

In this chapter, we extend the next-generation neural model introduced in Chapter 4 by coupling the gap-junction coupling strength and the average drive of the mass model to extracellular potassium dynamics. Extracellular potassium plays a crucial role in the genesis and sustainment of seizure states associated with neurological conditions such as epilepsy.

We identify bifurcations in the model through a Turing instability analysis and use insights from this analysis to further investigate the model's dynamics by varying parameters that influence potassium dynamics. We demonstrate how these parameters alter system behaviour via direct numerical simulation.

Julia code for the simulation and analysis of the field model discussed in this chapter is available at https://github.com/Jamesafross/Thesis_Code/tree/main/Neural_Field_with_potassium.

Chapter 7

In this final chapter, we summarise the main research chapters of this thesis and explore potential future work and possible extensions of this research.

CHAPTER 2

BACKGROUND

Before beginning the main research chapters of this thesis, it is important to provide some background material that lays the foundation for the subsequent research. This chapter, therefore, reviews fundamental neuroscience and biology concepts referenced throughout the thesis and introduces some neural models commonly found in the mathematical and computational neuroscience literature.

2.1 Physiology of the Brain

This section introduces the fundamental anatomy of a neuron, detailing the soma, dendrites, axon, and myelin sheath and explains how synapses allow communication between neurons. We then extend this to describe how action potentials synchronise to generate the large-scale electrical oscillations characteristic of different brain states.

2.1.1 Anatomy of a Neuron

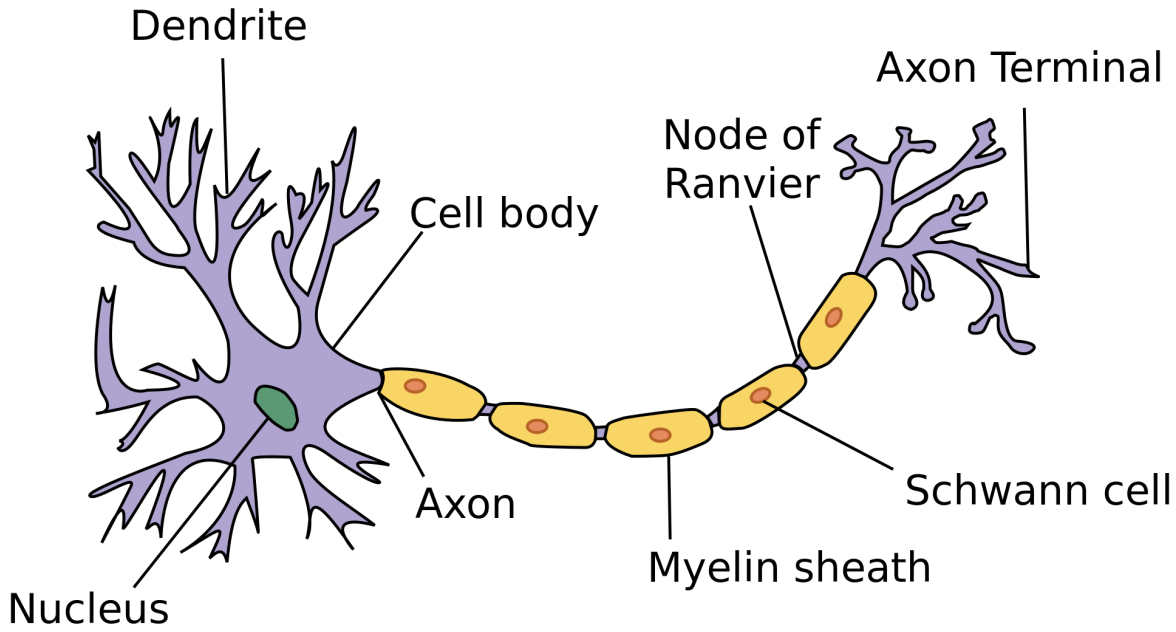

Figure 2.1: A diagram of a neuron. In this representation, we see the branching structure of the dendrites, the cell body, the axon terminals, and the long myelin-coated axon. This image was sourced from https://en.wikipedia.org/wiki/Myelin.

A neuron's primary functional components are:

- The *soma* or *cell body*, which contains the *nucleus* of the neuron and is the site of protein synthesis.
- The *axon*, a long cable-like structure that carries electrical spikes of activity, called *action potentials*, from the soma to the *axon terminals*.
- *Dendrites*, branch-like structures that extend from the soma and receive neurotransmitters released by another neuron.
- The *myelin sheath*, a protective layer that coats the axon, acting essentially as an electrical insulator around a wire.

2.1.2 Synapses

Neurons communicate with other neurons and cell types at synapses, which come in two forms: chemical and electrical.

At chemical synapses, an action potential triggers the release of neurotransmitters from the presynaptic neuron's axon terminal into a microscopic gap called the synaptic cleft, which is approximately 20–40 nanometres (nm) wide. These neurotransmitters are received by the postsynaptic neuron's dendrites and either increase or decrease the probability that the postsynaptic neuron will fire its own action potential, depending on whether the connection is excitatory or inhibitory.

At electrical synapses, the presynaptic and postsynaptic neurons are much closer (approximately 3.8 nm) and connect via *gap junctions*, which are channels that allow electrical signals to pass directly between them. Unless otherwise specified, the term 'synapse' usually refers to a chemical synapse.

2.1.3 From Action Potentials to Large-Scale Brain Oscillations

An action potential is an electrical impulse, typically around 100 mV in magnitude, that propagates from the axon hillock along the axon and triggers the release of neurotransmitters from the axon terminals into the synaptic cleft. This neurotransmitter release causes a change in the membrane potential of the postsynaptic neuron, which may then elicit its own action potential.

The frequency at which action potentials occur in a neuron is referred to as the *firing rate*, and a temporal chain of action potentials is known as a *spike train*. In Figure 2.2, we see a diagram of an action potential, shown as a measure of voltage across the neuron's membrane.

When large numbers of neurons fire synchronously and periodically, they generate detectable oscillations in the brain's electric field, known as brain rhythms. These rhythms are classified into different frequency bands, which are often associated with distinct physical or mental states [3]:

- *Delta* $(0.5 - 4\text{Hz})$: Sleep.
- *Theta* $(4 - 8\text{Hz})$: Extreme relaxation.
- *Alpha* $(8 - 12\text{Hz})$: Deep relaxation, passive attention.
- *Beta* $(12 - 35\text{Hz})$: Normal wakefulness, active, external attention.
- *Gamma* $(> 35\text{Hz})$: Focus/concentration.

These brain oscillations are strong enough to be detected by sensors outside the human skull. The next section discusses the technology that neuroscientists use to measure these oscillations.

2.2 EEG, MEG, and Neuroimaging

Brain imaging encompasses a variety of techniques for studying brain activity. Common methods include functional magnetic resonance imaging (fMRI), electroencephalography (EEG), and magnetoencephalography (MEG).

fMRI is a neuroimaging technique that measures fluctuations in blood flow to determine variations in brain activity. It has very high spatial resolution but relatively low temporal resolution [4].

MEG and EEG, on the other hand, have very high temporal resolution but relatively low spatial resolution compared to fMRI. EEG records electrical activity fluctuations on the scalp, usually via electrodes placed on the head's surface [5]. A more invasive

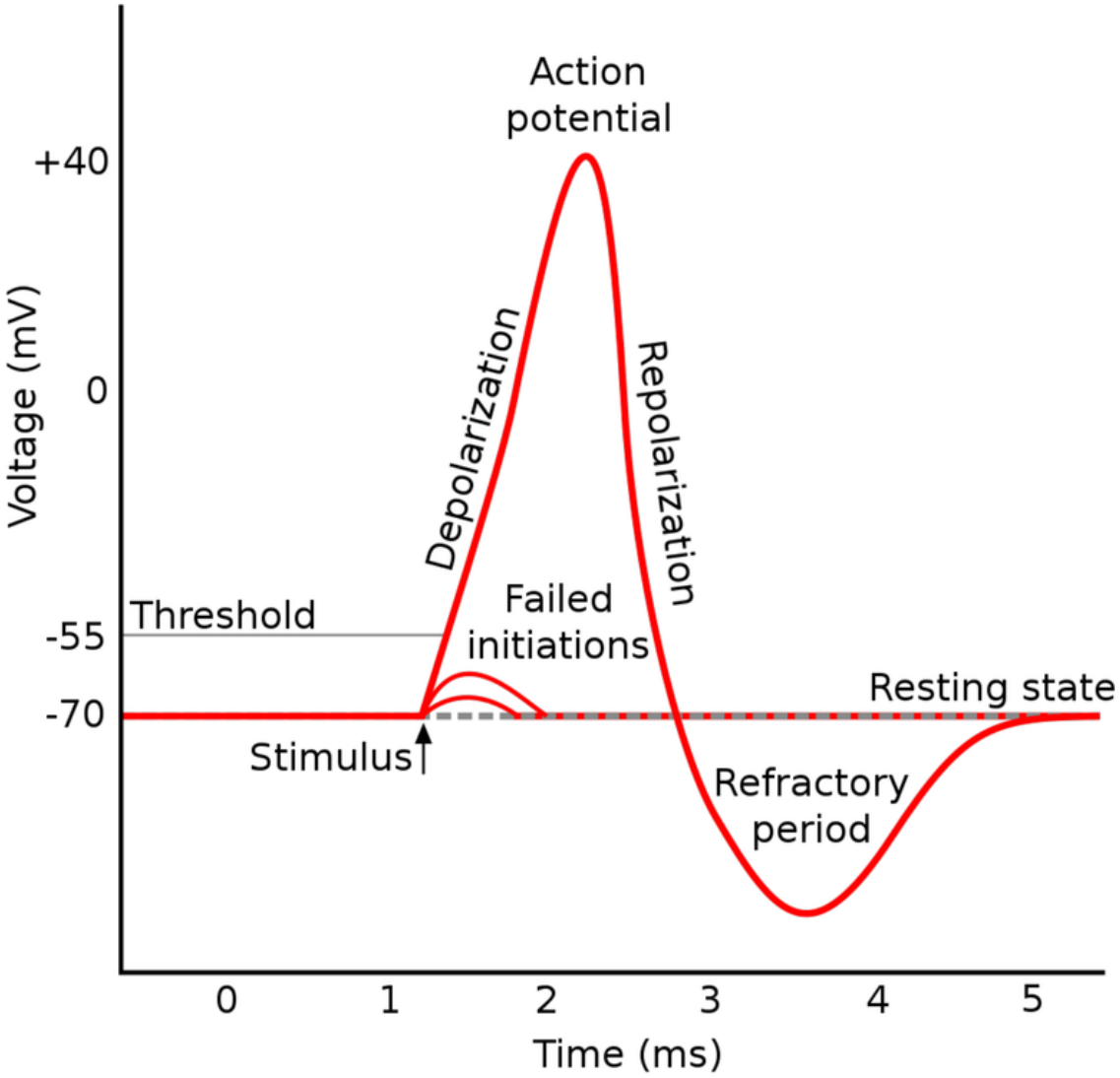

Figure 2.2: A demonstration of an action potential shown as a measure of the potential across the neuron membrane. The voltage starts at a resting state of −70 mV, and when the neuron receives enough stimulus to push the potential above the threshold (−55 mV here), an action potential occurs, pushing the membrane potential up to 40 mV. After the peak of the action potential, the voltage falls below resting potential during the refractory period before returning to its resting state. This image was sourced from https://en.wikipedia.org/wiki/Action_potential.

form, known as intracranial EEG, involves electrodes being placed directly on the skull.

Similarly, MEG measures fluctuations in the magnetic field outside the head, caused by changes in electrical activity within the brain [6]. Both MEG and EEG capture the activity of neuronal ensembles via variations in electric or magnetic fields. A stronger signal is detected when large groups of neurons fire synchronously.

2.3 Neural Mass Modelling

The sheer complexity of the brain, with vast numbers of neurons and neural connections, presents an interesting and challenging problem for mathematical modellers. Mathematical neuroscientists have sought to simplify this problem by developing models that are mathematically tractable while still capturing the essential dynamics of the biological system.

There is a broad range of complexity and scale in neural modelling, from detailed conductance-based single-neuron models, such as the Hodgkin-Huxley model [7], to simplified integrate-and-fire models [8], [9] that capture the essence of a firing neuron but scale more easily to large networks.

Neural mass models are widely used in mathematical neuroscience due to their simplicity and scalability, allowing for large scale modelling of brain activity [10], [11] . Rather than modelling individual neurons, these models track macroscopic variables such as the average activity and firing rate of a dense cluster of neurons. Popular examples include the Wilson-Cowan model [12] and the Jansen-Rit model [13], which have proven useful in modelling brain rhythms observed in EEG/MEG recordings. More recently, next-generation neural mass models, derived from networks of cou-

pled quadratic integrate-and-fire neurons, have been developed. These models offer improved accuracy in capturing neuronal synchrony, a fundamental feature of normal brain dynamics that underlies population-level effects like beta rebound [14], [15], [16], and can also be involved in pathological activity such as seizures [73], [93].

2.3.1 Mathematical Framework of Neural Mass Models

Mass models typically take the form of time-dependent ordinary differential equations (ODEs) that track variables such as population-average conductance, potential, and firing rate. Mass models usually take the form,

$$Qu = f(u), \tag{2.1}$$

where $u \in \mathbb{R}^N$ represents the mean post-synaptic conductance of one or more sub-populations of neurons, $f : \mathbb{R}^N \to \mathbb{R}^N$ is the firing rate of a population, and Q is a linear differential operator representing post-synaptic processing. Most neural mass models are phenomenological in nature; they are not derived from a detailed network of spiking neuron models but are motivated by neurobiology.

Firing Rate Function

The mean firing rate of a cluster of neurons is the average frequency at which these neurons fire action potentials. This would naturally seem to be a function of the post-synaptic conductance and is also constrained by the natural refractory period of neurons. Hence, a common phenomenological choice of a firing rate function is the sigmoid function,

$$f(x) = \frac{1}{1 + \mathrm{e}^{-\beta(x-\theta)}}, \tag{2.2}$$

where β is the steepness and θ is the threshold. This firing rate has been used in models such as the Wilson–Cowan model [12] and the Jansen–Rit model [13], but next-generation mass models improve on this by deriving their firing rate exactly from the underlying dynamics of a network of quadratic integrate-and-fire models.

Synaptic Processing

One commonality between many different neural mass models is synaptic processing or the synaptic filter. A post-synaptic conductance change $g(t)$ could be given as

$$g(t) = \bar{g}\eta(t - T), \quad t \geq T, \tag{2.3}$$

where $\bar{g}$ is a constant and $\eta(t)$ is typically of first-order form:

$$\eta(t) = \alpha \mathrm{e}^{-\alpha t} H(t), \tag{2.4}$$

which models synapses with exponential decay once excited, or second-order form:

$$\eta(t) = \alpha^2 t \mathrm{e}^{-\alpha t} H(t), \tag{2.5}$$

which models both decay and temporal delay due to the synapse processing the action potential. Both of these may be written as the Green's function of a linear differential operator, $Q\eta = \delta$, where Q takes the form $(1 + \alpha^{-1}\mathrm{d}/\mathrm{d}t)$ in the first-order case or $(1 + \alpha^{-1}\mathrm{d}/\mathrm{d}t)^2$ in the second-order case. Unless otherwise stated, this thesis will primarily be using the second-order form.

2.3.2 Analytical Tools for Neural Mass Models

Often, the first line of analysis for neural mass models is some form of linear analysis. The most prevalent form of analysis in this thesis is linear stability analysis, where we identify parameter regimes in which the steady state loses stability to periodic solutions. Various tools are available for this type of analysis. For simple models, pen and paper are sufficient, but for more complex models, we make use of XPPAUT [17]. With this tool, we can find bifurcations and also continue these bifurcations in parameter space.

2.3.3 Neural Mass Model Examples

In this section, we briefly present some examples of neural mass models that are commonly used throughout the mathematical and computational neuroscience literature, either precisely in the form shown here or with slight augmentations. We also provide an overview of the possible dynamics and applications of these models.

Wilson–Cowan Model

Jack Cowan and Hugh Wilson are considered pioneers of mathematical neuroscience for the mass model they developed [12]. The model describes neural dynamics in terms of the mean activity, e.g. the proportion of cells firing, in two interacting neuron subpopulations, excitatory (E) and inhibitory (I), coupled via first-order synapses. It may be written simply in terms of two coupled ODEs:

$$\begin{aligned} \frac{1}{\alpha_E}\frac{\mathrm{d}}{\mathrm{d}t}E &= -E + f(\kappa_{EE}E + \kappa_{EI}I + P_E), \\ \frac{1}{\alpha_I}\frac{\mathrm{d}}{\mathrm{d}t}I &= -I + f(\kappa_{IE}E + \kappa_{II}I + P_I). \end{aligned} \tag{2.6}$$

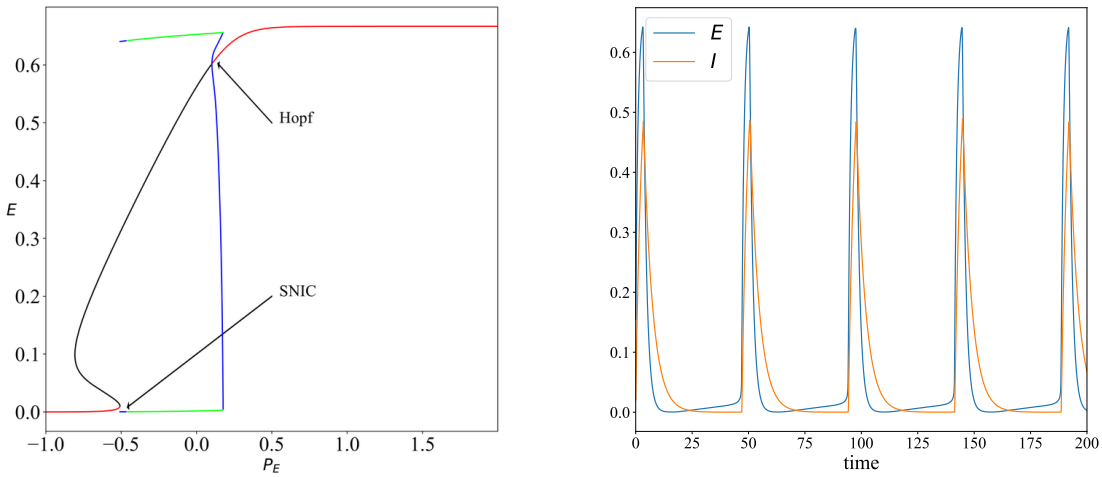

Figure 2.3: Left: Bifurcation diagram of the Wilson–Cowan model showing stable and unstable equilibria (red and black lines) as well as stable and unstable periodic orbits (green and blue lines). The Hopf and saddle-node on invariant cycle (SNIC) bifurcations are highlighted. Right: Oscillations in the Wilson–Cowan model with parameters $\kappa_{EE} = \kappa_{IE} = -\kappa_{II} = 10$, $\kappa_{EI} = -12$, $P_E = 0$, $P_I = -1$, $\alpha_E = 3$, $\alpha_I = 8$, $\beta = 10$, $\theta = 0.05$.

Here, κ_{ab} for $a, b \in E, I$ are coupling strengths, and f is the sigmoid function (2.2). In Figure 2.3, we show that the Wilson–Cowan model supports oscillatory solutions, which can emerge via a Hopf bifurcation or terminate via a SNIC bifurcation. We also show a direct simulation of the model in the oscillatory regime.

Jansen–Rit Model

The Jansen–Rit model [13] extends the Wilson–Cowan framework by modelling three interacting neuronal subpopulations: pyramidal cells (P), excitatory interneurons (E), and inhibitory interneurons (I). It was originally developed to describe EEG activity in the alpha frequency range [13], and has also been used to model pathological brain states such as those observed in epileptic seizures [18]. The model may be written

as:

$$\begin{aligned} Q_E g_P &= \kappa_P f(g_E - g_I), \\ Q_E g_E &= \kappa_E f(w_E g_P) + A, \\ Q_I g_I &= \kappa_I f(w_I g_P), \end{aligned} \tag{2.7}$$

where g_P, g_E, and g_I represent the post-synaptic potentials of the pyramidal, excitatory, and inhibitory subpopulations, respectively. The operators Q_E and Q_I are second-order synaptic filters of the form $Q_a = \left(1 + \alpha_a^{-1} \frac{d}{dt}\right)^2$. The function f denotes the non-linear firing rate function defined in equation (2.2). The parameters κ_P, κ_E, and κ_I are synaptic coupling strengths, and w_E and w_I determine the strength of projections from the pyramidal population to the excitatory and inhibitory interneurons, respectively. The term A represents a constant external input to the excitatory interneurons, often interpreted as input from the thalamus or other brain areas [13]. In Figure 2.4, we show that the Jansen–Rit model supports periodic solutions. Fur-

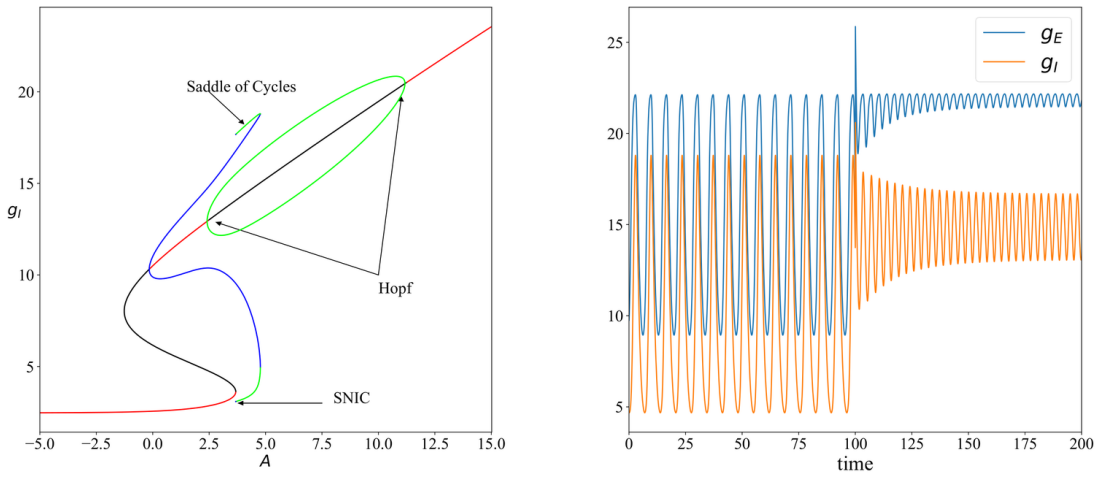

Figure 2.4: Left: One-parameter bifurcation diagram of the Jansen–Rit model showing stable and unstable equilibria (red and black lines) as well as stable and unstable periodic orbits (green and blue lines). Right: A transition between two stable limit cycles induced by applying a small perturbation. Parameters: $A = 4.76$, $\kappa_P = 0.1625$, $\kappa_E = 17.5$, $\kappa_I = 73.51$, $w_E = 135$, $w_I = 34.2$, $\alpha_E = 100$, $\alpha_I = 50$, $\beta = 0.56$, $\theta = 6$.

thermore, there exists a set of parameters where two stable periodic orbits coexist: one with high amplitude and low frequency, and another with low amplitude and high frequency. It is possible to transition between these states by applying a perturbation, as demonstrated in the simulation shown in Figure 2.4. This transition between orbits may be interpreted as a switch between a normal brain state and a seizure state observed in epilepsy [18], [19].

Next-Generation Models

Although the Wilson–Cowan and Jansen–Rit models have been successful in predicting certain aspects of brain dynamics, they are inherently phenomenological, meaning they describe neural activity at a macroscopic level without being directly derived from the underlying biophysical properties of individual neurons. These models are best suited for representing large groups of nearly identical, interconnected neurons that typically operate in a coherent manner. As a result, they are not well suited to studying phenomena associated with changes in synchrony. Newer models based on exact mean-field reductions of integrate-and-fire neuron networks are now becoming popular in the mathematical neuroscience community [20], [21], [22]. One particular example of these so-called *next-generation* models is the one studied by S. Coombes and Á. Byrne [15]. This model is able to capture synchrony related phenomena such as post-movement beta rebound [14]. Another advantage of these models is that they are derived from an underlying network of single neuron models, allowing important biological features to be incorporated at the cellular level. For example, gap junctions [2], [23] and synaptic plasticity [24]. The model is based on a network of quadratic integrate-and-fire (QIF) neurons, which are driven by a voltage-shunted post-synaptic

current and a Lorentzian random variable:

$$\begin{aligned} \tau \frac{\mathrm{d}v_i}{\mathrm{d}t} &= v_i^2 + \eta_i + g(V_{syn} - v_i), \quad \text{if } v_i > v_{th} \text{ then } v_i \leftarrow v_r, \\ Qg &= \frac{\kappa_s}{N} \sum_{j=1}^{N} \sum_{m \in \mathbb{Z}} \delta(t - t_j^m). \end{aligned} \tag{2.8}$$

Here, $g(V_{syn} - v_i)$ is the voltage-shunted post-synaptic current of the ith neuron, v_i represents the voltage of the ith post-synaptic neuron, V_{syn} is the membrane reversal potential, τ is the membrane time constant, Q is a linear differential operator, and g is the membrane conductance and $v_{th} = -v_r \to \infty$ meaning that if $v_j \to \infty$ then neuron j spikes and is reset to $-\infty$. The variables η_i are random variables that determine the natural frequency of each QIF neuron in the network and are drawn from the Lorentzian distribution:

$$L(\eta) = \frac{1}{\pi} \frac{\Delta}{(\eta - \eta_0)^2 + \Delta^2}, \tag{2.9}$$

where η_0 is the location of the peak of the distribution,and Δ is the half-width at half maximum of the distribution. Although other distribution choices can still yield an exact mean-field reduction, the choice of a Lorentzian distribution yield a relatively simple firing rate equation, see [25]. A mean-field reduction using the Lorentzian distribution then leads to the mass model:

$$\begin{aligned} \frac{\mathrm{d}R}{\mathrm{d}t} &= 2RV + \frac{\Delta}{\pi\tau}, \\ \frac{\mathrm{d}V}{\mathrm{d}t} &= \eta_0 + V^2 - \pi^2\tau^2 R^2 + g(V_{syn} - V), \\ Qg &= \kappa_s R. \end{aligned} \tag{2.10}$$

Here R is the mean firing rate, V is the mean membrane potential, and g is the mean synaptic conductance. A similar model, with pulsatile synaptic coupling, has also been formulated and utilised by E. Montbrió *et al.* [21], where they also show that the state

variables R and V relate to the Kuramoto order parameter $Z \in \mathbb{C}$ via the conformal map

$$Z = \frac{1 - \omega^*}{1 + \omega^*}, \tag{2.11}$$

where $\omega = \pi\tau R + iV$, and * denotes the complex conjugate. The population synchrony and phase can therefore be calculated by taking the modulus and angle of Z, respectively. The Kuramoto order parameter is a measure of the synchrony of a population of oscillators and is defined as

$$Z \equiv re^{i\psi} = \frac{1}{N}\sum_{j=1}^{N} e^{i\theta_j}, \tag{2.12}$$

where θ_j is the phase of oscillator j. The variable $r \in [0, 1]$ represents the phase coherence of the oscillators, and the variable ψ is the mean phase of the oscillators. When $r = 0$, there is no synchrony in the population of oscillators, and when $r = 1$, there is total synchrony in the population of oscillators.

The corresponding mass model in the Kuramoto order parameter framework can be derived from a θ-neuron network (for θ-neuron definition, see [26]), which is obtained under the transformation $v_i = \tan(\theta_i/2)$. Equation (2.10) then becomes:

$$\begin{aligned} \frac{dZ}{dt} &= \frac{(Z+1)^2}{2}[-\Delta + i\eta_0 + iV_{syn}g] - i\frac{(Z-1)^2}{2} - g\frac{Z^2-1}{2}, \\ Qg &= \kappa f(Z), \quad f(Z) = \frac{1}{\pi\tau}\frac{1 - Z^*}{1 + Z^*}. \end{aligned} \tag{2.13}$$

A model with two interacting subpopulations can also be constructed in a similar

manner:

$$\begin{aligned}
\frac{\mathrm{d}R_a}{\mathrm{d}t} &= 2R_aV_a + \frac{\Delta_a}{\pi\tau_a}, \\
\frac{\mathrm{d}V_a}{\mathrm{d}t} &= \eta_0^a + V_a^2 - \pi^2\tau_a^2R_a^2 + \sum_{b\in E,I} g_{ab}(V_{syn}^{ab} - V_a), \quad a \in \{E, I\}. \\
Q_{ab}g_{ab} &= \kappa_s^{ab}R_a,
\end{aligned} \tag{2.14}$$

Here the subscripts $a, b \in \{E, I\}$ represent excitatory and inhibitory neuron populations. A full derivation of a next-generation model with gap junction coupling is demonstrated in Chapter 4. For a recent perspective on next-generation neural mass models see [27] z => 3.5

2.4 Neural Mass Networks and Neural Fields

Neural mass models are commonly used to describe the collective behaviour of ensembles of neurons, either within small, arbitrary areas of the brain or across entire brain regions. Whole-brain dynamics are often modelled by linking neural mass models through structural connectivity data (see for example, [28], [29], [30], [31]), which represents the physical connections between different areas of the brain. This creates a network of interconnected neural mass models.

Structural connectivity refers to the anatomical connections between brain regions, typically measured using techniques such as diffusion MRI [32], [33]. On the other hand, functional connectivity describes the statistical dependence or synchrony between activity in different brain regions, often measured through techniques like fMRI or EEG [34].

Networks of neural mass models informed by real-world structural connectivity data have been used to explore the relationship between structural connectivity and func-

tional connectivity [35], [36].

2.4.1 Networks of Neural Mass Models

A general network of neural mass models may be constructed simply as

$$Qu_i = \kappa_s \sum_{j=1}^{N} W_{ij} f(u_j), \tag{2.15}$$

where Q is a differential operator modelling the dynamics of the synapses, f is a firing rate function, u_i is some state variable for the neural mass model on node i, W_{ij} is the connection strength between node i and node j, and κ_s is a positive constant affecting the strength of all the global connections.

Networks of neural mass models have been instrumental in exploring the relationship between functional connectivity, defined as the correlation in time series data between brain regions, and structural connectivity. Simulations have shown that functional and structural connectivity can vary significantly, showing the complexity of their relationship. Attempts to understand the connection between structural and functional connectivity, as well as the influence of local dynamics [37], are common. For instance, in [16], M. Forrester *et al.* present a network of a two population next generation mass model, incorporating real connectivity data from 68 brain regions. Each individual mass model represents a specific brain region. Studies on networks of neural mass models suggest that structural information alone cannot fully explain functional connectivity patterns. Instead, local dynamics are likely to play a crucial role in improving a model's fit to real world functional connectivity data. For example, [31] found that incorporating gap junction coupling into a model improved the alignment between its functional connectivity patterns and real functional connectivity, compared to a model without gap junction coupling. Similarly, [38] demonstrated that in a Wilson Cowan

based network model, balancing local inhibition through a form of synaptic plasticity, alongside the global structural excitatory connection, resulted in a model whose functional connectivity more closely matched empirical data. A review of classical and modern neural mass models can be found in [16].

2.4.2 Framework of Neural Field Models

Neural field models usually take the form of nonlinear integro-differential equations and have been effective in capturing certain qualitative behaviours of neural activity such as binocular rivalry [39], [40], visual hallucinations [41], and modelling EEG and MEG dyanamics [42]. Neural fields contain all the necessary ingredients to support travelling wave solutions as well as many other types of solutions, such as static bumps and a variety of spatio-temporal patterns [43], [44], [45], [46]. Variants date back to Beurle's development in the 1950s [47], Wilson and Cowan's extension [12], and Amari's work in the 1970s [48].

Given the variety of neural mass models, one can construct a variety of neural field models from different mass models. Multi-population models that take into account inhibitory and excitatory neurons, as well as refractoriness, have been studied in detail [12]. These multi-population models can be difficult to mathematically analyse and are computationally expensive. Therefore, in this section, we focus on a single-population sigmoid firing rate-type neural field, in which the state variable $u(\mathbf{r}, t)$ represents local neural activity. This may be expressed in the integral form:

$$u(\mathbf{r}, t) = \int_D \mathrm{d}\mathbf{r}' W(|\mathbf{r} - \mathbf{r}'|) \int_{-\infty}^{t} \mathrm{d}t' \eta(t - t') f(u(\mathbf{r}', t')), \quad \mathbf{r} \in D \subseteq \mathbb{R}^2. \tag{2.16}$$

Here, $W(r)$ is the connectivity function that determines the global spatial interactions in the model, f is the firing rate function (2.2), and $\eta(t)$ is a synaptic filter that is the

Green's function of a linear operator Q, as discussed in Section 2.3.1. Applying the linear operator Q to equation (2.16) leads to the familiar integro-differential form:

$$Qu = \psi, \quad \psi(\mathbf{r}, t) = \int_D \mathrm{d}\mathbf{r}' W(|\mathbf{r} - \mathbf{r}'|) f(u(\mathbf{r}', t)), \quad \mathbf{r} \in D \subseteq \mathbb{R}^2. \tag{2.17}$$

2.4.3 Analytical Tools for Neural Fields

The dynamics exhibited by neural fields can be investigated using a Turing instability analysis. First proposed by Alan Turing in the context of reaction-diffusion equations, this form of analysis allows for the investigation of the linear stability of a homogeneous steady state in a continuum model. It is useful for identifying where bifurcations occur in parameter and the type of patterns that will form beyond the bifurcations. This particular type of analysis is used frequently throughout the main research chapters of this thesis. For a review of analytical tools in neural fields, see [45], [46], [49]).

2.4.4 Brain-Wave Equations

A partial differential equation (PDE) formulation for neural activity that includes axonal delays was proposed by Paul Nunez in 1974 [50] and derived from an integro-differential equation similar to the field model (2.16) in 1996 by V.K. Jirsa and H. Haken [51]. The PDE formulation, called the 'brain-wave equation,' has proven useful for the modelling of EEG data [50] and is also beneficial for computational simulations, as it allows for the use of standard numerical techniques for PDEs instead of the more numerically challenging delayed integro-differential equation. The method for this reformulation uses Fourier transforms in both space and time and exploits the

convolution structure of the delayed integro-differential formulation:

$$\begin{aligned} &Qu(\mathbf{r},t) = \psi(\mathbf{r},t), \\ &\psi(\mathbf{r},t) = \int_D \mathrm{d}\mathbf{r}' W(\mathbf{r}-\mathbf{r}') f \circ u\left(\mathbf{r}', t-|\mathbf{r}-\mathbf{r}'|/c\right), \quad \mathbf{r} \in \mathbb{R}^N, N \in \{1,2\}, \end{aligned} \tag{2.18}$$

where c is the action potential velocity. Detailed derivations of the PDE formulations are shown in [51], [52] and are also demonstrated for a more general model in Chapter 3.

When working in $\mathbb{R}$, it is possible to derive an exact PDE formulation:

$$\left[\left(\frac{1}{\sigma}+\frac{1}{v}\partial_t\right)^2 - \partial_{xx}\right]\psi(r,t) = \left(\frac{1}{\sigma}+\frac{1}{v}\partial_t\right) f \circ u(r,t), \quad r \in \mathbb{R}. \tag{2.19}$$

In two spatial dimensions, using the 2D exponential connectivity function $W(\mathbf{r}) = \exp(-|\mathbf{r}|/\sigma)/2\pi$, taking the Fourier transform leads to a term that resembles $(1 + |\mathbf{k}|^2)^{3/2}$. After an inverse Fourier transform, this leads to a differential operator $(1 - \nabla^2)^{3/2}$. Since it is unclear what raising a differential operator to a non-integer power actually means, we expand $(1 + |\mathbf{k}|^2)^{3/2}$ around $|k| = 0$ and, after removing higher-order terms, obtain $1 + (3/2)|\mathbf{k}|^2$. This is the so-called long-wavelength approximation and leads to the PDE formulation:

$$\left[\left(\frac{1}{\sigma}+\frac{1}{v}\partial_t\right)^2 - \frac{3}{2}\nabla^2\right]\psi(\mathbf{r},t) = f \circ u(\mathbf{r},t), \quad \mathbf{r} \in \mathbb{R}^2. \tag{2.20}$$

2.5 Discussion and Shortcomings of Neural Modelling

In this chapter, we have discussed the basic anatomy of a neuron and how large ensembles of firing neurons can produce measurable signals. Furthermore, we have intro-

duced some neural mass and field models. Although the current generation of neural mass and field models has provided good insight into the behaviour of neural tissue, there are several shortcomings that this thesis aims to address. In later chapters, we will build on some of the models discussed here and further develop these neural mass and field models. Firstly, many neural field models do not account for dendritic depth. The inclusion of dendritic depth in neural models is particularly important because the dendritic tree not only filters incoming synaptic currents but also generates an electrical dipole moment that underlies the EEG signal, a feature that point models cannot replicate due to their inability to represent spatial separations between current sinks and sources. In Chapter 3, we present a model that incorporates this feature and demonstrate how it can generate a more direct measure of LFP/EEG signals. Secondly, we utilise newer mean-field models derived from networks of QIF neurons to include gap junctions, which are known to be important in neural dynamics, especially in the context of synchrony [53]. Despite their importance, gap junctions are often not accounted for in neural mass and field models. Although, phenomenological model of their effect in Wilson-Cowan style neural fields has been developed by Steyn-Ross *et al.* [54], and more recently within the exact next generation mass and field framework has been developed by Laing [23]. This latter work is developed in the theta-neuron framework and requires an ad-hoc regularisation. We will show in Chapter 4, that by working in the voltage framework of quadratic integrate-and-fire neurons that such as regularisation can be circumvented (yielding a model without any unnecessary regularisation parameters). Brain tissue is composed of more than just neurons, for many clinical applications coupling to the extracellular space would be beneficial. For example, extracellular potassium (K^+) is thought to have an important role in the genesis and propagation of seizure states seen in epilepsy [55]. Again, relatively few models incorporate extracellular dynamics, with a notable exception being the work of Martinet

et al. in [56]. In Chapter 6 we pursue this with a natural extension of a the next-generation coupled to a reaction-diffusion equation for extracellular K^+. Furthermore, in 5 we develop and employ a genetic algorithm to fit a next-generation mass model with gap junctions to real MEG data.

CHAPTER 3

A NEURAL FIELD MODEL WITH AXO-DENDRITIC CONNECTIONS

Contemporary biophysical theories propose that EEG signals captured by a single scalp electrode are the result of synchronous activity from around 100 million pyramidal neurons in the brain's cortex. These neurons are positioned so that their dendrites are aligned both parallel to each other and perpendicular to the surface of the cortex. The process of synaptic activation on these dendrites leads to the generation of a net ionic current across the neuron's membrane. This current acts as a sink, generating a negative extracellular potential for excitatory synapses, and as a source, creating a positive extracellular potential for inhibitory synapses. Due to the brain tissue's inability to sustain long-term charge storage, this synaptic current must flow out of the cell, particularly through regions with significant surface area like the soma. Consequently, this outflow establishes a distributed extracellular source or sink, depending on whether the synapse functions as a source or a sink, respectively. The elongated shape of pyramidal neurons typically results in a distinct separation between electri-

cal sinks and sources, which effectively forms a current dipole. As a result, when a group of cortical pyramidal cells is activated simultaneously at the population level, the potential field they generate mimics that of a layer of current dipoles. The role that individual dendritic trees play in creating extracellular electric field potentials has been acknowledged for a while [57]. These contributions to the electric field can be quantified through the application of Maxwell's equations, but are typically not accounted for in neural field models. In the discussion in Section 2.4.2, we explored neural field models that account for synaptic processing but overlook dendritic filtering. However, the emergence of laminar electrodes, which allow for recording across various cortical layers, highlights the need to refine these models to include dendritic depth. This inclusion is crucial for achieving more accurate measures of LFP/EEG. Moreover, the advantages of brain-wave equations, detailed in Section 2.4.4, for the effective and fast simulation of complex neural field models mean that a generalisation of the brain-wave equation proposed by Nunez in [58], by encompassing both axons and dendrites along with their interconnectivity patterns, would be of benefit to the wider neuroscience community. This chapter therefore introduces a model that includes dendritic depth and presents a novel approach to the brain-wave equation. A generalised brain-wave equation is derived and explored numerically. Validation of the numerical method is carried out by a study that compares the equation's predictions on wave propagation speed, using a Heaviside function to model the firing rate, against theoretical expectations. We also employ further numerical investigations to examine the equation's performance in a broader context, specifically focusing on travelling waves. This comprehensive approach allows for a deeper insight into the equation's utility and the behaviour of wave propagation.

The content of this chapter is based on previously published work in [1]. A key part of my role was to build on the foundational analytical work done by my collaborators, in-

troducing numerical experiments for a complex, fully non-linear model. The challenge of simulating this model by computational means was non-trivial, as it involves solving a wave equation in tandem with a diffusive process that operates on the domain that the wave equation is posed on. Additionally, I took on the task of conducting all the detailed numerical spectral and bifurcation analyses in Section 3.5.2.

3.1 Background

In this section, a brief biological description of the function and structure of dendrites is presented, and we also discuss a brief history of dendrite modelling and how we incorporate dendrite models into the neural activity model used here.

3.1.1 Dendrites and Cable Theory

Dendrites are branching, tree-like protrusions of the neuronal cell body and specialise in receiving electrochemical synaptic inputs from presynaptic neurons. When a synaptic input is received at the dendritic terminal, the signal spreads through the structure and ultimately influences the state of the soma of the neuron. A dendritic tree can have up to 200,000 synapses and is the largest volumetric component of neural tissue [59]. Dendrites come in many different morphologies, ranging from compact to wide-reaching, elaborate branching patterns. An example of two neurons with different dendrite structures is given in Figure 3.1.

Mathematical modelling of electrical behaviour in the dendrite dates back to Wilfrid Rall's work in 1962, where the *cable equation* description of the voltage in a dendritic tree was introduced [60]. The uniform cable equation with an injected current may be

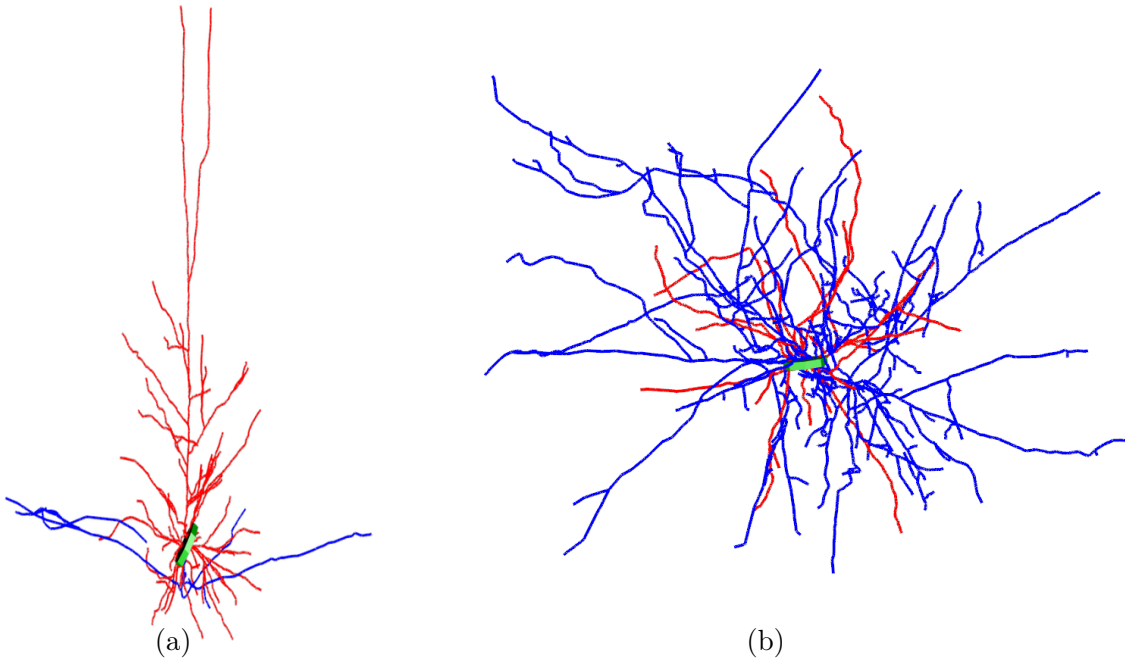

(a) (b)

Figure 3.1: A digital reconstruction of a human (a) pyramidal neuron and (b) interneuron. The colours highlight different anatomical structures of the neurons, with dendrites represented in red, axons in blue, and the soma in green. The neuron morphology data was sourced from https://neuromorpho.org.

written in the form:

$$\frac{\partial}{\partial t}V(x,t) = -\frac{1}{\tau}V(x,t) + D\frac{\partial^2}{\partial x^2}V(x,t) + I(x,t), \tag{3.1}$$

where $V(x,t)$ is the membrane potential at point $x \in \mathbb{R}$ and time t on the cable, $I(x,t)$ is proportional to an external current input, D is the cable diffusion coefficient, and τ is the membrane time constant. These coefficients represent underlying physical properties of the cable, such that $\tau = R_m C_m$, $\lambda = \sqrt{r_c R_m / 2R_f}$, and $D = \lambda^2/\tau$, where R_m is the cell membrane resistance per unit length, C_m is the capacitance per unit length of the cell membrane, λ is the electrical length constant (the distance that a stationary current will influence the potential of the cable), which is typically in the range $0.1 - 1.0$ mm, r_c is the radius of the cable, and R_f is the resistance of the intracellular fluid. Under the assumption of vanishing initial data, e.g. $V(x,0) = 0$,

the solution to the cable equation on an infinite domain may be written as:

$$V(x,t) = (G \otimes I)(x,t), \tag{3.2}$$

where $\otimes$ represents a spatio-temporal integration:

$$(G \otimes I)(x,t) = \int_{-\infty}^{\infty} \mathrm{d}x' \int_{0}^{t} \mathrm{d}t' G(x,x',t,t') I(x',t'), \tag{3.3}$$

and G is the Green's function, $G(x,x',t,t') = G_\infty(x-x',t-t')$, where

$$G_\infty(x,t) = \frac{1}{\sqrt{4\pi D t}} e^{-x^2/(4Dt)} e^{-t/\tau} H(t). \tag{3.4}$$

where H is a Heaviside step-function.

An idealised model for a dendritic tree could simply be a single uniform cable equation posed on a bounded, semi-infinite, or infinite domain, with a soma located at $x = 0$. The first model of a dendrite that Rall considered was a uniform cable equation on a finite domain, where the soma lies at $x = 0$ and dendrite terminals at $x = L$, with boundary conditions $\partial V/\partial x = 0$. In this case, the Green's function is $G(x,x',t,t') = G_\infty(x-x',t-t') + G_\infty(x+x',t-t')$ [60].

Rall then expanded on his work by introducing a so-called compartmental approach, where a dendrite is represented as a chain of equivalent circuits representing successive branches on the dendritic tree [61]. Realistic dendrites can also be modelled by posing the cable equation on a graph and specifying boundary conditions. A Green's function can be constructed by solving a PDE with these boundary conditions using various applied mathematics techniques, which are reviewed by Tuckwell in [62] and Johnston and Wu in [63].

Abbot and colleagues introduced the so-called *sum-over-trips* approach and showed that it is possible to construct Green's functions for arbitrary dendritic branching geometries based on the Green's function of the infinite cable and a set of trip coefficients [64].

3.2 The Model

The model introduced here builds on well-known Wilson–Cowan-type neural fields by introducing a dendritic spatial coordinate $x \in \mathbb{R}$, with $\mathbf{r} \in \mathbb{R}^2$ as the somatic coordinate. Neurons may either be pyramidal (P) or inhibitory (I), and the voltage $V(x, \mathbf{r}, t)$ on the dendrites evolves according to the (previously mentioned) uniform cable equation:

$$\frac{\partial}{\partial t} V_a(x, \mathbf{r}, t) = -\frac{1}{\tau_a} V_a(x, \mathbf{r}, t) + D_a \frac{\partial^2}{\partial x^2} V_a(x, \mathbf{r}, t) + I_a(x, \mathbf{r}, t), \tag{3.5}$$

where $a \in \{P, I\}$ denotes the type of neuron. The input into the cable equation $I_a(x, \mathbf{r}, t)$ is split into excitatory and inhibitory parts:

$$I_a(x, \mathbf{r}, t) = g_{aP}(x, \mathbf{r}, t)(V_+ - V(x, \mathbf{r}, t)) + g_{aI}(x, \mathbf{r}, t)(V_- - V(x, \mathbf{r}, t)). \tag{3.6}$$

Here, V_+ and V_- are positive and negative reversal potentials, respectively, and $g_{ab}(x, \mathbf{r}, t)$ is a conductance that evolves according to the neural field equation:

$$g_{ab}(x, \mathbf{r}, t) = \int_{-\infty}^{t} \mathrm{d}s \eta_{ab}(t - s) \int_D \mathrm{d}\mathbf{r}' W_{ab}(x, \mathbf{r}, \mathbf{r}') f_b(h_b(\mathbf{r}', s - |\mathbf{r} - \mathbf{r}'|/v_{ab})), \quad \mathbf{r} \in D, \tag{3.7}$$

where v_{ab} is the velocity of action potential from population b to a, f_b is a sigmoid firing rate function, $\eta_{ab}(t) = \alpha_{ab}^2 t \exp(-\alpha_{ab} t) H(t)$ is the α-function synaptic filter where H is

a Heaviside step function, and $W_{ab}(x, \mathbf{r}, \mathbf{r}')$ is the axo-dendritic connectivity function between populations a and b. It is chosen as the distribution

$$W_{ab}(x, \mathbf{r}, \mathbf{r}') = W_{ab}^0 w_{ab}(|\mathbf{r} - \mathbf{r}'|)\delta(x - d_{ab} - \kappa_{ab}|\mathbf{r} - \mathbf{r}'|), \tag{3.8}$$

where $d_{ab} \geq 0$ is the contact point on the infinite cable closest to the soma, $W_{ab}^0 > 0$ is a connection strength constant between neuron populations, and $\kappa_{ab} \geq 0$ is the correlation between dendritic and somatic coordinates, incorporating the fact that synapses are located further away from the soma as the separation between neurons increases [65]. This observation is based on findings that, in the olfactory cortex, the recurrent collaterals of pyramidal cells project back onto the basal dendrites of proximal cells and the apical dendrites of more distant pyramidal cells [66]. For $\kappa_{ab} = 0$, there is no correlation between somatic and dendritic coordinates, and synapses occur at a fixed distance d_{ab} from the soma.

h_a is taken to be the potential at $x = 0$, so that $h_a(\mathbf{r}, t) = V_a(0, \mathbf{r}, t)$, where we have fixed the coordinate $x = 0$ as the point on the cable where the soma lies. The function $w_{ab}(\mathbf{r})$ describes how the strength of interactions changes with separation between cell bodies. It is possible to use the Green's function from Equation (3.4) to find $h_a(\mathbf{r}, t)$. However, an explicit formula is not possible due to I_a depending on V_a. By repeated substitution and truncating terms at second order in the conductances, we obtain

$$\begin{aligned} h_a(\mathbf{r}, t) &= (G_a \otimes [g_{aP}V_+ + g_{aI}V_-])(0, \mathbf{r}, t) \\ &- (G_a \otimes \{[g_{aP} + g_{aI}]G_a \otimes [g_{aP}V_+ + g_{aI}V_-]\})(0, \mathbf{r}, t). \end{aligned} \tag{3.9}$$

When simulating the model, we may simply evolve the cable equation and substitute $h_a(\mathbf{r}, t)$ with $V_a(0, \mathbf{r}, t)$. This method is employed in the simulations in Section 3.3 and Section 3.4. A diagram of the model is shown in Figure 3.2.

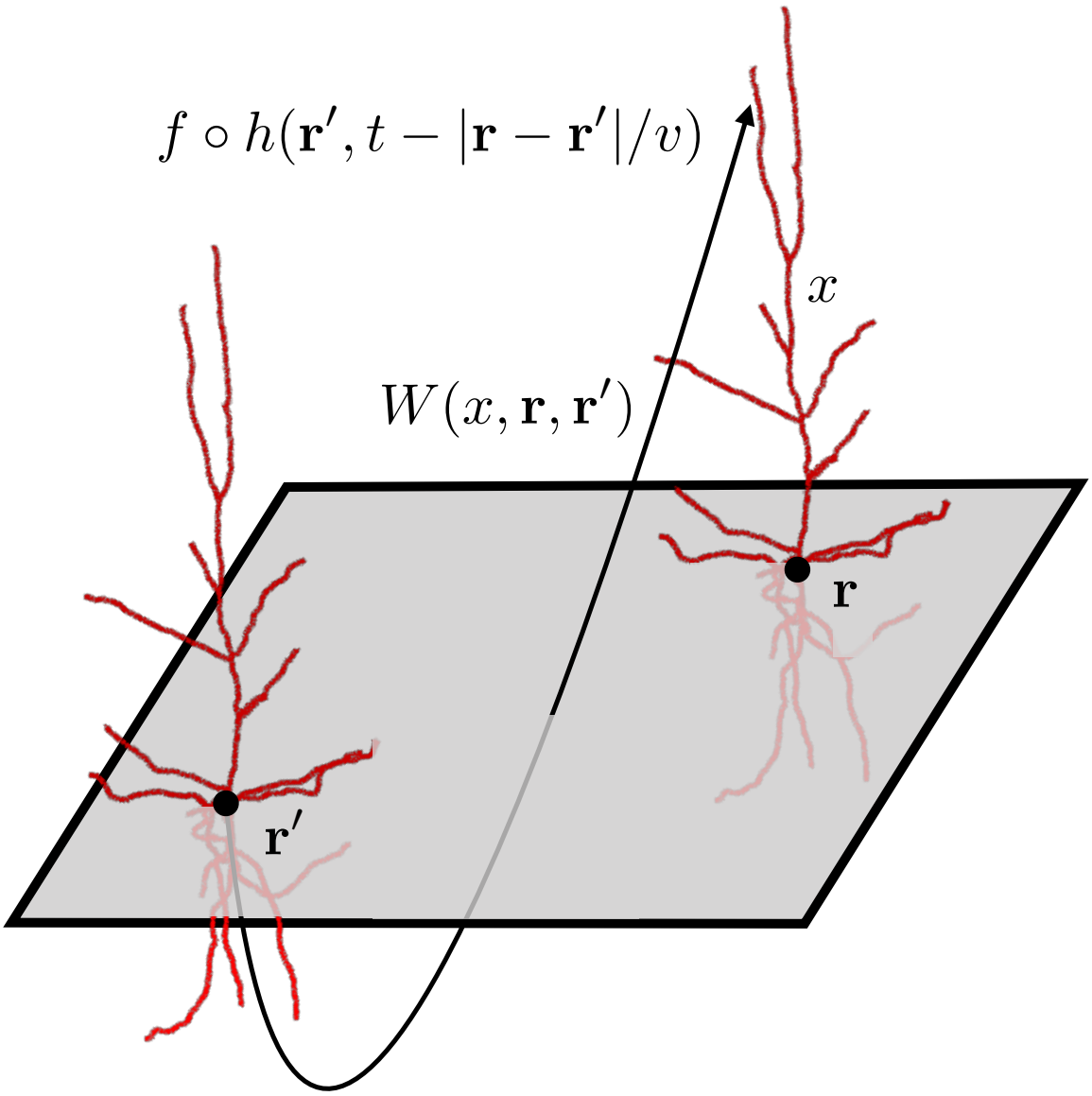

Figure 3.2: A schematic of the neural field model incorporating dendrites. The dendrites are shown with realistic structure, though for simplicity, we only consider idealised unbranched dendrites in the model formulation. The black filled circles indicate the position of the cell body or soma. The black line shows the contact on the dendrite that can be varied with the parameter d_{ab} in our model and $f \circ h$ is the firing rate.

3.2.1 Wave Fronts

Here we study wave fronts in a single population model in one somatic dimension with a second order synaptic filter as discussed in Section 2.3.1 with the exponential connectivity function:

$$w(r) = \frac{\mathrm{e}^{-|r|/\sigma}}{2\sigma} \tag{3.10}$$

To allow for an exact calculation of the speed of the wave front we assume voltage shunting to be absent so that the input into the cable equation is directly proportional to the conductance so that

$$\left(1 + \frac{1}{\alpha}\frac{\partial}{\partial t}\right)^2 I(x,r,t) = \int_{-\infty}^{\infty} \mathrm{d}r' w(r-r')\delta(x - d - \kappa|r-r'|)\times$$
$$f \circ h(r', t - |r-r'|/v), \tag{3.11}$$

where $h(r,t) = V(0,r,t)$. Subscripts have been dropped as only a single population is being considered and we set $W_0 = 1$. The firing rate f is set to a Heaviside function with threshold θ (found in the limit $\beta \to \infty$ of the sigmoid function (2.2)). By utilising the Green's function in equation (3.4) the solution to the cable equation can be expressed as:

$$V(x,r,t) = \int_{-\infty}^{\infty} \mathrm{d}y \int_{-\infty}^{t} \mathrm{d}s G(x-y, t-s) I(y,r,s). \tag{3.12}$$

Combining this and equation (3.11) in integral form leads to the evolution for the somatic potential,

$$h(r,t) = \int_{-\infty}^{\infty} \mathrm{d}y \int_{-\infty}^{\infty} \mathrm{d}r' \int_{0}^{\infty} \mathrm{d}s \int_{0}^{\infty} \mathrm{d}s' G(y,s)\times$$
$$w(r')\delta(y - d - \kappa|r'|)\eta(s') f \circ h(r-', t - s - s' - |r'|/v), \tag{3.13}$$

where $\eta(t) = \alpha^2 t e^{-\alpha t} H(t)$. Travelling front solutions have the form $h(\xi)$ with $\xi = r - ct$, and satisfy the equation:

$$h(\xi) = \int_0^\infty \mathrm{d}s \eta(s) \psi_1(\xi + cs), \tag{3.14}$$

where

$$\psi_1(\xi) = \int_{-\infty}^{\infty} \mathrm{d}z \int_0^\infty \mathrm{d}s G(d + \kappa|z|, s) w(|r|) \times$$
$$f \circ h(\xi - z + cs + c|z|/v). \tag{3.15}$$

In order to simplify the integral, the spatial correlation between the soma and dendrites are not taken into account which means that $\kappa = 0$. This reduces the double integral to

$$\psi_1(\xi) = \int_0^\infty \mathrm{d}s G(d, s) \psi_2(\xi + cs), \tag{3.16}$$

where

$$\psi_2(\xi) = \int_{-\infty}^{\infty} \mathrm{d}z w(r) H[h(\xi - z + c|r|/v) - \theta]. \tag{3.17}$$

By choosing $h(\xi) > \theta$ for ß < 0 and $h(\xi) \leq \theta$ for $\xi \geq 0$ then 3.17 is:

$$\psi_2(\xi) = \begin{cases} \int_{\frac{\xi}{1-c/v}}^{\infty} \mathrm{d}z w(z) & \xi \geq 0, \\ \int_{\frac{\xi}{1+c/v}}^{\infty} \mathrm{d}z w(z) & \xi < 0. \end{cases} . \tag{3.18}$$

Since $h(0) = \theta$ then from (3.14) it is found that

$$\theta = \int_0^\infty \mathrm{d}s \eta(s) \psi_1(cs). \tag{3.19}$$

By introducing a Laplace transform $\widetilde{G}(d,\gamma) = \int_0^\infty dsG_\infty(d,s)\exp(-\gamma s)$ so that from (3.4)

$$\widetilde{G}(d,\gamma) = \frac{\exp(-\Lambda(\gamma)d)}{2\lambda\Lambda(\gamma)}, \quad \Lambda^2(\gamma) = \frac{1/\tau+\gamma}{D} \tag{3.20}$$

we can write

$$\psi_1(\xi) = \frac{1}{2}\widetilde{G}\left(d, \frac{c}{\sigma(1-c/v)}\right)\exp\left(-\frac{\xi}{\sigma(1-c/v)}\right). \tag{3.21}$$

which leads to the implicit equation for wave speed c

$$2\theta = \widetilde{G}\left(d, \frac{c}{\sigma(1-c/v)}\right)\left(\widetilde{\eta}(\frac{c}{\sigma(1-c/v)}\right), \tag{3.22}$$

where $\widetilde{\eta}(\lambda) = \int_0^\infty \mathrm{d}s\eta(s)\mathrm{e}^{-\lambda s}$ is the Laplace transform of $\eta(t)$. This analytical result is compared to numerical results in Figure 3.3.

3.2.2 Generalised Brain-Wave Equation in 2D

As in the previous chapter, it is possible to derive a partial differential equation formulation for the model in two spatial dimensions. The method for deriving the brain-wave equation for this model is similar to that of Section 2.4.4. Using the fact that $\eta_{ab}(t)$ is the Green's function of a linear differential operator Q_{ab}, we may write Equation (3.7) in the form

$$Q_{ab}g_{ab} = \psi_{ab}, \quad \psi_{ab}(\mathbf{r},t) = \int_{-\infty}^{\infty}\mathrm{d}s\int_{\mathbb{R}^2}\mathrm{d}r'\Omega_{ab}(|\mathbf{r}-\mathbf{r}'|,x,t-s)\times f_b(h_b(\mathbf{r}',s)), \quad \mathbf{r}\in\mathbb{R}^2, \tag{3.23}$$

where

$$\Omega_{ab}(x,\mathbf{r},t) = W(x,\mathbf{r})\delta(t-|\mathbf{r}|/v_{ab}), \tag{3.24}$$

and

$$W_{ab}(x,\mathbf{r}) = W^0_{ab} w_{ab}(\mathbf{r})\delta(x - d_{ab} - \kappa_{ab}|\mathbf{r}|), \tag{3.25}$$

where $w_{ab}(\mathbf{r}) = \exp(-|\mathbf{r}|/\sigma_{ab})/2\pi\sigma^2_{ab}$. A Fourier transform in the following form is introduced:

$$\mu(x,\mathbf{r},t) = \frac{1}{2\pi}\int_{-\infty}^{\infty} \mathrm{d}p \mathrm{e}^{ipx}\widehat{\mu}(\mathbf{r},p,t), \tag{3.26}$$

so that

$$\widehat{\psi}_{ab}(\mathbf{r},p,t) = \int_{-\infty}^{\infty}\mathrm{d}s\int_{\mathbb{R}^2}\mathrm{d}\mathbf{r}' H_{ab}(|\mathbf{r}-\mathbf{r}'|,p,t-s)\rho_b(\mathbf{r}',s), \tag{3.27}$$

where

$$H_{ab}(\mathbf{r},p,t) = W^0_{ab} e^{-ip(d_{ab}+\kappa|\mathbf{r}|)} w_{ab}(r)\delta(t-|\mathbf{r}|/v_{ab}), \tag{3.28}$$

and $\rho_b(\mathbf{r},t) = f_b(h_b(\mathbf{r},t))$. By taking further Fourier transforms with respect to $\mathbf{r}$ and t, we obtain

$$\widehat{\psi}_{ab}(k,p,\omega) = \widehat{H}_{ab}(k,p,\omega)\widehat{\rho}_b(k,\omega), \tag{3.29}$$

where

$$\widehat{H}_{ab}(k,p,\omega) = \frac{W^0_{ab}}{\sigma_{ab}}\frac{A_{ab}(p,\omega)}{(A^2_{ab}(p,\omega)+k^2)^{3/2}}\mathrm{e}^{ipd_{ab}}, \tag{3.30}$$

and $A_{ab}(p,\omega) = 1/\sigma_{ab} + i\omega/v_{ab} + ip\kappa_{ab}$. By cross-multiplying, utilising the long-wavelength approximation, as discussed in Section 2.4.4, expanding $\widehat{H}_{ab}(k,p,\omega)$ around $k=0$, and taking the inverse Fourier transform, we find that

$$\left[\mathcal{A}^2_{ab} - \frac{3}{2}\nabla^2\right]\psi_{ab}(x,\mathbf{r},t) = \frac{W^0_{ab}}{\sigma_{ab}}\delta(x-d_{ab})f_b(h_b(\mathbf{r},t)), \tag{3.31}$$

where

$$\mathcal{A}_{ab} = \frac{1}{\sigma_{ab}} + \frac{1}{v_{ab}}\frac{\partial}{\partial t} + k_{ab}\frac{\partial}{\partial x}.$$

A similar method can be employed to find the wave equation in $\mathbb{R}$ using the connectivity function $w_{ab}(r) = \exp(-|r|/\sigma_{ab})/2\sigma_{ab}$ to obtain the PDE

$$\left(\left[\mathcal{A}_{ab}^2 - \frac{\partial^2}{\partial r^2}\right]\right)\psi_{ab}(x,r,t) = \frac{W_{ab}^0}{\sigma_{ab}}\Big[\left(\frac{1}{\sigma_{ab}} + \kappa_{ab}\frac{\partial}{\partial x}\right)\times \\ \delta(x-d) + \frac{1}{v_{ab}}\frac{\partial}{\partial t}\Big] f_b \circ h_b(r,t). \quad (3.32)$$

Unlike in $\mathbb{R}^2$, a long-wavelength approximation is not needed, and the wave equation in $\mathbb{R}$ is exact.

3.3 Numerics

In this section, we discuss the numerical method for solving the PDEs in this chapter and provide verification that our numerical method is accurate by comparing numerical results with some theoretically derived results.

3.3.1 Numerical Scheme and Method

Here, we describe the numerical scheme for evolving a single population with only excitatory interactions. This allows us to suppress the indices a, b, although the extension to include inhibition is straightforward by generalising the scheme below.

We note that expanding the differential operator $\mathcal{A}^2$ in Equations (3.32) and (3.31) gives rise to a so-called 'negative diffusion' term that, if not handled appropriately, could lead to numerical instabilities. To circumvent this potential numerical issue, we write $\mathcal{A}^2\psi$ in the coupled form $\mathcal{A}^2\psi = \mathcal{A}y$, where $y = \mathcal{A}\psi$, which transforms the negative diffusion term into two advection terms that are far more numerically stable.

After spatial discretisation, the model in two spatial dimensions (one somatic and one dendritic dimension), given by (3.32), takes the form of a system of coupled first-order ordinary differential equations, which can be written as

$$\begin{aligned}
\frac{\mathrm{d}Y_1}{\mathrm{d}t} &= -v\left(\frac{1}{\sigma}U + k\Delta_x^{(b)}U - \Delta_{rr}^{(c)}\psi \right.\\
&\qquad \left. -\frac{W^0}{\sigma^2}f(V_0-h)\delta(x-d) - \frac{W^0\kappa}{\sigma}\Delta_x^{(b)}f(V_0-h)\delta(x-d)\right),\\
\frac{\mathrm{d}\psi}{\mathrm{d}t} &= -v\left(\frac{1}{\sigma}\psi + k\Delta_x^{(b)}\psi - U\right),\\
\frac{\mathrm{d}Y_2}{\mathrm{d}t} &= \alpha(\psi - Y_2),\\
\frac{\mathrm{d}g}{\mathrm{d}t} &= \alpha(Y_2 - g),\\
\frac{\mathrm{d}V}{\mathrm{d}t} &= -\frac{V}{\tau} + D\Delta_{xx}^{(c)}V + I,
\end{aligned} \tag{3.33}$$

where $I = g(V_+ - V)$, $U = Y_1 + W^0 f(V_0 - h)\delta(x-d)/\sigma$, $V_0 = V(0,x,t)$, and $\Delta_x^{(b)}$ is the first-order backward difference operator acting on x. The operators $\Delta_{rr}^{(c)}$ and $\Delta_{xx}^{(c)}$ are second-order central difference operators in the r and x directions, respectively.

Here, the variables (Y_1, ψ, Y_2, g, V) are interpreted as vectors on the corresponding (uniform) spatial meshes.

A similar approach may be taken for the three-dimensional model (two somatic dimensions and one dendritic dimension), given by (3.31). This yields essentially the same equations, with finite-difference operators along the x direction replaced by the Kronecker sum of the second-order central difference operators along the r_1 and r_2 directions, which we denote by $\Delta_{\mathbf{rr}}^{(c)}$, and the further replacement:

$$\begin{aligned}
\frac{\mathrm{d}Y_1}{\mathrm{d}t} &= -v\left(\frac{1}{\sigma}Y_1 + k\Delta_r^{(b)}Y_1 - \frac{3}{2}\Delta_{\mathbf{rr}}^{(c)}\psi - \frac{W}{\sigma^2}f(V_0-h)\delta(x-d)\right),\\
\frac{\mathrm{d}\psi}{\mathrm{d}t} &= -v\left(\frac{1}{\sigma}\psi + k\Delta_r^{(b)}\psi - Y_1\right).
\end{aligned} \tag{3.34}$$

Here, $V_0 = V(0, \mathbf{r}, t)$. The time integration was performed using an adaptive solver from the Julia package DifferentialEquations.jl [67], [68]. The delta function was approximated using the Gaussian distribution:

$$\delta_a(x) = \frac{1}{|\Delta x|\sqrt{\pi}} \exp(-\left(x^2/\Delta x^2\right)), \tag{3.35}$$

which preserves the normalisation property of the delta function for $|\Delta x| \ll 1$.

Care must also be taken when considering the boundary conditions for the PDE. Since the Fourier transforms were performed on an infinite domain, periodic boundaries are suitable in the somatic spatial dimension. The electronic length of the cable equation is known to be $\sqrt{D\tau}$ [69]. Therefore, Neumann boundary conditions may be applied on the dendritic boundaries as long as the dendrite boundary coordinates $X_\pm$ satisfy the condition $|d - X_\pm| > \sqrt{D\tau}$.

3.3.2 Verification of the Numerical Method

To verify the numerical scheme, simulated wave speeds were compared to analytical results from the analytical results in Section 3.2.1 using the one-somatic-dimension wave equation:

$$\left(\left[\frac{1}{\sigma} + \frac{1}{v}\frac{\partial}{\partial t}\right]^2 - \frac{\partial^2}{\partial r^2}\right)\psi(x, r, t) = \left[\left(\frac{1}{\sigma}\right)\delta(x - d) + \frac{1}{v}\frac{\partial}{\partial t}\right] H(V(0, r, t) - \theta), \tag{3.36}$$

$$\left(1 + \frac{1}{\alpha}\frac{\partial}{\partial t}\right)^2 I(x, r, t) = \psi(x, r, t), \quad \frac{\partial}{\partial t} I(x, r, 0) = 0. \tag{3.37}$$

The speed of the wave was compared for varying values of the threshold θ of the firing rate function and input position d. In these simulations, the system was initialised with a pulse input and was allowed to evolve for a sufficient amount of time such that

any residual effects on the wave due to initial conditions were negated.

The wave speeds from the implicit equation (3.22) were found using a root-finding algorithm. The results are shown in Figure 3.3, where it can be seen that there is excellent agreement between the numerical wave speed and the theoretical wave speed. We can therefore be confident in the accuracy of our numerical scheme.

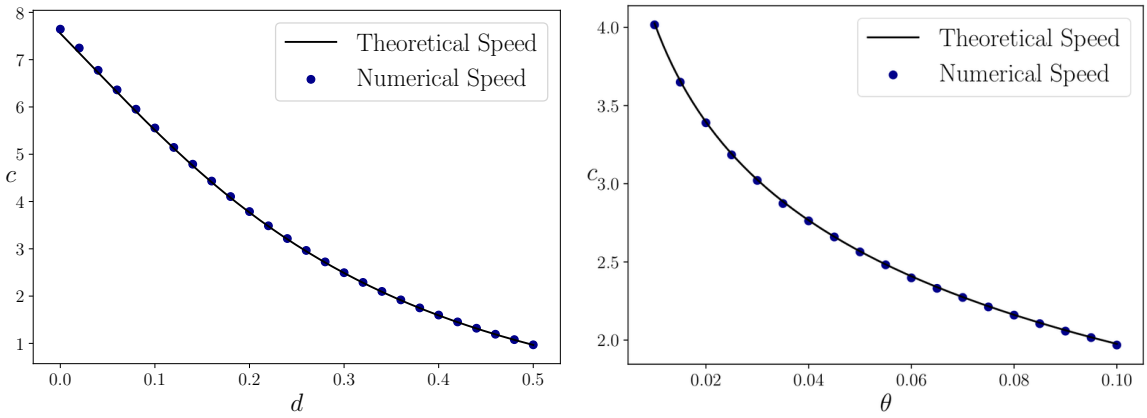

(a) (b)

Figure 3.3: Front wave speed comparison of theory vs. numerical simulation for the model in two spatial dimensions (one somatic and one dendritic dimension) with a Heaviside firing rate. Here, the dendritic input current is $I(x, r, t) = g(x, r, t)$, and $\kappa = 0$ when (a) the input position d changes and (b) the threshold of the Heaviside function θ changes. Parameters: $W_0 = 1$, $v = 8$, $\alpha = 1$, $\Delta x = 0.01$, with $X_\pm = \pm 1$, (a) $\theta = 0.001$, and (b) $d = 0$.

3.4 Simulation and Results

In this section we begin a computational investigation of a more general model. This more general model reintroduces the voltage shunts and uses a sigmoidal firing rate function instead of the Heaviside function.

3.4.1 One Somatic Dimension

We begin by exhibiting a travelling wave in a single somatic spatial dimension. In Figure 3.4 we show snapshots in time of a wave front in both the conductance variable g and the voltage variable V. We see a travelling wave initiated with a Gaussian bump of activity in the centre of the somatic spatial domain spreading in both of the somatic space directions. We also see a spread of activity away from the soma along the dendrite. We now exhibit some further computational experiments on the relation between various parameters and wave front speed, c. We see in Figure 3.5 the effect of increasing κ at contact distances $d = 0.0$, $d = 0.02$, $d = 0.04$ and $d = 0.06$ For all of these values of d we find that wave speed is largest for smaller values of d and also that wave speed decreases with increasing κ for all values of d. In Figure 3.6 the effects of changing the time-to-peak of the synapse α^{-1} for three values of the cable equation diffusion parameter, $D = 1 \times 10^{-4}$, $D = 9 \times 10^{-4}$, $D = 1 \times 10^{-2}$. For all of these values of the cable equation diffusion parameter we see that the wave front speed decreases as the time-to-peak of the synapses increases. In Figure 3.7 we demonstrate the effect of changing the reversal potential on the wave front speed. We find that as the reversal potential increases, wave front speed also increases. When considering the variation of the correlation strength κ we find that for $\kappa = 0$ the peak of the wave response along the dendrite occurs at a distance d from the soma, as expected. However, with an increase in κ this peak response shifts slightly away from d to a larger distance from the soma. We illustrate this effect in Figure 3.8, where we also see an increase in the width of the activity that spreads into the dendrite away from the contact point at $r = d$.

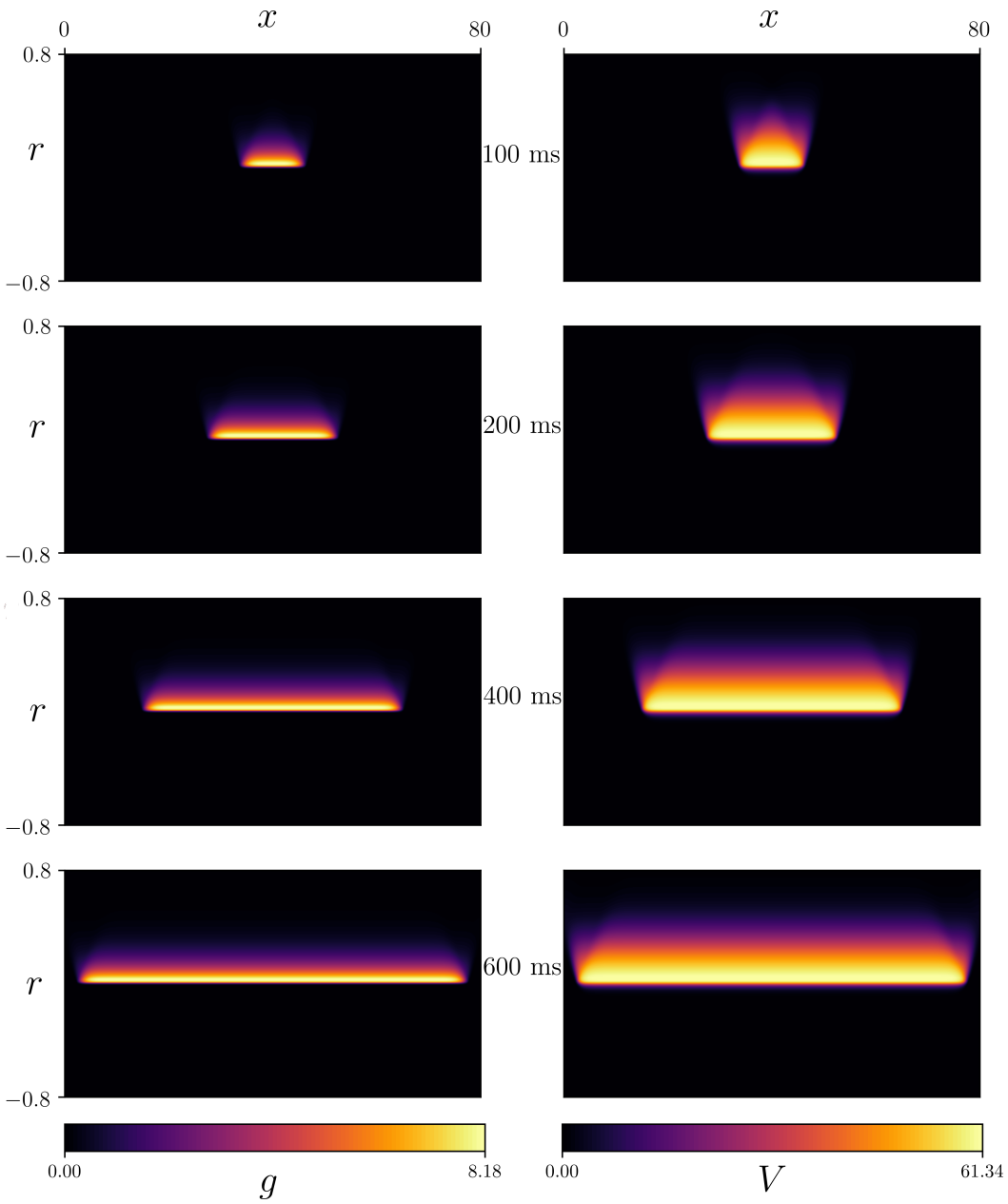

Figure 3.4: Travelling wave in the model with 2 spatial dimensions (one somatic and one dendritic dimension) shown for conductance (left) and voltage (right) with a shunted current $I(x,r,t) = (V_+ - V(x,r,t))g(x,r,t)$ and a sigmoidal firing rate. Parameters: $V_+ = 70$, $W^0 = 1$, $\kappa = 0.1$, $v = 8$, $\alpha = 1$, $\Delta r = 0.01$, $d = 0.02$, $X_\pm = \pm 0.8$, $\beta = 100$, and $\theta = 0.15$.

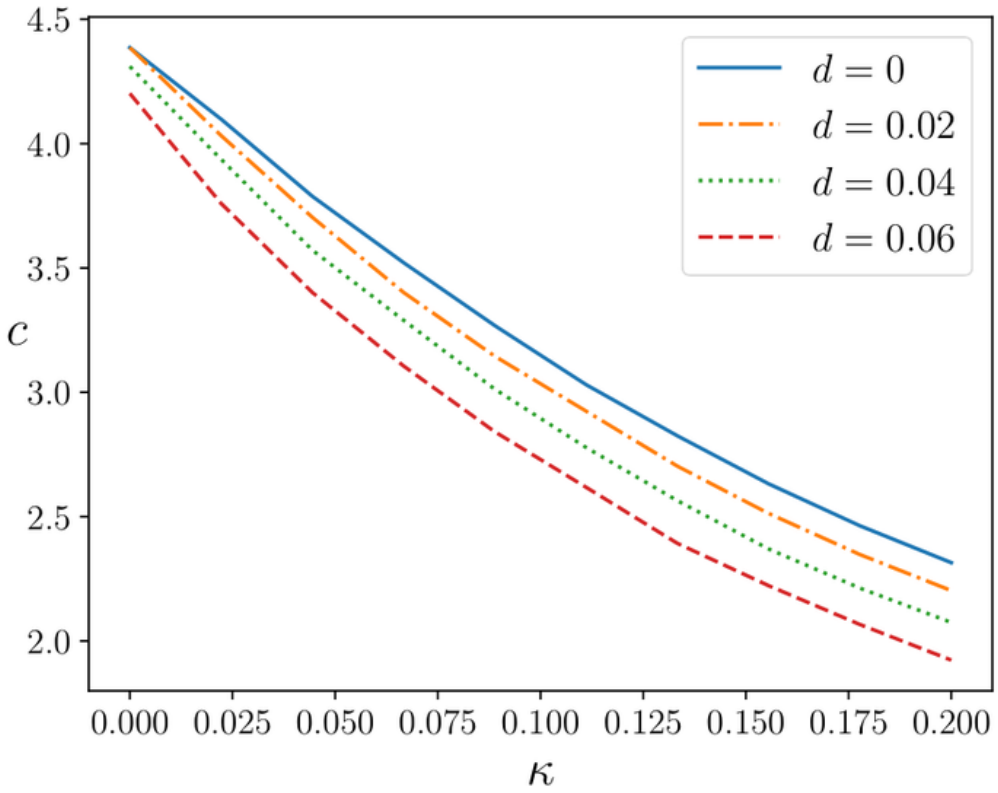

Figure 3.5: Wave front speed as the correlation strength κ is increased for various values of the synaptic contact parameter d with $I(x,r,t) = g(x,r,t)$ and a Heaviside firing rate function. Parameters: $W^0 = 5$, $v = 8$, $\alpha = 1$, $\Delta r = 0.02$, $X_\pm = \pm 1$, and $\theta = 0.01$.

3.4.2 Two Somatic Dimensions

Finally, we present a simulation of a travelling wave in two somatic spatial dimensions. In Figure 3.9 slices through the dendritic dimension at $x = 0.01$, $x = 0.02$, $x = 0.03$ of a travelling wave solution are shown where $d = 0.02$. We again show both the conductance and voltage state variables. We see clearly the effect shown in Figure 3.8 with the largest magnitude of the wave occurring above the contact point d.

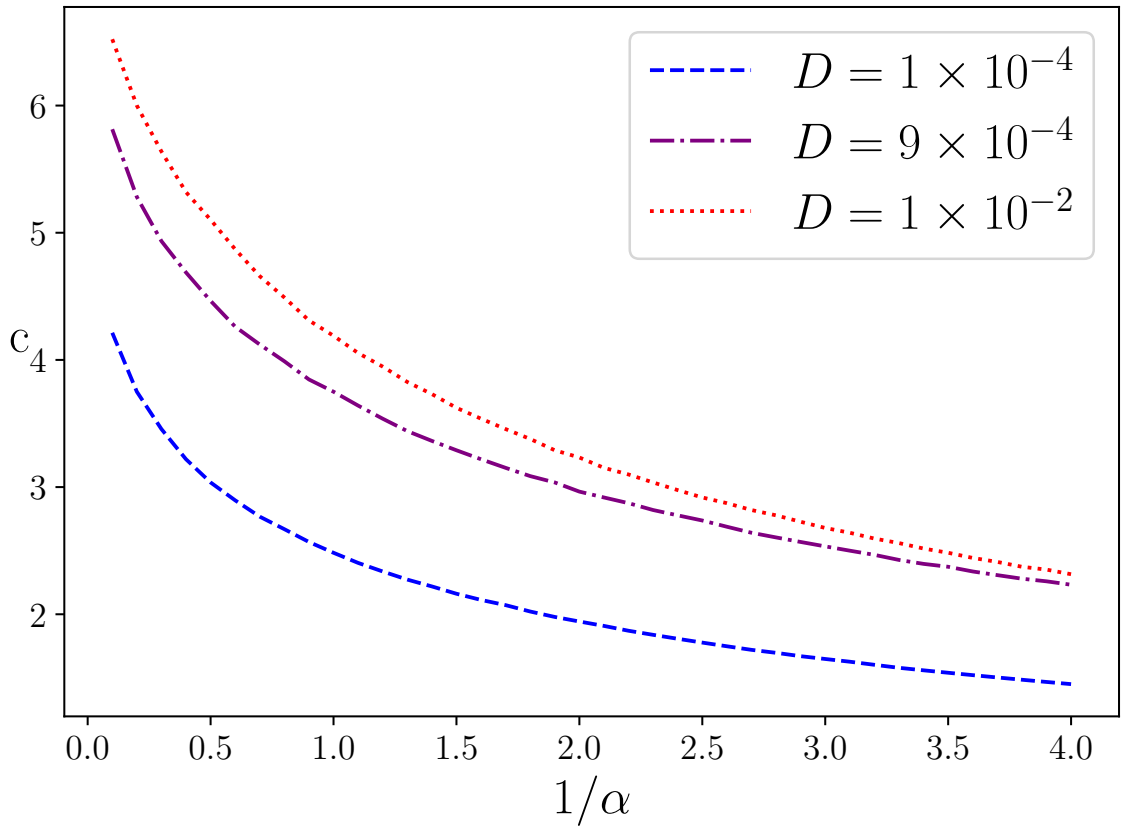

Figure 3.6: Wave front speed with an increase in the synaptic time-to-peak α^{-1} with $I(x,r,t) = g(x,r,t)$, a Heaviside firing rate, and three differing electrotonic lengths. Parameters: $W^0 = 3$, $\kappa = 0$, $v = 8$, $\Delta r = 0.01$, $d = 0.03$, $X_\pm = \pm 0.5$, and $\theta = 0.01$.

3.5 Two population model

We now turn our attention to the full two population model. In particular we will be investigating spatial and spatio-temporal patterns that form from an instability of a homogeneous steady state of the model. We consider a revised version of the model introduced in Section 3.2 where an external conductance g_{ext}^{ab} has been added and for simplicity voltage shunts have been dropped so that the model can now be written

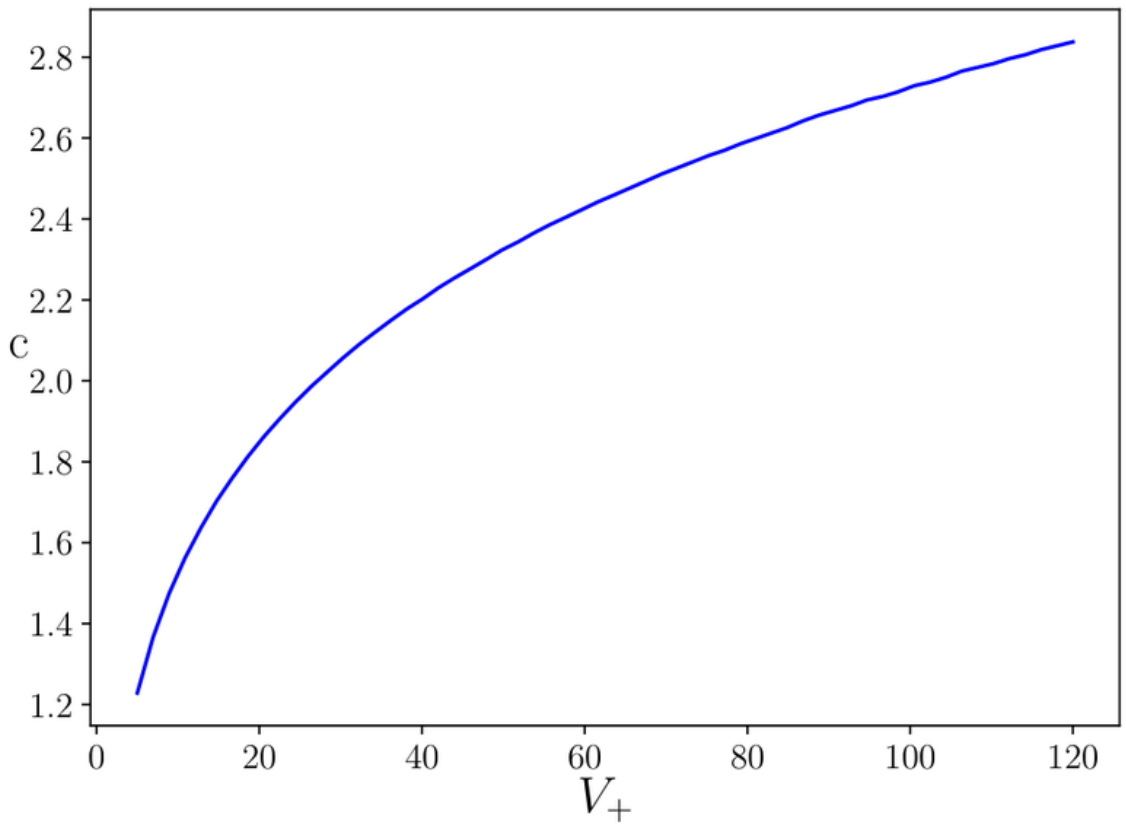

Figure 3.7: Wave front speed in a model with a shunted current $I(x,r,t) = (V_+ - V(x,r,t))g(x,r,t)$ as a function of the excitatory synaptic reversal potential V_+ , with a sigmoid firing rate. Parameters: $W^0 = 4$, $\kappa = 0.1$, $v = 8$, $\alpha = 1$, $\Delta r = 0.01$, $d = 0.04$, $X_\pm = \pm 0.5$, $\beta = 100$, and $\theta = 0.15$.

as:

$$\begin{aligned} g_{ab}(x,r,t) &= g^{ab}_{\text{ext}} + \int_{-\infty}^{t} \mathrm{d}s \eta_{ab}(t-s) \int_{\mathbb{R}} \mathrm{d}r' W_{ab}(x,r,r') f_b(h_b(r', s - |r-r'|/v_{ab})), \\ \frac{\partial V_a}{\partial t} &= -\frac{V_a}{\tau} + D\frac{\partial^2 V_a}{\partial x^2} + I_a(x,r,t). \end{aligned} \tag{3.38}$$

Here, $I_a(x,r,t) = g_{aP}V_+ + g_{aI}V_-$.

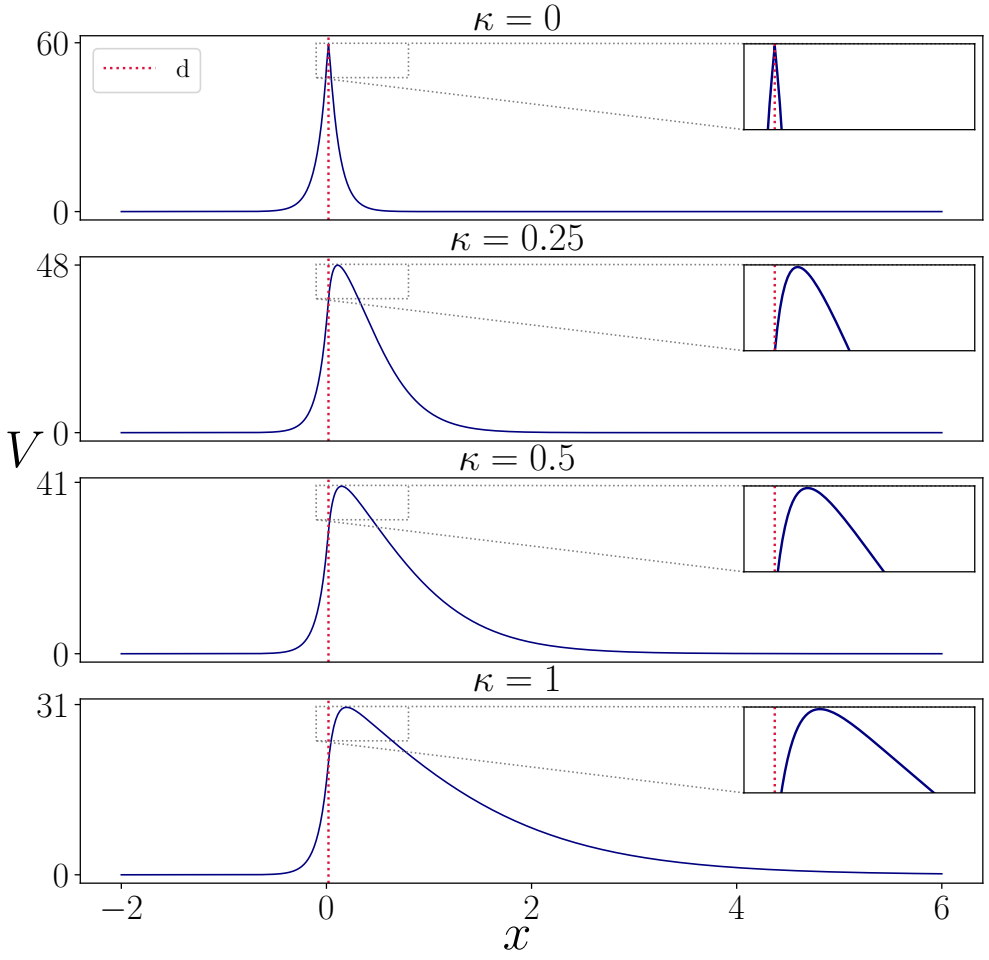

Figure 3.8: Slices along the r dimension of a voltage front where it can be seen that increasing κ causes the peak response to shift away from d (marked as the red vertical dotted line) and away from the soma. Parameters: $V_+ = 70$, $W^0 = 4$, $v = 8$, $\alpha = 1$, $\Delta r = 0.01$, $d = 0.02$, $X_- = -2$, $X_+ = 6$, $\beta = 100$, and $\theta = 0.1$.

3.5.1 Turing Instability Analysis

To ensure that a homogeneous steady state exists in the model we use the firing rate function,

$$f_a(x) = \tanh(\beta_a x), \tag{3.39}$$

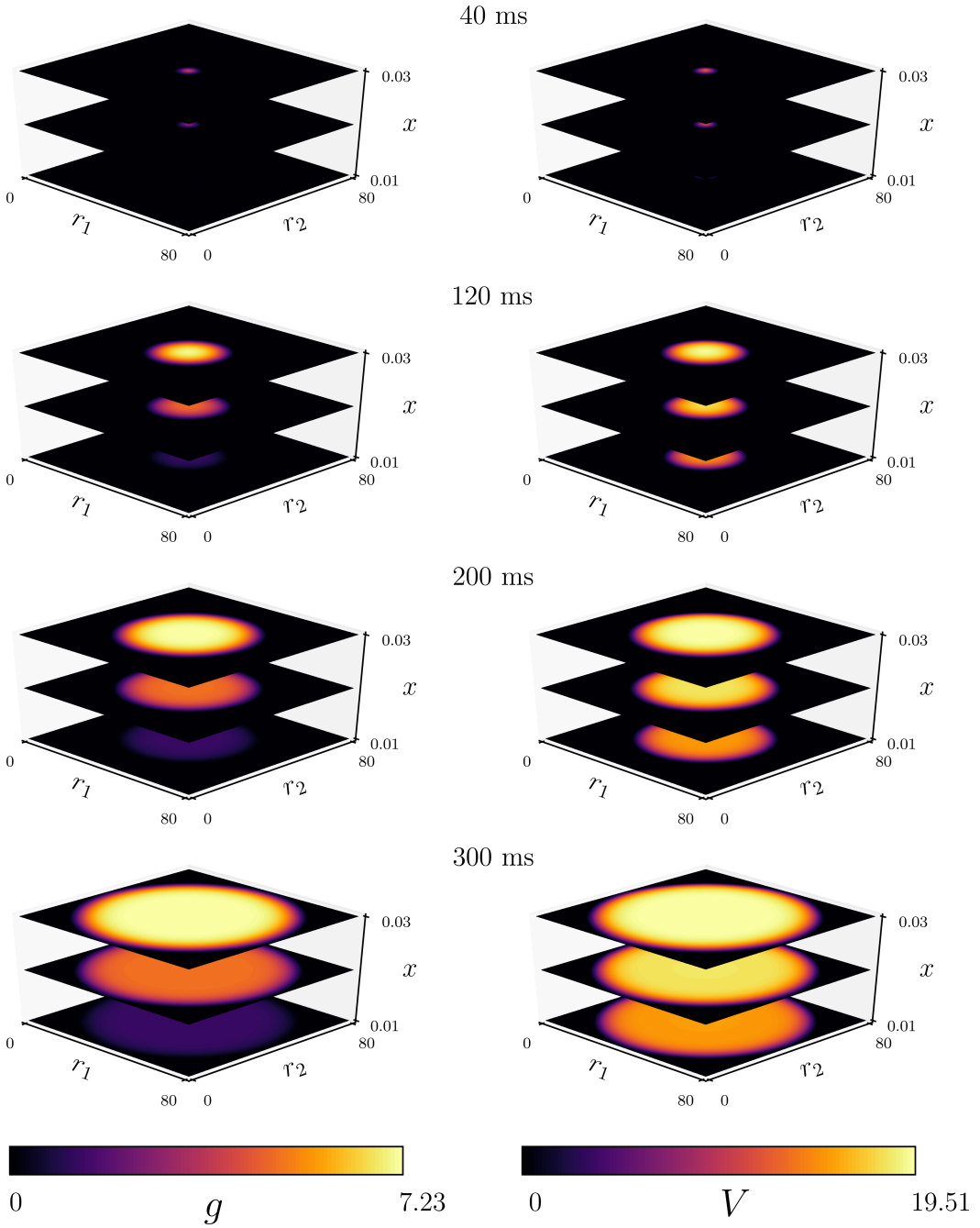

Figure 3.9: Travelling wave in the 3 dimensional model (two somatic and one dendritic), with a sigmoid firing rate, shown for conductance (left) and voltage (right) with $I(x,r,t) = (V_+ - V(x,r,t))g(x,r,t)$. Parameters: $V_+ = 70$, $W^0 = 1$, $\kappa = 0.1$, $v = 8$, $\alpha = 1$, $\Delta r = 0.01$, $d = 0.02$, $X_\pm = \pm 0.5$, $\beta = 100$, and $\theta = 0.15$.

and by choosing $V_- = -V_+$ and $g^{ab}_{\text{ext}} = g_{\text{ext}}$ we ensure that the homogeneous steady state is found at $(g_{ab}, h_b) = (g_{\text{ext}}, 0)$. We apply a small perturbation to the steady

state of the form $h_a = \bar{h}_a e^{\lambda t} e^{ikr}$ where $\bar{h}_a \ll 1$ and $\lambda = \mu + i\omega$. The perturbations in the conductances take the form $g_{ab} = \bar{g}_{ab} e^{\lambda t} e^{ikr}$ where

$$\bar{g}_{ab} = \widetilde{\eta}_{ab}(\lambda)\widehat{W}_{ab}(x, \lambda, k)\beta_b \bar{h}_b, \tag{3.40}$$

and

$$\widetilde{\eta}_{ab}(\lambda) = \int_0^\infty \mathrm{d}s \eta_{ab}(s) e^{-\lambda s} = \frac{\alpha_{ab}^2}{\alpha_{ab}^2 + \lambda^2}, \tag{3.41}$$

$$\widehat{W}_{ab}(x, \lambda, k) = \int_{\mathbb{R}} \mathrm{d}r' W_{ab}(x, |r'|) e^{ikr'} e^{-\lambda |r'|/v_{ab}}. \tag{3.42}$$

Remembering that h_a can be expressed using the Green's function (G_a) of the cable equation:

$$\begin{aligned} h_a(r,t) &= (G_a \otimes [g_{aP}V_+ + g_{aI}V_-])(0, \mathbf{r}, t) \\ &- (G_a \otimes \{[g_{aP} + g_{aI}]G_a \otimes [g_{aP}V_+ + g_{aI}V_-]\})(0, \mathbf{r}, t). \end{aligned} \tag{3.43}$$

To first order in the perturbations we find that,

$$\bar{h}_a = V_+ \bar{h}_P \beta_P \widetilde{\eta}_{aP} F_{aP}(k, \lambda) + V_- \bar{h}_I \beta_I \widetilde{\eta}_{aI} F_{aI}(k, \lambda),$$

and

$$F_{ab}(k, \lambda) = \int_0^\infty \mathrm{d}y \widetilde{G}(y, \lambda) \widehat{W}(y, \lambda, k),$$

where

$$\widetilde{G}(x, \lambda) = \frac{1}{D_a \epsilon_a(\lambda)} \exp(-\epsilon_a(\lambda)|x|),$$

and

$$\epsilon_a^2(\lambda) = \frac{\frac{1}{\tau_a} + \lambda}{D_a}.$$

Using the connectivity function

$$W(x,|z|) = W^0_{ab}\delta(x - d_{ab} - \kappa_{ab}|z|)\exp(-|z|/\sigma_{ab})/2\sigma_{ab},$$

we have

$$F_{ab}(k,\lambda) = \frac{W^0_{ab}}{\sigma_{ab}}\widetilde{G}(d,\lambda)\frac{\mathcal{A}_{ab}(\lambda)}{\mathcal{A}_{ab}(\lambda)^2 + k^2}, \tag{3.44}$$

where $\mathcal{A}_{ab} = 1/\sigma_{ab} + \lambda/v_{ab} + \kappa_{ab}\epsilon_a(\lambda)$. The continuous spectrum $\lambda = \lambda(k)$ can be found by solving the equation

$$\mathcal{E}(k,\lambda) = \det(\mathcal{D}(k,\lambda)V_D - I),$$

where $V_D = \mathrm{diag}(V_+, V_-)$ and,

$$\mathcal{D}(k,\lambda)_{ab} = \beta_b\widetilde{\eta}_{ab}(\lambda)F_{ab}(\lambda,k).$$

The system undergoes a bifurcation when a solution branch $\lambda(k)$ of $\mathcal{E}(k,\lambda)$ touches the imaginary axis, $\mu(k_c) = 0$, where k_c is the critical wave number. Bulk oscillation can be found beyond a Hopf bifurcation which occurs when $k_c = 0$ and $|\omega(k_c)| > 0$, spatio-temporal oscillations can be found beyond a a Turing-Hopf bifurcation which occurs when $|k_c| > 0$ and $|\omega(k_c)| > 0$ and static patterns can be found beyond a Turing bifurcation which occurs when $|k_c| > 0$ and $|\omega(k_c)| = 0$.

3.5.2 Bifurcations and Numerical Simulations

We now present bifurcations found with various parameter configurations and simulations close to those bifurcations. We first turn our attention to the case where $\sigma_{Ea} > \sigma_{Ia}, a \in \{E, I\}$, that is when the excitatory neurons have a wider spatial reach

than inhibitory neurons. In Figure 3.10 we show the spectrum of system at a Hopf bifurcation. We also show two views of a simulation just beyond this bifurcations, the first view shows a snapshot in time of the $x - r$ dimension. The second view shows a time series of the simulation in the r dimension at $x = 0.1$. Further simulations using these parameters for state variable g_{EE}, g_{IE}, g_{EI}, and g_{II} can be found in appendix A. Decreasing the conductance velocity v_{ab} can lead to the formation of spatio-temporal patterns that form via a Turing-Hopf bifurcation. In Figure 3.11 we show the spectrum of the system at a Turing-Hopf bifurcation as well as two views of simulations in the V_E variable just beyond the bifurcation. The first view is a snapshot in time of the standing wave patterns that form beyond the Turing-Hopf bifurcation in the $x-r$ dimension view. The second view is a time series showing how the standing wave solution evolves in time in the r dimension at $x = 0.1$ over 250ms. Again, Further simulations using these parameters for state variable g_{EE}, g_{IE}, g_{EI}, and g_{II} can be found in appendix A.

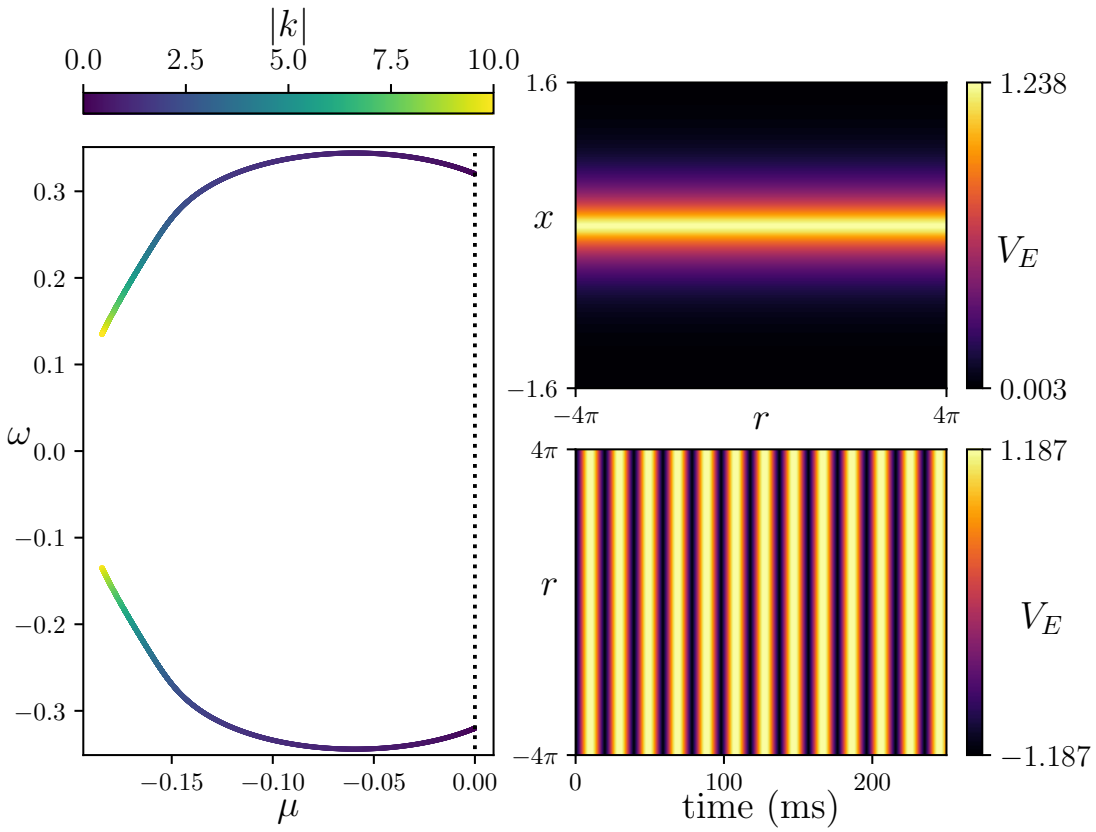

Figure 3.10: Left: The spectrum of the system at a Hopf bifurcation that occurs at $|k| = 0$ where μ and ω are the real and complex parts of the spectrum respectively , when $\beta_E = \beta_I = 0.295$. Right top: A snapshot in time of the standing wave patterns in the V_E variable found just beyond the bifurcation at $\beta_E = \beta_I = 0.31$. Right bottom: Simulation showing the bulk oscillations evolving in time in the V_E variable on a slice along the dendrite axis at $x = d_{EE}$. The oscillations were initiated by perturbing the steady state uniformly with a value of 0.01. Parameters: $\alpha_{EE} = 0.5, \alpha_{EI} = 0.5, \alpha_{IE} = 0.7, \alpha_{II} = 0.2, \sigma_{EE} = \sigma_{IE} = 1.5, \sigma_{EI} = \sigma_{II} = 0.2, \tau_E = \tau_I = 2, \kappa_{EE} = \kappa_{EI} = \kappa_{IE} = \kappa_{II} = 0.01, d_{EE} = d_{EI} = d_{IE} = d_{II} = 0.1, W^0_{EE} = 1, W^0_{EI} = 2.2, W^0_{IE} = 2.0, W^0_{II} = 2.7, D_E = D_I = 0.05, v_{EE} = v_{EI} = v_{IE} = v_{II} = 0.1, \theta_E = \theta_I = 0, g_{ext} = 50, V_+ = -V_- = 1$.

We now turn our attention to the case where $\sigma_{Ea} < \sigma_{Ia}$, meaning that inhibitory neurons have a wider spatial reach than excitatory neurons. In this configuration, static spatial patterns emerge through a Turing bifurcation. Figure Figure 3.12 displays the (purely real) spectrum of the system at a Turing bifurcation, along with two views of

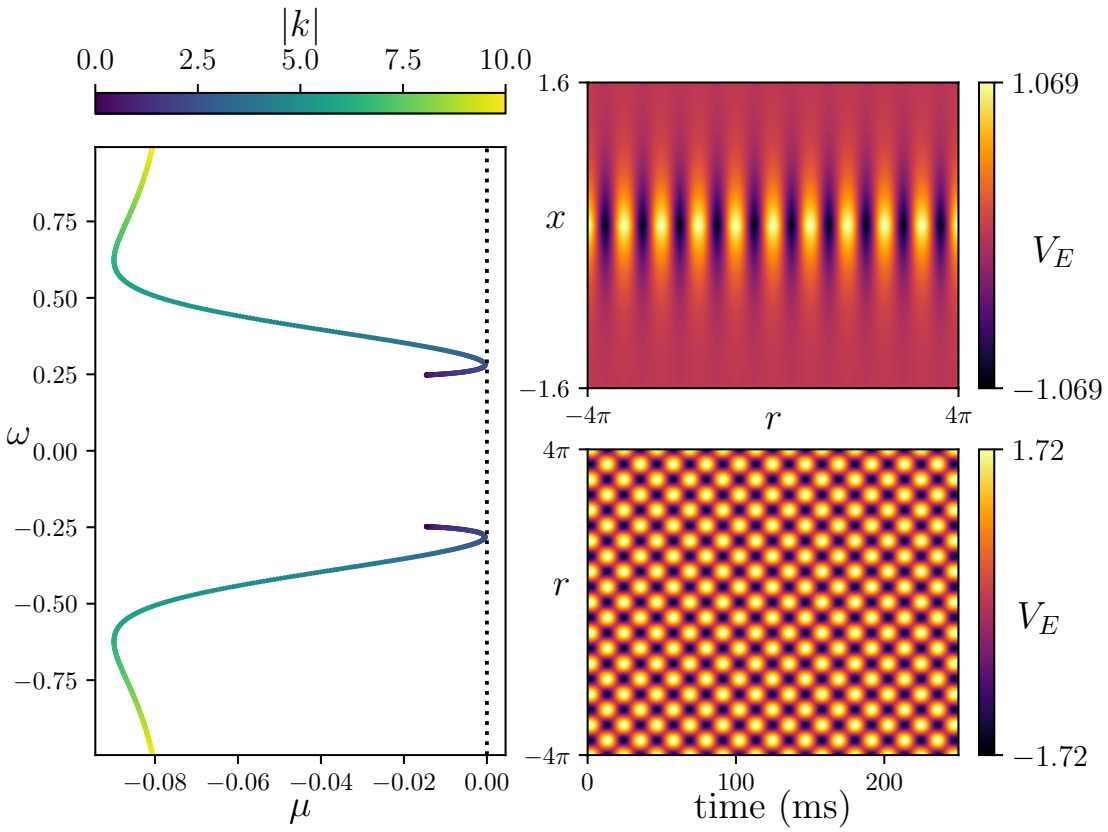

Figure 3.11: Left: The spectrum of the system at a Turing-Hopf bifurcation that occurs at $|k| \approx 2.47$ when $\beta_E = \beta_I \approx 0.379$ and where μ and ω are the real and complex parts of the spectrum respectively. Right top: A snapshot in time of the standing wave patterns in the V_E variable found just beyond the bifurcation at $\beta_E = \beta_I = 0.4$. Right bottom: Simulation showing the standing wave pattern's evolution in time in the V_E variable on a slice along the dendrite axis at $x = d_{EE}$. These dynamic patterns were initiated by perturbing the steady state with the function $0.01\cos(2.47r)$ Parameters: $\alpha_{EE} = 0.5, \alpha_{EI} = 0.5, \alpha_{IE} = 0.7, \alpha_{II} = 0.2, \sigma_{EE} = \sigma_{IE} = 1.5, \sigma_{EI} = \sigma_{II} = 0.2, \tau_E = \tau_I = 2, \kappa_{EE} = \kappa_{EI} = \kappa_{IE} = \kappa_{II} = 0.01, d_{EE} = d_{EI} = d_{IE} = d_{II} = 0.1, W^0_{EE} = 1, W^0_{EI} = 2.2, W^0_{IE} = 2.0, W^0_{II} = 2.7, D_E = D_I = 0.05, v_{EE} = v_{EI} = v_{IE} = v_{II} = 1, \theta_E = \theta_I = 0, g_{ext} = 50, V_+ = -V_- = 1$

.

simulations just beyond this bifurcation. The $x - r$ dimension view reveals periodic patterning with peak excitatory voltages at 31.11 mV, demonstrating how activity spreads along the dendritic dimension. A time series of the r dimension at $x = 0.1$ is also presented. Appendix A contains simulations using these parameters for state variables g_{EE}, g_{IE}, g_{EI}, and g_{II}.

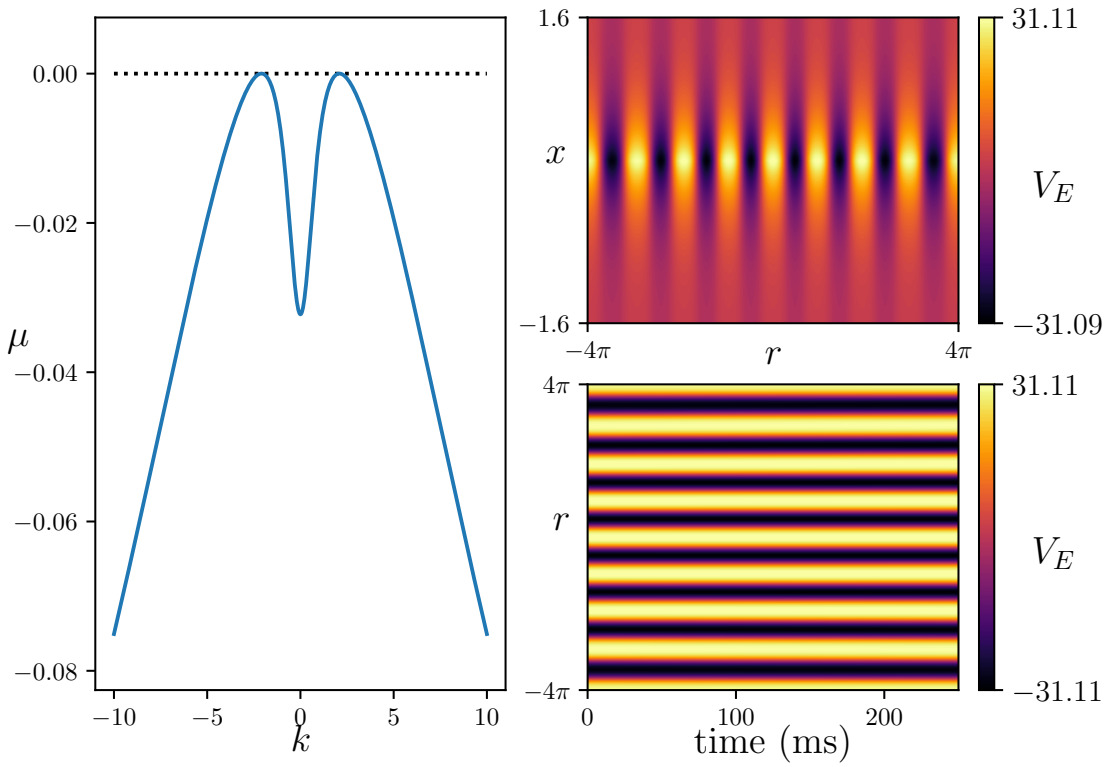

Figure 3.12: Left: The (purely real) spectrum of the system at a Turing bifurcation that occurs at $|k| \approx 2.09$ when $\beta_E = \beta_I = 0.018$ and where μ is the real of the spectrum . Right top: A snapshot in time of the static pattern in the V_E variable found just beyond the bifurcation at $\beta_E = \beta_I = 0.019$. Right bottom: Simulation showing the static pattern in the V_E variable on a slice along the dendrite axis at $x = d_{EE}$. These static patterns were initiated using the function $0.01\cos(2.09r)$. Parameters: $\alpha_{EE} = 0.5$, $\alpha_{IE} = 0.7$, $\alpha_{II} = 0.2$, $\sigma_{EE} = \sigma_{IE} = 0.1$, $\sigma_{EI} = \sigma_{II} = 1.2$, $\tau_E = 5$, $\tau_I = 5$, $\kappa_{EE} = \kappa_{EI} = \kappa_{IE} = \kappa_{II} = 0.01$, $d_{EE} = d_{EI} = d_{IE} = d_{II} = 0.1$, $W^0_{EE} = 3.0$, $W^0_{EI} = 1.0$, $W^0_{IE} = 3.0$, $W^0_{II} = 1.0$, $D_E = D_I = 0.05$, $v_{EE} = v_{EI} = v_{IE} = v_{II} = 1$, $g_{ext} = 50$, $V_+ = -V_- = 5$.

Finally, Figure 3.13 presents a simulation where the system is moved further beyond the Turing-Hopf bifurcation observed in Figure 3.11. This figure displays simulations of the state variables V_I and V_E, including a time series view and a snapshot view, similar to previous figures. The system was again initiated with a cosine function, and with these parameters, periodic travelling waves emerge, propagating from the centre

of the domain to the boundaries. Appendix A contains further simulations using these parameters for state variables g_{EE}, g_{IE}, g_{EI}, and g_{II}.

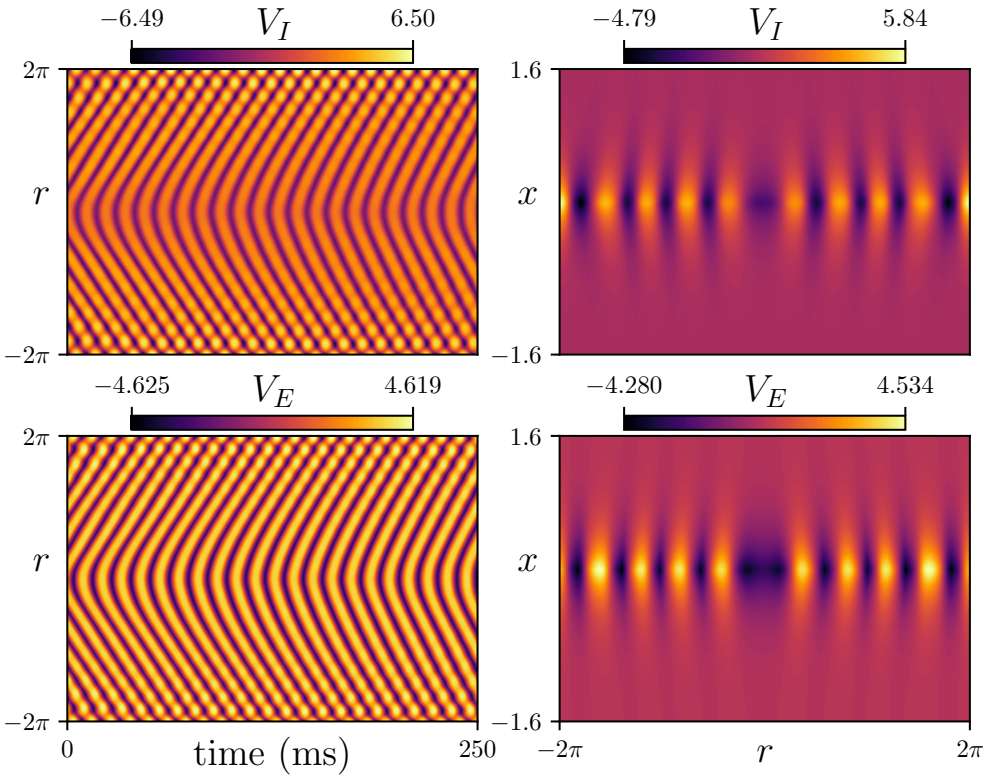

Figure 3.13: Periodic waves found beyond the Turing-Hopf bifurcation found in Figure 3.11. These periodic waves were initiated by perturbing the steady state with the function $0.01\cos(2.47r)$ Parameters: $\beta_E = \beta_I = 0.8$, $\alpha_{EE} = 0.5, \alpha_{EI} = 0.5, \alpha_{IE} = 0.7, \alpha_{II} = 0.2, \sigma_{EE} = \sigma_{IE} = 1.5, \sigma_{EI} = \sigma_{II} = 0.2, \tau_E = \tau_I = 2, \kappa_{EE} = \kappa_{EI} = \kappa_{IE} = \kappa_{II} = 0.01, d_{EE} = d_{EI} = d_{IE} = d_{II} = 0.1, W^0_{EE} = 1, W^0_{EI} = 2.2, W^0_{IE} = 2.0, W^0_{II} = 2.7, D_E = D_I = 0.05, v_{EE} = v_{EI} = v_{IE} = v_{II} = 0.1, g_{ext} = 50, V_+ = -V_- = 1$

3.6 Discussion

In this chapter, we introduced a modified version of the Wilson-Cowan neural field model, incorporating dendritic filtering. We demonstrated the ability to derive an analytical expression for the velocity of travelling waves within a single population

framework. Additionally, we presented the derivation of a generalised equation for brain waves and used it to show travelling front solutions, along with a numerical analysis of wave speed and form.

Neural fields typically do not account for dendritic depth, with the exception of the work of Bressloff in [65], yet incorporating this is important for generating more direct measures of LFP/EEG. This importance comes from the realisation that currents flowing along dendrites can generate electromagnetic fields [70], [71]. Specifically, the transmembrane current I_a^{mem} at any point along the dendritic cable is governed by the equation:

$$I_a^{mem} = \frac{1}{r_a}\frac{\partial^2 V_a}{\partial x^2}, \tag{3.45}$$

where r_a represents the specific resistance per unit length for currents traversing the dendrite, given by:

$$r_a = \frac{4R_a}{\pi d^2}, \tag{3.46}$$

with R_a denoting the axial resistance and d the diameter of the dendrite. If the extracellular space is assumed to homogeneous, purely resistive, and infinity in extent with conductivity σ then the potential $\Phi(x, \mathbf{r}, t)$ generated by these currents at any point in space and time can be described by the following integral equation [71]:

$$\Phi(x, \mathbf{r}, t) = \frac{1}{4\pi\sigma}\sum_{a\in\{E,I\}}\int_{-\infty}^{\infty} \mathrm{d}x' \int_{\mathbb{R}^2} \mathrm{d}\mathbf{r}' \frac{I_a^{mem}(x', \mathbf{r}', t)}{d(x, x', \mathbf{r}, \mathbf{r}')}, \tag{3.47}$$

where σ denotes the electrical conductivity of the extracellular medium and $d(x, x', \mathbf{r}, \mathbf{r}') = \sqrt{((x - x')^2 + |\mathbf{r} - \mathbf{r}'|^2)}$. This equation shows the direct correlation between dendritic currents and the resultant electromagnetic field, highlighting the importance of considering dendritic depth in neural field models. In Figure 3.14 we show the solution to equation (3.47) using the the voltage solutions of the neuronal model, V_E and V_I, in

the equation 3.45. We see that a drop off can be observed in the potential Φ further away from the soma similar to V_E and V_I. Here we used the same parameters as in Figure 3.12, where the solution resolves to a static Turing pattern, and only show one time point.

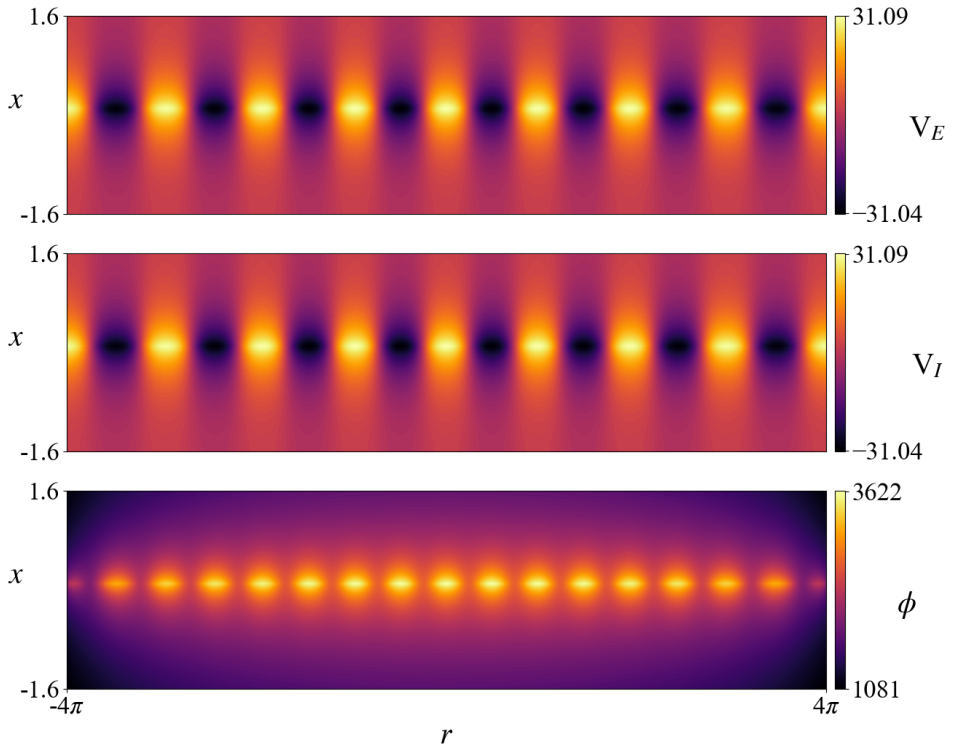

Figure 3.14: Results from solving equation (3.47). The top two panels show the voltage solutions for the excitatory and inhibitory population respectively, the bottom panel shows potential generated by the dendritic currents which is the solution to the (3.47). The parameters used here are the same as in the simulations presented in Figure 3.12.

Brain-wave equations, such as the model introduced in this chapter, serve a crucial role in facilitating effective and fast computer simulations of neural field models. They provide a way to circumvent the need for simulating the much more complex and computationally demanding delay integro-differential equations associated with non-

local neural fields that include axo-dendritic delays, which is often prohibitive. The reduction to wave-equation form presented here significantly opens up opportunities for practical investigations. However, for simulations on surfaces more complex than the planar ones used in this chapter, the integro-differential equations remain valuable, allowing for a broader range of applications.

We used this brain-wave equation to investigate the full two population model in one somatic dimension with some reductions and simplifications, namely the removal of voltage shunts, and analysed the stability of the homogeneous steady state and found parameter regimes where bulk oscillation, spatio-temporal patterns, and static patterns could form. We also conducted studies on how various system parameters impact the velocity of moving wave fronts, demonstrating that the relationship between somatic and dendritic coordinates in axo-dendritic connectivity patterns can significantly influence the wave's speed. Specifically, as the correlation parameter κ increases, there is a noticeable slowing of the wave speed, accompanied by a shift of the peak response further from the soma.

Further work on this model could include a more detailed numerical continuation of the bifurcations identified in this chapter, providing additional insight into their structure. Furthermore, an extended bifurcation analysis could be conducted in the case of a two-population model with two somatic dimensions, allowing for a broader exploration of the system's dynamical properties. Numerical simulations could also be carried out to examine the model's behaviour under different parameter conditions. However, such an approach would require substantial computational resources due to the large system of equations necessary for accurately evolving this model.

CHAPTER 4

NEXT GENERATION NEURAL ACTIVITY MODELS WITH GAP JUNCTION COUPLING

Gap junction coupling between neurons are thought to play an important role in the promotion of synchrony in neuronal populations [53], [72] and contribute to both normal and abnormal brain rhythms such as epilepsy [56], [73]. Recent theories suggest that the plasticity of gap junctions, dependent on activity, may serve as a method for controlling oscillations within the cortex [74]. In Chapter 2, we discussed a range of neural mass models prominently featured in the current literature. Each of the models discussed was connected through mechanisms simulating chemical synapses, but did not take into account the role of electrical synaptic coupling by gap junctions. This chapter aims to investigate the dynamics of a neural mass model, which is derived from a network of quadratic integrate-and-fire models, and incorporates local gap junction coupling. We show that the model can robustly produce oscillations via a Hopf bifurcation through increasing the gap junction strength parameter, and eventually build up to showing how local gap junction coupling can facilitate more complex

spatio-temporal dynamics in one- and two-population neural field models. The work discussed in this chapter is based on the work presented in [2]. My contributions to this work include performing a bifurcation analysis and simulations of neural mass models, as well as simulations of a single population neural field model. Additionally, I conducted numerical spectral analysis and simulations of a two-neuronal population model.

4.1 Background

Several studies have explored the function of gap junctions in neural modelling, employing different methodologies. Researchers like Carlo Laing [23] and Bastian Pietras *et al.* [75] have focused on incorporating gap junctions locally, developing mass models based on networks of Theta neurons or QIF neurons, respectively. On the other hand, Steyn-Ross *et al.* [76] adopts a more phenomenological approach, utilising a global diffusion term to depict gap junction coupling within a neural field model. In this section, we briefly discuss the biology and function of gap junctions with respect to neuroscience, and highlight how their function differs from chemical synapse coupling.

4.1.1 Electrical Synapses and Gap Junction Modelling

Electrical synapses are specialised channels that allow for the flow of electrical impulses between extremely narrow gaps between neurons called *gap junctions*. gap junctions are composed of two connexon hemichannels, which are pores that connect across the intercellular space between neurons and allow for the bidirectional flow of ions between the cells. A graphical representation of a gap junction is shown in Figure 4.1 where we see the connexon channel connecting two cells across a gap of around

$2-4$ nm wide. The primary functional differences between electrical synapses and

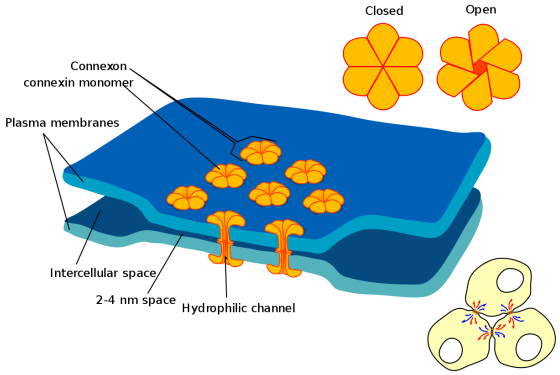

Figure 4.1: A depiction of two cells meeting at gap junctions. A gap junction is the meeting of two connexons that connect cells across the intercellular space allowing for the flow of ions between the cells. This diagram was sourced from: https://en.wikipedia.org/wiki/Gap_junction

chemical synapses is that electrical synapses are much faster, they lack signal gain, and permit subthreshold transmission [77]. While chemical synapses typically exhibit a synaptic delay ranging from 1 to 100 milliseconds, electrical synapses formed via gap junctions can be as low as 0.2 ms [78]. This means that conduction changes at the post-synaptic neuron due to signals from the pre-synaptic neuron via gap-junctions are almost instantaneous, though the signal received at the post-synaptic neuron is of the same, or smaller, magnitude as the pre-synaptic signal. In contrast to the work of Steyn-Ross *et al.* [76] we follow Carlo Laing [23] and Bastian Pietras [75] and include gap junction coupling into the local dynamics of the mass model. We derive an exact mean field reduction of a network of globally coupled firing models.

4.1.2 Integrate and Fire Model

As in Section 2.3.1 we choose the underlying neural model as a network of QIF neurons. It is common for gap junctions to be viewed as simply a channel that conducts current according to a simple ohmic model. For two neurons with voltages v_i and v_j the

current flowing into cell i from cell j via a gap junction is proportional to $v_j - v_i$. This leads to the globally coupled QIF model:

$$\begin{aligned} \tau \frac{\mathrm{d}v_i}{\mathrm{d}t} &= v_i^2 + \eta_i + \kappa_s g + \frac{\kappa_v}{N} \sum_{j=1}^{N} (v_j - v_i), \quad \text{if } v_i > v_{th} \text{ then } v_i \leftarrow v_r \\ Qg &= \frac{\kappa_s}{N} \sum_{j=1}^{N} \sum_{m \in \mathbb{Z}} \delta(t - t_j^m), \end{aligned} \tag{4.1}$$

where κ_s is the synaptic coupling strength, κ_v is the gap junction coupling strength - which could be interpreted as reflecting the degree of electrical connectivity between neurons, with higher values indicating more open gap junctions and thus more effective transmission of ionic currents that influence membrane potentials directly - Q is a linear differential operator, g is the post-synaptic conductance, and η_i are random variables drawn from the Lorentzian distribution:

$$g(\eta) = \frac{1}{\pi} \frac{\Delta}{(\eta - \eta_0)^2 + \Delta^2}. \tag{4.2}$$

For clarity of exposition our global synaptic input does not include voltage shunts (as in Section 2.3), though the extension is straightforward.

4.1.3 Mean-Field reduction

To derive a mean-field model of the network of coupled QIF models we follow the approach developed by E. Montbrió and colleagues in [21]. We consider the thermodynamic limit $N \to \infty$ of equation 4.1. The distribution of voltage values is denoted $\rho(v|\eta, t)$ and the continuity equation for ρ is

$$\frac{\partial}{\partial t}\rho + \frac{\partial}{\partial v}\rho\dot{v} = 0, \tag{4.3}$$

where

$$\tau\dot{v} = v^2 + \eta + \kappa_s g + \kappa_v V - \kappa_v v, \quad Qg = R(t), \tag{4.4}$$

and

$$V(t) = \lim_{N\to\infty} \frac{1}{N} \sum_{j=1}^{N} v_j(t), \tag{4.5}$$

$$R(t) = \lim_{N\to\infty} \frac{1}{N} \sum_{j=1}^{N} \sum_{m\in\mathbb{Z}} \delta(t - t_j^m), \tag{4.6}$$

which are the population average voltage and the population firing rate respectively. We now assume that solutions to equation (4.3) have a Lorentzian function shape so that

$$\rho(v|\eta, t) = \frac{1}{\pi} \frac{x(\eta, t)}{(v - y(\eta, t))^2 + x(\eta, t)^2}. \tag{4.7}$$

This assumption on the shape of $\rho(v|\eta, t)$ is known as the Lorentzian Ansatz (LA) [21]. One way to motivate this choice is by considering the continuity equation (4.3). In the steady state this reduces to $\rho\dot{v} =$ constant. Since, $\dot{v}$ is quadratic in v it makes sense to look for a distribution that has a reciprocal quadratic structure. To make this time dependent one can consider a Lorentzian with a time dependent centre and width as in (4.7) and look for self-consistent solutions that determine the dynamics for these two variables. For a fixed value of η the firing rate $r(\eta, t)$ is found as $\rho(v \to \infty|\eta, t)\dot{v}(v \to \infty|\eta, t)$ which gives the identity

$$x(\eta, t) = \pi\tau r(\eta, t). \tag{4.8}$$

We note that $y(\eta, t)$ is the mean voltage for each η so that

$$y(\eta, t) = \mathrm{PV} \int_{-\infty}^{\infty} \rho(v|\eta, t) v \mathrm{d}v, \tag{4.9}$$

where PV denotes the Cauchy principal value. After averaging over the distribution of single neuron drives given by (4.2)) we obtain

$$R(t) = \frac{1}{\tau\pi}\int_{-\infty}^{\infty} x(\eta,t)g(\eta)\mathrm{d}\eta, \tag{4.10}$$

$$V(t) = \int_{-\infty}^{\infty} y(\eta,t)g(\eta)\mathrm{d}\eta. \tag{4.11}$$

Substituting the LA into the continuity equation (4.3) and balancing powers of v shows that x and y obey two coupled equations that may be written in complex form as

$$\tau\dot{w} = -\kappa_v w + i[\eta + \kappa_s g + \kappa_v V - w^2], \tag{4.12}$$

where $w(\eta,t) = x(\eta,t) + iy(\eta,t)$. Evaluating the integrals in (4.10) and (4.11) using contour integration and the fact that $g(\eta)$ has poles at $\eta_0 \pm i\Delta$ we find the coupled equations for population firing rate and mean voltage as

$$\begin{aligned} \tau\dot{R} &= -\kappa_v R + 2RV + \frac{\Delta}{\tau\pi} \\ \tau\dot{V} &= \eta_0 + V^2 - \pi^2\tau^2R^2 + \kappa_s g \end{aligned} \tag{4.13}$$

As in Section 2.8 the R and V variables relate to the Kuramoto order parameter via the conformal map in Equation (2.11). In order to validate our mean-field reduction we simulate 1000 neurons of the network of coupled QIF neurons and compare the results to our mean-field model and we see in Figure 4.2 that there is very good agreement between the two models.

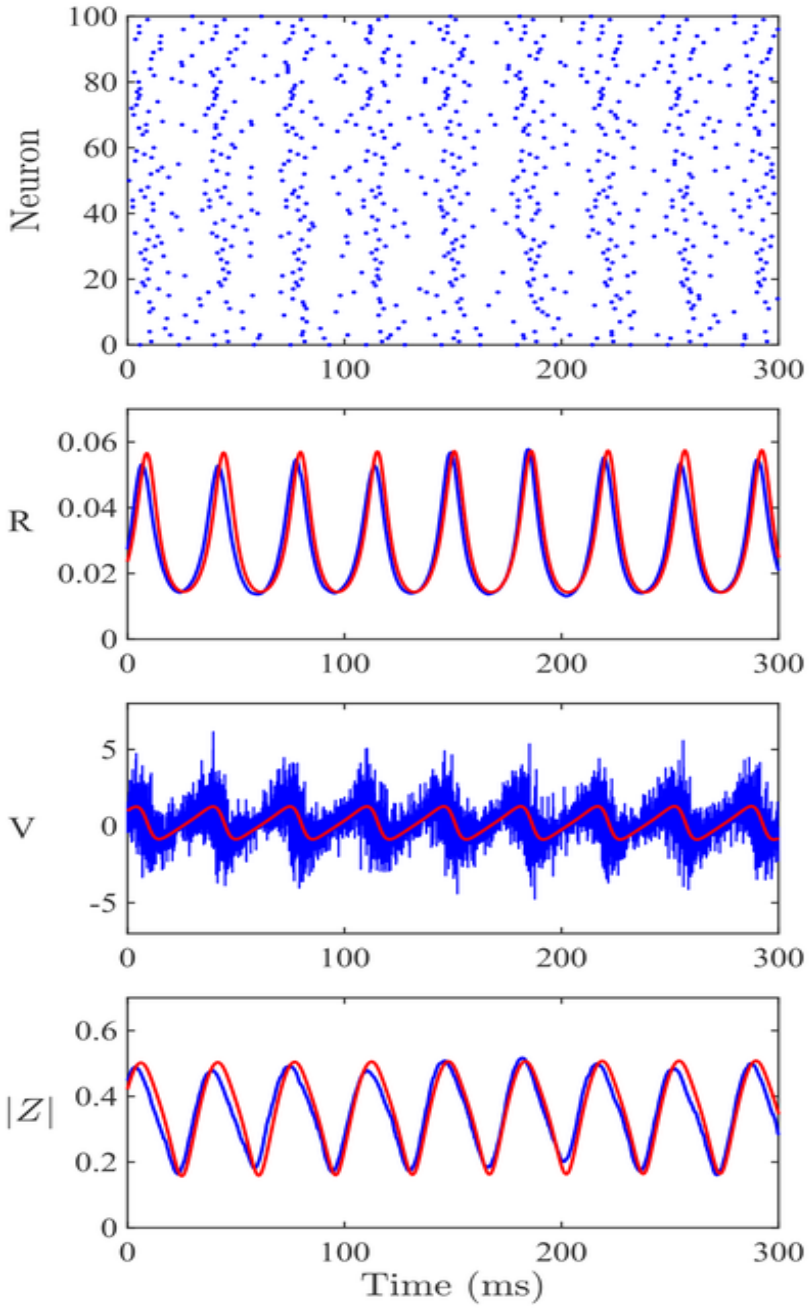

Figure 4.2: Validity of the mean-field reduction. A comparison of the mean-field dynamics (red) with the corresponding network of spiking neurons (blue). The top panel shows a raster plot for a sample of 100 of the 1000 neurons in the network of coupled QIF neurons. Below are comparisons of the mean firing rate R, average membrane potential V and within population synchrony $|Z|$ for the spiking network and mean-field model. Parameter values: $\eta_0 = 2$, $\kappa_v = 1$, $\kappa_s = 1$, $\tau = 16$, $\alpha = 0.5$, $\gamma = 0.5$,$v_{th} = -v_r = 1000$.

4.2 Mass Model Bifurcation Analysis and Simulation

In this section, we use bifurcation analysis to investigate the dynamics of the neural mass model with one and two neuronal sub-populations and also exhibit the dynamics found in these models beyond the bifurcations. Model parameters are kept within realistic physiological range. We use second order synapses, so that

$$Q = (1 + \alpha^{-1}\mathrm{d}/\mathrm{d}t)^2,$$

the speed of the synapse is controlled by the parameter α in the synapse model, as discussed in Chapter 2, where α^{-1} is the time-to-peak of the synapse. Typically fast synapses have a time-to-peak 1ms and slow synapses have a time-to-peak of 100ms, so a realistic range for α is 0.01 - 1 ms^{-1}. V_{syn} is set to either a positive or negative value depending on if the connection between neurons is excitatory. κ_v and κ_s are both used a bifurcation parameters and therefore varied outwith of biophysical range.

4.2.1 Single Population

We start the analysis of the model by first looking at a single population model mass model (4.13). In Figure 4.3 a numerical bifurcation analysis is shown. It can be seen that increasing gap junction strength coupling leads to oscillations via a Hopf bifurcation. We also show a two-parameter continuation (η_0 vs κ_v) of the Hopf-bifurcations for three values of Δ which shows that the models supports a Hopf bifurcation for a large range of parameter choices. In Figure 4.4 a simulation of the system beyond a Hopf bifurcation is shown and the oscillations that occur with this parameter set are

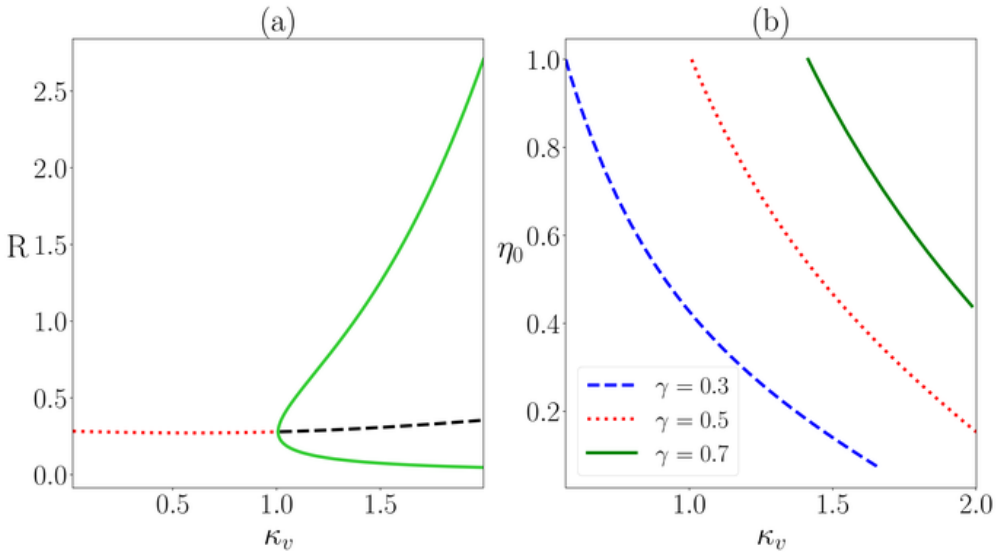

Figure 4.3: Single population bifurcation diagrams. (a) A Hopf bifurcation is found with an increase in the strength of gap junction coupling κ_v, giving rise to limit cycle oscillations. Red (black) lines denote the stable (unstable) fixed point, while the green lines show the minimum and maximum of the oscillation. (b) A two parameter bifurcation diagram in the (κ_v, η_0)-plane tracing the locus of Hopf bifurcations for different values of Δ. Oscillations emerge to the right of each curve. Parameter values: $\eta_0 = 1$, $\kappa_s = 1$, $\tau = 15$, $\alpha = 0.5$, $\Delta = 0.5$.

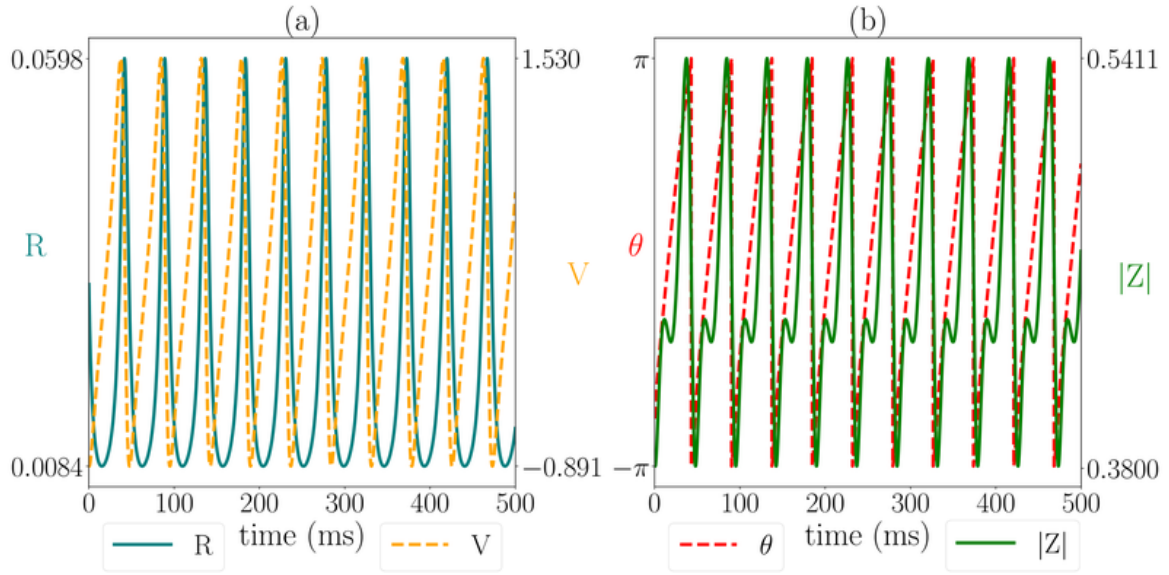

Figure 4.4: Single population dynamics. (a) Oscillations in the population firing rate R (teal) and average membrane voltage V (yellow), (b) Corresponding oscillations in the complex Kuramoto order parameter $Z = |Z|e^{i\theta}$, where $|Z|$ reflects the degree of within-population synchrony (green), and θ a corresponding phase (red). Parameter values: $\eta_0 = 1$, $\kappa_v = 1.2$, $\kappa_s = 1$, $\tau = 15$, $\alpha = 0.5$, $\Delta = 0.5$.

in the beta frequency band.

4.2.2 Two Interacting Sub-populations

We now turn our attention to a mass model with two sub-populations. The two sub-populations of neurons we are representing are excitatory and inhibitory type neurons and we use an all-to-all chemical synaptic coupling scheme and gap junction coupling only within the same sub-population. The model can be written as:

$$\begin{aligned}
\tau_a \dot{R}_a &= -\kappa_v^a R_a + 2R_a V_a + \frac{\Delta_a}{\tau_a \pi}, \\
\tau_a \dot{V}_a &= \eta_0^a + V_a^2 - \pi^2 \tau_a^2 R_a^2 + \sum_{b \in \{E,I\}} g_{ab}, \\
Q g_{ab} &= \kappa_s^{ab} R_b.
\end{aligned} \tag{4.14}$$

The indices $a, b \in \{E, I\}$ denote excitatory and inhibitory neuronal sub-populations. A numerical bifurcation analysis of the model (4.14) is presented in Figure 4.5 for different values of κ_v^E and κ_v^I. We see that when $\kappa_v^E = 0$ and $\kappa_v^I = 0$ oscillation emerge via a subcritical Hopf bifurcation at $\eta_0^I \simeq -6$ and $\eta_0^I \simeq 7$. When gap junction coupling is turned on in the inhibitory population we see that another Hopf occurs at $\eta_0^I \simeq 3$ with stable oscillations occurring for low values of η_0^I. Similar results occur when excitatory gap junction coupling is turned on exclusively, though the oscillations are smaller in the inhibitory population. When $\kappa_v^E = \kappa_v^I = 0.5$ the limit cycle stability in the low η_0^I range is lost and a new unstable limit cycle appears via a Hopf bifurcation when $\eta_0^I \simeq 0$. Simulation of this model reveals the complex bursting-like oscillations

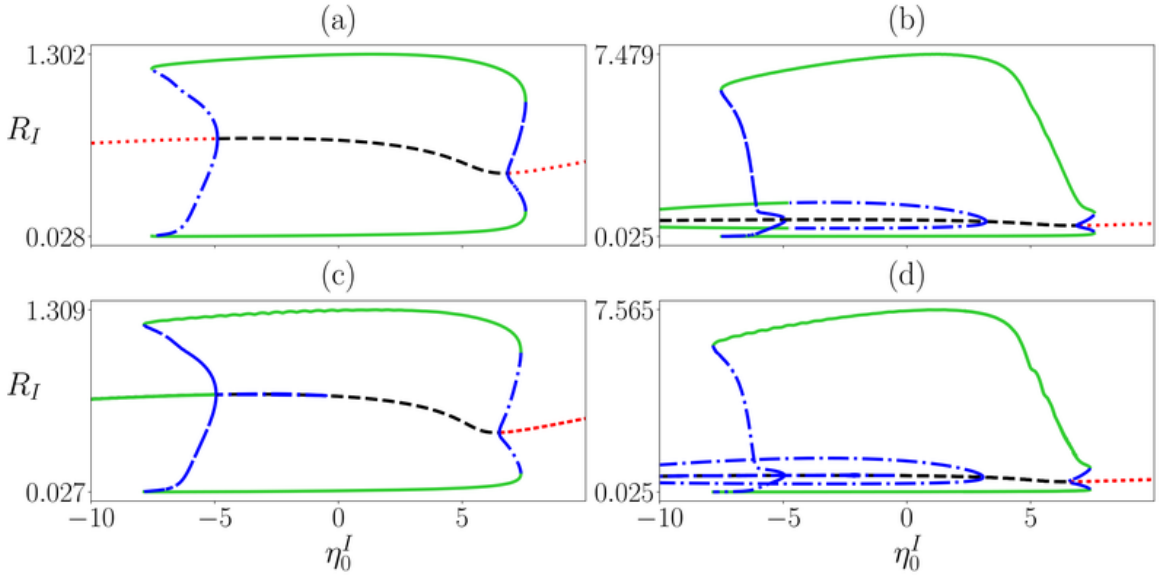

Figure 4.5: Two population bifurcation diagrams: Continuations in the median background drive to the inhibitory population η_0^I for different combinations of gap junction coupling strengths κ_v^E and κ_v^I. Red (black) lines denote the stable (unstable) fixed point, while the green (blue) lines show the minimum and maximum of the stable (unstable) oscillation (a) No gap junction coupling, $\kappa_v^E = 0$, $\kappa_v^I = 0$ (b) Gap junction coupling in the inhibitory population only, $\kappa_v^E = 0$, $\kappa_v^I = 0.5$ (c) Gap junction coupling in the excitatory population only, $\kappa_v^E = 0.5$, $\kappa_v^I = 0$ (d) Gap junction coupling in both populations, $\kappa_v^E = 0.5$, $\kappa_v^I = 0.5$. Other parameters: $\eta_0^E = 5$, $\kappa_s^{EE} = 15$, $\kappa_s^{IE} = 25$, $\kappa_s^{EI} = -15$, $\kappa_s^{II} = -15$, $\tau_E = 1, \tau_I = 1$, $\alpha_{EE} = 0.2$, $\alpha_{IE} = 0.1$, $\alpha_{EI} = 0.07$, $\alpha_{II} = 0.06$, $\Delta_E = \Delta_I = 0.5$.

that can occur in this model. In Figure 4.6 we see a simulation with bursts occurring in the beta band frequency and intra-burst oscillations in the gamma band frequency. These bursts of high frequency and high amplitude are a pattern of activity that is typical of epileptic seizures [79].

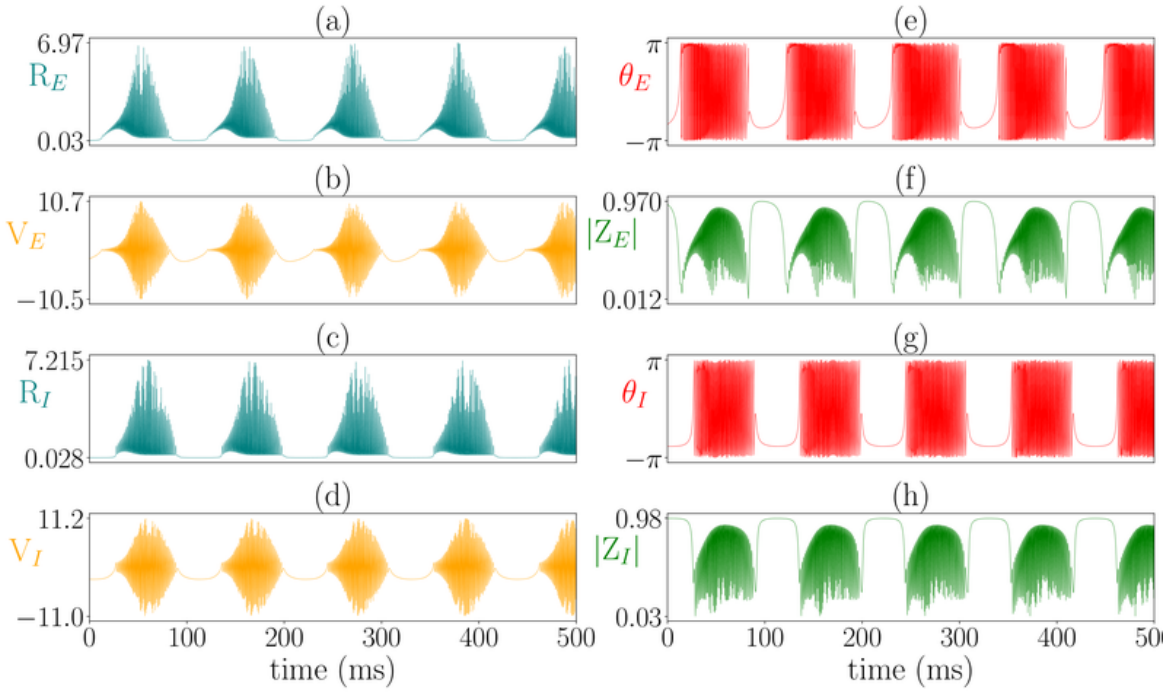

Figure 4.6: Excitatory-inhibitory network dynamics: Oscillations in (a) the excitatory population firing rate R_E (teal), and (b) in the average membrane potential V_E (yellow). Corresponding oscillations for the inhibitory population, (c) R_I and (d) V_I. Kuramoto order parameters for the excitatory population (e) $Z_E = |Z_E|e^{i\theta_E}$, $|Z_E|$ (green) and (f) θ_E (red). Corresponding traces for (g) $|Z_I|$ and (h) θ_I of the inhibitory population. Parameter values: $\eta_0^E = 5$, $\eta_0^I = -3$, $\kappa_v^E = \kappa_v^I = 0.5$, $\kappa_s^{EE} = 15$, $\kappa_s^{IE} = 25$, $\kappa_s^{EI} = -15$, $\kappa_s^{II} = -15$, $\tau_E = 1, \tau_I = 1$, $\alpha_{EE} = 0.2$, $\alpha_{IE} = 0.1$, $\alpha_{EI} = 0.07$, $\alpha_{II} = 0.06$, $\Delta_E = \Delta_I = 0.5$.

4.2.3 Comparison to Laing's Model

Our approach for including gap junctions is similar to Laing's approach, as outlined in [23]. However, our work diverges in that Laing constructs a mean-field model based on a network of theta neurons, as opposed to the QIF neurons we employ. Laing's framework involves a network of theta neurons with gap junction coupling, as described by:

$$\frac{\mathrm{d}\theta_j}{\mathrm{d}t} = 1 - \cos\theta_j - \kappa_v \sin\theta_j + (1+\cos\theta_j)\left[\eta_j + \frac{\kappa_v}{N}\sum_{k=1}^{N}\tan\left(\frac{\theta_k}{2}\right)\right]. \tag{4.15}$$

However, this approach faces a challenge: $\tan(\theta/2)$ tends toward infinity as θ approaches π. To address this issue, Laing introduces an ad-hoc corrective measure, substituting $\tan(\theta/2)$ with:

$$q(\theta) = \frac{\sin\theta}{1+\cos\theta+\epsilon}, \tag{4.16}$$

where ϵ represents a small constant. Our approach of developing the mean-field model from the QIF framework negates the need for this correction term, and hence our model is an exact representation of the underlying QIF network. The correction term in Laing's introduces an alteration to the mean field equation, resulting in a distinct mean field model compared to that discussed in Chapter 4. Laing's mean field model with instantaneous synapses, where the synaptic speed parameter $\alpha \to \infty$ and therefore the post-synaptic conductance is simply $\kappa_S * R$, is expressed as:

$$\begin{aligned} \frac{\mathrm{d}R}{\mathrm{d}t} &= -\kappa_v R + 2RV + \frac{\gamma}{\pi}, \\ \frac{\mathrm{d}V}{\mathrm{d}t} &= \eta_0 + V^2 - \pi^2 R^2 + \kappa_s R + \kappa_v (C - V), \end{aligned} \tag{4.17}$$

where $\kappa_v(Q - V)$ is the termed gained by using the correction term and

$$C(t) = \sum_{m=1}^{\infty} (b_m z^m + c.c), \tag{4.18}$$

where $z = (1 - \pi R + iV)/(1 + \pi R - iV)$ and

$$b_m = \frac{i(\rho^{m+1} - \rho^{m-1})}{2(\rho + 1 + \epsilon)}, \tag{4.19}$$

with $\rho = \sqrt{2\epsilon + \epsilon^2} - 1 - \epsilon$. For numerical purposes, the sum in (4.18) is truncated at $m = 200$ and ϵ is set to 0.01 as in Laing's publication. For clarity on the distinctions between Laing's approach and ours, we have included Laing's model in Appendix B.1. While the overall behaviour of the models is similar, small differences exist, especially when ϵ is large. A comparative computational analysis of a single neural population using our model and Laing's model, with various of ϵ values, is presented in Figure 4.7. Here we see that as the value of ϵ decreases the solutions to each of the two mass models begin to converge as expected. For simplicity and staying in line with Laing's publication, we employed instantaneous synapses in this comparison, and the relevant equations are further detailed in appendix B.2.

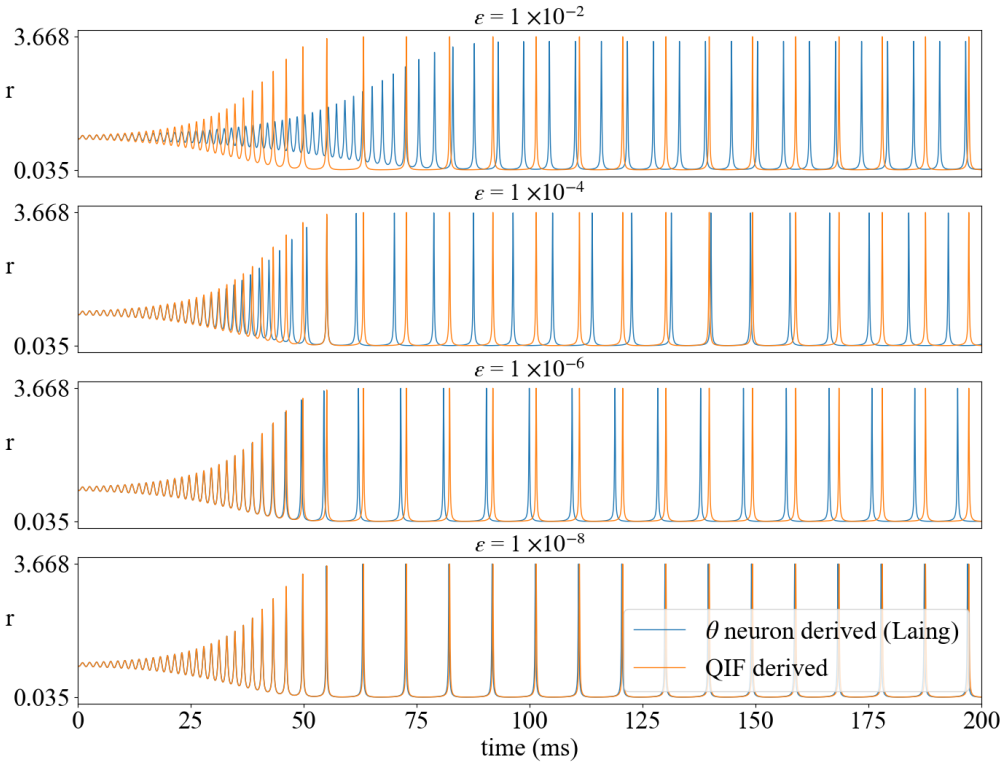

Figure 4.7: A comparison between Laing's mass model, derived from a network of θ neurons, and the model presented in this chapter, which is derived from a network of QIF neurons, with varying values of the correction parameter ϵ. Values of ϵ decrease from the top panel to the bottom, showing that the solutions of the two models converge to the same dynamics as ϵ gets smaller. Parameters: $\Delta = 0.5$, $\eta_0 = -0.3$, $\kappa_s = 3.0$.

4.3 Neural Field Model

We now move on to studying a single population field model, constructing this by replacing the full temporal derivatives by partial temporal derivatives in (4.13) and the dynamics for g are now governed by the non-local equation:

$$\begin{aligned} &Qg = \psi, \\ &\psi(\mathbf{r}, t) = \kappa_s \int_{\mathbb{R}} w(|\mathbf{r} - \mathbf{r}'|) R\left(\mathbf{r}, t - \frac{|\mathbf{r} - \mathbf{r}'|}{c}\right) \mathrm{d}\mathbf{r}' \quad \mathbf{r} \in \mathbb{R}^N, N \in \{1, 2\} \end{aligned} \tag{4.20}$$

Here c is the action potential speed. In the cortex, excitatory synaptic interactions predominantly involve long-range connections, facilitated by myelinated axons of excitatory pyramidal cells extending to various cortical areas. Conversely, inhibitory interactions are generally confined to shorter distances. Specifically, in macaque monkeys, the strength of excitatory connections between different cortical regions decreases exponentially relative to the wiring distance between them, featuring a characteristic distance of about 11mm [80]. A variety of connectivity functions $w(x)$ could be considered but we focus on a so-called inverted 'wizard hat' type function as this models the long range excitation and short range inhibition seen in the brain at large spatial scales. This function can be written as:

$$w(x) = (|x| - 1)\mathrm{e}^{-|x|}, \tag{4.21}$$

in 1 spatial dimension and,

$$w(\mathbf{r}) = (|\mathbf{r}|/2 - 1)\frac{\mathrm{e}^{-|\mathbf{r}|}}{2\pi}, \tag{4.22}$$

in 2 spatial dimensions. In our model the sign of κ_s can be used to change the type of coupling with $\kappa_s < 0$ for standard 'wizard hat' coupling and $\kappa_s > 0$ for inverted 'wizard hat' coupling, examples of these connectivity functions in 1 spatial dimension can be found in Figure 4.8. A schematic of the model can be found in Figure 4.9. The simulations in this chapter going forward primarily use long-range excitatory connections alongside short-range inhibitory ones.

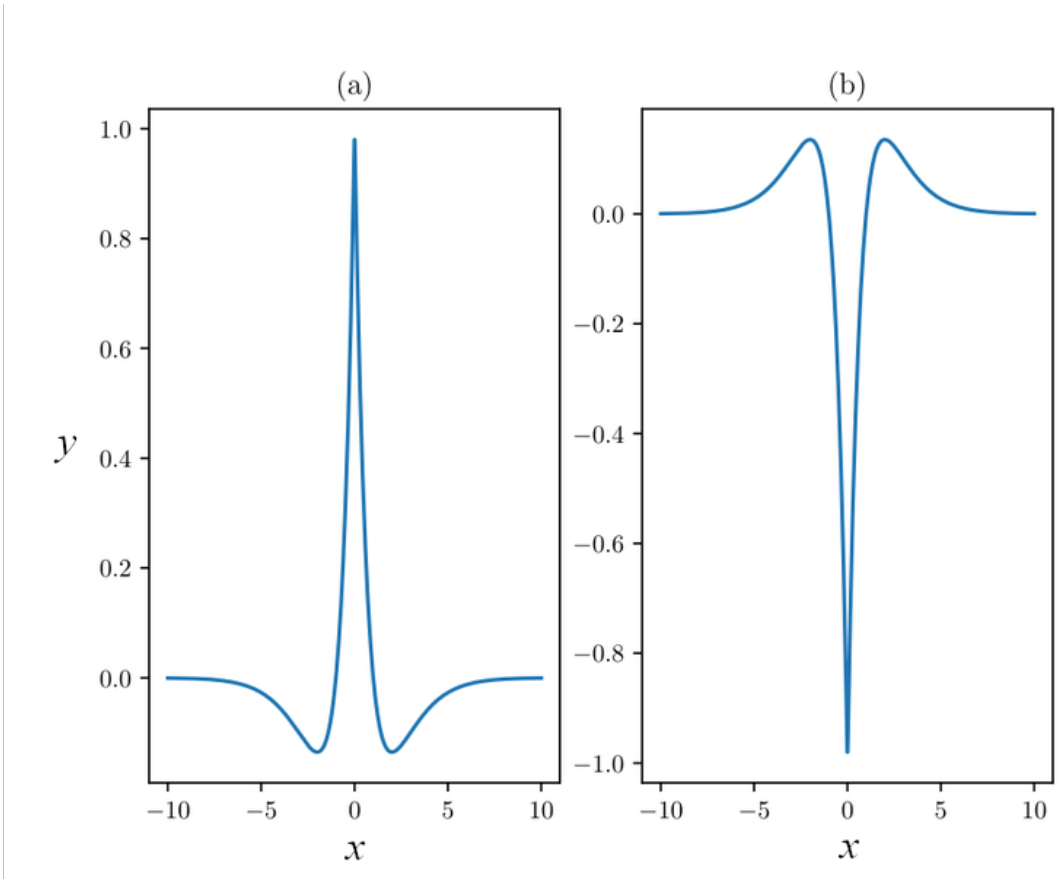

Figure 4.8: Examples of connectivity functions used in this section. (a) An example of a standard 'wizard hat' connectivity function (b) An exampled of a inverted 'wizard hat' connectivity function.

4.3.1 Numerics

In a similar manner to section 2.4.4 a PDE formulation, or so-called *brain-wave equation*, of the convolution ψ in (4.20) can be found and is shown for both the 1 dimensional case and the 2 dimensional case in appendix B.3. The PDE formulation is used for the numerical simulations of the model and further information about the methods used when simulating the model may be found in appendix B.5.

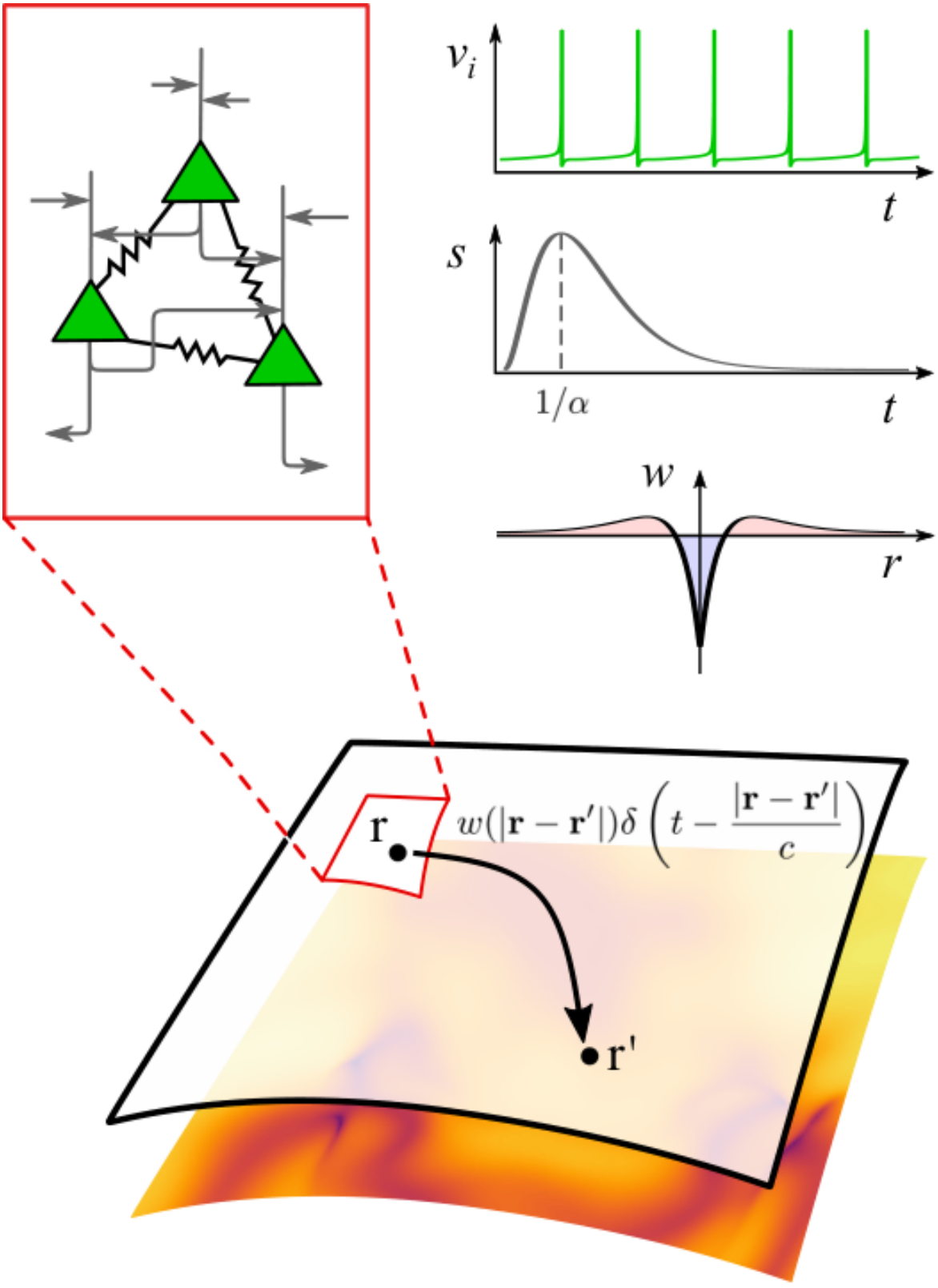

Figure 4.9: Model schematic. At each point in a two-dimensional spatial continuum there resides a density of QIF neurons whose mean-field dynamics are described by the triple (R, V, U), where R represents population firing rate, V the average membrane potential, and U the synaptic activity. The non-local interactions are described by a kernel w, taken to be a function of the distance between two points. The space-dependent delays arising from signal propagation along axonal fibres are determined in terms of the speed of the action potential c.

4.3.2 1D Instability Analysis and Numerical Simulation

A Turing instability analysis, as previously demonstrated in Section 3.5, allows us to investigate the dynamics of the field model and the details of this analysis can be found in appendix B.4. Similar to the bifurcation diagrams studied for the mass model, one can find bifurcations for the field model where bulk oscillations emerge at Hopf bifurcations. Static patterns emerge at Turing bifurcations. Dynamic patterns emerge at Turing-Hopf bifurcations.

We first investigate dynamics in a model with inverted wizard hat coupling. A bifurcation diagram is shown in Figure 4.10 and we see that for $\kappa_v \lesssim 0.8$ the steady state is always stable to the applied perturbations. With low c and $\kappa_v > 0.8$ we see that the system first undergoes a Hopf bifurcation and then a Turing-Hopf bifurcation. For faster action potential speeds $c \gtrsim 0.2$ the order of the bifurcations switch and the system now first undergoes a Turing-Hopf bifurcation and then a Hopf bifurcation with increasing κ_v. In Figure 4.10 we also show three simulations, the first showing global oscillations close to a Hopf bifurcation. The next simulation shows standing waves close to the Hopf and Turing-Hopf Bifurcation. Finally, close to the Turing-Hopf bifurcation (but before the Hopf) we find periodic travelling waves.

To investigate the effect of gap junction coupling on the model, we fixed $c = 0.11$ and explored the dynamics of the synchrony variable $|Z|$ for increasing values of κ_v. In Figure 4.11 we show three simulations where in (I) $\kappa_v = 0.86$ we find standing waves that oscillate at a low level of synchrony. (II) $\kappa_v = 1.0$ we see bulk oscillations with slightly higher levels of synchrony within the population. (III) $\kappa_v = 1.2$ we find mixed dynamics with even higher levels of synchrony. The tissue is now highly synchronised, confirming the belief that gap junction coupling increases the level of synchronisation.

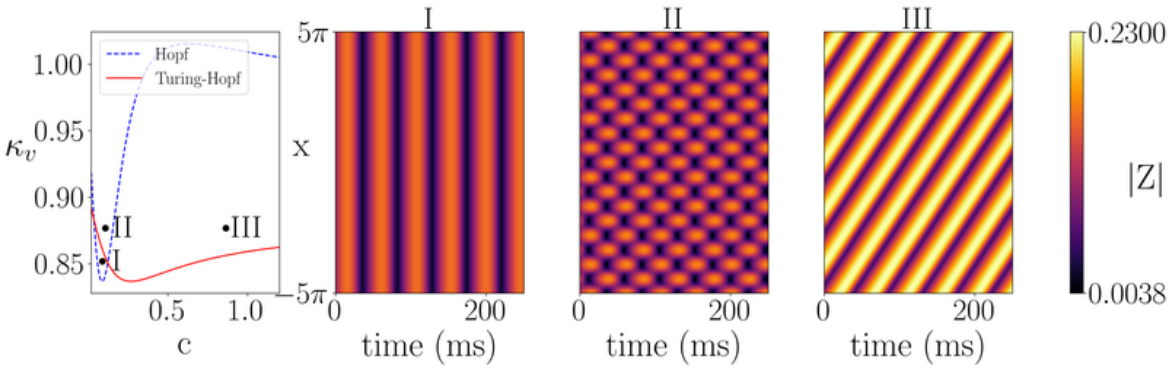

Figure 4.10: Turing instability analysis for the one-dimensional neural field model. The left panel shows the Hopf and Turing-Hopf curves as a function of the action potential speed c and gap junction coupling strength κ_v. Above these curves patterned states emerge. The three right hand panels show simulations near Hopf, and two Turing-Hopf points: (I) Bulk oscillation with $c = 0.1$, $\kappa_v = 0.85$, (II) Standing wave with $c = 0.11$, $\kappa_v = 0.855$, (III) Periodic travelling wave with $c = 1.0$, $\kappa_v = 0.88$. Other parameter values: $\eta_0 = 1$, $\kappa_s = 10$, $\tau = 15$, $\alpha = 0.5$, $\gamma = 0.5$.

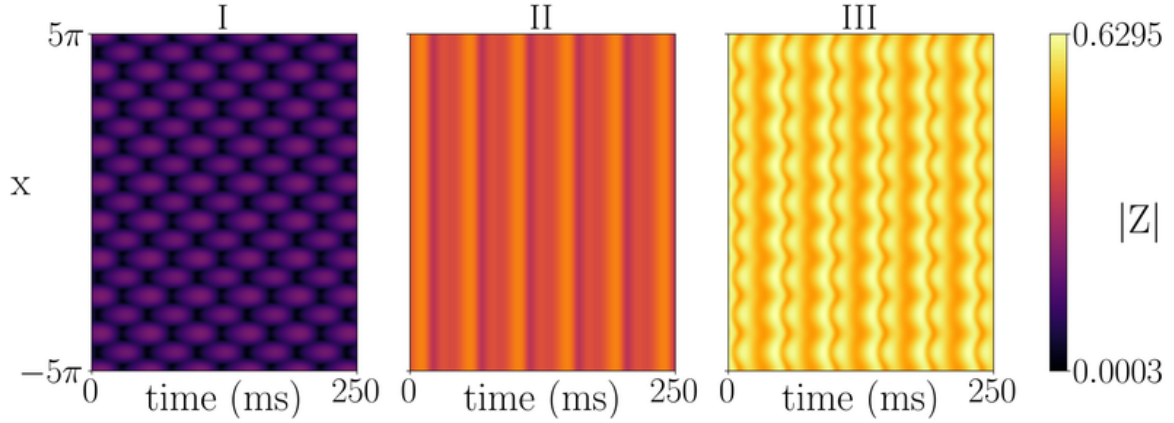

Figure 4.11: Simulations of the one-dimensional neural field model under variation in κ_v: (I) Standing wave with $\kappa_v = 0.86$, (II) Bulk oscillations with $\kappa_v = 1.0$, (III) Mixed dynamics with $\kappa_v = 1.2$. Other parameters $c = 0.11$, $\eta_0 = 1$, $\kappa_s = 10$, $\tau = 15$, $\alpha = 0.5$, $\gamma = 0.5$.

Thus far we have only investigated behaviour when $\kappa_s > 0$, however using $\kappa_s < 0$ results in a model with standard wizard-hat connectivity (proximal excitation and distal inhibition) and in this configuration the model supports static Turing patterns. In Figure 4.12 we see a bifurcation diagram when $\kappa_s = -60$ and a numerical simulation when the system is near a Turing and a Hopf bifurcation. In the bifurcation diagram we see that for low η_0 and increasing κ_v the model first undergoes a pitchfork and Hopf

almost simultaneously and then a Turing-Hopf. Around $\eta_0 = 0$ and low κ_v Turing patterns emerge and increasing κ_v leads to a Hopf, then a Turing-Hopf bifurcation. For larger η_0 a Hopf and then a Turing-Hopf bifurcation occurs for increasing κ_v. A simulation near the Turing and Hopf bifurcations results in interesting dynamics with alternating bumps of high synchrony and an area of lower synchrony that also has a dynamic temporal structure, these patterns are reminiscent of so-called 'chimeras' seen in networks of coupled oscillators, where a fraction of the oscillators are phase-locked or silent while the others oscillate incoherently [81], [82], [83].

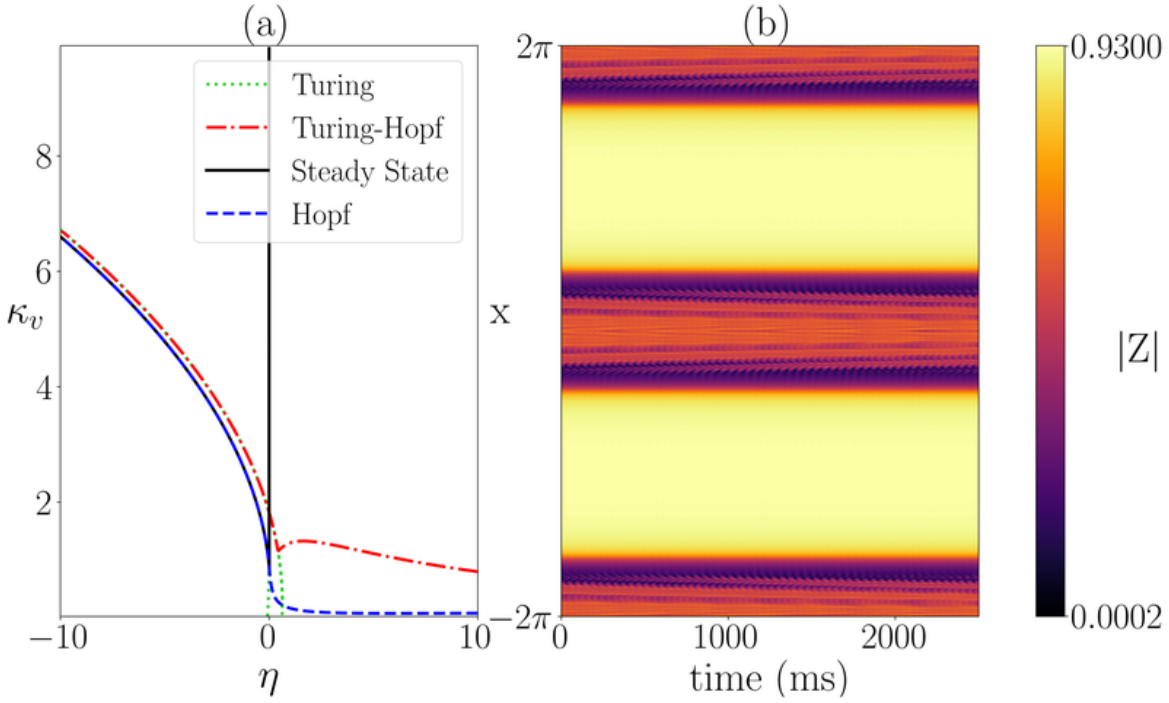

Figure 4.12: Bumps in the one-dimensional neural field model. (a) Bifurcation diagram for a standard wizard hat coupling kernel. (b) Simulation close to the Turing and Hopf curves $\eta_0 = 0.02$ and $\kappa_v = 0.3$. Other parameter values: $c = 10$, $\kappa_s = -60$, $\tau = 12$, $\alpha = 0.5$, $\gamma = 0.5$.

4.3.3 2D Instability Analysis and Numerical Simulation

We now begin an analysis of a 2D field model. In a similar manner to the 1D analysis, we perform a Turing instability analysis, which is shown in appendix B.4, and present

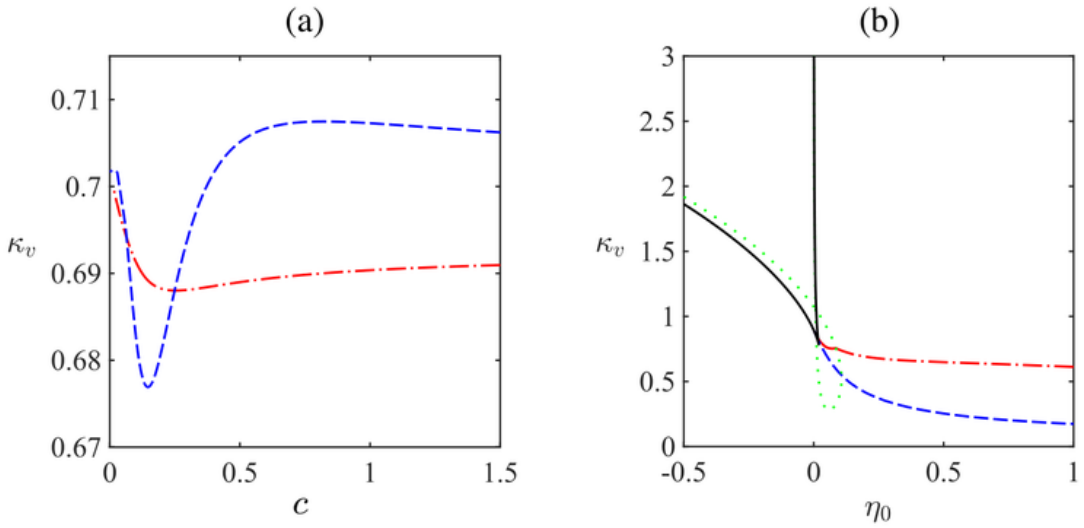

Figure 4.13: Bifurcation diagrams of the 2D field model Hopf curves in blue dotted lines, Turing-Hopf curves in red dotted lines, Turing curves in green dots and a change in steady state in solid black, where a new steady state emerges at the left curve, and a steady state disappears on the right curve.
. Parameter values used are (a) $\eta_0 = 2$, $\kappa_s = 12$, $\tau = 20$, $\alpha = 0.5$ and (b) $\kappa_s = -25$, $\tau = 1$, $\alpha = 5$, $\gamma = 0.5$.

bifurcations diagrams of the model for both standard and inverted wizard hat coupling in Figure 4.13. In (a) we show that when using $\kappa_s > 0$ the system undergoes Turing-Hopf bifurcation and then a Hopf bifurcation for very low c and increasing κ_v, for slightly larger c the order of the bifurcations switches and for even larger c the order of the bifurcations switches again. In (b) we show that when $\kappa_s < 0$ and increasing κ_v the system undergoes a pitchfork bifurcation and then a Turing bifurcation for small η_0. When η_0 is increased the system first undergoes a Turing, then a Hopf and then a Turing-Hopf bifurcation as κ_v is increased. As η_0 increases even further the system undergoes a Hopf and then a Turing-Hopf bifurcation with increasing κ_v. In Figure 4.14 snapshots of a direct simulations in the R, V, $|Z|$, and θ variables are shown. We see that when the system initiated with a periodic lattice type structure and in a Turing-Hopf parameter regime then we find a solution with multiple oscillating cores and spiral waves winding around these cores. We also show a space clamped time

series for each variable and a movie of the full temporal dynamics can be found in appendix B.6.

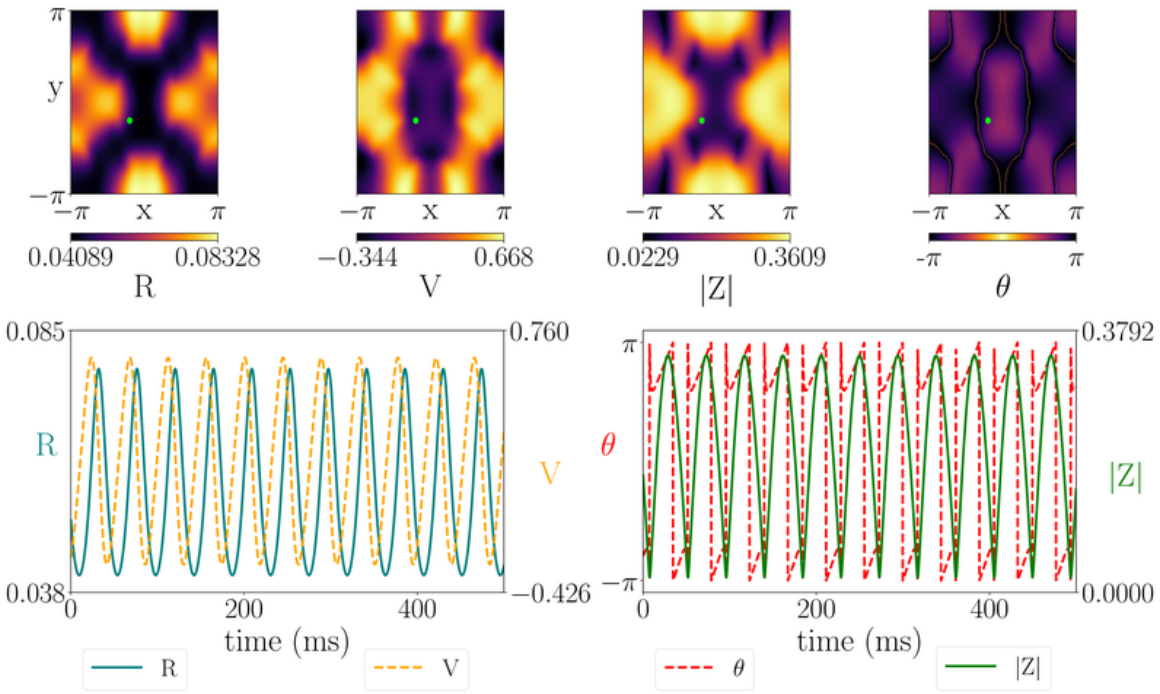

Figure 4.14: Simulations of the two-dimensional neural field model showing that, beyond a dynamic Turing instability, rotating waves with source and sink dynamics may emerge. Top: a snapshot of a patterned state in the (R, V) and $(|Z|, \theta)$ variables. Bottom: the corresponding time-series for the point marked by the small green circle in the top panel. A movie illustrating how this pattern evolves in time is given in appendix B.6. Parameter values: $c = 1$, $\eta_0 = 2$, $\kappa_v = 0.695$, $\kappa_s = 12$, $\tau = 20$, $\alpha = 0.5$, $\gamma = 0.5$.

Increasing κ_v leads to these spirals becoming more pronounced and tightly wound, as seen in Figure 4.15. A movie showing these tightly wound spiral patterns can be found in appendix B.6.

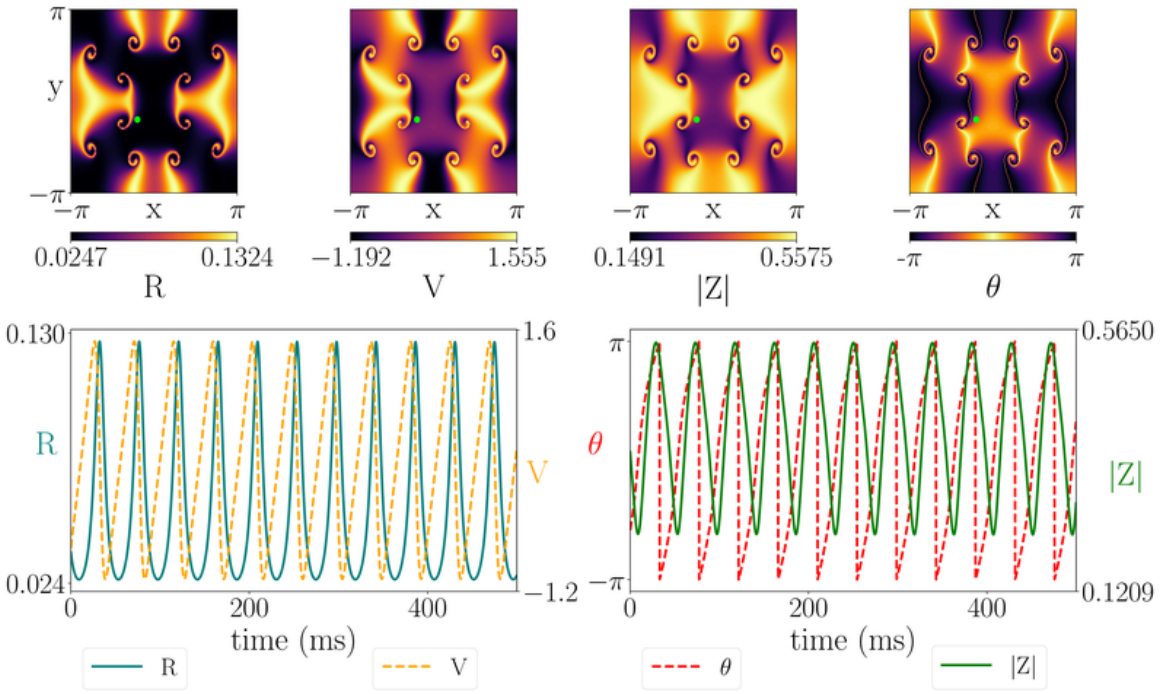

Figure 4.15: Simulations of the two-dimensional neural field model with moderate gap junction coupling strength. In this case robust spiral waves emerge at the centre of rotating cores. The spiral is tightly wound with a diffused tail of high amplitude activity that propagates into the rest of the domain and interacts with the other rotating waves. Top: a snapshot of a patterned state in the (R, V) and $(|Z|, \theta)$ variables. Bottom: the corresponding time-series for the point marked by the small green circle in the top panel. The full spatio-temporal can be seen in appendix B.6. Parameter values: $c = 1$, $\eta_0 = 2$, $\kappa_v = 0.8$, $\kappa_s = 12$, $\tau = 20$, $\alpha = 0.5$, $\gamma = 0.5$.

In Figure 4.16 we show a direct simulation when $\kappa_s < 0$, in effect inverting the connectivity function so that we have proximal excitation and distal inhibition. The results are analogous to the chimera like bump states seen in the 1 dimensional field model. We see the plane has one central bump and 4 semi-bumps and these have internal temporal structure. A time series shows the periodic oscillations in time at a spatial point inside a bump. A movie of these chimera-like dynamic patterns can be found in appendix B.6

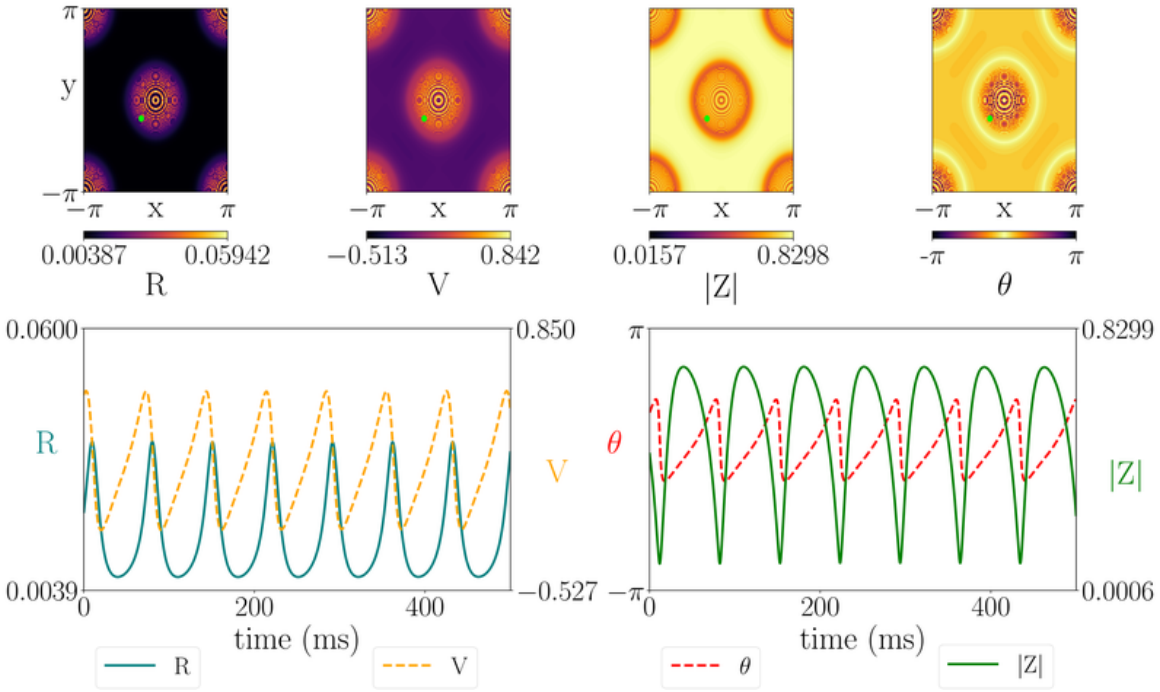

Figure 4.16: Simulations of the two-dimensional neural field model with short-range excitation and long-range inhibition, showing the emergence of a spatially localised spot solution (top panel). Note that the core of the spot has a rich temporal dynamics, as indicated in the bottom panel showing the time course for a point within the core (green dot in top panel). A movie showing the full spatio-temporal can be found in appendix B.6. Parameters values: $c = 10.0$, $\eta_0 = 0.1$, $\kappa_v = 1.0$, $\kappa_s = -25$, $\tau = 1$, $\alpha = 5$, $\gamma = 0.5$.

4.4 Two population field model with voltage shunts

We now turn our attention to a model with two neuronal populations comprised of excitatory and inhibitory neurons. We also now include voltage shunts such that the model may be written in integro-differential equation form as:

$$\begin{aligned}
&\psi_{ab} = \int_{\Omega} w_{ab}(\mathbf{x},\mathbf{x}')R_b(y, t-\tau_{ab}(\mathbf{x},\mathbf{x}'))dy, \quad \Omega \subset \mathbb{R}^N, \quad \tau_{ab}(\mathbf{x}) = \tau_{ab}^0 + |\mathbf{x}|/c_{ab}, \\
&\left(1+\frac{1}{\alpha_{ab}}\partial_t\right)^2 g_{ab} = \kappa_{ab}^s \psi_{ab}, \\
&\tau_a \frac{\partial}{\partial t} R_a = -R_a \sum_b (g_{ab} + \kappa_{ab}^v) + 2R_a V_a + \frac{\Delta_a}{\tau_a \pi}, \\
&\tau_a \frac{\partial}{\partial t} V_a = \kappa_{ab}^v (V_b - V_a) + \sum_b g_{ab}(V_{syn}^{ab} - V_a) - \tau_a^2 \pi^2 R_a^2 + V_a^2 + \eta_a,
\end{aligned} \tag{4.23}$$

with $a, b \in \{E, I\}$ and $\kappa_{EI}^v = \kappa_{IE}^v$ and V_{syn}^{ab} are the synaptic reversal potentials. Here, c_{ab} represents the conduction speed of action potentials. Speeds can range from approximately 0.5 m/s in unmyelinated axons to up to 150 m/s in myelinated axons within the peripheral nervous system. Within the human cortex, axonal speeds between different areas tend to peak within a range of 5 to 10 m/s [84].

4.4.1 1D Instability Analysis and Numerical Simulation

In order to analyse the dynamics of this model, we again perform a Turing instability analysis. We now use an exponential connectivity function of the form

$$w_{ab}(x) = \frac{\exp(-|x|/\sigma_{ab})}{2\sigma_{ab}}.$$

Here, σ_{ab} controls the spatial range of neural connections. The full Turing instability analysis is shown in Appendix B.7.

We show in Figure 4.17 that the model can exhibit global oscillations that form via a Hopf bifurcation, where we can see the excitatory synchrony oscillating between $|Z_E| \approx 0.12$ and $|Z_E| \approx 0.33$, and inhibitory synchrony oscillating between $|Z_I| \approx 0.04$ and $|Z_I| \approx 0.34$.

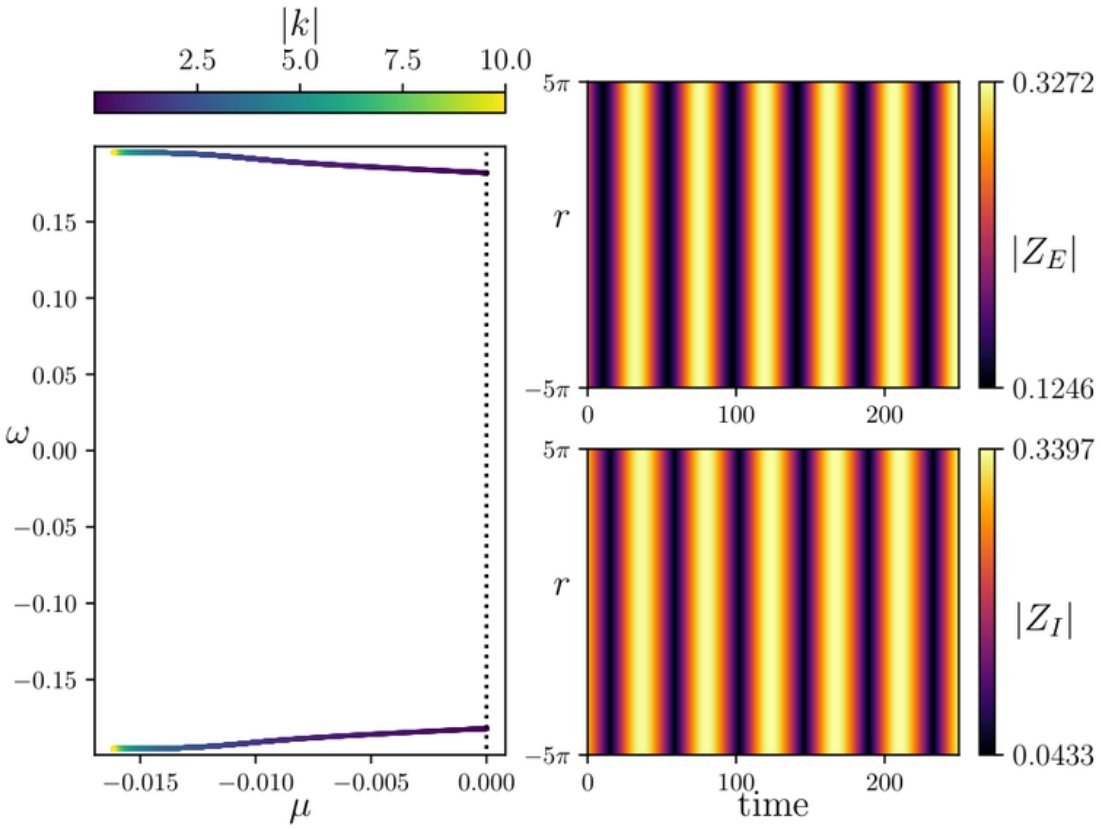

Figure 4.17: Left: The spectrum of the system at a Hopf bifurcation that occurs at $|k| = 0$ when $\kappa^v_{EE} = \kappa^v_{EI} = \kappa^v_{IE} = \kappa^2_{II} = 0.19$. Right top: Time series of the excitatory population's synchrony $|Z_E|$ just beyond the Turing-Hopf bifurcation. Time series of the inhibitory population's synchrony $|Z_I|$ just beyond the Turing-Hopf bifurcation. Parameters: $\alpha_{EE} = 0.7, \alpha_{EI} = 0.5, \alpha_{IE} = 0.7, \alpha_{II} = 0.8, \sigma_{EE} = \sigma_{IE} = 0.5, \sigma_{EI} = \sigma_{II} = 1.5, \tau_E = 12, \tau_I = 15, \kappa^s_{EE} = 4.8, \kappa^s_{EI} = \kappa^s_{IE} = 5.5, \kappa^s_{II} = 4.1, c_{EE} = c_{EI} = c_{IE} = c_{II} = 0.1, \kappa^v_{EE} = \kappa^v_{EI} = \kappa^v_{IE} = \kappa^2_{II} = 0.2, \Delta_E = \Delta_I = 0.5, V^{EE}_{syn} = 15, V^{EI}_{syn} = -V^{IE}_{syn} = 10, V^{II}_{syn} = -15.5, \eta_E = \eta_I = 1$.

In Figure 4.18, we show the spectrum at a Turing-Hopf bifurcation and simulations just beyond this bifurcation, where standing waves can be found. The synchrony of the excitatory population oscillates in the range $|Z_E| \approx 0.22$ to $|Z_E| \approx 0.31$, and

the synchrony of the inhibitory population oscillates in the range $|Z_I| \approx 0$ to $|Z_I| \approx 0.3$.

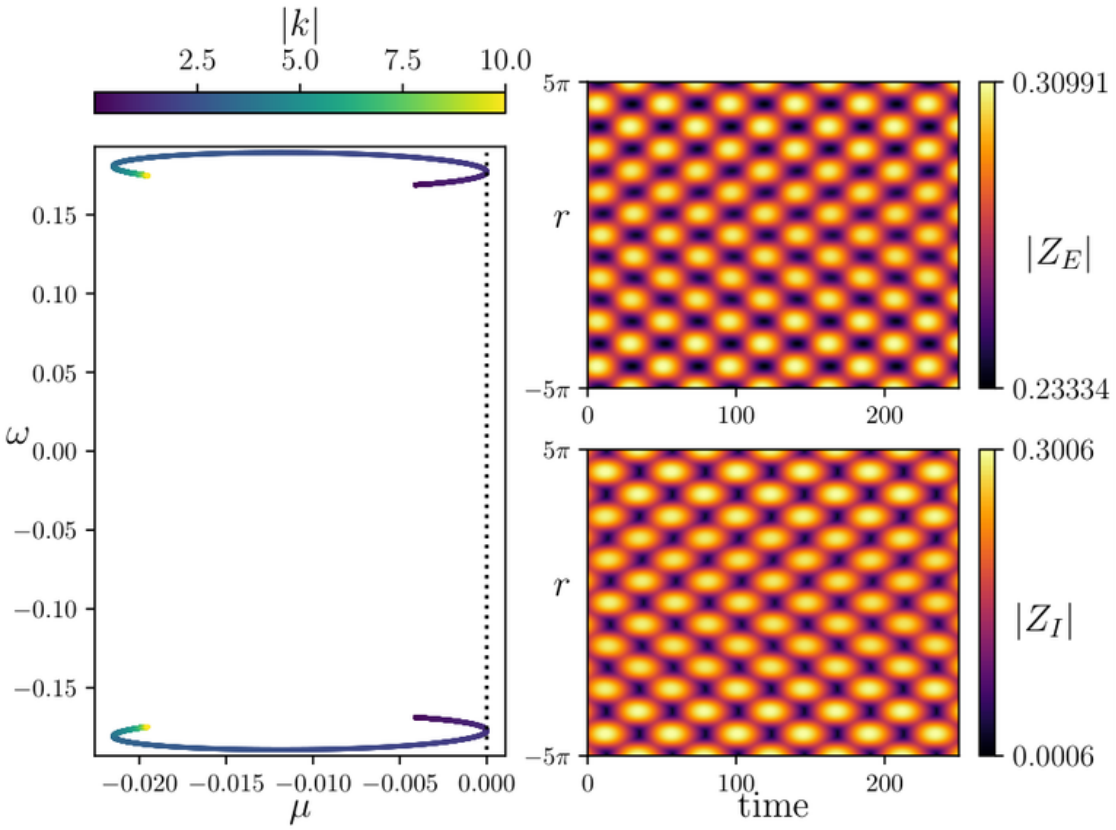

Figure 4.18: Left: The spectrum of the system at a Turing-Hopf bifurcation that occurs at $|k| = 1.36$ when $\kappa_{EE}^v = \kappa_{EI}^v = \kappa_{IE}^v = \kappa_{II}^2 = 0.19$. Right top: Time series of the excitatory population's synchrony $|Z_E|$ just beyond the Turing-Hopf bifurcation. Time series of the inhibitory population's synchrony $|Z_I|$ just beyond the Turing-Hopf bifurcation. Parameters: $\alpha_{EE} = 0.7, \alpha_{EI} = 0.5, \alpha_{IE} = 0.7, \alpha_{II} = 0.8, \sigma_{EE} = \sigma_{IE} = 0.5, \sigma_{EI} = \sigma_{II} = 1.5, \tau_E = 12, \tau_I = 15, \kappa_{EE}^s = 4.8, \kappa_{EI}^s = \kappa_{IE}^s = 5.5, \kappa_{II}^s = 4.1, c_{EE} = c_{EI} = c_{IE} = c_{II} = 0.1, \kappa_{EE}^v = \kappa_{EI}^v = \kappa_{IE}^v = \kappa_{II}^2 = 0.2, \Delta_E = \Delta_I = 0.5, V_{syn}^{EE} = 16, V_{syn}^{EI} = -V_{syn}^{IE} = 10, V_{syn}^{II} = -15.5, \eta_E = \eta_I = 1$.

In Figure 4.19, we show the effect of moving beyond the bifurcation shown in Figure 4.18 by changing the gap junction strengths. Increasing κ_v^{EE} to 0.6, while keeping the remaining gap junction strengths at 0.2, results in periodic travelling waves. The excitatory synchrony ranges from $|Z_E| \approx 0.23$ to $|Z_E| \approx 0.35$, while inhibitory syn-

chrony ranges from $|Z_I| \approx 0.06$ to $|Z_I| \approx 0.36$. Setting $\kappa_v^{EI} = \kappa_v^{IE} = 0.6$ with the remaining strengths at 0.2 also produces travelling waves, with excitatory synchrony increasing from $|Z_E| \approx 0.08$ to $|Z_E| \approx 0.4$ and inhibitory synchrony from $|Z_I| \approx 0.4$ to $|Z_I| \approx 0.6$.

Setting $\kappa_v^{II} = 0.6$ while keeping other coupling values at 0.2 results in travelling waves, with excitatory synchrony ranging from $|Z_E| \approx 0.2$ to $|Z_E| \approx 0.36$ and inhibitory synchrony from $|Z_I| \approx 0.03$ to $|Z_I| \approx 0.4$. When $\kappa_v^{EE} = \kappa_v^{IE} = \kappa_v^{EI} = 0.6$ and $\kappa_v^{II} = 0.2$, travelling waves are observed with excitatory synchrony between $|Z_E| \approx 0.2$ and $|Z_E| \approx 0.4$, and inhibitory synchrony between $|Z_I| \approx 0.1$ and $|Z_I| \approx 0.46$.

Setting $\kappa_v^{EE} = \kappa_v^{II} = 0.6$ while the remaining coupling strengths remain at 0.2 results in periodic travelling waves propagating from a central core. Excitatory synchrony ranges from $|Z_E| \approx 0.0$ to $|Z_E| \approx 0.5$, while inhibitory synchrony ranges from $|Z_I| \approx 0.0$ to $|Z_I| \approx 0.7$. Finally, when all gap junction coupling strengths are set to 0.6, a slight increase in maximum synchrony is observed, with excitatory synchrony ranging from $|Z_E| \approx 0.0$ to $|Z_E| \approx 0.61$, and inhibitory synchrony ranging from $|Z_I| \approx 0.12$ to $|Z_I| \approx 0.74$.

4.4.2 2D Instability Analysis and Numerical Simulation

We now move on to the two-dimensional case, where we use the 2D connectivity function

$$w_{ab}(|\mathbf{r}|) = \frac{\exp(-|\mathbf{r}|/\sigma_{ab})}{2\sigma_{ab}^2\pi}.$$

We again perform a Turing instability analysis, which is detailed in Appendix B.7. We show in Figure 4.20 a Turing-Hopf bifurcation occurring at $|\mathbf{k}| \approx 2.02$, where we observe spiral patterns forming just beyond this bifurcation. We now perform a similar numerical investigation as in Figure 4.19. Firstly, in Figure 4.21, we set $\kappa_v^{EE} = 0.8$,

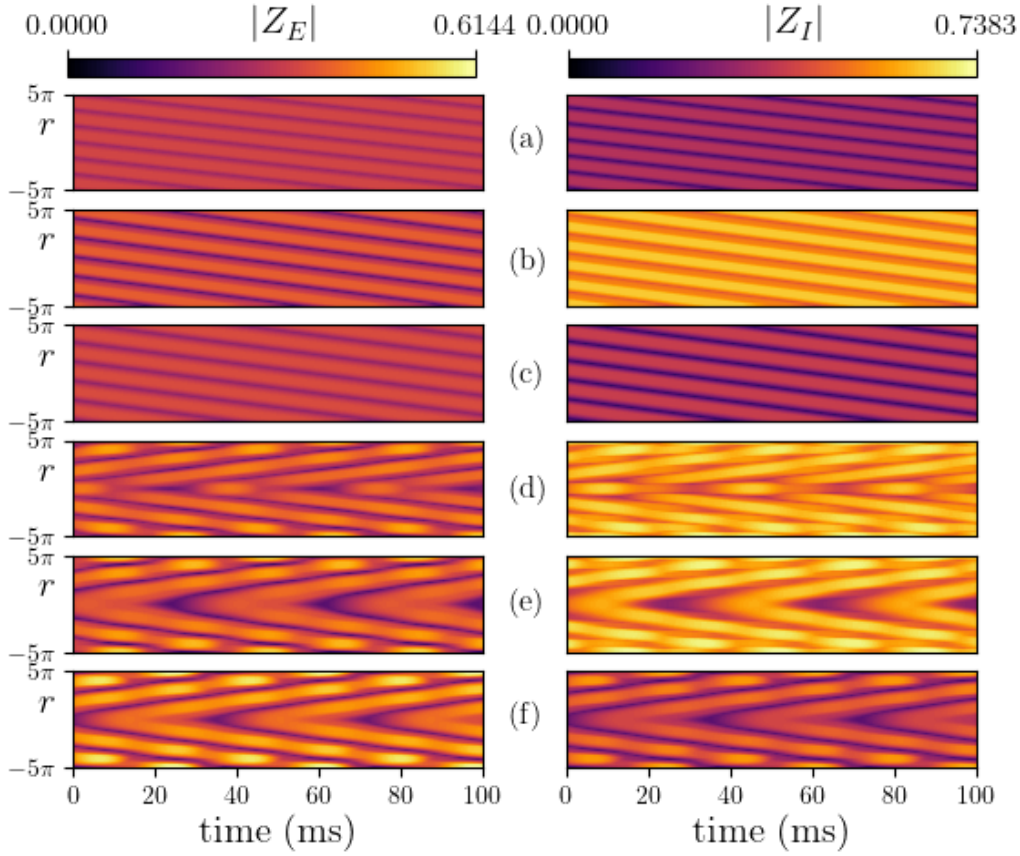

Figure 4.19: Showing the affect of various configurations of gap junction coupling.(a) $\kappa_v^{EE} = 0.6$,$\kappa_v^{EI} = \kappa_v^{IE} = \kappa_v^{II} = 0.2$. (b) $\kappa_v^{EE} = \kappa_v^{EI} = \kappa_v^{IE} = 0.2.$, $\kappa_v^{II} = 0.6$ (c) $\kappa_v^{EE} = 0.2$, $\kappa_v^{EI} = \kappa_v^{IE} = 0.6$, $\kappa_v^{II} = 0.2$ (d) $\kappa_v^{EE} = \kappa_v^{EI} = \kappa_v^{IE} = 0.6$, $\kappa_v^{II} = 0.2$ (e) $\kappa_v^{EE} = 0.6$, $\kappa_v^{EI} = \kappa_v^{IE} = 0.2$, $\kappa_v^{II} = 0.6$ (f) $\kappa_v^{EE} = 0.2$, $\kappa_v^{EI} = \kappa_v^{IE} = \kappa_v^{II} = 0.6$ (g) $\kappa_v^{EE} = \kappa_v^{EI} = \kappa_v^{IE} = \kappa_v^{II} = 0.6$. All other parameters are the same as in

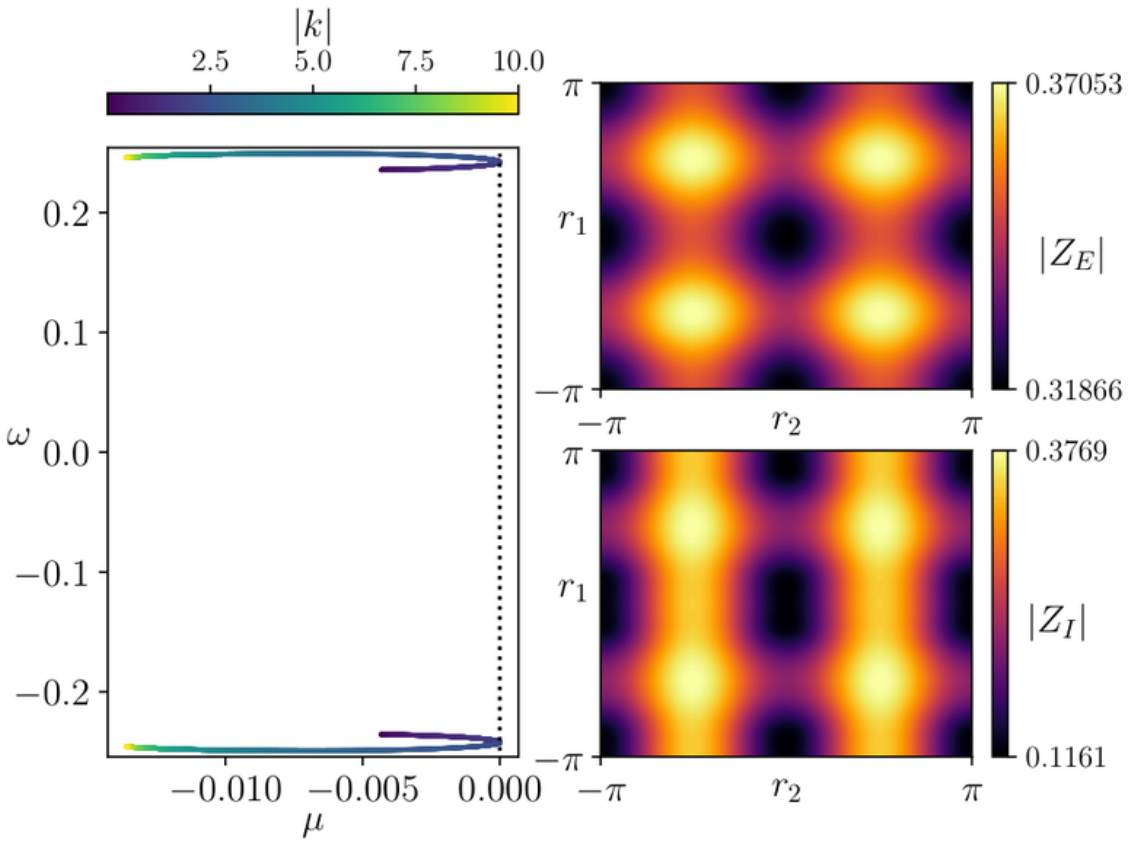

Figure 4.20: Left: A slice along the $k_2 = 0$ axis of the rotationally invariant spectrum of the system at a Turing-Hopf bifurcation occurring at $|\mathbf{k}| \approx 2.02$ when $\kappa^v_{EE} = \kappa^v_{EI} = \kappa^v_{IE} = \kappa^2_{II} = 0.435$. Right top: Time series of the excitatory population's synchrony $|Z_E|$ just beyond the Turing-Hopf bifurcation. Time series of the inhibitory population's synchrony $|Z_I|$ just beyond the Turing-Hopf bifurcation. Parameters: $\alpha_{EE} = 0.7, \alpha_{EI} = 0.5, \alpha_{IE} = 0.7, \alpha_{II} = 0.8, \sigma_{EE} = \sigma_{IE} = 0.4, \sigma_{EI} = \sigma_{II} = 0.8, \tau_E = 10, \tau_I = 11, \kappa^s_{EE} = 4.8, \kappa^s_{EI} = \kappa^s_{IE} = 5.5, \kappa^s_{II} = 4.1, c_{EE} = c_{EI} = c_{IE} = c_{II} = 0.1, \kappa^v_{EE} = \kappa^v_{EI} = \kappa^v_{IE} = \kappa^2_{II} = 0.44, \Delta_E = \Delta_I = 0.5, V^{EE}_{syn} = 16, V^{EI}_{syn} = -V^{IE}_{syn} = 10, V^{II}_{syn} = -15.5, \eta_E = \eta_I = 1$.

with all other gap junction coupling strengths set to 0.44. With this configuration, we observe similar dynamics to Figure 4.20, with spiral waves propagating around 16 nodes. The excitatory synchrony ranges from $|Z_E| \approx 0.35$ to $|Z_E| \approx 0.83$, while the inhibitory synchrony ranges from $|Z_I| \approx 0.0$ to $|Z_I| \approx 0.58$.

In Figure 4.22, we set $\kappa_v^{II} = 0.8$, while all other gap junction coupling strengths remain at 0.44. In this configuration, the spiral waves become more pronounced compared to Figure 4.21, with excitatory synchrony ranging from $|Z_E| \approx 0.21$ to $|Z_E| \approx 0.44$ and inhibitory synchrony from $|Z_I| \approx 0.46$ to $|Z_I| \approx 0.72$.

In Figure 4.23, we set $\kappa_v^{II} = \kappa_v^{EI} = \kappa_v^{IE} = 0.8$, with all other gap junction coupling strengths at 0.44. In this configuration, the spiral waves become more tightly wound compared to Figure 4.22, and maximum synchrony increases in both sub-populations. The excitatory synchrony ranges from $|Z_E| \approx 0.18$ to $|Z_E| \approx 0.52$, while the inhibitory synchrony ranges from $|Z_I| \approx 0.41$ to $|Z_I| \approx 0.76$.

In Figure 4.24, we set all gap junction coupling strengths to 0.8. In this configuration, spiral patterns persist, and maximum synchrony increases compared to Figure 4.23. The excitatory synchrony ranges from $|Z_E| \approx 0.0$ to $|Z_E| \approx 0.8$, while the inhibitory synchrony ranges from $|Z_I| \approx 0.04$ to $|Z_I| \approx 0.83$.

Links to movies showing the full spatial and temporal dynamics of the simulations in Figures 4.21, 4.22, 4.23, and 4.24 can be found in Appendix B.8.

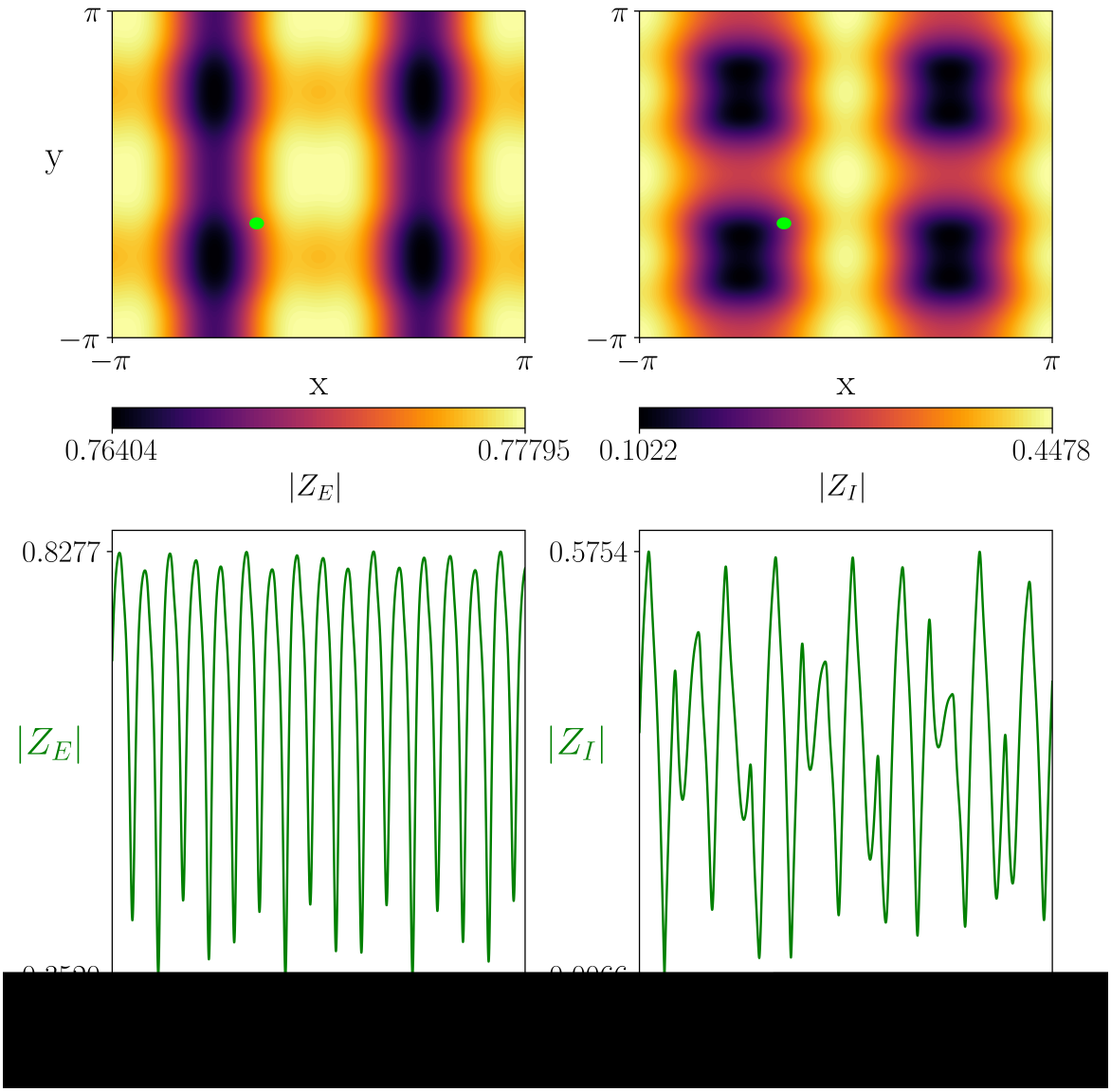

Figure 4.21: Top: Snapshots in time of a simulation of the synchrony variables where κ_v^{EE} is set to 0.8. The domain is patterned with 16 oscillatory spiral cores with high levels of inhibitory synchrony and intermediate levels of excitatory synchrony. Bottom: Time series of the synchrony variables for the green point in the upper panels. All remaining parameters are the same as in Figure 4.20.

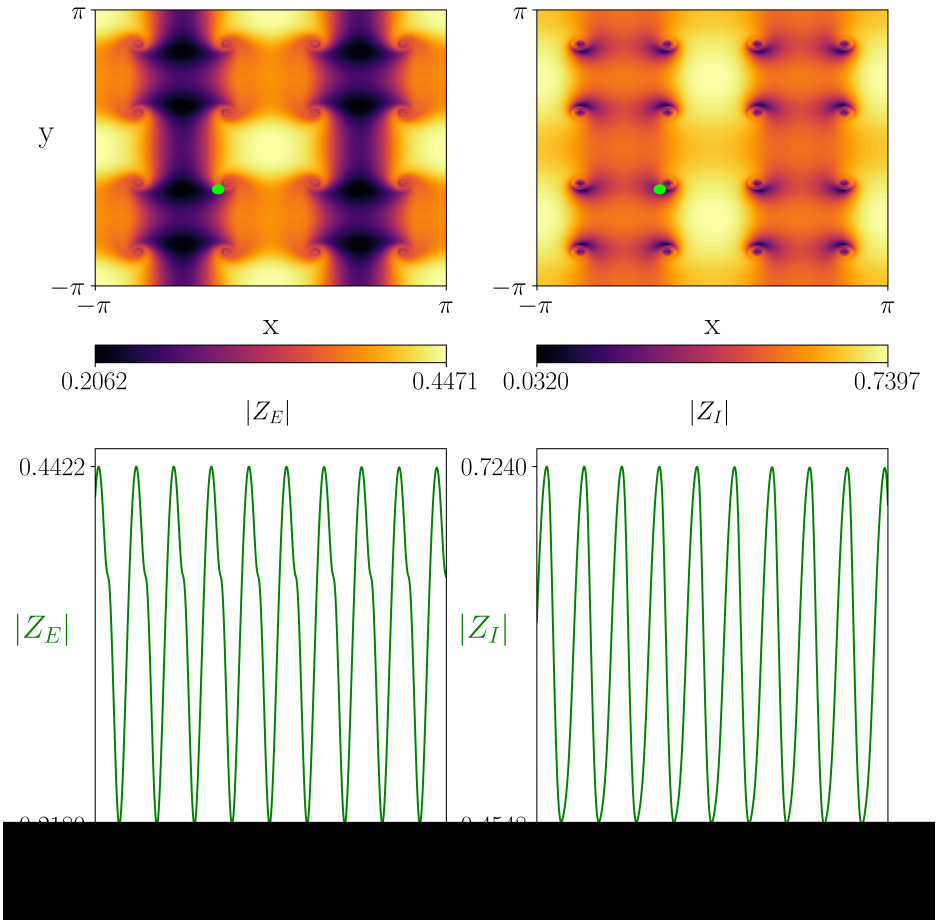

Figure 4.22: Top: Snapshots in time of a simulation of the synchrony variables where $\kappa_v^{II} = 0.8$. The domain is patterned with oscillatory spiral cores, which are slightly more tightly wound than those in Figure 4.21. Bottom: Time series of the synchrony variables for the green point in the upper panels. All remaining parameters are the same as in Figure 4.20.

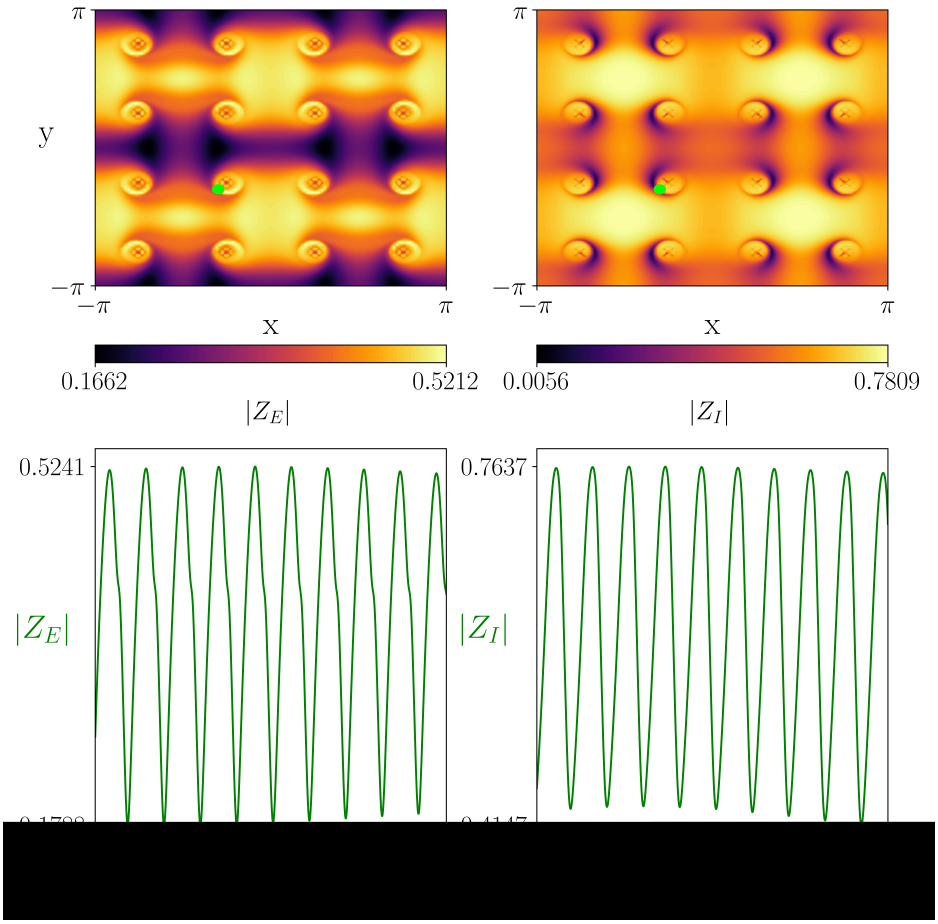

Figure 4.23: Top: Snapshots in time of a simulation of the synchrony variables where $\kappa_v^{II} = \kappa_v^{EI} = \kappa_v^{IE} = 0.8$. The domain is patterned with spiral patterns, showing intermediate synchrony in the excitatory population and high synchrony in the inhibitory population. The spirals are even more tightly wound than in Figure 4.23. Bottom: Time series of the synchrony variables for the green point in the upper panels. All remaining parameters are the same as in Figure 4.20.

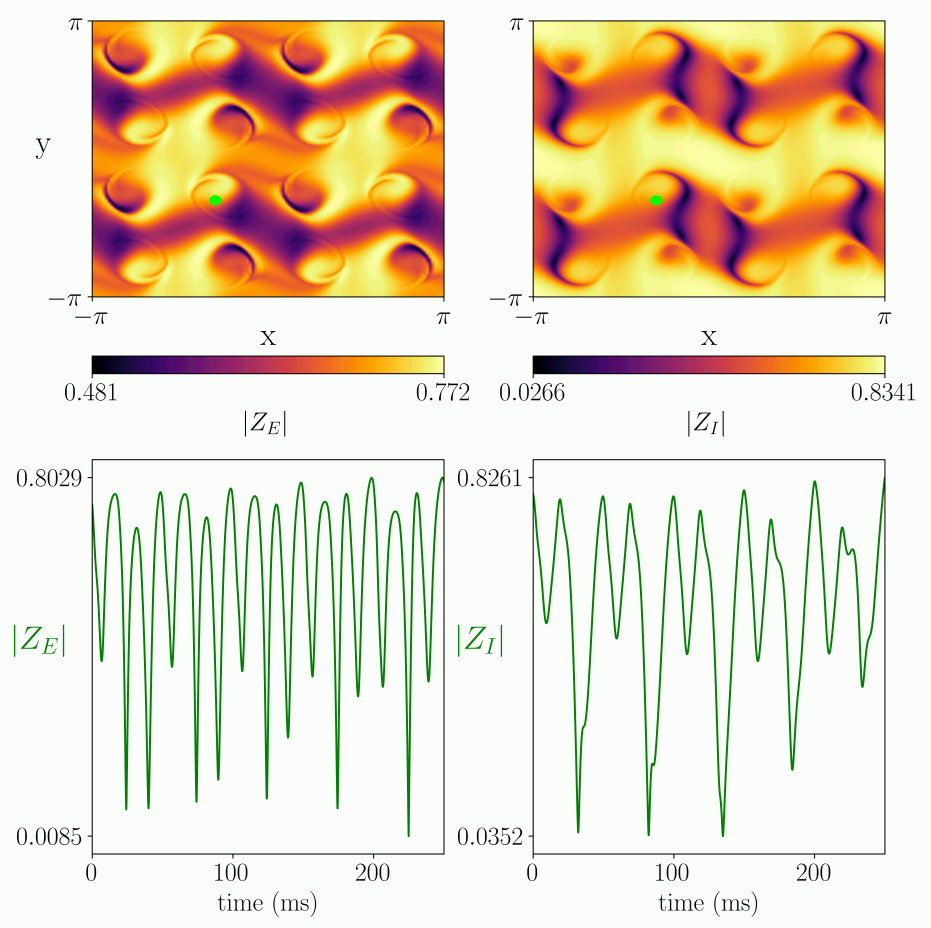

Figure 4.24: Top: Snapshots in time of a simulation of the synchrony variables where $\kappa_v^{EE} = \kappa_v^{EI} = \kappa_v^{IE} = \kappa_v^{II} = 0.8$. The domain is again patterned by 16 spiral cores, even more tightly wound than in Figure 4.23, with an increase in both excitatory and inhibitory synchrony. Bottom: Time series of the synchrony variables for the green point in the upper panels. All remaining parameters are the same as in Figure 4.20.

4.5 Discussion

In this chapter, we have developed and examined a neural model derived from a network of QIF models incorporating local gap junction coupling. Through bifurcation analysis, we demonstrated that an increase in gap junction coupling induces oscillations via a Hopf bifurcation within a single-population mass model, alongside presenting numerical simulations of these oscillations. Additionally, we conducted a numerical bifurcation analysis on a model comprising two interacting neuronal sub-populations, specifically excitatory and inhibitory neurons, revealing that this model can generate complex and intriguing oscillations through computational simulations.

We further explored a field model in which each spatial point represented a single-population mass model, interconnected with other points through a non-local connectivity function. By conducting a Turing instability analysis in both one and two spatial dimensions, we examined the impact of enhanced gap junction coupling strength. Our direct numerical simulations indicated that the model is capable of producing exotic spatio-temporal patterns, which vary with the gap junction coupling strength. Lastly, we investigated a neural field model consisting of two interacting neuronal populations, excitatory and inhibitory neurons, and found that it also supports interesting dynamic patterns.

The models presented in this chapter exhibited a variety of spiral and bump-like states with incoherent cores, reminiscent of chimera states recently seen in coupled oscillator models [85]. Chimera states are hypothesised to have biological significance as well, with R. Ma *et al.* hypothesising that chimeras could underlie the oscillatory dynamics observed in uni-hemispheric sleep, where one half of the brain sleeps while the other remains awake [86]. Some evidence of chimera like states in EEG recordings have

been reported as well, with Tongoli and Kelso observing clusters of coordinated and uncoordinated activity during a human study [87]. We also found an abundance of spiral waves in this chapter, demonstrating that spiral wave dynamics can also be easily found in a next-generation neural field model with gap junctions. Spiral waves are believed to play an important role in *status epilepticus*, where spiral waves form after the annihilation of a wavefront [88] and have been observed in an animal EEG study [89]. The specific patterns observed depended on the configuration of gap junction strength between the neuronal populations.

An advantage of this model lies in its foundation on a network of interacting spiking neurons, where the QIF model effectively simulates the shape of action potentials. This means that we can have a more precise representation of gap junctions at the cellular level. Gap junctions are known to facilitate synchrony in neural tissues, as demonstrated by studies, and they play an important role in neural coordination [53], [90]. Furthermore, the strength of these connections has been associated with the heightened synchrony that characterises epileptic seizures [91], which was also seen in the simulations presented in this chapter. It is also important to recognise the significant role of the extracellular space on seizure dynamics, which is explored in depth in [92].

Recent work by Martinet *et al.* [56] highlights the value of applying computational models to this issue by building on the Steyn-Ross diffusion approach to modelling gap junctions in a neural field model, discussed in Section 4.1, with a simple dynamic model for local extracellular potassium concentration. This approach involves modelling gap junctions by adding a diffusive term to a standard neural field model. Increases in local extracellular potassium concentration lead to a decrease in the inhibitory-to-inhibitory gap junction diffusion coefficient, simulating the closing of gap junctions due to slow

acidification of the extracellular environment late in seizures.

In Chapter 6, we delve deeper into the framework introduced in this chapter. Drawing inspiration from the work of Martinet *et al.*, we construct a model that links extracellular potassium dynamics to the gap junction neural field model discussed here. The possibility of examining different disorders associated with hyper-synchronisation, along with the ability to explore models that connect extracellular dynamics with gap junction strength, highlights the importance of this model in investigating neural dynamics—specifically, its value for understanding conditions characterised by unusual neural synchrony.

CHAPTER 5

USING A GENETIC ALGORITHM TO FIT A STOCHASTIC NEURAL MASS MODEL TO MEG BETA-BURST DATA

Recent studies have demonstrated that a next-generation neural mass model is capable of exhibiting beta-bursting behaviour that closely resembles the patterns observed in real, non-averaged magnetoencephalography (MEG) and electroencephalography (EEG) data [16]. However, despite this qualitative similarity, no attempts were made in that work to fit the model systematically to empirical data.

In this chapter, we build upon this research by employing a stochastic neural mass model to generate beta-bursting dynamics. To analyse and compare these bursts quantitatively, we use a hidden Markov model (HMM) to detect beta bursts in both simulated neural mass model data and real MEG recordings. Furthermore, we develop a Genetic Algorithm (GA) to optimise the model parameters, ensuring that the simulated beta-bursting characteristics align with certain statistical properties derived from real MEG data. The implementation of the GA, along with the associated code, is publicly available at https://github.com/Jamesafross/BetaBurstGA.

5.1 Background

Large scale neural oscillations are detectable through the use of EEG or MEG and are thought to be the product of a vast ensemble of neurons oscillating synchronously [93]. These rhythmic oscillations are categorised by frequency bands, for example: alpha (8-13Hz), beta (13-30Hz) and gamma (30+Hz). Oscillations in the beta band frequency are of particular interest due to abnormal activity in the beta band being linked to a variety of brain diseases and disorders such as Parkinson's disease and schizophrenia [94], [95], [96]. Experiments where human participants perform motor tasks (such as ballistic finger movements) produce robust results that demonstrate a drop in beta-band power during the movement (movement related beta decrease) followed by a transient large increase in power before returning to baseline (known as post-movement beta rebound) [97]. This behaviour has been successfully replicated with a next-generation neural mass model [14]. Classically, beta frequency brain oscillations were thought to be sustained oscillations that varied in amplitude over time due to certain tasks being performed, however this picture was formed by looking at trial averaged data and more recent studies investigating non-averaged data suggests that beta oscillations occur in so-called 'bursts' which are transient spikes in power in the beta frequency range, rather than smooth oscillations [98]. Stochastic next-generation neural mass models are able to exhibit similar bursting behaviour as that seen in MEG data and in Figure 5.1 we show an example of a spectrogram from a beta-bursting mass model simulation and an example of an averaged spectrogram across many simulations. This is similar to human trial averaged data. Burst detection methods typically have employed some form of threshold detection where one would filter the time series data (from an EEG or MEG reading) by frequency band and use an amplitude threshold to determine when the bursting was occurring, however

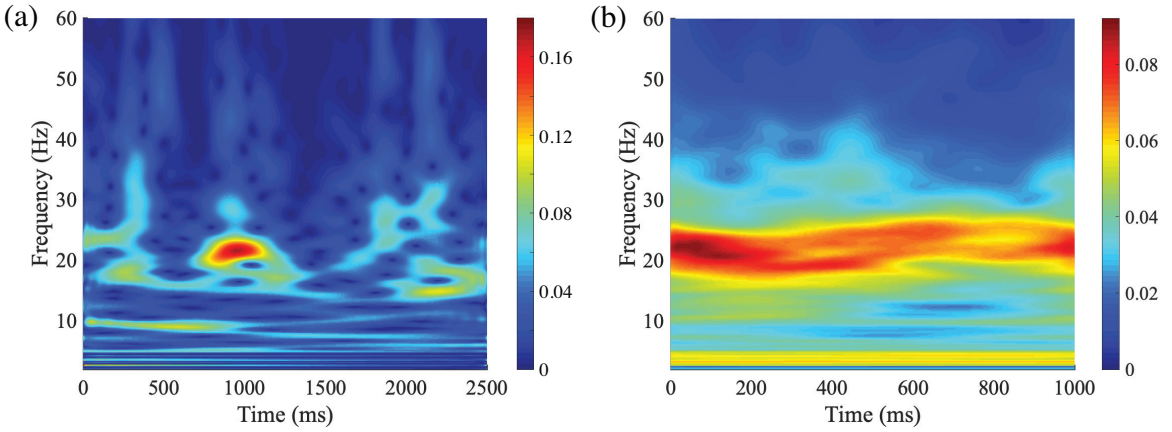

Figure 5.1: A spectrogram showing the power in specific frequency bands of simulated stochastic mass models with red indicating high power and blue indicating low power. Left: An example of a beta-burst using a single realisation of a stochastic mass model simulations. Right: An example of mass model data that has been averaged across many simulations that is similar to spectrograms seen in trial averaged human data.

recently a HMM was developed to identify bursting states in MEG time series data that provides a more objective way of detecting burst states by looking at specific spectral patterns rather than just amplitude in a single frequency band [94].

5.2 The Model

Stochastic neural mass models are able to support beta-bursting like behaviour [16] and authors such as Powanwe and Longtin [99] have used a stochastic two population Wilson-Cowan model to investigate bursting behaviour in the Gamma (30+Hz) frequency band and developed a method where they could directly link model parameters to burst duration and envelope by using statistical averaging methods. Here, we consider a two population next-generation stochastic neural mass model adapted from the deterministic model that was discussed in Chapter 4. We adapt the model in equation (4.14) by including an additive stochastic forcing term, S_a, that is the solution to an Ornstein-Uhlenbeck process [100] which we use here to generate low-pass

filtered white noise [101]. This low-pass filtering of the noise was done due to beta bursts often occurring alongside alpha-band activity [102]. The model may be written as a set of coupled stochastic equations,

$$\begin{aligned}
\tau_a \mathrm{d}R_a &= \left[-R_a \sum_b (g_{ab} + \kappa^v_{ab}) + 2R_a V_a + \frac{\Delta_a}{\tau_a \pi}\right] \mathrm{d}t, \\
\tau_a \mathrm{d}V_a &= \left[\sum_b \kappa^v_{ab}(V_b - V_a) + \sum_{b\in\{E,I\}} g_{ab}(V^{ab}_{syn} - V_a) + V_a^2 - \pi^2\tau_a^2 R_a^2 + \eta^a_0 + S_a\right] \mathrm{d}t, \\
\frac{1}{\alpha_{ab}} \mathrm{d}g_{ab} &= [(-g_{ab} + p_{ab})]\,\mathrm{d}t, \\
\frac{1}{\alpha_{ab}} \mathrm{d}p_{ab} &= [(-p_{ab} + \kappa^s_{ab} R_b)]\,\mathrm{d}t, \\
\mathrm{d}S_a &= -\frac{S_a}{\tau^x_a}\mathrm{d}t + \sigma_a \mathrm{d}W_a,
\end{aligned} \tag{5.1}$$

where $a, b \in \{E, I\}$ denotes the population type (excitatory or inhibitory), W_a is a Weiner process (i.e. a one dimensional Brownian motion), σ_a^2 is the variance of the Gaussian noise for population a, and τ^x_a controls the time-scale of the filtered noise variable S_a. This set of equations are solved numerically using an Euler-Maruyama scheme. In order to achieve beta bursting behaviour in our model we pose the system close to a Hopf bifurcation and use small σ_a so that the amplitude of the Gaussian noise is small. If the oscillations beyond this bifurcation are within the beta-band frequency then we would achieve beta band bursts when the stochastic term pushes the system beyond bifurcation. The parameters that were chosen for optimisation were $\sigma_a, \tau^x_a, \kappa^v_{ab}, \kappa^s_{ab}, \alpha_{ab}$. Since MEG detects signals based on ionic currents (inferred via magnetic field changes), the output time-series that we pass to the optimisation algorithm will be the sum of post-synaptic excitatory and inhibitory currents:

$$I_{net} = I_E + I_I, \qquad I_a = \sum_b g_{ab}(V^{ab}_{syn} - V_a). \tag{5.2}$$

5.3 Methods and Tools

In this section, we discuss the methods employed to detect beta-bursts in the MEG and model time series, as well as the optimisation algorithm developed to fit the neural mass model to the MEG data.

5.3.1 Hidden Markov Model

HMMs are a type of statistical Markov model. A time-series is assumed to be composed of mutually exclusive 'hidden' states Y that govern the observed time-series X. The series is assumed to be Markovian such that the state at time t is only conditionally dependent on time $t-1$. Following [94] the HMM used here assumes 3 hidden states (though if not enough evidence of 3 states, it will instead assume only 2 states) that correspond to an autocovariance pattern that is defined over 230ms which contains the spectral information of the state that is active. The state who's probability timecourse correlated highest with the beta amplitude envelope is determined to be the beta-bursting state. For a more in-depth description, analysis of the HMM, and results and discussion around more than 3 hidden states (provided in the supplementary information), refer to the paper by Z. Seedat *et al.* [94] and the GitHub repository https://github.com/OHBA-analysis/HMM-MAR.

5.3.2 MEG Data

The MEG data analysed in this chapter is drawn from a subset of a larger dataset originally published as part of a 2018 study conducted by Hunt *et al.* [103]. This study, which investigated neural activity using MEG, was reviewed and approved by the University of Nottingham Medical School Research Ethics Committee to ensure compliance with ethical research standards. Following its initial publication, the dataset was subsequently utilised in further analyses, including those presented by Z. Seedat *et al.* in [94].

The MEG recordings were acquired using a 275-channel CTF MEG system, a high-resolution neuroimaging device capable of detecting and capturing minute fluctuations in magnetic fields generated by neural activity. Data were collected at a sampling rate of 1200 Hz, providing fine temporal resolution necessary for the detailed examination of neural dynamics. The cortex was then parcellated into 78 regions according to the automated anatomical labelling (AAL) atlas [104] such that after processing each subject dataset contained 78 time-series. Further discussion on the processing of the data may be found in [94].

For the purposes of this chapter, a subset of the original dataset was selected, specifically comprising recordings from three participants (so, in total 234 time-series). Each participant underwent 5 minute MEG recording during a 'resting state', a practice commonly employed in neuroscience to assess baseline neural activity in the absence of specific task engagement. During these sessions, participants were instructed to remain seated with their eyes open while attempting to maintain a mental state free of directed thoughts. A fixation cross was projected onto a screen, providing a focal point for the participants.

For further details regarding the experimental design, data acquisition, and analyses, see the original publication by Hunt *et al.* [103].

5.3.3 The Genetic Algorithm

In this section, we adapt a GA to optimise the parameters of our model. GAs belong to a class of iterative optimisation techniques inspired by Charles Darwin's theory of evolution. They were first developed by John Holland and his colleagues in the 1960s and 1970s as a method for solving complex optimisation problems by mimicking natural selection. For a comprehensive review of GAs, their applications, and future research directions, see [105].

The GA begins by generating an initial population of candidate parameter sets, known as phenotypes, which are created randomly. Each phenotype represents a potential solution to the optimisation problem. The algorithm then evaluates the fitness of each phenotype by assessing how well it performs according to the fitness function. In our case, fitness is determined by comparing statistical properties of the model's output to those observed in real data.

Once fitness scores are assigned, the algorithm selects a subset of the fittest phenotypes using a specified selection method. These selected phenotypes are then used to create the next generation through the application of genetic operators, which include mutation and crossover. Mutation introduces small random changes to individual parameters, while crossover combines aspects of two parent phenotypes to produce new offspring. This iterative process continues over multiple generations, progressively refining the parameter sets to improve the fit between the model and the data.

The objective of applying a GA in this context is to identify a set of parameters for the stochastic neural mass model that results in a close match to empirical MEG

data. Specifically, we aim to fit the model to three statistical properties extracted from human MEG resting-state recordings:

- Beta-burst duration (the length of time that bursts of neural activity persist),
- Number of beta-bursts (the frequency of burst events)
- Beta-burst power (the amplitude or intensity of bursts).

In order to quantify the overall fitness of a parameter set, we compute the average relative absolute difference between the statistical properties of the simulated data and those observed in real MEG recordings. This metric ensures that the optimisation process prioritises solutions that minimise discrepancies across all three statistical features.

In Figure 5.2 a flowchart that succinctly describes the process of the GA is shown.

The Fitness Function

The GA relies on a fitness function to evaluate how well the neural model aligns with the MEG data. Developing an appropriate fitness function for this model involved an iterative refinement process. For instance, during initial tests, a fitness function was implemented that compared only the mean and standard deviation of beta-bursts between the real data and the model output. While this approach provided some level of success, it failed to account for discrepancies in the skew of the data distributions. To address this, additional statistical parameters, namely skew and kurtosis, were incorporated into the fitness function. The final version of the fitness function is as follows:

$$F = \frac{1}{12} \sum_{i} \sum_{j} M_{ij}, \tag{5.3}$$

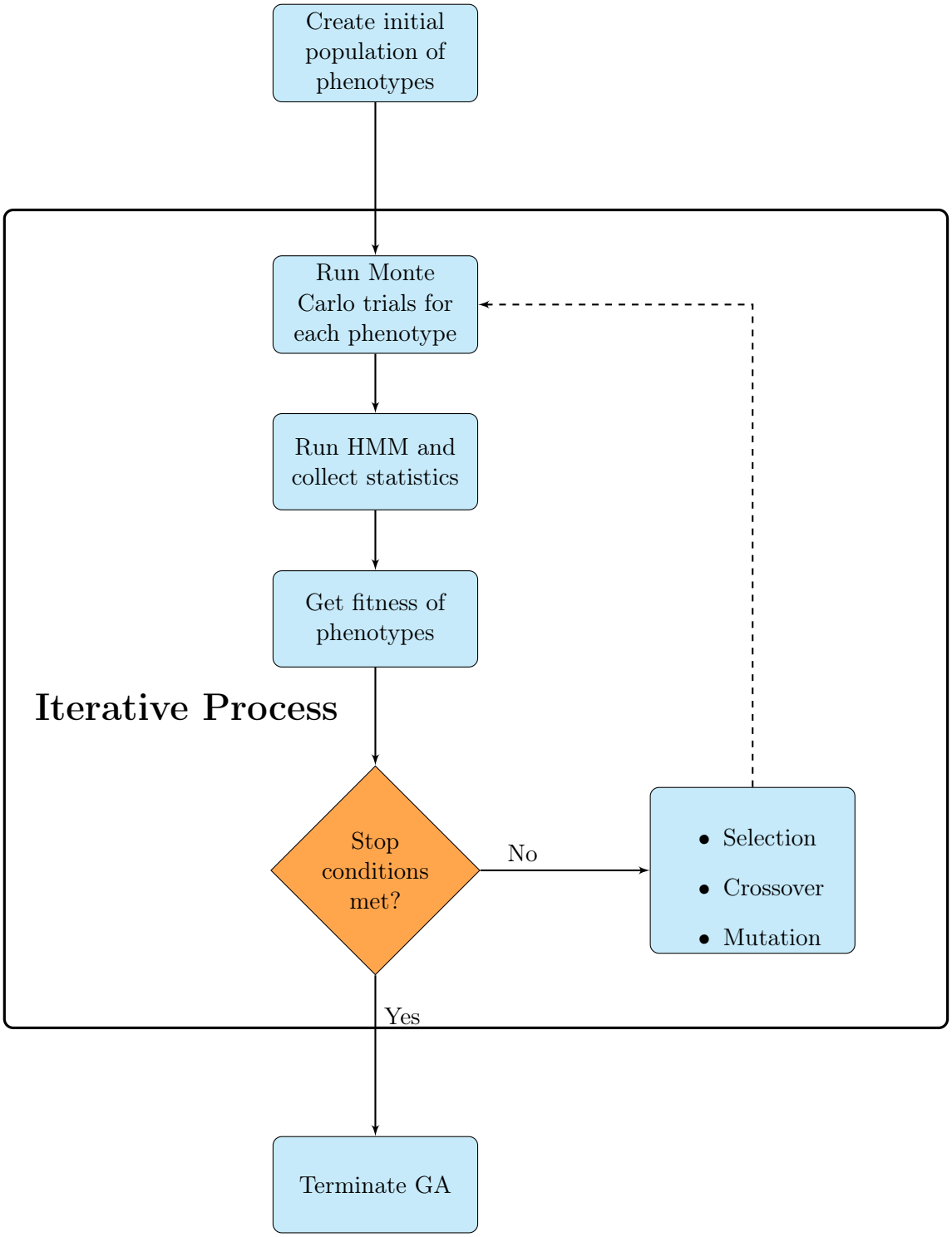

Figure 5.2: A basic flow chart diagram of the GA showing the iterative process that the algorithm goes through in order to find optimal parameter sets.

where M is the 4 by 3 matrix of absolute relative differences of all the target statistics and is shown in (5.4) and a lower evaluation of F corresponds to a better fit.

$$M = \begin{bmatrix} |D^m_{MEG} - D^m_{model}|/D^m_{MEG} & |P^m_{MEG} - P^m_{model}|/P^m_{MEG} & |N^m_{MEG} - N^m_{model}|/N^m_{MEG} \\ |D^s_{MEG} - D^s_{model}|/D^s_{MEG} & |P^s_{MEG} - P^s_{model}|/P^s_{MEG} & |N^s_{MEG} - N^s_{model}|/N^s_{MEG} \\ |D^{sk}_{MEG} - D^{sk}_{model}|/D^{sk}_{MEG} & |P^{sk}_{MEG} - P^{sk}_{model}|/P^{sk}_{MEG} & |N^{sk}_{MEG} - N^{sk}_{model}|/N^{sk}_{MEG} \\ |D^k_{MEG} - D^k_{model}|/D^k_{MEG} & |P^k_{MEG} - P^k_{model}|/P^k_{MEG} & |N^k_{MEG} - N^k_{model}|/N^k_{MEG} \end{bmatrix} \tag{5.4}$$

Here D stands for mean beta-burst duration, P stands for beta-burst power and N stands for number of beta-bursts (per second) and are all real valued numbers. Superscripts indicate the statistic type, m for mean, s for standard deviation, sk for skew and k for kurtosis. Subscripts indicate whether the statistic is from the MEG data or the model. All the time series were combined and used to calculate each statistic, for example D^s_{MEG} is calculated by taking the average burst duration from each of the 234 MEG time series, then calculating the standard deviation.

Selection Method

The selection method used here is a variation of *tournament selection*, a commonly used selection method. In this variation, phenotypes are first divided into two groups: Group A and Group B. Each phenotype in Group A is paired with a phenotype in Group B, and the phenotype with the better fitness from each pair advances to the next round while the other is discarded. This process is repeated iteratively until either the maximum number of rounds is reached or a specified number of phenotypes have been eliminated. Both of these stopping conditions can be adjusted by the user of the algorithm.

Genetic operators

Genetic operators are functions that are used in the creation of the next generation of phenotypes by applying transformations to the phenotypes from the previous generation in a GA. In this GA, we utilise the two most common genetic operators: *crossover* and *mutation*.

The crossover operator combines two *parent* phenotypes by exchanging a randomly selected subset of parameters between them, producing two *child* phenotypes as a result. An example of crossover applied to two parameter sets is shown below.

Firstly, two parent phenotypes are passed to the crossover function, denoted as P_0 and P_1 with parameters $p_{a,b} \in P_a$ and $b \in [0, 11]$:

$P_0 \rightarrow$ $p_{0,0}$ $p_{0,1}$ $p_{0,2}$ $p_{0,3}$ $p_{0,4}$ $p_{0,5}$ $p_{0,6}$ $p_{0,7}$ $p_{0,8}$ $p_{0,9}$ $p_{0,10}$ $p_{0,11}$

$P_1 \rightarrow$ $p_{1,0}$ $p_{1,1}$ $p_{1,2}$ $p_{1,3}$ $p_{1,4}$ $p_{1,5}$ $p_{1,6}$ $p_{1,7}$ $p_{1,8}$ $p_{1,9}$ $p_{1,10}$ $p_{1,11}$

The swap positions are then selected as 0,4,5 and 8 then the output 'child' phenotypes C_0 and C_1 will be:

$C_0 \rightarrow$ $p_{1,0}$ $p_{0,1}$ $p_{0,2}$ $p_{0,3}$ $p_{1,4}$ $p_{1,5}$ $p_{0,6}$ $p_{0,7}$ $p_{1,8}$ $p_{0,9}$ $p_{0,10}$ $p_{0,11}$

$C_1 \rightarrow$ $p_{0,0}$ $p_{1,1}$ $p_{1,2}$ $p_{1,3}$ $p_{0,4}$ $p_{0,5}$ $p_{1,6}$ $p_{1,7}$ $p_{0,8}$ $p_{1,9}$ $p_{1,10}$ $p_{1,11}$

The *mutation* operator promotes diversity in the population and prevents convergence to local optima. The operator takes a single phenotype as an input and alters a random number of parameter values in this phenotype by a small amount. As an example, mutation we take C_0 and apply a mutation to parameters 4,7, and 8. We denote the mutated child phenotype as C'_a and mutated parameters as $p'_{a,b}$ the result is:

$C_0 \rightarrow$ $p_{0,0}$ $p_{0,1}$ $p_{0,2}$ $p_{0,3}$ $p_{0,4}$ $p_{0,5}$ $p_{0,6}$ $p_{0,7}$ $p_{0,8}$ $p_{0,9}$ $p_{0,10}$ $p_{0,11}$

$C'_0 \rightarrow$ $p_{0,1}$ $p_{0,1}$ $p_{0,2}$ $p_{0,3}$ $p'_{0,4}$ $p_{0,5}$ $p_{0,6}$ $p'_{0,7}$ $p'_{0,8}$ $p_{0,9}$ $p_{0,10}$ $p_{0,11}$

5.3.4 Running the Algorithm

This section provides a detailed demonstration of the GA, including its initialisation and iterative steps.

Initiating the Algorithm

An initial population of size N_{pop} (chosen as $N_{pop} = 100$ for this study) is generated with random parameter values within desired boundaries, i.e. such that time constants are ensured to be non-negatives and other parameters do not exceed a pre-determined magnitude,

$$init\_pop = \begin{bmatrix} p_0^1 & p_0^2 & p_0^3 & \cdots & p_0^n \\ p_0^1 & p_0^2 & p_0^3 & \cdots & p_0^n \\ \vdots & \vdots & \vdots & \ddots & \vdots \\ p_{N_{pop}}^1 & p_{N_{pop}}^2 & p_{N_{pop}}^3 & \cdots & p_{N_{pop}}^n \end{bmatrix}$$

See appendix C.2 for further details and a table displaying information about the optimised and static parameters. The parameters used in this analysis are tested to confirm that the system is near a bifurcation. This is achieved by first evaluating the eigenvalues for a given set of parameters, ensuring that all the real parts of each of the eigenvalues are below 0. Then, small perturbations are applied to the η_0^a variables, which are the variables the noise drives, and then the eigenvalues are recalculated. If the stability of the system changes after these perturbations, it indicates proximity to a bifurcation. The model is then simulated for N_{trial} (chosen as $N_{trial} = 100$ for this study) Monte Carlo trials for each parameter set. Each time-series output is then analysed for beta-bursts using the HMM and the statistics on the burst duration, power and number are collected.

Evaluating and ranking fitness, and Choosing breeders

Once the statistics for each phenotype (parameter set) are collected, we then can rank the phenotypes in order of fitness. A phenotype will be denoted P_i with $i \in 1, 2, ..., N_{pop}$ so that:

$$P_i = p_i^0, p_i^1, ..., p_i^n.$$

The ranking of phenotype fitness is done by using the fitness function and letting the phenotype with the smallest fitness value be the *most fit* and the phenotype with the largest fitness value be the *least fit*. For instance, consider a set of 10 phenotypes with varying fitness levels, as shown in Table 5.2.

Table 5.1:

Fitness Rank	Parameter Set	Fitness
1	P_0	3
2	P_1	6
3	P_2	10
4	P_3	14
5	P_4	16
6	P_5	20
7	P_6	23
8	P_7	24
9	P_8	30
10	P_9	51

Table 5.2: Example set of phenotypes with various fitness values and fitness ranks.

Breeders are then selected by using the previous described tournament selection process. These breeders are then randomly paired for crossover in order to generate a population of phenotypes of size N_{pop}. Each of these phenotypes has a probability

of p_m to mutate and a small amount of the phenotypes generated are replaced with randomly generated phenotypes in order to promote diversity in the population. The phenotypes after this process are now the phenotypes that will be carried to the next generation. The process is then repeated until a suitable solution is found or the maximum number of generation is reached. This whole process is described in pseudocode in Algorithm 1.

Algorithm 1 Genetic Algorithm for Parameter Optimisation

Initialisation:
Generate an initial population of N_{pop} random phenotypes.
Set iteration counter: $n \leftarrow 0$.
while $n <$ max iterations **or** Best Fitness $<$ Goal Fitness **do**
    Evaluation:
    for each phenotype $i \in \{1, 2, \ldots, N_{pop}\}$ **do**
        for each trial $j \in \{1, 2, \ldots, N_{\text{trial}}\}$ **do**
            Simulate the Stochastic Neural Mass Model using Monte Carlo methods.
        end for
        Analyse the phenotype using Hidden Markov Models (HMM) to extract burst statistics.
        Compute the fitness score F_i based on model-data comparison.
    end for
    Selection:
    Rank phenotypes based on fitness scores $\{F_i\}$.
    Select top-performing phenotypes for reproduction.
    Reproduction:
    Generate the next generation via:
        (i) **Crossover** — Combine traits of selected phenotypes.
        (ii) **Mutation** — Introduce small random variations.
    Add new randomly generated phenotypes to maintain population diversity.
    Iteration Update:
    $n \leftarrow n + 1$.
end while
Termination:
Stop when maximum iterations are reached or best fitness meets goal.

5.3.5 Results

In this section we discuss results from the GA optimised model. We compare model statistics to the MEG data statistics for unoptimised parameter sets and optimised parameter sets. We first present in Figure 5.3 the points in a time-series where the HMM detects beta-bursting (highlighted in red) in the output of the stochastic neural mass model and the corresponding frequency spectrogram. In this figure we see that there is good correlation between HMM detected bursting states and high amplitude in the beta band frequencies. We now turn our attention to the performance of the GA in identifying parameter sets that fit the MEG data well.

Figure 5.4a, presents the statistics of the model with *unoptimised* parameters compared to the MEG data statistics. Without GA optimisation, the fit to the real data is quite poor, with a fitness score of around 20. As a point of reference, fitness scores at the initiation of the algorithm ranged from around 18 - 50. A fitness of around 1-3 would be a reasonably good fit, with much lower fitness being excellent fits.

For burst duration, the *unoptimised* model has a mean of approximately 50 ms, compared to around 250 ms in the real data, and its distribution is considerably narrower. In terms of the number of bursts, the unoptimised model produces an average of 4 bursts per second, whereas the real data shows only about 1 burst per second. Despite this discrepancy, the model reasonably captures the overall spread of the distribution. Finally, for power, while the unoptimised mass model closely matches the mean of the distribution, the variance in the real data is significantly higher.

In Figure 5.4b, we present the statistics of the model after applying *optimised* parameters and after 100 iterations of the algorithm. Compared to simulations using an unoptimised parameter set, the fitness value of the mass model has improved signifi-

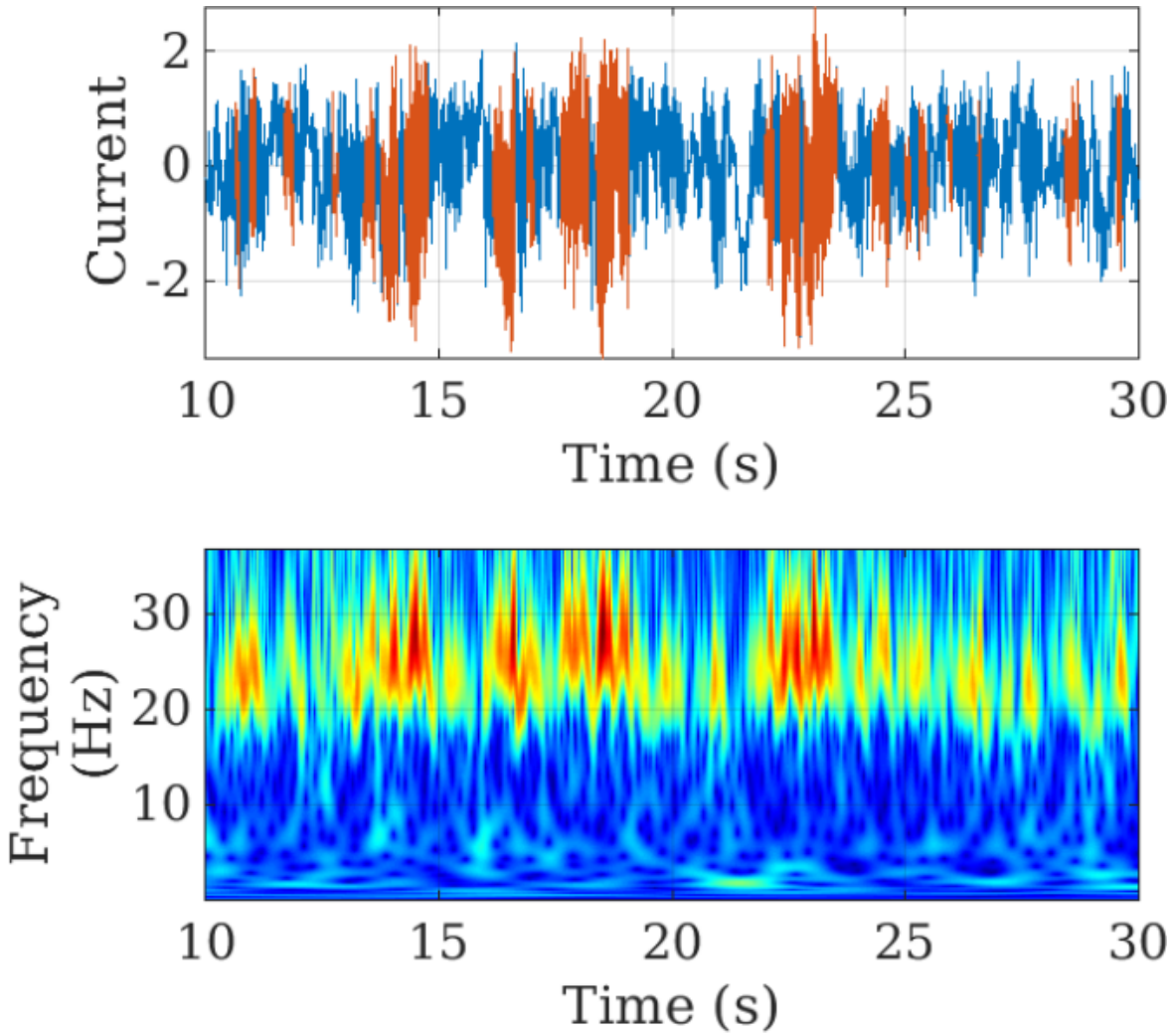

Figure 5.3: Top: Time-series of the net current of the stochastic neural mass model showing the times where the HMM detects a beta-bursting state in red. Bottom: Spectrogram of the current time-series.

cantly, reaching approximately 1.9.

For burst duration, the GA has adjusted the model to better align with the mean observed in the real data while also improving the spread. In terms of the number of bursts, the optimised model now exhibits an excellent fit, with the GA refining the parameters to achieve a mean value much closer to 1 burst per second. Finally, for power, the GA has further enhanced the fit, maintaining the previously reasonable

match to the mean while increasing variance in the mass model to better reflect the real data.

Across all statistics, the GA has improved the fit to the real data, with the most significant improvement seen in the number of bursts per second.

5.4 Limitations of the Genetic Algorithm

While the GA successfully improved the model's fitness, it is still far from ideal. Several factors may be limiting the potential for a very good fit. An important consideration is that we are fitting a single neural mass model to whole-brain data, which, by nature, does not fully capture the complexity of brain dynamics. A possible solution to this would be to fit a network of mass models to the MEG data, but this would be very computationally intensive due to the need to simulate many Monte-Carlo trials of a large network and was not tried here, although in the next section we consider network studies with fixed optimised parameters. Secondly, the need for running large amount of simulations meant that a cycle of one generation was slow and the GA needed to cycle through many generations to find fit parameter sets. Generally, the bottleneck of the algorithm was the HMM. The HMM was written in Matlab and, although MEX files were used to speed up the process, perhaps using a programming language that has better performance (such as Julia or C++) would benefit the process of optimisation. These are all consideration for future work.

5.5 Network of Stochastic Mass Models

In this section we investigate how well a network of identical mass models performs against real data when using our optimised parameters. In order to do this, we use

connectivity data gathered from diffusion tensor imaging (DTI) of human subjects that to estimate structural connectivity between brain regions as a weight matrix for our network, as well as Euclidean distances between brain regions to derive delays between nodes assuming a common axonal conduction speed.

5.5.1 Structural Connectivity and Distance Data

It is now increasingly popular to use real world structural connectivity and distance data in brain network models. For example, The Virtual Brain [28] and studies employing computational methods to investigate pathologies such as epilepsy [29], [30], along with research exploring the relationship between structural and functional connectivity [31], [38] and studies on neural network changes due to brain stimulation [106].

Structural connectivity measures the strength of connections between different areas of the brain. It can be assessed using Diffusion Tensor Imaging (DTI), a non-invasive technique that enables the in vivo mapping of white matter by tracking the directional diffusion of water molecules to reconstruct major fibre tracts between brain regions [107]. To further model these connections, tractography generates streamlines, which estimate the trajectories of fibre tracts using either deterministic or probabilistic approaches. Importantly, streamline count has been shown to provide a reliable estimation of white matter pathway projection strength [108]. One draw back to this approach is that it is not possible to determine the directionality of the tracts [109] and therefore the resulting connectivity matrix is symmetric. For discussion of the limitations and open problems in building connectomes from DTI data see [32]. It is common with these methods to parcellate the brain into N regions of interest (ROI) and generate a symmetric $N \times N$ matrix that represents the number of fibre tracts

between each region. This number of fibre tracts between each ROI is then log transformed and the resulting matrix is normalised by dividing by the largest element. A full description of the method for obtaining structural connectivity matrices can be found in [110]. The distance between regions can be calculated either by Euclidean distance between regions or measuring the length of the reconstructed fibre tracts. In Figure 5.5 we show an example of a structural connectivity matrix and a distance matrix that represents the Euclidean distance between brain regions. In this particular case the brain has been brain parcellated into 82 regions and the data used here was acquired from the Human Connectome Project [111].

5.5.2 The Model

In order to build the brain network, we use 82 nodes representing different brain regions where each brain region is modelled as one stochastic next-generation mass model. This can be interpreted as each of the 82 neural mass models representing the average activity of each of the 82 brain regions, We use real structural connectivity data and Euclidean distance data to determine the global excitatory-excitatory coupling strengths and the distance between these regions respectively. We assume that only excitatory-excitatory synaptic connections are distally coupled and the remaining connections only couple within local mass populations, which is consistent with large scale brain anatomy [112]. Using equation 5.1 as the mass model on each node we

may write the network model as:

$$
\begin{aligned}
\tau_a \mathrm{d}R_i^a &= \left[-R_i^a \sum_b (g_i^{ab} + \kappa_{ab}^v) + 2R_i^a V_i^a + \frac{\Delta_a}{\tau_a \pi} \right] \mathrm{d}t, \\
\tau_a \mathrm{d}V_i^a &= \left[\sum_b \kappa_{ab}^v (V_i^b - V_i^a) + \sum_{b \in \{E,I\}} g_i^{ab} (V_{syn}^{ab} - V_i^a) + (V_i^a)^2 - \pi^2 \tau_a^2 (R_i^a)^2 + \eta_0^a + S_a \right] \mathrm{d}t, \\
Q_{EE} g_i^{EE} &= \kappa_{EE} R_i^E + \kappa_g \sum_{j \neq i} W_{ij} R_j^E (t - D_{ij}/c), \\
Q_{EI} g_i^{EI} &= \kappa_{EI} R_i^I, \\
Q_{IE} g_i^{IE} &= \kappa_{IE} R_i^E, \\
Q_{II} g_i^{II} &= \kappa_{II} R_i^I, \\
\mathrm{d}S_i^a &= -\frac{S_i^a}{\tau_a^x} \mathrm{d}t + \sigma_a \mathrm{d}W_i^a, \\
a, b &\in \{E, I\}, \quad i \in \{1, ..., 82\}
\end{aligned}
\tag{5.5}
$$

Where W is the 82×82 structural connectivity matrix and D is the 82×82 Euclidean distance matrix. The model is simulated using an Euler-Maruyama stochastic delay differential equation solver that uses the method of steps to handle the delays and is from the Julia StochasticDelayDiffEq.jl package [68], [113], [114].

5.5.3 Fitness in the Network

When incorporating the optimised parameters into the network model we found that the fit to the real data statistics was not drastically affected when the network coupling strength parameter (κ_g) was low but the fit increasingly worsened for larger κ_g. This is demonstrated in Figure 5.6 where we show the average fit (over 15 trials) of the network simulations to the real data statistics used in the previous section. We tested a variety of network coupling strengths from $\kappa_g = 0.01$ to $\kappa_g = 0.2$. Although variance exists

in the fit as coupling strength increases, a clear pattern emerges: as κ_g increases, the fitness to real data decreases. However, for low global coupling strengths, the model still achieves a good fit. This means that it may be possible just to fit a single node model instead of a whole brain model to the data as long as the desired global coupling remains low.

5.6 Discussion

In this chapter, a GA was used to fit a neural mass model to beta-bursting MEG resting state data. The GA managed to increase fitness significantly, although seemingly lacked the power to find highly optimised parameters. This may be due to a variety of factors. One significant consideration is that we are currently fitting a single-node model to whole-brain data, which, while computationally manageable, is an oversimplification of the brain's true complexity. This model assumes that the entire brain can be represented by a single node, which is unlikely to accurately capture the intricate effects from the coupling between brain regions. To address this limitation, one approach might involve fitting a more sophisticated stochastic network model to the MEG data. This would allow us to better represent the network-level dynamics of the brain, incorporating the interactions between multiple regions. However, this solution comes with its own set of challenges, as running multiple Monte Carlo trials of the network model would be vastly more computationally intensive, requiring significant processing power and time. Despite these challenges, the potential insights gained from a more detailed, network-based model could significantly improve our understanding of the underlying brain dynamics especially as computational technology improves, for example in the form of cheap GPU nodes.

In future, a few improvements and tweaks to the algorithm could be considered, for

example although a method for analysing beta-bursts using a HMM was used here, other methods for analysing burst statistics also exist. A thresholding method, such as the one developed by Briley *et al.* in [115], could be easily integrated into the GA optimisation in place of the HMM. Switching to a thresholding method might also improve the speed of the GA as it is computationally cheaper than the HMM. Furthermore, some of the GAs settings were restricted by memory constraints, namely N_{trial} and N_{pop}, it may be possibly to optimise some of the Julia and Matlab code to further optimise memory usage, or using a system with a larger RAM capacity. Other changes to the algorithm might also help improve the quality of the optimisation. For example, using adaptive mutation or crossover could make the GA more flexible across generations. At the moment, the mutation strength and crossover probabilities are fixed, but in practice it might make more sense for these to change over time, e.g. allowing for larger mutations early on to explore the space, and smaller, more local tweaks later when the population has started to converge (See [116] for an array of comparisons between static and adaptive mutation). These could also be tied to stagnation, so if the best fitness has not improved for a while, the mutation rate could increase to help the GA escape local minima. Another possible change would be to revisit the fitness function itself. Right now it relies on summary statistics, but it might be more informative to a metric which directly compares the shape of the distributions. One option would be the Earth Mover's Distance (EMD) [117], which measures how much 'work' it would take to turn one distribution into another. This could also help mitigate the issue of local optima to some degree, as the fitness function would only consider three metrics (EMD for burst power, duration, and number) rather than the twelve used in this chapter.

Finally, when incorporating the optimised parameters into the network we saw that the fitness was quite robust to that of low coupling strengths, though as the network

coupling strength parameter increased the fitness decreased. This gives some hope to being able to optimise parameters at a single node, though better results would still be expected when optimising parameters for a specific network. Future work on the network model could include optimising the parameters on each node of the network, such that the nodes are non-identical, which might improve the fitness of the network model, although this would be very computationally demanding

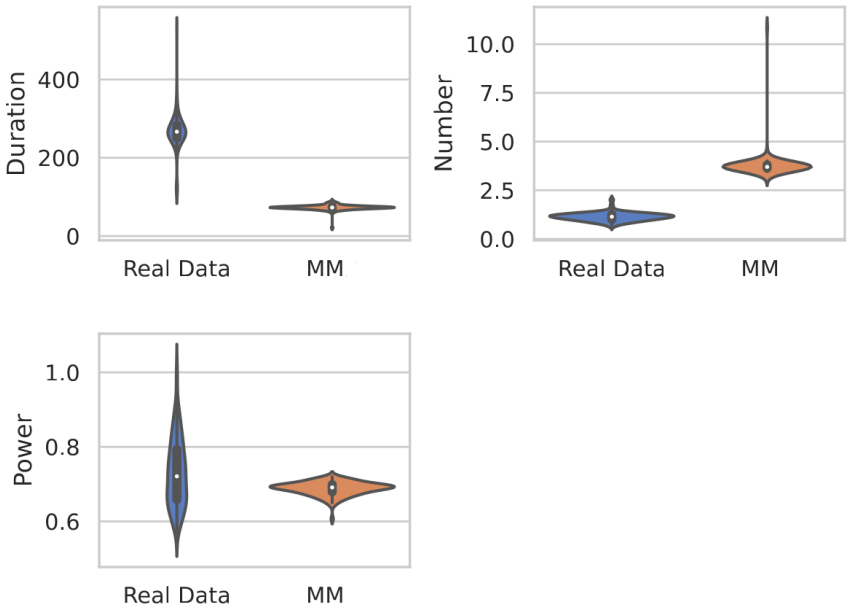

(a)

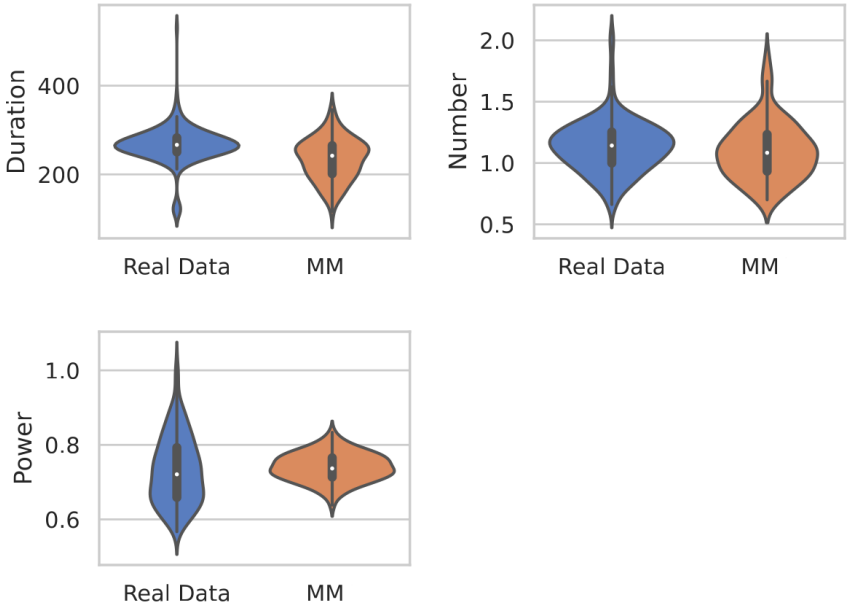

(b)

Figure 5.4: (a) Violin plots of statistics from beta-burst MEG data (blue) and the mass model with unoptimised parameters where the fitness was found to be around 20 (orange). (b) Violin plots of statistics from beta-burst MEG data (blue) and the mass model with optimised parameters with a fitness of around 1.9 (orange). Parameters: $\sigma_E = 0.0732467$, $\sigma_I = 0.0245387$, $\tau_E^x = 96.2379$, $\tau_x^I = 83.527$, $\kappa_{EE}^s = 1.05445$, $\kappa_{IE}^s = 1.25752$, $\kappa_{EI}^s = 1.69066$, $\kappa_{II}^s = 1.14127$, $\alpha_{EE} = 0.0916871$, $\alpha_{IE} = 0.19345$, $\alpha_{EI} = 0.912817$, $\alpha_{II} = 0.432702$, $\kappa_{EE}^v = 0.123881$, $\kappa_{EI}^v = \kappa_{IE}^v = 0.225644$, $\kappa_{II}^v = 0.230313$, $V_{syn}^{EE} = V_{syn}^{IE} = 9$, $V_{syn}^{II} = V_{syn}^{EI} = -10$, $\eta_0^E = 2.0$,$\eta_0^I = 1.04$, $\tau_E = 12$, $\tau_I = 15$, $\Delta_E = \Delta_I = 0.2$.

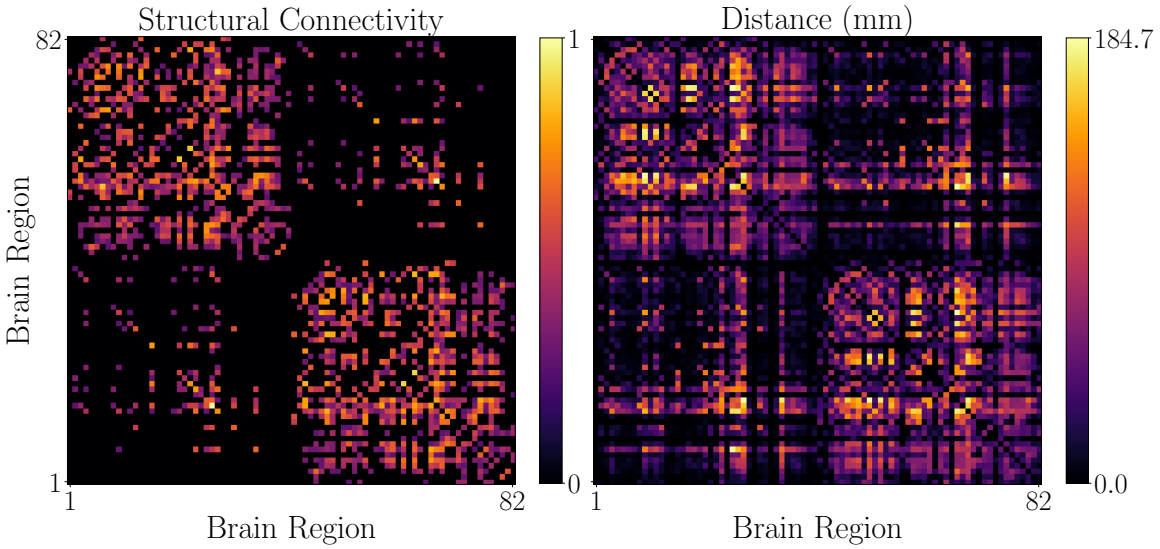

Figure 5.5: Left: Structural connectivity matrix based on the fibre tracts between 82 brain regions. Right: Distance between 82 regions measured as the length of the fibre tracts. Data sourced from the Human Connectome Project (https://www.humanconnectomeproject.org/).

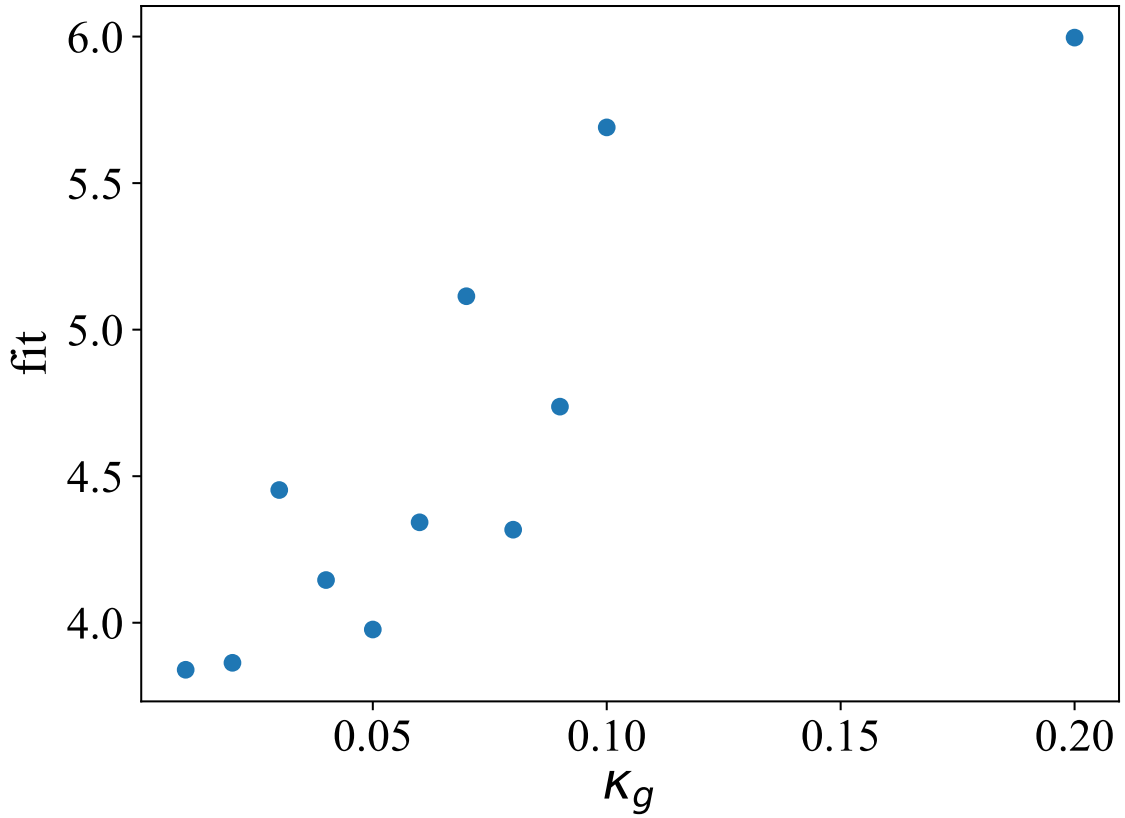

Figure 5.6: The fitness of network simulations statistics to the MEG bursting data with varying values of κ_g from $\kappa_g = 0.01$ to $\kappa_g = 0.2$ using parameters that were optimised on a single node. As κ_g increases the fitness to the real data decreases.

CHAPTER 6

COUPLING A NEURAL ACTIVITY MODEL TO EXTRACELLULAR SPACE

Epilepsy is a group of neurological disorders that affect approximately 65 million people globally. It is primarily characterised by recurrent abnormal brain activity, known as seizures [118]. An increase in the concentration of potassium ions (K^+) in the brain's extracellular space is thought to be a key factor in the development of seizures. This buildup of K^+ has a depolarizing effect on neurons, leading to hyper-excitability and potentially triggering seizures [55].

While research has shown that an increase in extracellular K^+ alone may not be enough to induce seizures, understanding the role of potassium in seizure generation remains an important area of study [119]. Elevated K^+ levels are also linked to the closure of gap junctions due to the slow acidification of the extracellular space [120]. Previous studies suggested that enhancing gap junction coupling could promote hyper-synchronous neuronal activity, potentially leading to seizures. However, other findings indicate that the relationship may be more complex.

In addition, recent research has proposed that a decrease in gap junction coupling could also contribute to seizures by reducing the dynamic stability of neuronal networks. This effect is thought to depend on the strength and duration of the seizure [91].

In this chapter, we build upon the model introduced in Chapter 4 by incorporating a dynamic mechanism for modulating gap junction strength. This is achieved through the inclusion of a model for extracellular potassium dynamics, which directly influences gap junction behaviour. The main goal of this chapter is to present the model and conduct computational analysis, including bifurcation analysis and direct simulations. This work serves as an initial step toward developing next-generation neural mass models that incorporate extracellular dynamics.

6.1 Background

Neural models have a history of being able to accurately simulate the temporal dynamics seen in EEG recordings during epileptic seizure states. For example, the Jansen-Rit model (as discussed in Chapter 2) [121] is able to exhibit resting alpha-band activity and epileptic spikes [122], [123]. Epileptic seizure states are known to be associated with drastic changes in extracellular (and intracellular) ionic concentrations [124] and therefore population level neural activity models that are coupled to extracellular ion concentrations are an important area of research within the fields of mathematical and computational neuroscience. It is important to recognise that brain tissue comprises more than just neurons. For many clinical applications, such as epilepsy, coupling to the extracellular space is beneficial due to the critical role K^+ plays in the genesis and propagation of seizure states. Despite its importance, relatively few neural models account for coupling to extracellular currents. However, various methods have been explored to integrate the coupling of population-level neural models with the extracellular

space. One notable exception is the model studied by Martinet *et al.*, which employed an adapted Wilson-Cowan-type field model with a sigmoidal firing rate function. In their study, the local extracellular K^+ concentration was shown to elevate the resting potentials of neuronal subpopulations while decreasing inhibitory-inhibitory gap junction coupling [56]. This model revealed interesting spatial dynamics: an initial stimulus applied to a region of the 2D plane triggered a wavefront, which subsequently generated further propagating waves within the area recruited by the initial wavefront. Another example is the work of Rabuffo *et al.* who developed a mean-field model of a network of conductance based neurons (Hodgkin-Huxley type neurons) that include the dynamics of various ion exchanges [125].

6.2 The Model

The model we use to investigate the effect of extracellular K^+ concentration on neural activity is an adapted next-generation neural field model. The model has two neuronal populations, excitatory and inhibitory, and has local gap junction coupling between the inhibitory populations. We follow Martinet *et al.* [56] and assume that extracellular K^+ concentration increases with neuronal activity (firing rate and mean membrane potential) and add a decay term to model uptake of K^+ by glial cells and other mechanisms. We also account for the spread of K^+ through the extracellular space with a diffusion term. The differential equation governing the extracellular K^+ dynamics may therefore be written as:

$$\beta_1 \frac{\partial}{\partial t} K = -\delta K + f_1(R_E, R_I) + A_3 \nabla^2 K, \tag{6.1}$$

where $K = K(\mathbf{x}, t)$ is the extracellular K^+ concentration at the spatial point $\mathbf{x} \in \Omega \subset \mathbb{R}^2$ and time point $t \in \mathbb{R}$, β_1 is a time constant, $\delta > 0$ is the K^+ decay rate due to reuptake , f_1 is an increasing and saturating function of the mean firing rates and, and $A_3 > 0$ controls the diffusivity of K^+ in the extracellular space. Local K^+ concentration is assumed to increase the mean drives η_i of the system, effectively increasing the excitability of the neurons which mimics the depolarising effect of K^+, and decrease the gap junction coupling strength, modelling the observed affect of gap junctions closing due to the slow acidification of the extracellular space that is associated with an increase in K^+ concentration. The following system of differential equations describe the dynamics of the excitatory and inhibitory mean drives and the inhibitory to inhibitory gap junction coupling strengths:

$$\begin{aligned} \beta_2 \frac{\partial}{\partial t} \eta_E &= -\eta_E + f_2(K), \\ \beta_3 \frac{\partial}{\partial t} \eta_I &= -\eta_I + f_3(K), \\ \beta_4 \frac{\partial}{\partial t} \kappa_{II}^v &= -\kappa_{II}^v + f_4(K), \end{aligned} \tag{6.2}$$

where $\beta_2, \beta_3, \beta_4$ are time constants. Further to this, the neural activity model used in this study is a next-generation model with second order synaptic coupling and axonal delays (similar to the model utilised in Chapter 4). The full model may therefore be

written as:

$$
\begin{aligned}
\psi_{ab} &= \int_{\Omega} w_{ab}(\mathbf{x},\mathbf{x}')R_b(\mathbf{x},\tau_{ab}(\mathbf{x},\mathbf{x}'))\mathrm{d}\mathbf{x}' \quad \tau_{ab}(\mathbf{x}) = \tau_{ab}^0 + |\mathbf{x}|/c_{ab},\\
\left(1+\frac{1}{\alpha_{ab}}\partial_t\right)^2 g_{ab} &= \kappa_{ab}^s\psi_{ab},\\
\tau_E\frac{\partial}{\partial t}R_E &= -R_E\sum_b g_{Eb} + 2R_EV_E + \frac{\Delta_E}{\tau_E\pi},\\
\tau_I\frac{\partial}{\partial t}R_I &= -R_I\sum_b g_{Ib} - R_I\kappa_{II}^v + 2R_IV_I + \frac{\Delta_I}{\tau_I\pi},\\
\tau_E\frac{\partial}{\partial t}V_E &= \sum_b g_{Eb}(V_{syn}^{Eb}-V_E) - \tau_E^2\pi^2R_E^2 + V_E^2 + \eta_E,\\
\tau_I\frac{\partial}{\partial t}V_I &= \sum_b g_{Ib}(V_{syn}^{Ib}-V_I) - \tau_I^2\pi^2R_I^2 + V_I^2 + \eta_I,\\
\beta_1\frac{\partial}{\partial t}K &= -\delta K + f_1(R_E,R_I) + A_3\nabla^2K,\\
\beta_2\frac{\partial}{\partial t}\eta_E &= -\eta_E + f_2(K),\\
\beta_3\frac{\partial}{\partial t}\eta_I &= -\eta_I + f_3(K),\\
\beta_4\frac{\partial}{\partial t}\kappa_{II}^v &= -\kappa_{II}^v + f_4(K).
\end{aligned}
\tag{6.3}
$$

Where $w_{ab}(x)$ is an exponential connectivity function (see chapters 3 and 4)). For this chapter the parameter values used (unless otherwise stated) are as given in Table C.1 and we used the following functions in the equations governing the extracellular K^+, mean drives and inhibitory-inhibitory gap junction strength dynamics:

$$
\begin{aligned}
f_1(R_E,R_I) &\equiv (R_E+R_I)F(R_E+R_I;A_1,A_2,A_3),\\
f_2(K) &\equiv F(K;B_1,B_2,B_3),\\
f_3(K) &\equiv F(K;C_1,C_2,C_3),\\
f_4(K) &\equiv F(K;D_1,D_2,D_3),
\end{aligned}
\tag{6.4}
$$

where F is a sigmoid function of the form $F(x; a, b, c) = a/(1 + \exp(-b(x - c)))$ and $B_2, C_2 > 0$ such that the mean drives increase as extracellular K^+ concentration increases, and $D_2 < 0$ so that gap junction coupling decreases as extracellular K^+ concentration increases. This means that for this study the extracellular K^+ dynamics are dependent on the sum of population firing rates which is in line with the model used by Martinet *et al.* [56].

Table 6.1: Parameter List

Parameter	Value 1D (2D)	Description	Unit
α_{EE}	0.7	Time constant for synapses $E \to E$	ms^{-1}
α_{EI}	0.5	Time constant for synapses $I \to E$	ms^{-1}
α_{IE}	0.7	Time constant for synapses $E \to I$	ms^{-1}
α_{II}	0.8	Time constant for synapses $I \to I$	ms^{-1}
κ^s_{EE}	3.1 (4.5)	$E \to E$ Synaptic strength	
κ^s_{EI}	$\frac{4.9}{5.0}\kappa^s_{EE}$	$I \to E$ Synaptic strength	
κ^s_{IE}	$\frac{4.9}{5.0}\kappa^s_{EE}$	$E \to I$ Synaptic strength	
κ^s_{II}	$\frac{3.0}{5.0}\kappa^s_{EE}$	$I \to I$ Synaptic strength	
τ_E	11	Membrane time constant for population E	ms^{-1}
τ_I	12	Membrane time constant for population I	ms^{-1}
Δ_E	0.2	Coherence for underlying neuronal population E	
Δ_I	0.2	Coherence for underlying neuronal population I	
V^{EE}_{syn}	12	Voltage shunts for connection $E \to E$	
V^{EI}_{syn}	$-\frac{10.0}{16.0}V^{EE}_{syn}$	Voltage shunts for connection $I \to E$	
V^{IE}_{syn}	$-V^{EI}_{syn}$	Voltage shunts for connection $E \to I$	

Continued on next page

Table 6.1: Parameter List (Continued)

Parameter	Value 1D (2D)	Description	Unit
V_{syn}^{II}	$-\frac{11.0}{16.0}V_{syn}^{EE}$	Voltage shunts for connection $I \to I$	
σ^{EE}	0.2	Spatial width for connection $E \to E$	mm
σ^{EI}	1.5	Spatial width for connection $I \to E$	mm
σ^{IE}	0.2	Spatial width for connection $E \to I$	mm
σ^{II}	1.5	Spatial width for connection $I \to I$	mm
c_{ab}	0.08 (0.15)	Axonal conductance velocity	m/s
A_1	1.0	Maximum of the sigmoid in the potassium equation	
A_2	2.0	Sensitivity of the sigmoid function in the potassium equation	
A_3	0.0	Half maximum of the sigmoid in the potassium equation	
A_4	0.3	Potassium diffusivity constant	
δ	0.2	potassium decay variable	
B_1	15.0	Maximum of the sigmoid in the excitatory drives equation	
B_2	8.0	Sensitivity of the sigmoid function in the excitatory drives equation	
B_3	1.0	Half maximum of the sigmoid in the excitatory drives equation	
C_1	15.0	Maximum of the sigmoid in the inhibitory drives equation	
C_2	8.0	Sensitivity of the sigmoid function in the inhibitory drives equation	

Continued on next page

Table 6.1: Parameter List (Continued)

Parameter	Value 1D (2D)	Description	Unit
C_3	1.0	Half maximum of the sigmoid in the inhibitory drives equation	
D_1	0.8	Maximum of the sigmoid in the gap junctions equation	
D_2	-2.0	Sensitivity of the sigmoid function in the gaps-junctions equation	
D_3	1.0	Half maximum of the sigmoid in the gaps-junctions equation	

6.3 Analysis and Computational Study in 1 Spatial Dimension

In this section we study the model (6.3) in the one spatial dimension case ($\Omega = \mathbb{R}$ and set $\mathbf{x} = r$), presenting findings from a Turing instability analysis and a computational study into the behaviour of the model when varying parameters relating to the extracellular K^+ dynamics.

6.3.1 Turing instability analysis

In order to investigate the dynamics of this model we first perform a Turing instability analysis. Since this analytical method has already been demonstrated in detail previously in Chapters 3 and 4 we omit the details here and direct the reader to appendix C.1 for a detailed description of the analysis. Bifurcations were found by finding branch solutions of the spectral equation $M(\lambda, k) = 0$ (here $\lambda \in \mathbb{C}$ is the eigenspectra and k is the spatial wave-number of the applied perturbations) that touch the imaginary axis.

This was done by first solving the steady state equations using a non-linear solver from the Julia package NLsolve.jl and then solving the spectral equations (again using a non-linear solver) and varying κ^s_{EE} until the largest real value of the eigenspectra was 0.

During the investigation of the model, Hopf and Turing-Hopf bifurcations were found in the parameter space. Although we did not explore static Turing bifurcations in this study, it is likely that it would also be possibly to find these types of patterns as well. In Figure 6.1 we show a Hopf bifurcation where the continuous eigenspectra touches the imaginary axis with $|k| = 0$ and also show the bulk oscillation solution that can be found just beyond this bifurcation. In Figure 6.2 we show a Turing-Hopf bifurcation where the continuous eigenspectra touches the imaginary axis with $|k| \approx 1.1$ and the emergent standing waves patterns that occur just beyond this bifurcation.

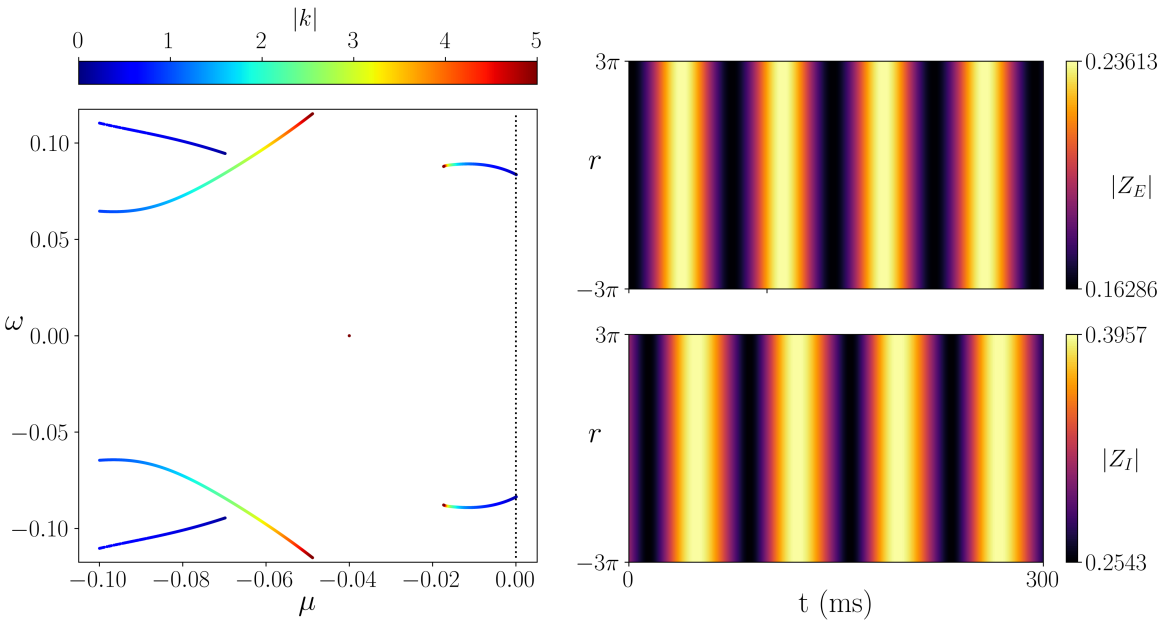

Figure 6.1: Left Panel: Points found numerically from the continuous eigenspectrum $\lambda = \mu + i\omega$ of the system at a Hopf bifurcation. The system crosses the imaginary access with $|k| = 0$. Right panels: Bulk oscillations found via direct numerical simulations just beyond this bifurcation by applying a small spatially homogeneous perturbation to the steady state. Parameters: $\kappa^s_{EE} = 2.3$, $v = 0.2$ and all other parameter values are given in Table C.1.

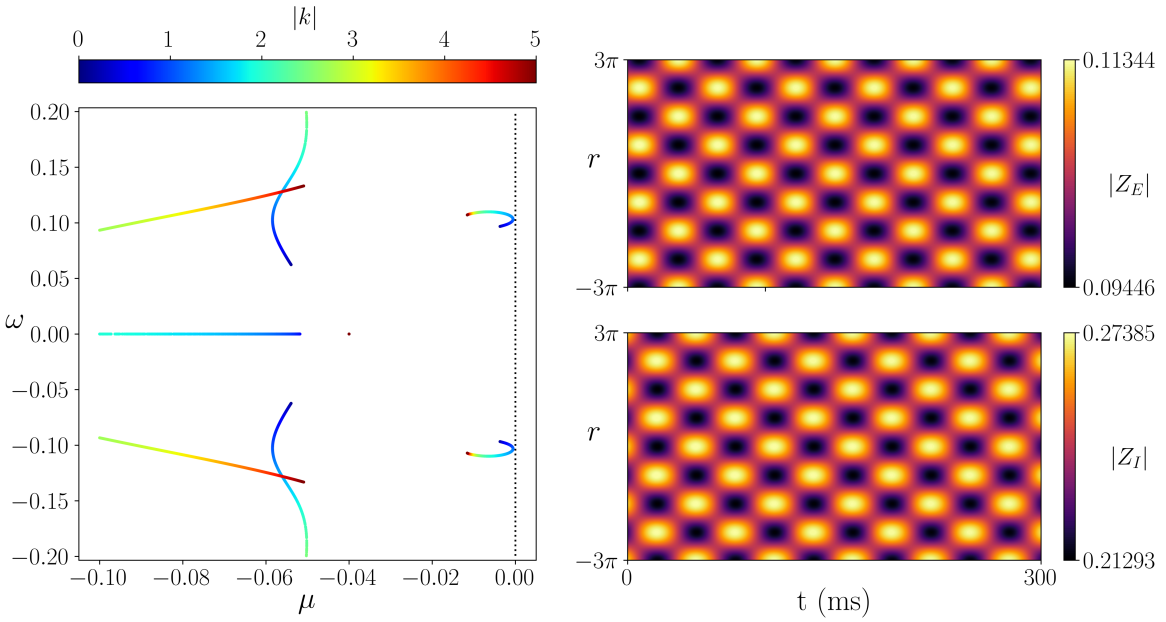

Figure 6.2: Left Panel: Points found from the continuous eigenspectrum $\lambda = \mu + i\omega$ of the system at a Turing-Hopf bifurcation. The system crosses the imaginary access with $|k| \approxeq 1.1$. Right panels: Periodic standing wave solutions found via direct numerical simulations just beyond this bifurcation by perturbing the system with the cosine function $0.01\cos(1.1r)$. Parameter values: $\kappa^s_{EE} = 2.9$ and all other parameter values are given in C.1

6.3.2 Computational Study in 1 Spatial Dimension

In this section the effect of changing some of potassium equation parameters are studied. In all of the following simulations the delay integro-differential equations described in equation (6.3) were again transformed into PDE equations using the same method employed in Chapters 3 and 4 and were simulated by first discretising the PDE equations using a finite difference (with central difference operators) method and then employing an adaptive time-stepper from the Julia [126] differential equations suite [68]. The code for the simulations can be found in a GitHub repository using the URL: https://github.com/Jamesafross/Thesis_Code/tree/main/Neural_Field_with_potassium/.

We start in a parameter regime that allows for dynamical spatial solutions to occur, that is beyond a Turing-Hopf bifurcation, and for most of the simulations we initialise the system with random initial conditions which then were allowed to resolve until t=20000 ms which from experimentation was found to be sufficiently long enough simulation time for the system to resolve into a steady dynamic pattern. We begin this computational study by firstly varying the variable A_1 which multiplies the maximum value of the sigmoid function governing the extracellular K^+ concentration, essentially controlling the maximum amount of K^+ in the extracellular space. It was found that with low A_1 only one homogeneous steady state exists but increasing A_1 leads to the emergence of two further homogeneous steady states: a low extracellular K^+ concentration state, intermediate extracellular K^+ state and a high extracellular K^+ state. The effects on the homogeneous steady state by varying A_1 can be seen in Figure 6.3 where we see that when $A_1 \lesssim 1.6$ there exists only one steady state and for $A_1 \gtrsim 1.6$ a further two steady states emerge. We found that when A_1 is low (and only one unstable steady state) that the model exhibited low synchrony periodic waves in the beta-band frequency ($\sim$ 25Hz) when applying random perturbations to the steady state. In the high A_1 case where 3 steady states exist, applying small amplitude random perturbations to the low K^+ steady state leads to beta-band frequency and low synchrony periodic travelling waves but by applying larger amplitude random perturbations we could find high frequency ($\sim$ 100Hz) waves with high synchrony in the excitatory population. These states are demonstrated in Figure 6.4 where we show two simulations, one with $A_1 = 2.0$ which shows the high frequency oscillations that the model exhibits when perturbing the low K^+ steady state with high amplitude random perturbations and another simulation with $A_1 = 0.1$ where only one the low extracellular K^+ concentration steady state exists, here we find periodic travelling waves that oscillate in the beta frequency band.

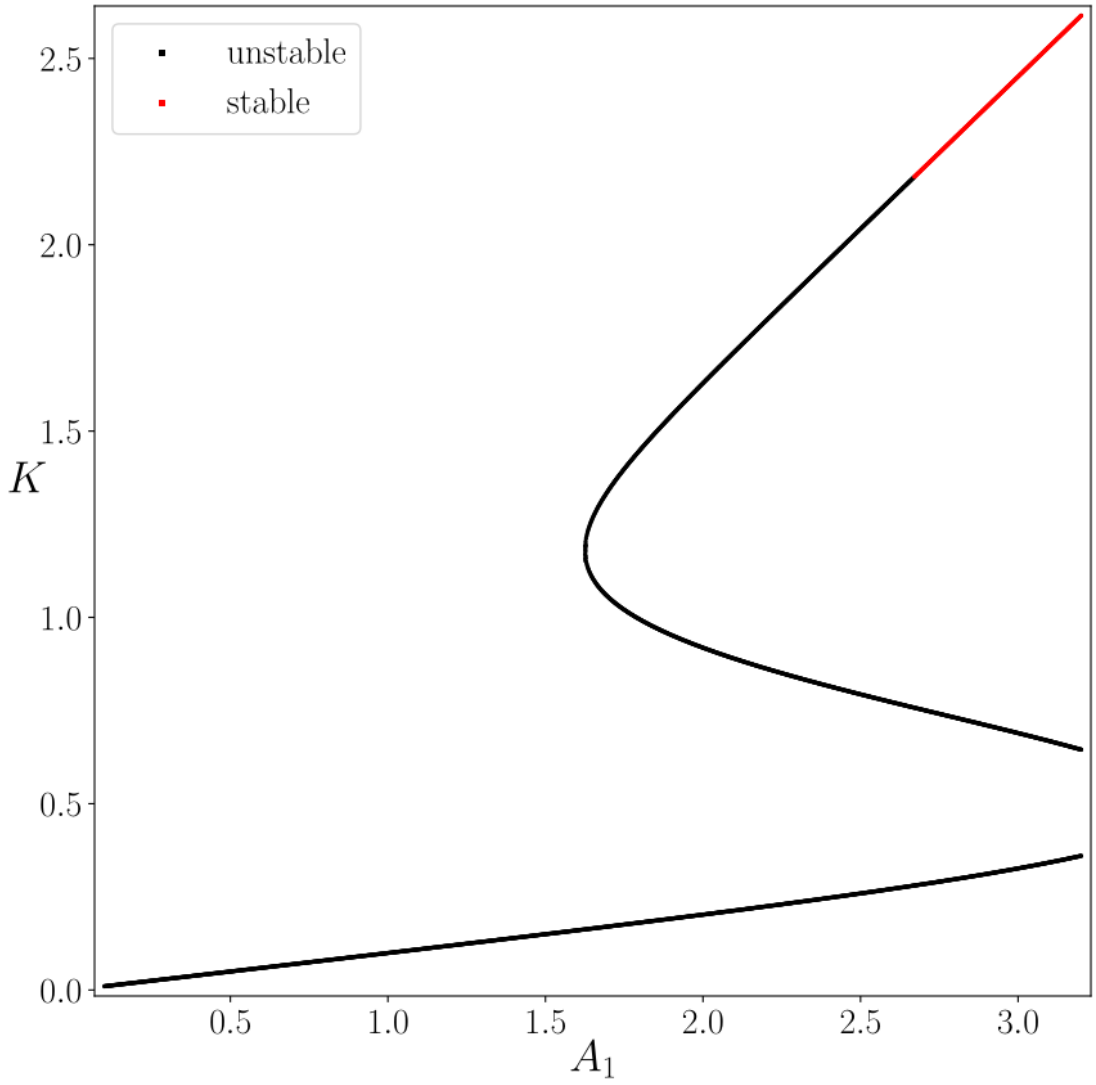

Figure 6.3: Values of the extracellular K^+ concentration variable K at the homogeneous steady states for varying values of A_1. For low values of A_1 there exists only 1 homogeneous steady state in-which the extracellular K^+ concentration is also low. When $A_1 \gtrsim 1.6$ 2 further homogeneous steady states emerge, an intermediate extracellular K^+ concentration state and a high extracellular K^+ concentration state.

We now investigate the effects of varying the extracellular K^+ decay parameter δ. When δ is high (more uptake of K^+ by glial cells and other various mechanisms) only one homogenous steady state exists - a low extracellular K^+ concentration state, similar to when A_1 is set low and we again found beta-band low synchrony periodic

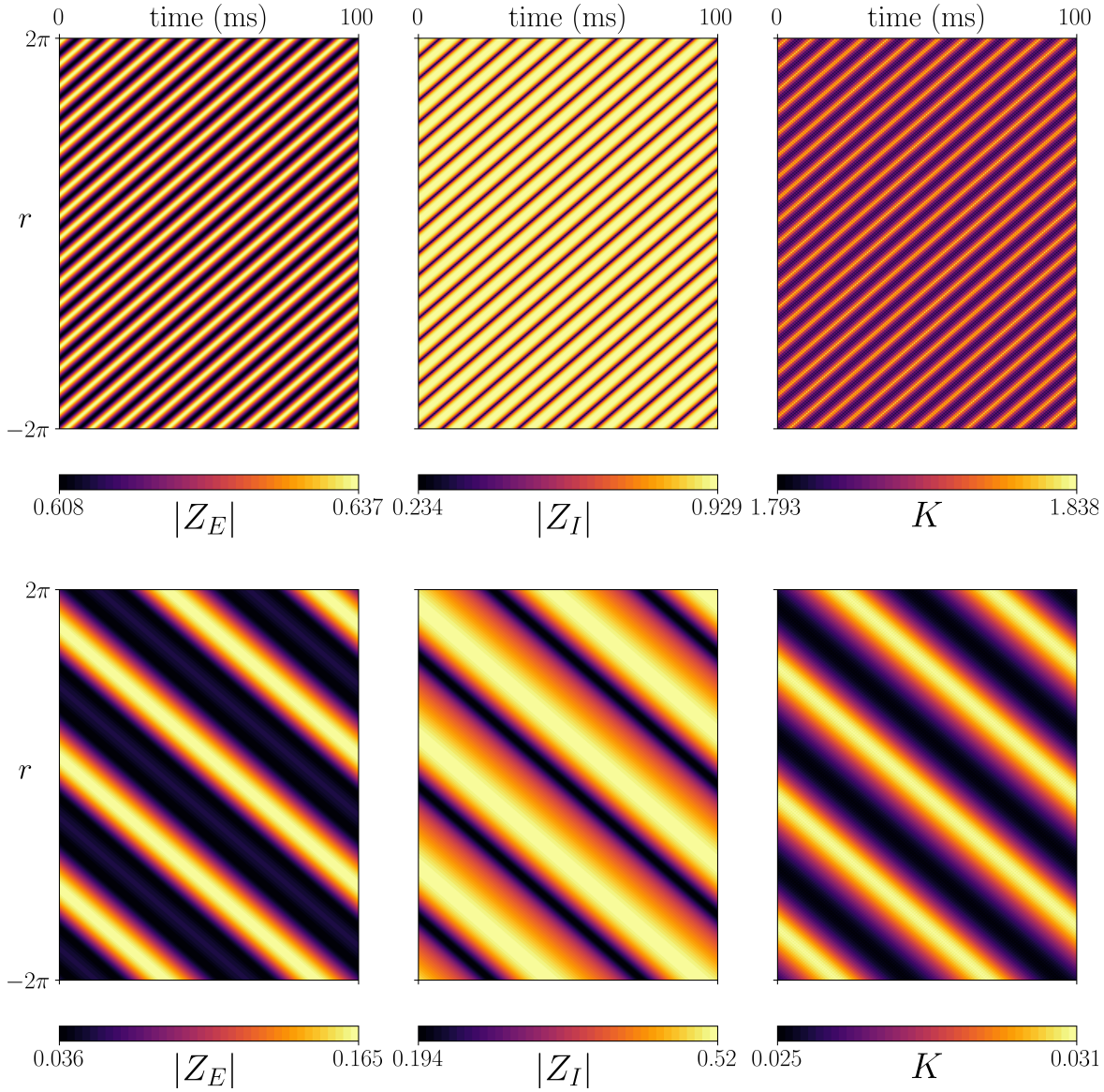

Figure 6.4: Top panels: Simulations where $A_1 = 2.0$ where we find high frequency ($\sim$ 100Hz) periodic travelling waves with high levels of synchrony and extracellular K^+. Bottom panels: Simulations where $A_1 = 0.1$ where we find beta-band ($\sim$ 25Hz) periodic travelling waves with low levels of synchrony and extracellular K^+.

travelling waves in this case. When δ is low (less K^+ uptake by glial cells etc.) we find that, similar to increasing A_1, two further steady states emerge and we are again able to find high frequency ($\sim$ 100 Hz) spiral waves with high synchrony. In Figure 6.5 we show two simulations, one where the decay parameter is low ($\delta = 0.09$) and

the low extracellular K^+ steady state is perturbed with high amplitude random initial conditions, this leads to high frequency periodic travelling waves. We also show simulations where the decay parameter is high ($\delta = 0.8$) where we find beta-band (~ 25Hz) periodic travelling waves.

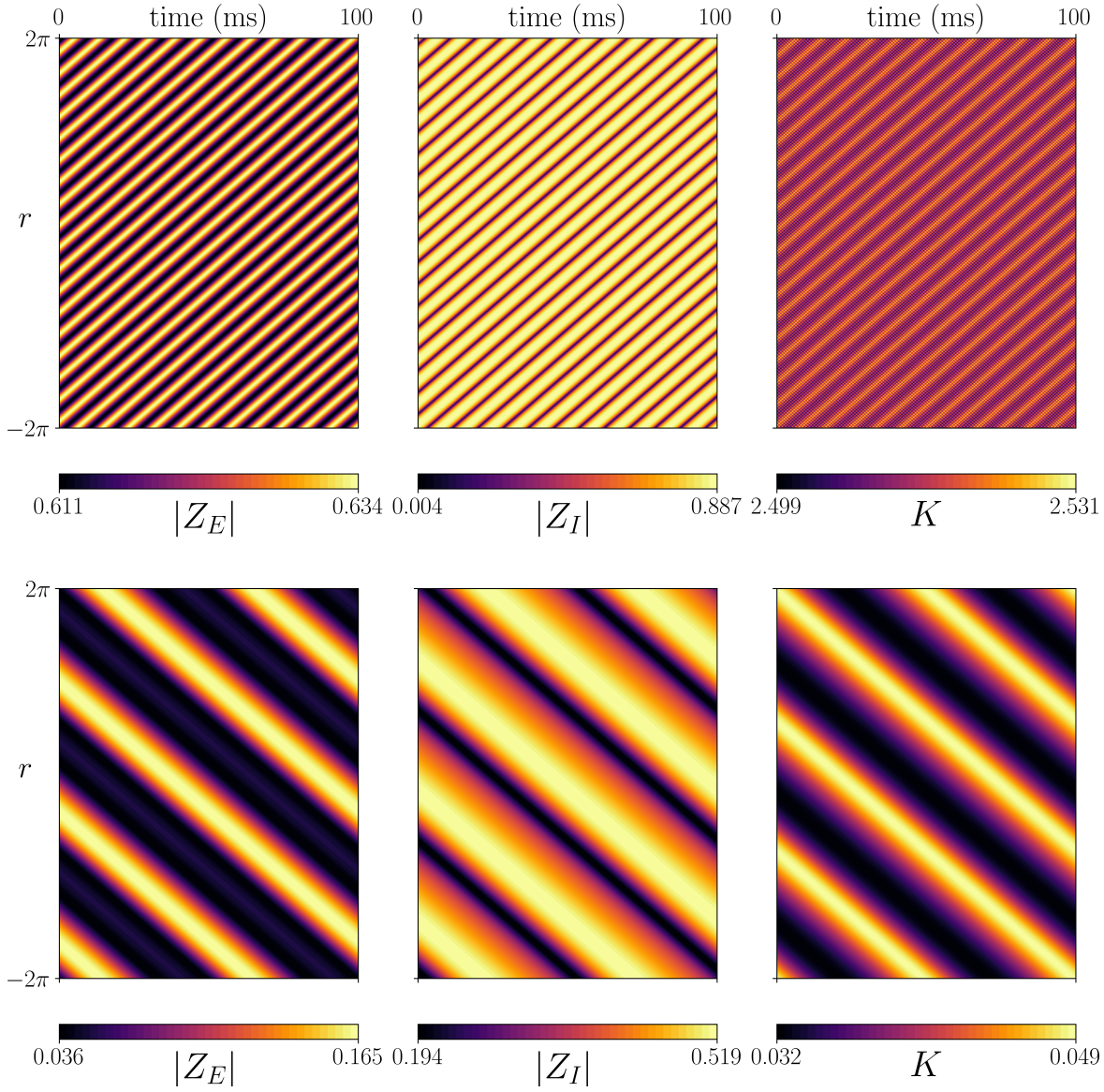

Figure 6.5: Top panels: Simulations where the extracellular K^+ decay rate is low with a value of $\delta = 0.09$ where we find high frequency (~ 100Hz) periodic waves with high levels of synchrony and extracellular K^+. Bottom Panels Simulations where the extracellular K^+ decay rate is high with a value of $\delta = 0.8$ and we find periodic travelling waves in the beta frequency band (~ 30Hz) with low levels of synchrony and extracellular K^+.

Now we investigate the effects of varying the extracellular K^+ diffusivity parameter D. We found that the resulting simulations when using either low diffusivity or high diffusivity did not significantly differ from each other, though there was some negligible differences in the extracellular K^+ concentration between the two cases. In both the high diffusivity and low diffusivity case we found only one homogenous steady state and the emergent travelling waves that occurred after initiating with random initial conditions oscillated in the beta frequency band. In Figure 6.6 we show these two cases and it can be seen that there is no significant differences between the solutions found for each case. When the high and intermediate extracellular K^+ concentration homogeneous steady states are present (from the studies here, either when A_1 is sufficiently large or δ is sufficiently low) it is possible to find travelling wave solutions by initiating the system with a bump of activity. This can be seen in Figure 6.7 where we see that the system has been initiated with an activity bump in the centre of the domain which then initiates a travelling front that connects the intermediate K^+ steady state to the high K^+ steady state. Interestingly it can be seen in the simulations that there is also some temporal oscillatory behaviour in the wake of the travelling wave. It was found that the linearisation around the high extracellular K^+ steady state had complex valued eigenvalues which would explain this oscillatory behaviour in the wake of the primary travelling front.

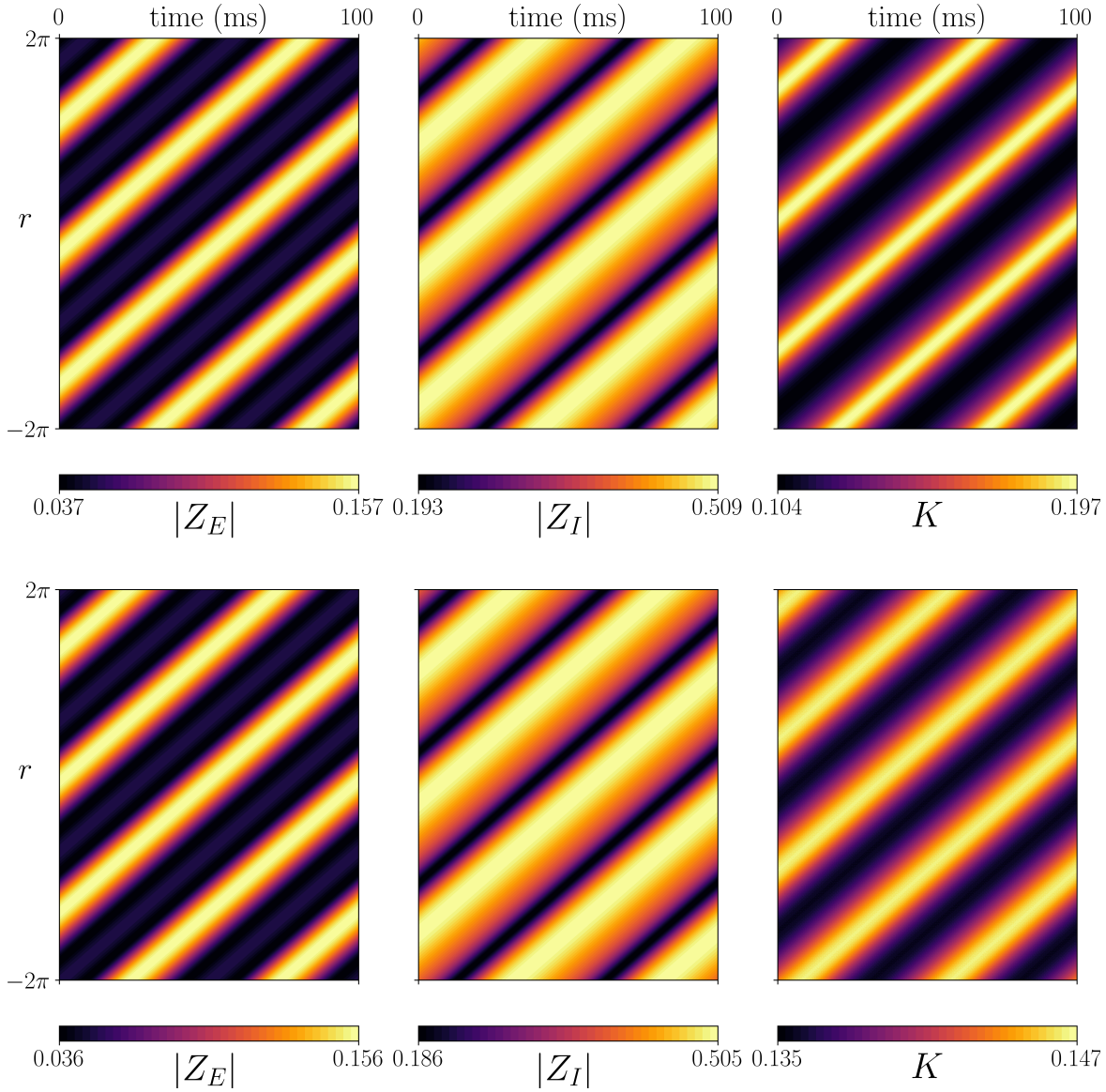

Figure 6.6: Top: Simulations where the extracellular K^+ diffusivity parameter is low ($D = 0.01$). Bottom: Simulations where the extracellular K^+ diffusivity parameter is set high ($D = 0.8$). In both the high diffusivity case and low diffusivity case we find similar beta-band oscillations and only one homogeneous steady state with negligibly high concentrations of extracellular K^+ in the low diffusivity case.

6.4 Computational Study in 2 Spatial Dimensions

We now turn our attention to the model (6.3) in 2 spatial dimensions, such that $\Omega = \mathbb{R}^2$ and letting $\mathbf{x} = (r_1, r_2)$. A Turing instability analysis of the homogenous steady state

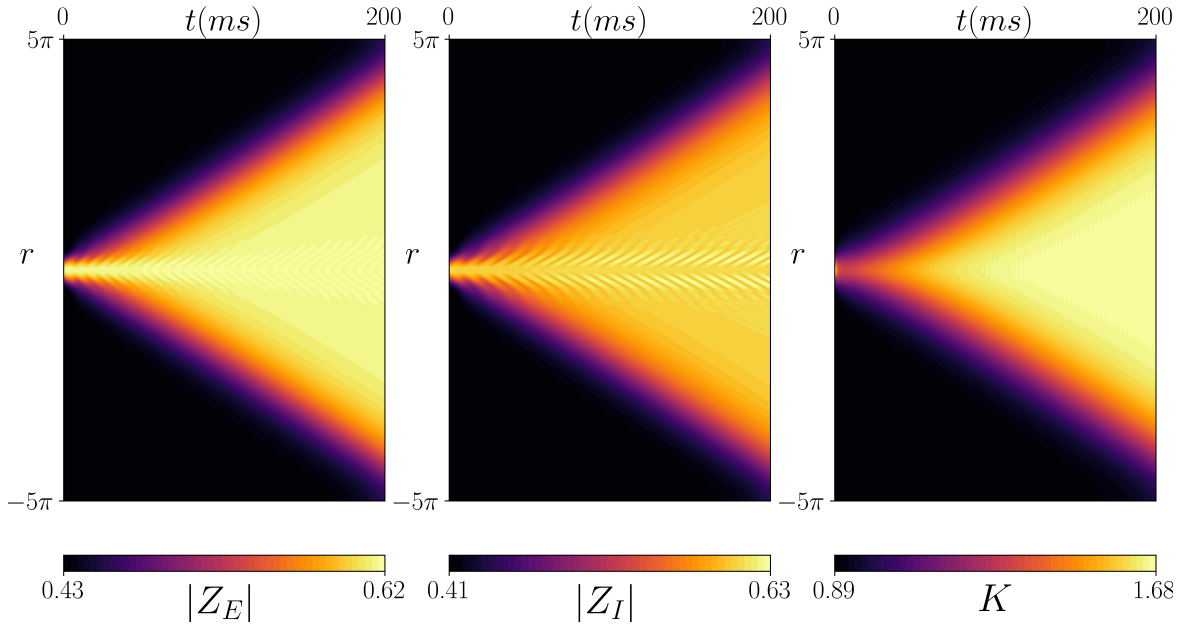

Figure 6.7: Simulations of a travelling wave found when setting $A_1 = 2.0$. The system is initiated with a Gaussian function in the centre of the domain which initiates a travelling wave that connects the intermediate extracellular K^+ concentration homogeneous steady state to the high extracellular K^+ concentration state (as seen in Figure 6.3).

was also performed in this case, again in order to find a parameter regime where dynamic solutions were possible and this analysis can again be found in appendix C.1. We see in this section that the 2 dimensional model supports a rich array of dynamical spatio-temporal patterns with various parameter sets. In order to investigate the effects of various model parameters in this 2 dimensional model, we again employ a computational study.

We begin in the same manners as the 1 dimensional section by demonstrating the effects of varying the parameter that affects the maximum value of the extracellular K^+ concentration, A_1. In this 2 dimensional model we are able to find more exotic spatio-temporal solutions. When A_1 is sufficiently large ($A_1 \gtrsim 1.6$) we again find 3 steady states, since the steady state equations are unchanged by the addition of a spatial dimension. In Figure 6.8 we show simulations where $A_1 = 2.0$ and where

$A_1 = 0.1$. Analogous to the single spatial dimension case, we find that when $A_1 = 2.0$ and we apply high amplitude perturbations the low extracellular K^+ homogenous steady state we find high frequency, and highly synchronous, spiral with high levels of extracellular K^+ that collide and destructively interfere with each other. In the case of $A_1 = 0.1$ we found beta-band frequency dynamic patterns that resemble periodic travelling waves with low excitatory synchrony, low extracellular K^+ concentration and intermediate synchrony in the inhibitory population. We also show corresponding time-series of these simulations in Figure 6.9 where we see the temporal oscillatory patterns of the same simulations shown in Figure 6.8.

In Figure 6.10 we show the effects of varying the potassium decay parameter δ. When the decay of extracellular potassium concentration is low ($\delta = 0.09$) we find similar colliding spiral waves as in Figure 6.8 with high excitatory synchrony and high extracellular K^+ concentration. These periodic waves behave very similarly compared to the simulation in Figure 6.8. When we set the decay parameter high ($\delta = 0.9$) we find beta-band travelling waves that have some phase switching occurring. We again show corresponding time-series of these simulations in Figure 6.11 where we see the temporal oscillatory patterns of the same simulations shown in Figure 6.10. In Figure 6.12 we demonstrate the effects of varying the diffusivity of the potassium. For high diffusivity ($D = 0.9$) we find periodic wave patterns in the beta frequency band with low-intermediate synchrony and low extracellular K^+ concentration. In the case of low diffusivity ($D = 0.01$) we find spiral-like waves (though the cores are less tightly wound here than the spiral waves seen in Figure 6.8 and Figure 6.10) with low-intermediate synchrony and low extracellular K^+ concentration and again in the beta frequency band. We again show corresponding time-series of these simulations in Figure 6.13 where we see the temporal oscillatory patterns of the same simulations shown in Figure 6.12.

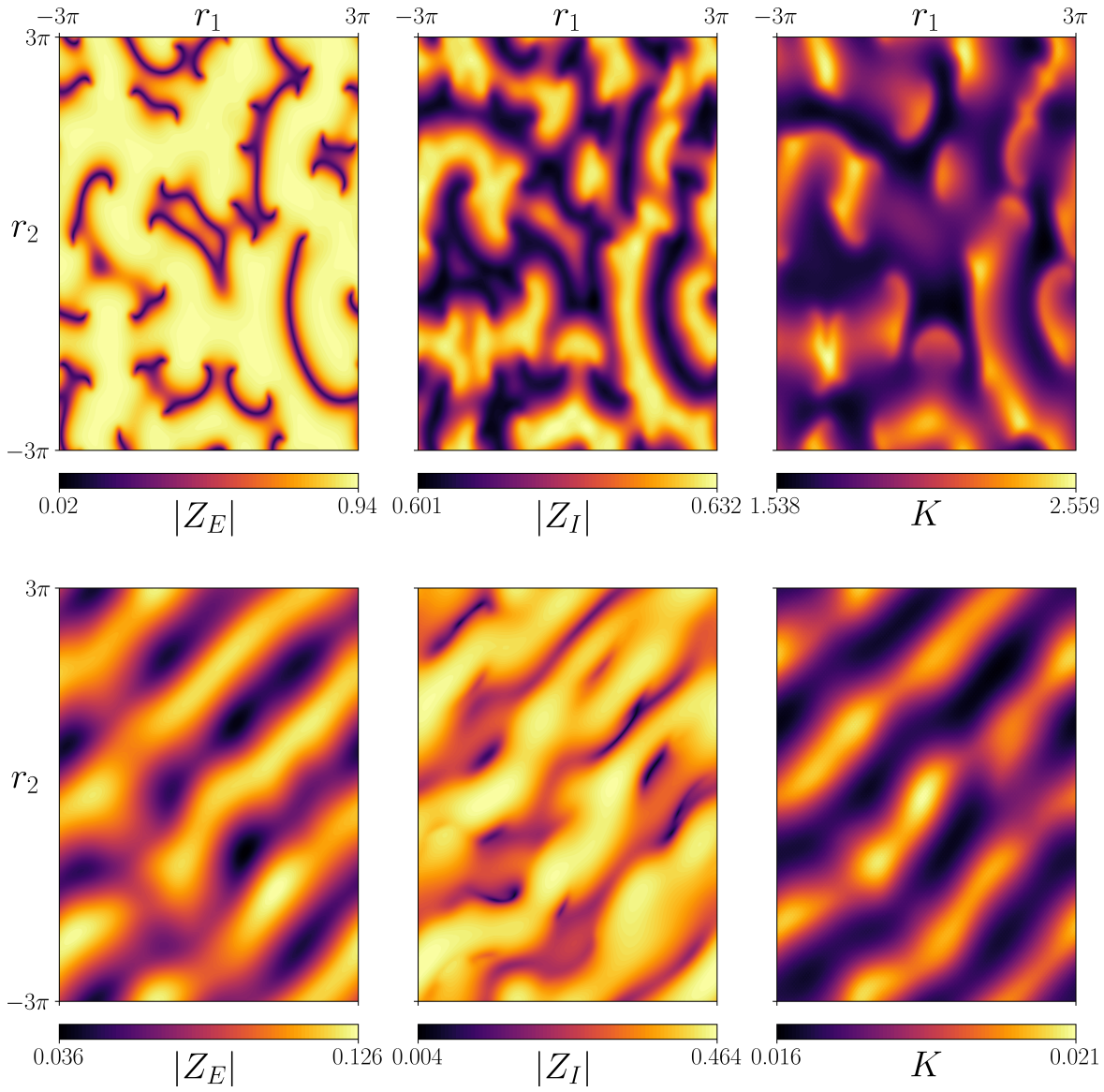

Figure 6.8: Top: Snapshots in time of simulations where $A_1 = 2.0$ initiated with random initial conditions. Here we find high frequency spiral waves that collide and interfere with each other and have high inter-population synchrony in the excitatory neurons and a high amount of extracellular K^+. Bottom: Snapshots in time of simulations where $A_1 = 0.1$. Here we find low frequency periodic travelling waves with low inter-population synchrony in the excitatory neurons and a low level of extracellular potassium. See appendix C.2 for movies of these simulations.

We can also find travelling wave solutions when a high potassium steady state is present in the 2D model. In Figure 6.14 we show a travelling wave solution found when $A_1 = 2.0$. The front was initiated with 2D Gaussian function and connects

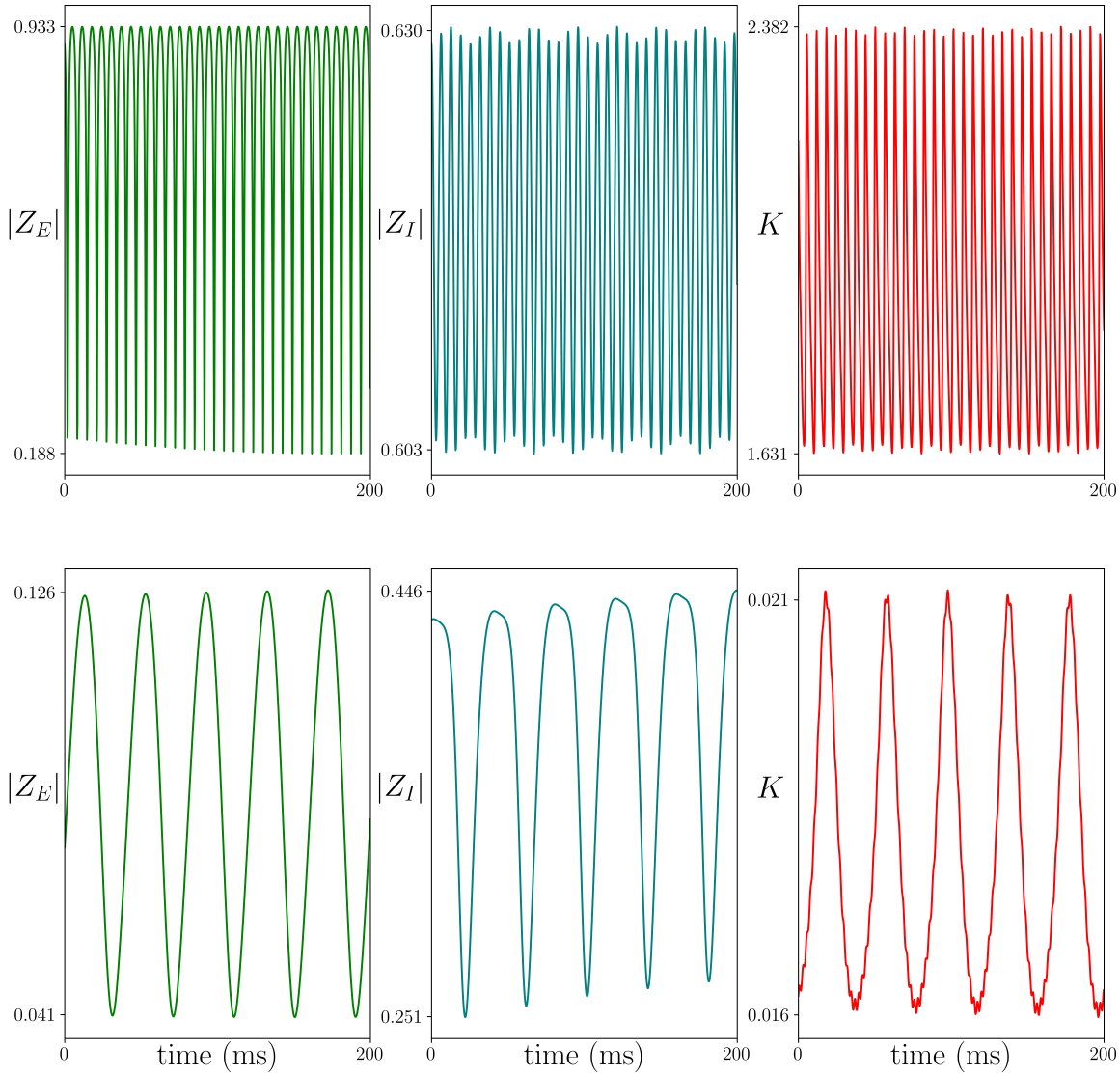

Figure 6.9: Time-series plots corresponding to the green dots in Figure 6.8 over a period of 200ms. The top panels are time-series from the simulation where $A_1 = 2.0$ and here we see fast gamma oscillations. The bottom panels are time-series at the g from the simulations where $A_1 = 0.1$ and here we see beta-band oscillations.

the mid potassium steady state and high potassium steady state (as shown in Figure 6.3). This wave solution also displays some oscillatory behaviour with small ripples propagating out from the centre of the core following the primary front.

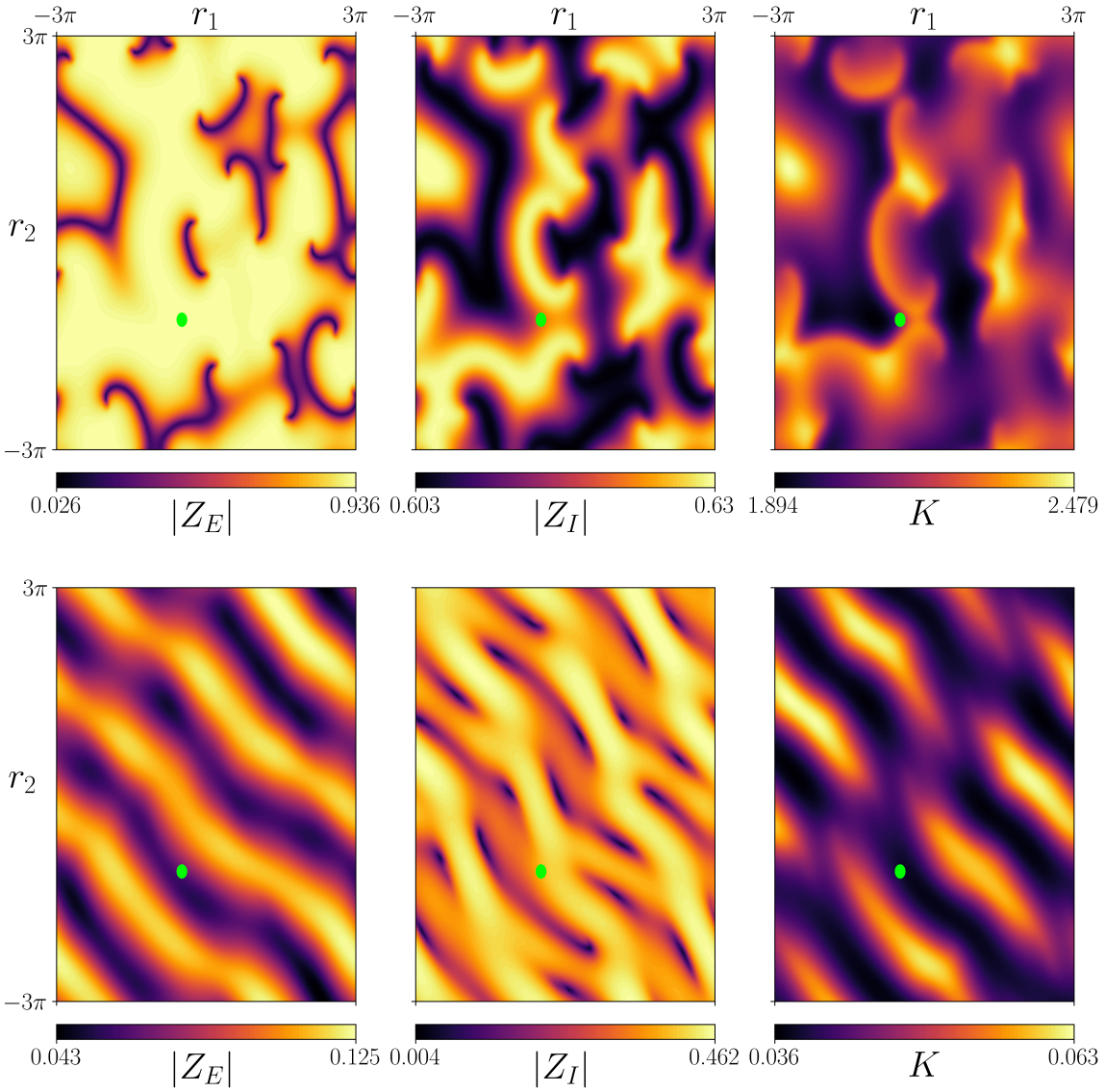

Figure 6.10: Top Panels: Snapshots of a simulation where the decay a parameter was set low ($\delta = 0.09$). Here we find high frequency spiral waves that collide and interfere with each other, very similar to the simulations seen in Figure 6.8. Bottom Panels: Snap shots of a simulation where the decay parameter was set high ($\delta = 0.9$) where we see periodic travelling waves oscillating in the beta frequency band. See appendix C.2 for movies of these simulations.

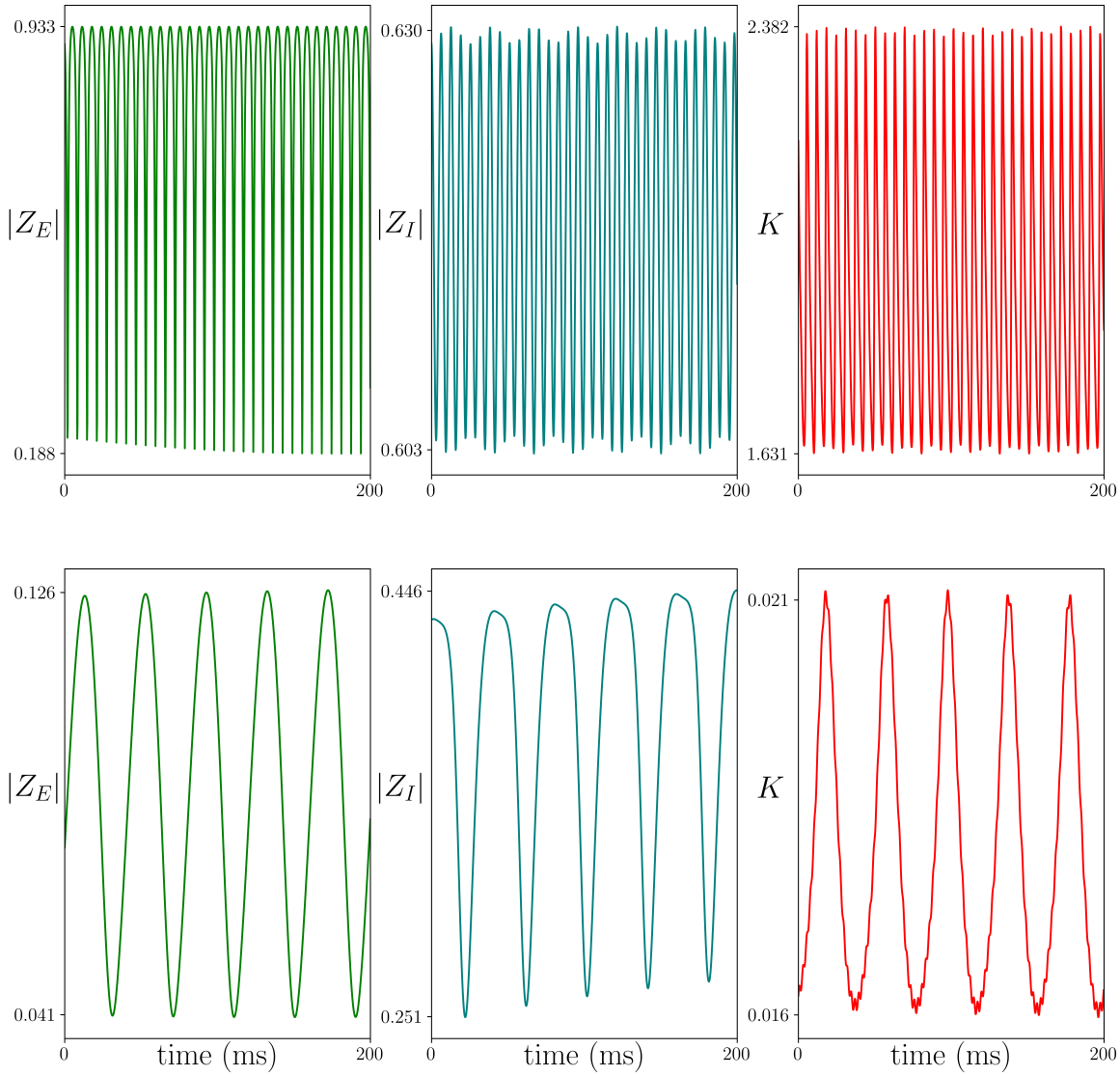

Figure 6.11: Time-series plots corresponding to the green dots Figure 6.10 over a period of 200ms. The top panels are time-series from the simulation where $\delta = 0.09$ and here we see fast gamma oscillations. The bottom panels are time-series from the simulations where $\delta = 0.9$ and here we see beta-band oscillations.

6.5 Discussion

The relationship between extracellular K^+ and the generation of seizure states is a crucial question in neuroscience. Modelling the interaction between extracellular K^+ and neuronal activity provides a valuable tool for investigating this relationship. In

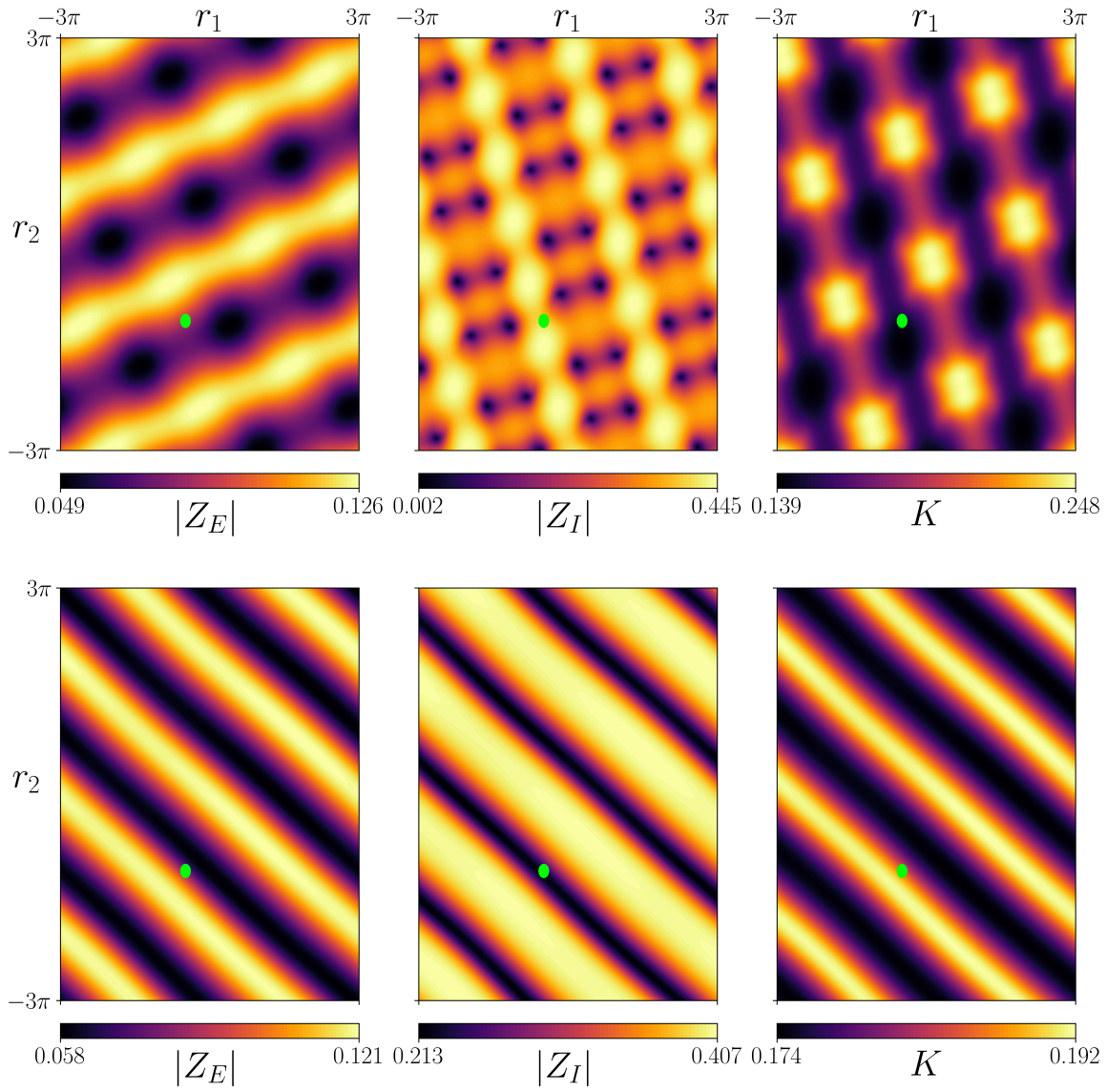

Figure 6.12: Top: Simulations where the potassium diffusivity parameter is set low at $D = 0.01$. Here we find spiral waves oscillating in the beta frequency band. Bottom: Simulations where the potassium diffusivity parameter is set high at $D = 0.9$. Here we find periodic travelling waves, again oscillating in the beta frequency band. Synchrony and extracellular K^+ concentration was quite similar between the two cases here. See appendix C.2 for movies of these simulations.

this chapter, we build on previous work by Byrne *et al.* [22] and Martinet *et al.* [56] by introducing a novel model that couples a next-generation neural field model to extracellular K^+ concentration.

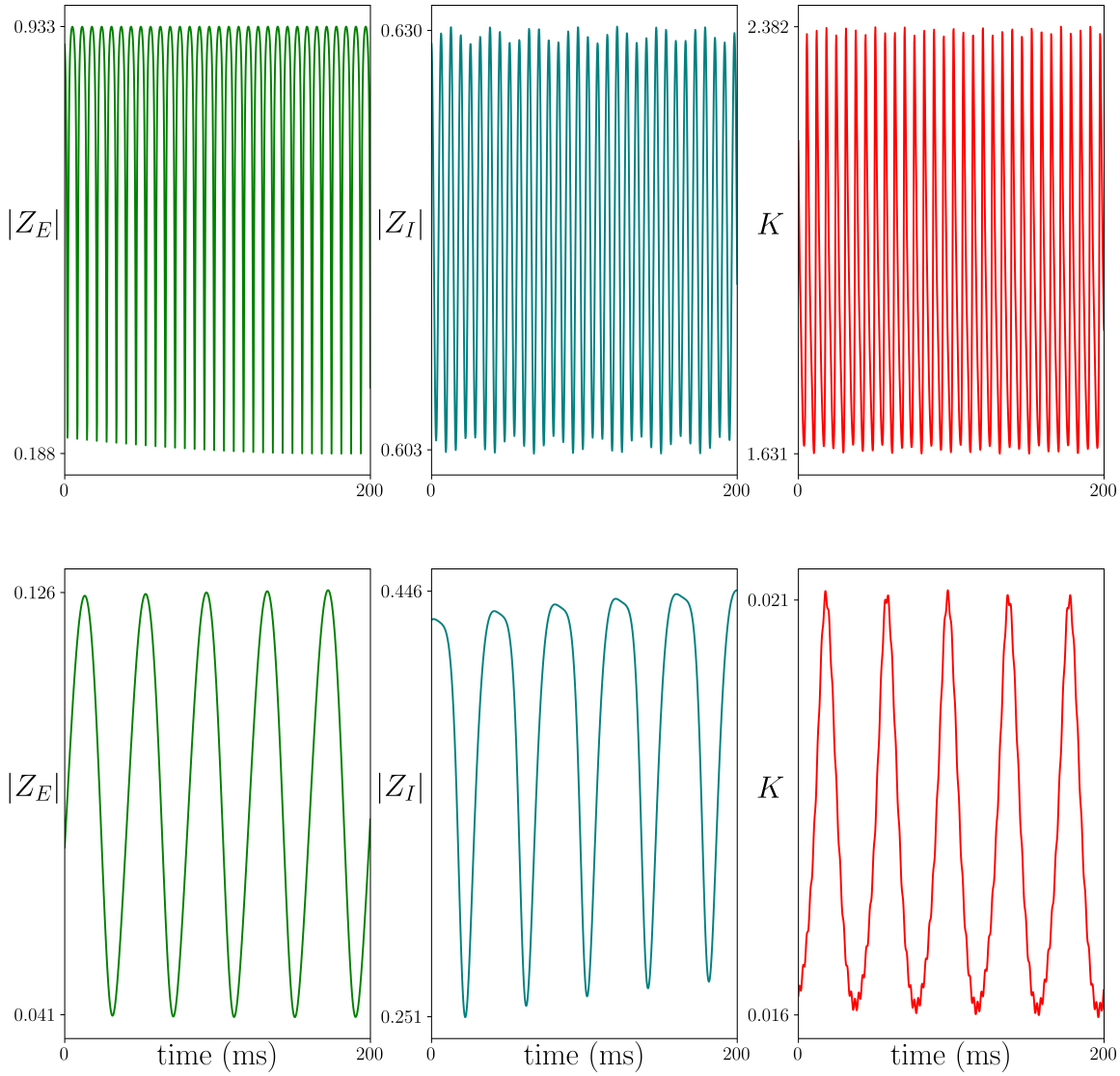

Figure 6.13: Time-series plots corresponding to the green dots in Figure 6.12 over a period of 200ms. The top panels are time-series from the simulation where $D = 0.01$ and the bottom panels are time-series from the simulations where $D = 0.9$. In both cases we see beta-band oscillations.

To analyse this model, we performed a Turing instability analysis and found that it supports a variety of dynamic solutions. We then conducted a computational study to examine the effects of varying key parameters governing extracellular K^+ dynamics. Specifically, we found that increasing the maximum potassium level (A_1) or decreasing the decay rate of K^+ in the extracellular space (δ) resulted in three distinct homoge-

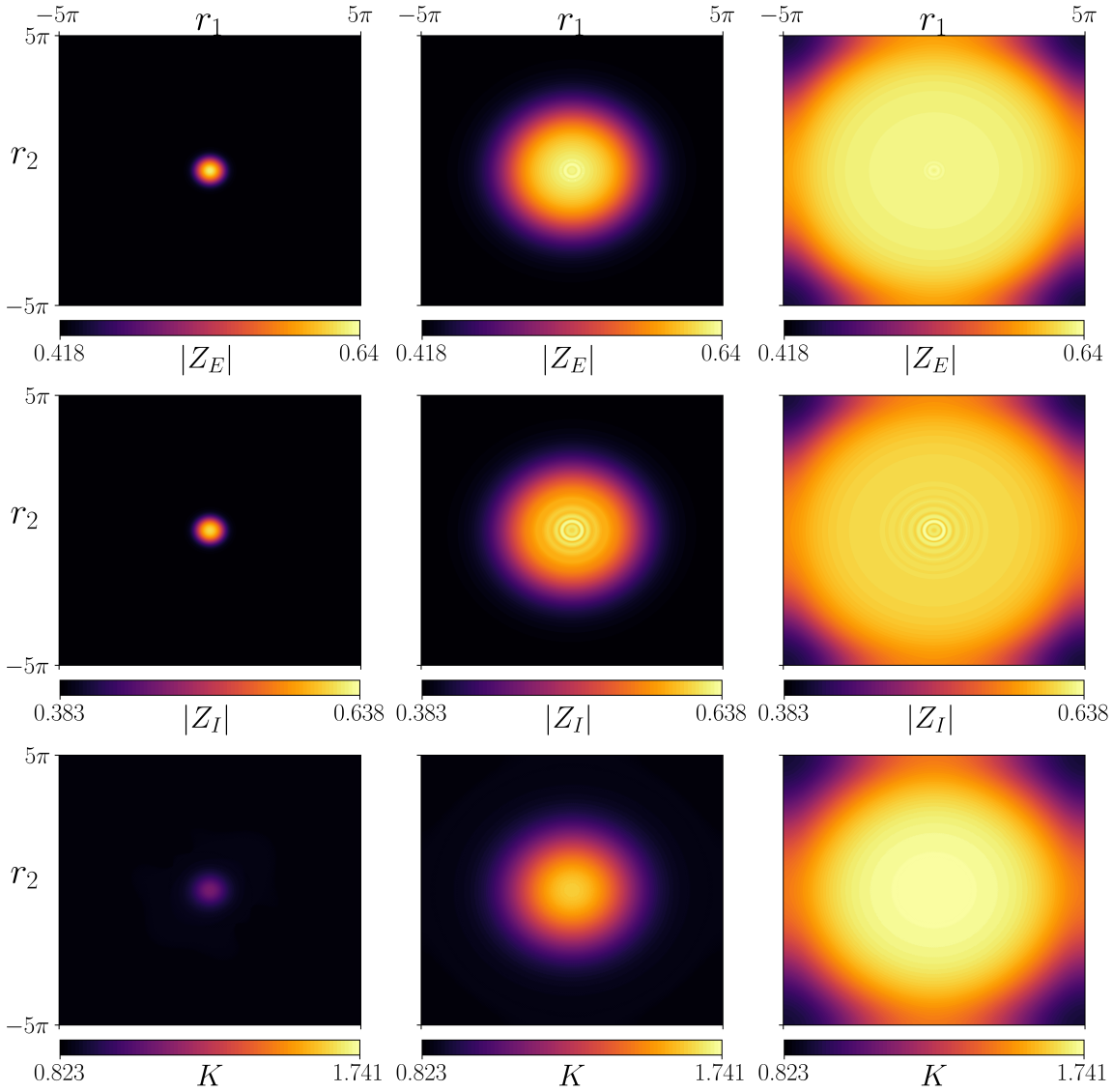

Figure 6.14: Travelling wave solution found when $A_1 = 2.0$ and initiated the system with a 2D Gaussian function in the centre of the domain. Top: Snapshots of the travelling wave solution in the Z_E variable. Middle: Z_I variable. Bottom: K variable. The travelling front connects the intermediate and high K^+ concentration homogeneous steady states (as shown in Figure 6.3) and has some oscillatory behaviour in the wake of the front. Movies of these simulations are linked in appendix C.2

neous steady states: a low extracellular K^+ state, an intermediate extracellular K^+ state, and a high extracellular K^+ state.

In parameter regimes where these three steady states existed, we observed that small

perturbations applied to the unstable low extracellular K^+ state led to dynamic solutions oscillating in the beta frequency band, which is characteristic of normal brain activity. In contrast, applying larger perturbations to the same state resulted in the formation of spiral waves oscillating at much higher frequencies ($\sim$ 100 Hz). This behaviour could be interpreted as a transition to a seizure state, similar to the switching between different limit cycles observed in the Jansen-Rit neural mass model discussed in Chapter 2 [121]. We also found that varying the diffusivity of extracellular K^+ (by adjusting the parameter D) alone did not significantly affect the dynamical behaviour of the model in the one-dimensional case. However, in the two-dimensional case, we observed that when diffusivity was low, spiral waves emerged, whereas high diffusivity led to planar waves. Unlike the prior simulations, both of these cases oscillated in the beta frequency band.

Although this model includes only inhibitory-inhibitory gap junction coupling (consistent with the model discussed by Martinet *et al.* [56]) and already exhibits rich dynamical behaviour, a logical next step would be to incorporate gap junction coupling between both neural populations. This would allow each gap junction connection to be influenced by extracellular K^+ concentration, providing further insight into how this affects the observed dynamics. Another interesting extension of this work would be to develop a stochastic variant of the model by introducing additive noise into the neural activity model, similar to the approach discussed in Chapter 5. Investigating how noise influences system behaviour would enable comparisons with previous studies of neural activity models coupled with gap junction coupling and extracellular space that inspired the model in this chapter [54], [56], [127], [128]. For example, further investigation into the wave fronts found in this chapter, with the addition of noise, could reproduce the ictal wave fronts found in the model in [56]. In [54] it was found that high gap junction coupling promoted static Turing states, whilst low allowed for

temporal oscillations, although Turing states were not explored in this chapter, we did find that increased extracellular K^+, and thereby lower inhibitory-inhibitory gap-junction coupling and increased mean-drives, led to a transition from beta oscillations to gamma oscillations - which have been associated with seizure onset [129], [130]. It could be interesting to investigate how gap junction strength modulates Turing states in the gap-junction models presented in this Thesis, as well as investigating this with extracellular K^+ dynamics, since in [56] the simulations of ictal waves begin with Turing-like mosaic patterns.

While this chapter has primarily focused on introducing and conducting an initial investigation into the dynamics of this model, future research could explore how well its behaviour aligns with real EEG/MEG data, particularly in replicating the temporal dynamics observed in epileptic seizure states. Furthermore, modelling work by Volman *et al.* [91] suggests that increases in gap junction coupling can either suppress seizure states (by promoting dynamical stability in a neural network) or facilitate them, depending on the strength and duration of the seizure. Future numerical studies could investigate whether similar behaviour can be reproduced in the model presented here.

CHAPTER 7

DISCUSSION OF THE THESIS

In this thesis, several different neural models were introduced and analysed. Firstly, in Chapter 3, a Wilson-Cowan type neural field model that included dendritic processing in the form of a cable equation. We demonstrated how this system of integro-differential equations could be transformed into a system of partial differential equations and by doing so this reduced the computational complexity required to simulate the model. We then analysed a single population model with a Heaviside firing rate function in relation to travelling waves, investigating travelling front speed in relation to several parameters and demonstrated some simulations in both the one somatic dimension model, and the two somatic dimension model. We also investigated the full two population model using a tanh firing rate function. Here we found that the model was able to exhibit various spatio-temporal patterns that were found past different bifurcations and we demonstrated these patterns by computational simulation. Going forward, this model, or an adapted form of this model, could be useful in the investigation of neural dynamics in layered cortical tissue. This is important because

it allows for the inclusion of dendritic depth. In the layered structure of the human cortex, different types of pyramidal neurons are found in each of the six layers (I–VI), with their dendrites extending vertically from their cell bodies toward layer I. For example, inputs from the thalamus—the sensory gateway to the cortex—arrive in layer IV, which can be far along the dendrites of neurons whose cell bodies reside in layers V and VI.

In Chapter 4 we introduced an adapted next-generation neural mass model that included gap-junction coupling. In this chapter we showed the effect of varying gap-junction strength in the mass and field models. We showed that oscillations can occur due to increasing gap-junction strength in the mass models and that a variety of spatio-temporal patterns, such as spiral waves and chimeras, can form due to different gap-junction strength configuration in the field models. Future work on this model could include further bifurcation analysis and continuations of these bifurcations (especially in the two population model). Further exploration and analysis to explore the chimera-like solutions would also be interesting. This could be done with a model reduction to phase oscillators, [131], and then exploiting techniques recently developed in [132].

We then explored a method of fitting a stochastic next-generation neural mass model to MEG data in Chapter 5. Here we looked at statistics associated with beta-bursting behaviour in MEG data and used a GA to find model parameters that resulted in distributions that were close to the real world. We found that the GA was able to optimise parameter sets quite well although some work is still needed to optimise the parameter sets further. When using GA optimised parameter sets in a network model we found that the fitness of the model bursting statistics did not significantly drop for low network coupling strengths, but did drop off as the network coupling strength

was increased. Future work here would consider the use of the next-generation mass model in other neural imaging contexts, such a functional connectivity studies [133] and refining the GA approach in order to fit whole brain networks, as opposed to single nodes, to either beta-bursting or resting state data.

Finally, in Chapter 6 we extended our investigation of gap-junctions by constructing a novel neural activity model that interacted with the extracellular space by coupling extracellular potassium concentration with inhibitory-inhibitory gap-junction coupling strength and mean drives of each neural population. Here we explored a variety of parameters that affected the potassium dynamics in the model and performed a computational study into the effects of varying these parameters. We found that for lower levels of extracellular potassium that the model exhibited beta band oscillations and then found that an increase in potassium concentration in the extracellular space led the model to support gamma band oscillations and spiral wave like solutions which could be viewed as increases in potassium concentrations leading to seizure states. We also found that the model could exhibit travelling wave solutions when multiple steady states existed. Going forward, this model could be extended to include dynamic gap-junction coupling in all possible connections instead of just inhibitory-inhibitory. Further bifurcations and continuations of these bifurcations would also be a good extension to the work on this model as well as a more thorough comparison to real seizure data.

Bespoke code was developed in Julia for all of the models in this thesis and is publicly available through the GitHub repositories: https://github.com/Jamesafross/Thesis_Code, https://github.com/Jamesafross/Neural_Field_with_gaps, https://github.com/Jamesafross/BetaBurstGA.

APPENDIX A

SUPPLEMENTARY MATERIAL: A NEURAL FIELD MODEL WITH AXO-DENDRITIC CONNECTIONS

The following figures are supplementary to the simulations shown in Section 3.5.

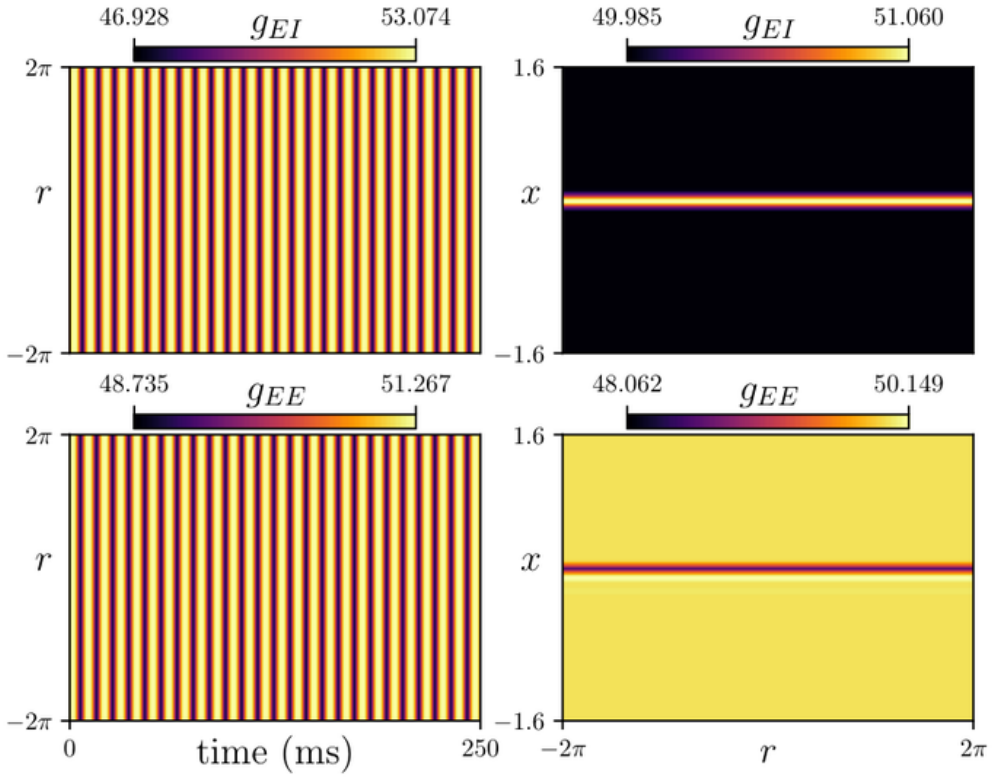

Figure A.1: Supplementary figure of Hopf simulations for state variables g_{EE} and g_{EI}. Here we see globally coherent oscillations over the somatic coordinate r with the amplitude of these oscillations decaying with the dendrite distance from the point of synaptic contact. Parameter values same as Figure 3.10.

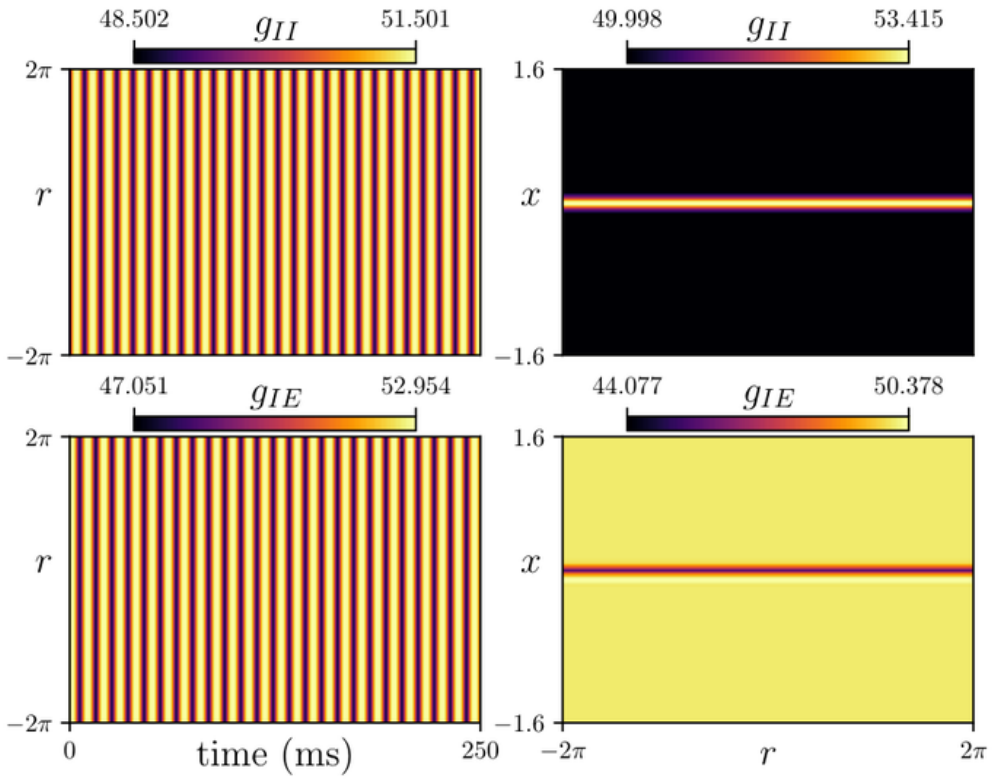

Figure A.2: Supplementary figure of Hopf simulations for state variables g_{IE} and g_{II}. Similarly to Figure A.1, we see globally coherent oscillations over the somatic coordinate r with the amplitude of these oscillations decaying with the dendrite distance from the point of synaptic contact. Parameter values same as Figure 3.10.

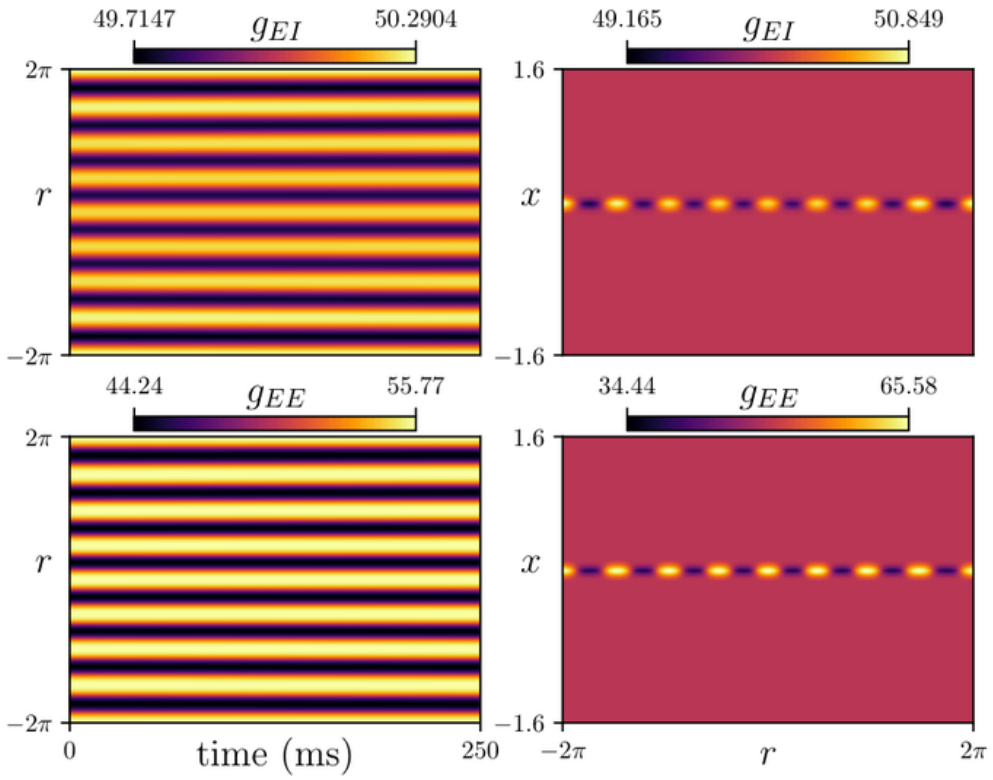

Figure A.3: Supplementary figure of Turing simulations for state variables g_{EE} and g_{EI}. Here we see static patterns in the somatic coordinate r with the magnitude of these decaying with the dendrite distance from the point of synaptic contact. Parameter values same as Figure 3.12.

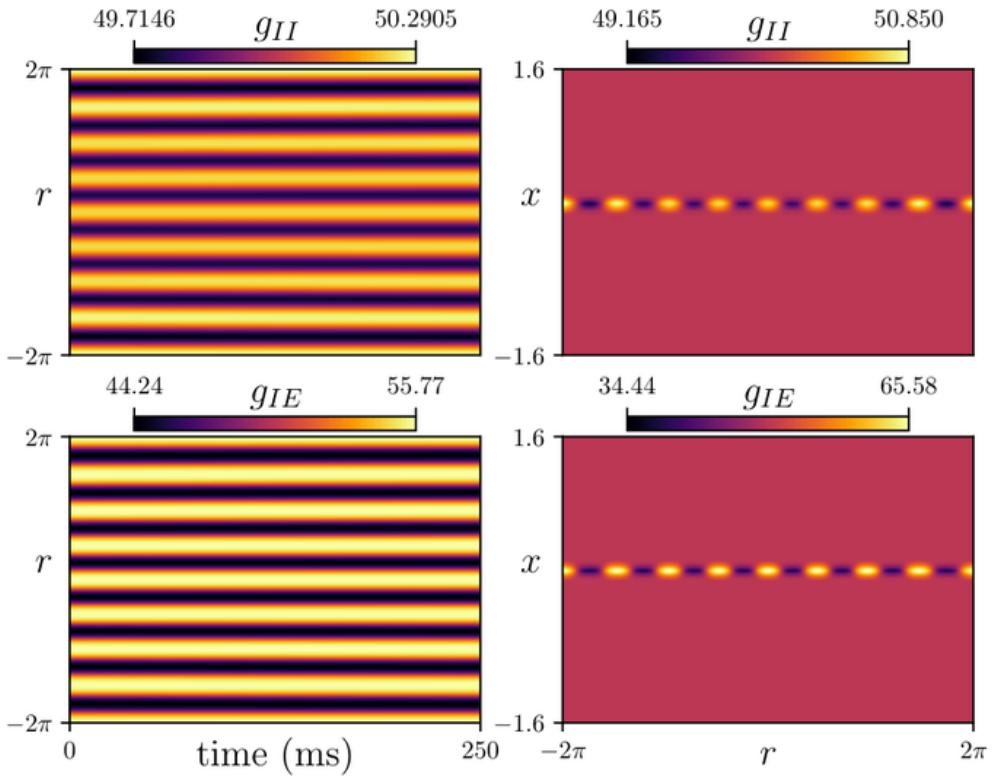

Figure A.4: Supplementary figure of Turing simulations for state variables g_{IE} and g_{II}. Similarly to Figure A.4 we see static patterns in the somatic coordinate r with the magnitude of these decaying with the dendrite distance from the point of synaptic contact. Parameter values same as Figure 3.12

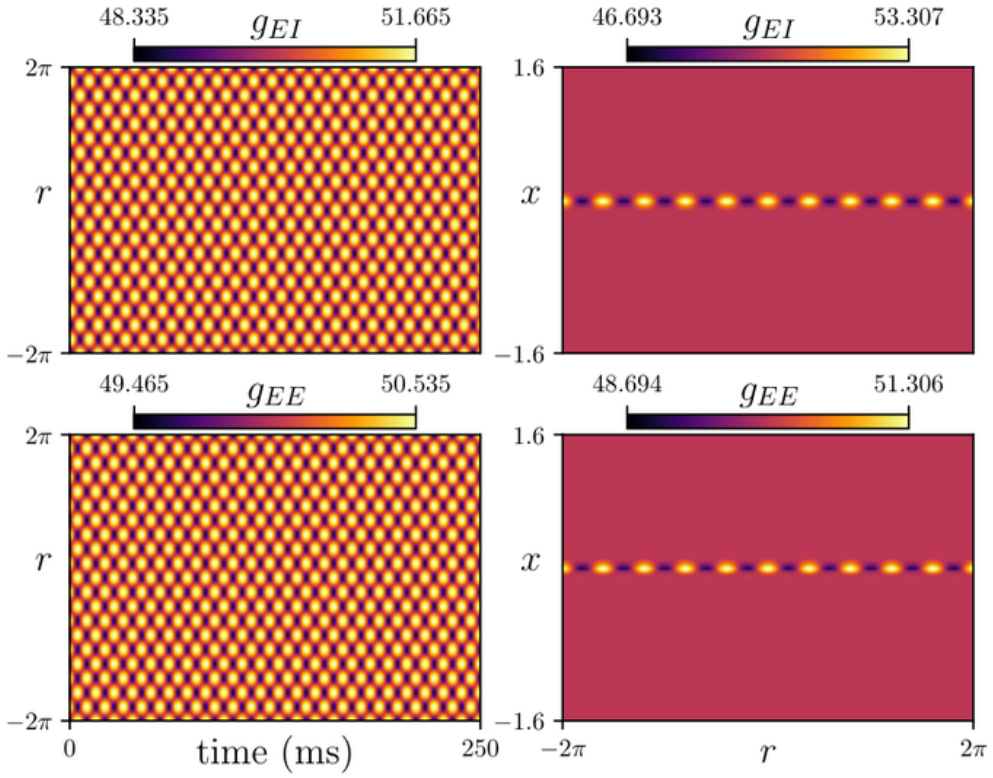

Figure A.5: Supplementary figure of Turing-Hopf simulations for state variables g_{EE} and g_{EI}. Here we see oscillatory patterns in the somatic coordinate r with the amplitude of these oscillations decaying with the dendrite distance from the point of synaptic contact. Parameter values same as Figure 3.11.

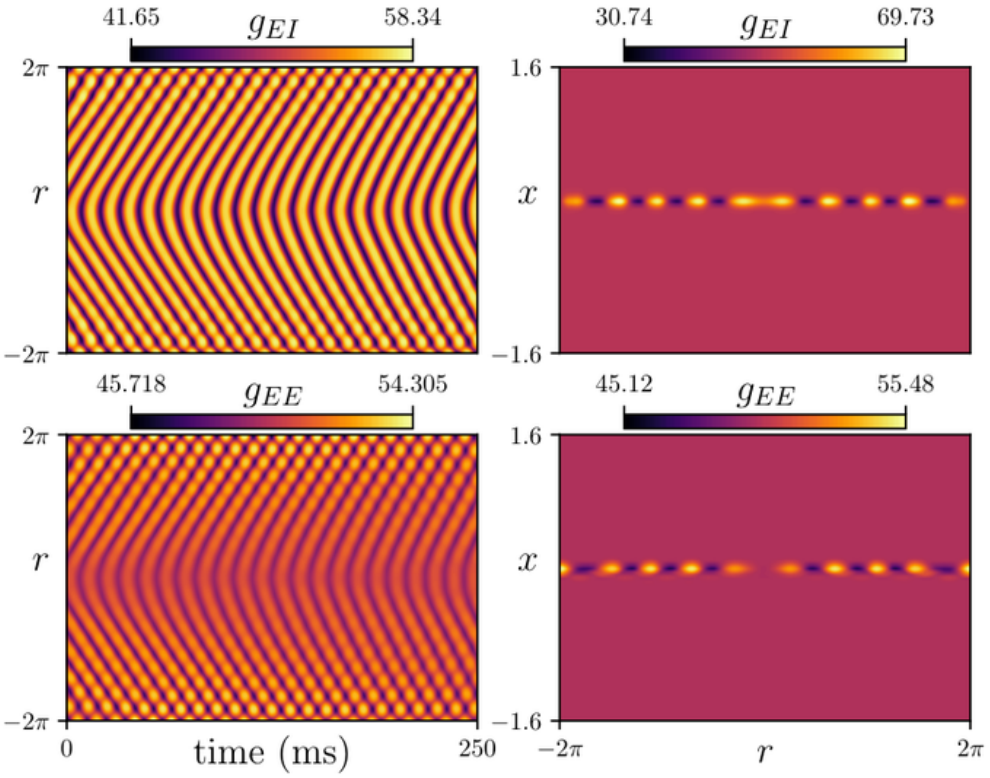

Figure A.6: Supplementary figure of periodic travelling wave simulations for state variables g_{EE} and g_{EI}. Here we see periodic travelling wave across the somatic coordinate r with the amplitude of these waves decaying with the dendrite distance from the point of somatic contact. Parameter values same as Figure 3.13.

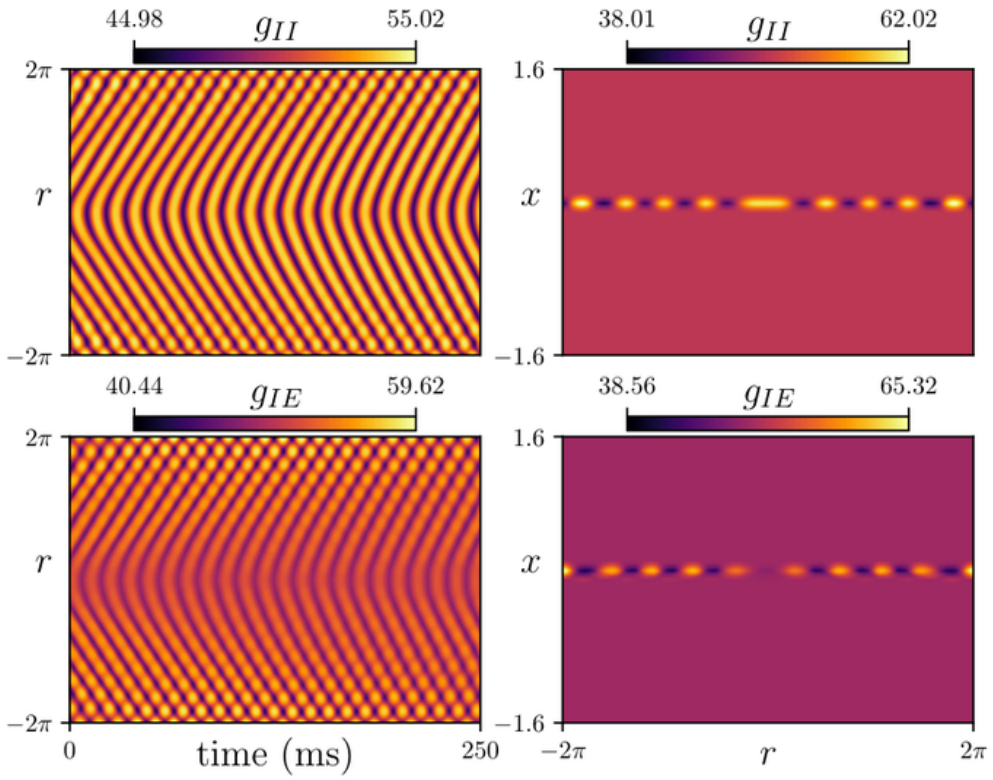

Figure A.7: Supplementary figure of periodic travelling wave simulations for state variables g_{IE} and g_{II}. Similarly to Figure A.6 we see periodic travelling wave across the somatic coordinate r with the amplitude of these waves decaying with the dendrite distance from the point of somatic contact Parameter values same as Figure 3.13.

APPENDIX B

SUPPLEMENTARY MATERIAL: NEXT GENERATION MASS AND FIELD MODEL WITH GAP JUNCTION COUPLING

B.1 Carlo Laing's Neural Mass Equations

The methodology utilised in chapter 4 is similar to Carlo Laing's work as outlined in [23], albeit with a nuanced variation in the derivation of the mean field. Laing's mean field model originates from the theta-neuron network equation:

$$\frac{\mathrm{d}\theta_j}{\mathrm{d}t} = 1 - \cos\theta_j - \kappa_v \sin\theta_j + (1+\cos\theta_j)\left[\eta_j + \frac{\kappa_v}{N}\sum_{k=1}^{N}\tan\left(\frac{\theta_k}{2}\right)\right]. \tag{B.1}$$

The challenge of the tan term approaching infinity when $\theta = \pi$ is mitigated by substituting $\tan(\theta/2)$ with the regularised form:

$$q(\theta) = \frac{\sin\theta}{1+\cos\theta+\epsilon}, \tag{B.2}$$

where ϵ represents a small constant. This modification introduces an alteration to the mean field equation, resulting in a distinct mean field model compared to that discussed in chapter 4. Laing's mean field model with instantaneous synapses is expressed as:

$$\begin{aligned} \frac{\mathrm{d}R}{\mathrm{d}t} &= -\kappa_v R + 2RV + \frac{\gamma}{\pi}, \\ \frac{\mathrm{d}V}{\mathrm{d}t} &= \eta_0 + V^2 - \pi^2 R^2 + \kappa_s R + \kappa_v (C - V), \end{aligned} \tag{B.3}$$

where $\kappa_v(C - V)$ is the termed gained by using the correction term and

$$C(t) = \sum_{m=1}^{\infty} (b_m z^m + c.c), \tag{B.4}$$

where $z = (1 - \pi R + iV)/(1 + \pi R - iV)$ and

$$b_m = \frac{i(\rho^{m+1} - \rho^{m-1})}{2(\rho + 1 + \epsilon)}, \tag{B.5}$$

with $\rho = \sqrt{2\epsilon + \epsilon^2} - 1 - \epsilon$. For numerical purposes, the sum in (B.4) is truncated at $m = 200$ and ϵ is set to 0.01 as in Laing's publication. Thus Laing's approach introduces two ad-hoc parameters, namely *epsilon* and m, and therefore results will be parameter dependent. In contrast, our approach is exact and no new parameters are introduced. We expect the two approaches to agree as *epsilon* $\to 0$ and $m \to \infty$.

B.2 Laing Comparison Models

For the comparison with Laing's model discussed above, we use our model from Section 4.1.3 with instantaneous synapses, instead of second order synapses. This can be written as:

$$\begin{aligned} \frac{\mathrm{d}R}{\mathrm{d}t} &= -\kappa_v R + 2RV + \frac{\gamma}{\pi}, \\ \frac{\mathrm{d}V}{\mathrm{d}t} &= \eta_0 + V^2 - \pi^2 R^2 + \kappa_s R. \end{aligned} \tag{B.6}$$

B.3 PDE formulation

A simple continuum model for an effective single population dynamics can be written in the form

$$\tau \frac{\partial R}{\partial t} = -\kappa_v R + 2RV + \frac{\gamma}{\pi\tau}, \tag{B.7}$$

$$\tau \frac{\partial V}{\partial t} = \eta_0 + V^2 - \pi^2\tau^2 R^2 + \kappa_s U \tag{B.8}$$

$$QU = \psi, \tag{B.9}$$

where $\psi = w \otimes R$. The symbol $\otimes$ is used to describe spatial interaction within the neural field model, while w represents structural connectivity. For example, in the plane we might consider
$(R, V, U) = (R(\mathbf{r}, t), V(\mathbf{r}, t), U(\mathbf{r}, t))$, with $\mathbf{r} \in \mathbb{R}^2$ and $t \geq 0$ with

$$[w \otimes R](\mathbf{r}, t) = \int_{\mathbb{R}^2} w(|\mathbf{r} - \mathbf{r}'|) R(\mathbf{r}', t - |\mathbf{r} - \mathbf{r}'|/c) \mathrm{d}\mathbf{r}', \tag{B.10}$$

where c represents the speed of an action potential. We note that (B.10) can be written as a convolution:

$$\psi(\mathbf{r}, t) = \int_{\mathbb{R}} \mathrm{d}t' \int_{\mathbb{R}^2} \mathrm{d}\mathbf{r}' G(\mathbf{r} - \mathbf{r}', t - t') R(\mathbf{r}', t'), \tag{B.11}$$

where $G(r, t) = w(r)\delta(t - r/c)$. For certain choices of w it is possible to exploit this convolution structure to obtain a PDE model, often referred to as a *brain-wave equation* [58], [134]. For the choice of an inverted balanced wizard hat function with

$w(r) = (r/2-1)\mathrm{e}^{-r}/(2\pi)$ this approach yields the following brain-wave equation:

$$\left[\left(1+\frac{1}{c}\frac{\partial}{\partial t}\right)^2 - \frac{3}{2}\nabla^2\right]^2 \psi = -\left\{\frac{1}{c}\frac{\partial}{\partial t}\left(1+\frac{1}{c}\frac{\partial}{\partial t}\right) - \frac{3}{2}\nabla^2\right\} R. \tag{B.12}$$

Note that (B.12) is only strictly valid for describing long-wavelength solutions. In one spatial dimension and using $w(x) = (|x|-1)\mathrm{e}^{-|x|}$ the brain-wave PDE is

$$\left[\left(1+\frac{1}{c}\frac{\partial}{\partial t}\right)^2 - \frac{\partial^2}{\partial x^2}\right]^2 \psi = -2\left\{\frac{1}{c}\frac{\partial}{\partial t}\left(1+\frac{1}{c}\frac{\partial}{\partial t}\right)^2 - \frac{\partial^2}{\partial x^2}\left(2+\frac{1}{c}\frac{\partial}{\partial t}\right)\right\} R, \tag{B.13}$$

and is an exact reduction of $\psi = w \otimes R$ [135].

B.4 Turing Instability Analysis

Consider the homogeneous steady state of (B.12) given by

$$(U(\mathbf{r},t), \psi(\mathbf{r},t), R(\mathbf{r},t), V(\mathbf{r},t)) = (0, 0, R_0, V_0) \tag{B.14}$$

where $(R_0, V_0)$are given by the simultaneous solution of the algebraic equations

$$0 = -\kappa_v R_0 + 2R_0 V_0 + \frac{\gamma}{\pi\tau}, \tag{B.15}$$

$$0 = \eta_0 + V_0^2 - \pi^2\tau^2 R_0^2. \tag{B.16}$$

We linearise around the steady state and consider perturbations of the form $(U(\mathbf{r},t), \psi(\mathbf{r},t), R(\mathbf{r},t), V(\mathbf{r},t)) = (0, 0, R_0, V_0) + \epsilon(\overline{U}, \overline{\psi}, \overline{R}, \overline{V})\mathrm{e}^{\lambda t}\mathrm{e}^{i\mathbf{k}\cdot\mathbf{r}}$ for $|\epsilon| \ll 1$ and $\lambda = \mu + i\omega$. Substitution into (B.12) and working to first order in ϵ gives the linear relationship

$$\left[\left(1+\frac{\lambda}{c}\right)^2 + \frac{3}{2}k^2\right]^2 \overline{\psi} = -\left\{\frac{\lambda}{c}\left(1+\frac{\lambda}{c}\right) + \frac{3}{2}k^2\right\} \overline{R}, \tag{B.17}$$

where $k = |\mathbf{k}|$. A linearisation for the dynamics of (R, V) gives

$$A(\lambda)\begin{bmatrix}\overline{R}\\ \overline{V}\end{bmatrix} = \begin{bmatrix}0\\ \kappa_s\overline{U}\end{bmatrix}, \quad A(\lambda) = \tau\lambda I_2 - J, \tag{B.18}$$

where I_2 is the 2×2 identity matrix and J is the Jacobian

$$J = \begin{bmatrix}-\kappa_v + 2V_0 & 2R_0\\ -2\pi^2\tau^2 R_0 & 2V_0\end{bmatrix}. \tag{B.19}$$

We may solve (B.18) using Cramer's rule to yield

$$\overline{R} = \frac{1}{|A(\lambda)|}\begin{vmatrix}0 & -2R_0\\ \kappa_s\overline{U} & \tau\lambda - 2V_0\end{vmatrix} = \frac{2\kappa_s R_0}{|A(\lambda)|(1+\lambda/\alpha)^2}\overline{\psi}, \tag{B.20}$$

where we have used the fact that $(1 + \lambda/\alpha)^2\overline{U} = \overline{\psi}$ (from (B.9)). Substitution of (B.20) into (B.17) and demanding a non-trivial solution for $\overline{\psi}$ leads to the condition $\mathcal{E}(\lambda, k) = 0$, where

$$\begin{aligned}\mathcal{E}(\lambda, k) = |A(\lambda)|\left(1+\frac{\lambda}{\alpha}\right)^2\left[\left(1+\frac{\lambda}{c}\right)^2 + \frac{3}{2}k^2\right]^2\\ + 2\kappa_s R_0\left[\frac{\lambda}{c}\left(1+\frac{\lambda}{c}\right) + \frac{3}{2}k^2\right].\end{aligned} \tag{B.21}$$

Thus, the continuous spectrum $\lambda = \lambda(k)$ is given by the roots of an eight order polynomial. A similar analysis of (B.13) gives

$$\mathcal{E}(\lambda, k) = |A(\lambda)| \left(1 + \frac{\lambda}{\alpha}\right)^2 \left[\left(1 + \frac{\lambda}{c}\right)^2 + k^2\right]^2 + 4\kappa_s R_0 \left[\frac{\lambda}{c}\left(1 + \frac{\lambda}{c}\right)^2 + k^2\left(2 + \frac{\lambda}{c}\right)\right]. \tag{B.22}$$

The system undergoes a bifurcation when a branch of solutions $\lambda(k)$ to $\mathcal{E}(\lambda, k) = 0$ touches the imaginary axis, $\mu(k_c) = 0$, where k_c is the critical wave number. By the implicit function theorem, this occurs when

$$\frac{\partial \mathcal{M}}{\partial k}\frac{\partial \mathcal{N}}{\partial \omega} - \frac{\partial \mathcal{M}}{\partial \omega}\frac{\partial \mathcal{N}}{\partial k} = 0, \tag{B.23}$$

where $\mathcal{M} = \mathrm{Re}\,(\mathcal{E})$ and $\mathcal{N} = \mathrm{Im}\,(\mathcal{E})$. A Hopf bifurcation of the spatially uniform state can be found by solving $\mathcal{E}(i\omega, 0) = 0$ for ω. A static Turing bifurcation is found by solving $\mathcal{E}(0, k_c) = 0$ and (B.23) for k_c non-zero, while a dynamic Turing-Hopf bifurcation is found by solving $\mathcal{E}(i\omega, k_c) = 0$ and (B.23) for non-zero ω and k_c. Interesting patterns tend to emerge when a Hopf and Turing-Hopf intersect at a codimension-2 point. Such a bifurcation can be found by solving $\mathcal{E}(i\omega_1, 0) = 0$, $\mathcal{E}(i\omega_2, k_c) = 0$ and (B.23) simultaneously for ω_1, ω_2 and k_c.

B.5 Computation and Simulation of the Model

All bifurcations diagrams were generated using XPPAUT [17]. The neural mass and neural field models were numerically solved using a finite difference scheme in Julia [67] using a default adaptive solver from the DifferentialEquations.jl package [68]. All code used to simulate the model can found found at https://github.com/Jamesafross/

Neural_Field_with_gaps

B.6 Supplementary Movies

Figure 4.14 movie:

https://github.com/Jamesafross/Neural_Field_with_gaps/blob/master/Movies/ESM_7.m4v Figure 4.15 movie:

https://github.com/Jamesafross/Neural_Field_with_gaps/blob/master/Movies/ESM_8.m4v Figure 4.16 movie:

https://github.com/Jamesafross/Neural_Field_with_gaps/blob/master/Movies/ESM_9.m4v

B.7 Two Population Turing Analysis

Here we show the Turing Analysis for the two population model using an exponential connectivity function.

$$
\begin{aligned}
&\psi_{ab} = \int_{-\infty}^{\infty} w_{ab}(|x-y|)R_b(y, \tau_{ab}(|x-y|))\mathrm{d}y, \quad \tau_{ab}(x) = \tau_{ab}^0 + |x|/v_{ab}, \\
&\left(1 + \frac{1}{\alpha_{ab}}\partial_t\right)^2 g_{ab} = \kappa_{ab}^s \psi_{ab}, \\
&\tau_a \frac{\partial}{\partial t} R_a = -R_a \sum_b (g_{ab} + \kappa_{ab}^v) + 2R_a V_a + \frac{\Delta_a}{\tau_a \pi}, \\
&\tau_a \frac{\partial}{\partial t} V_a = \kappa_{ab}^v (V_b - V_a) + \sum_b g_{ab}(V_{syn}^{ab} - V_a) - \tau_a^2 \pi^2 R_a^2 + V_a^2 + \eta_a.
\end{aligned}
\tag{B.24}
$$

Firstly, we define the homogeneous steady state, $(\bar{\psi}_{ab}, \bar{g}_{ab}, \bar{R}_a, \bar{V}_a)$, of equation (B.24) as:

$$\begin{aligned}
\bar{\psi}_{ab} &= \bar{R}_b \\
\bar{g}_{ab} &= \kappa^s_{ab}\psi_{ab} \\
0 &= -\bar{R}_a \sum_b (\bar{g}_{ab} + \kappa^v_{ab}) + 2\bar{R}_a\bar{V}_a + \frac{\Delta_a}{\tau_a \pi}, \\
0 &= \kappa^v_{ab}(\bar{V}_b - \bar{V}_a) + \sum_b \bar{g}_{ab}(V^{ab}_{syn} - \bar{V}_a) - \tau_a^2\pi^2\bar{R}_a^2 + \bar{V}_a^2 + \eta_a
\end{aligned} \tag{B.25}$$

We then apply a perturbation of the form

$$(\bar{\psi}_{ab}, \bar{g}_{ab}, \bar{R}_a, \bar{V}_a) + \exp(-\lambda t)\exp(ikx)(\psi^0_{ab}, g^0_{ab}, R^0_a, V^0_a)$$

to the homogenous steady state to obtain,

$$\begin{aligned}
\left(1 + \frac{\lambda}{\alpha_{ab}}\right)^2 g^0_{ab} &= \kappa^s_{ab}\psi^0_{ab} \\
\psi^0_{ab} &= \exp(-\lambda\tau^0_{ab}) \int_{-\infty}^{\infty} w_{ab}(|y|)\exp(-iky)\exp(-\lambda|y|/v_{ab})R^0_{ab}\mathrm{d}y \\
\lambda\tau_a R^0_a &= 2\bar{V}_a R^0_a - R^0_E \sum_b (\bar{g}_{Eb} + \kappa^v_{ab}) + 2\bar{R}_a V^0_a - \bar{R}_a \sum_b g^0_{ab} \\
\lambda\tau_a V^0_a &= -2\pi^2\tau_a^2\bar{R}_a R^0_a + 2\bar{V}_a V^0_a + \sum_b \kappa^v_{ab}(\bar{V}_b - \bar{V}_a) \\
&\quad - V^0_a \sum_b \bar{g}_{ab} + \sum_b g^0_{ab}(V^{ab}_{syn} - \bar{V}_a)
\end{aligned} \tag{B.26}$$

Note: $g^0_{ab} = e^{-\lambda\tau^0_{ab}}\tilde{\eta}_{ab}(\lambda)\kappa^s_{ab}\hat{w}_{ab}(k,\lambda)R^0_b = F_{ab}(\lambda,k)R^0_b$. Now the spectral equation can be written as:

$$0 = |M(\lambda, k)| \tag{B.27}$$

where M is a 4×4 matrix and can be written as:

$$\begin{bmatrix} A - \underline{\tau}\lambda & B \\ C & D - \underline{\tau}\lambda \end{bmatrix}, \tag{B.28}$$

$\underline{\tau}$ is the 2×2 matrix

$$\underline{\tau} = \begin{bmatrix} \tau_E & 0 \\ 0 & \tau_I \end{bmatrix},$$

and A, B, C, D are the 2×2 matrices with components:

$$\begin{aligned} A_{ab} &= \left[2\bar{V}_a - \sum_c (\bar{g}_{bc} + s\bar{\kappa}^v) \right] \delta_{ab} - \bar{R}_a F_{ab} \\ B_{ab} &= 2\bar{R}_b \delta_{ab} \\ C_{ab} &= \left[-2\pi^2 \tau_b^2 \bar{R}_b \right] \delta_{ab} + F_{ab}(V_{syn}^{ab} - \bar{V}_a) \\ D_{ab} &= \left[2\bar{V}_b - \sum_c (\bar{g}_{bc} + \kappa_{bc}^v) \right] \delta_{ab} + \kappa_{ab}^v \end{aligned} \tag{B.29}$$

The spectral equation (B.27) can then be solved using a non-linear equation solver.

B.8 2 Population Model Movies

Figure 4.21 movie:

https://github.com/Jamesafross/Thesis_Code/tree/main/Neural_Field_with_gaps/Movies/Figure_4.20.

Figure 4.22 movie:

https://github.com/Jamesafross/Thesis_Code/tree/main/Neural_Field_with_gaps/Movies/Figure_4.21.

Figure 4.23 movie:

https://github.com/Jamesafross/Thesis_Code/tree/main/Neural_Field_with_gaps/Movies/Figure_4.22.

Figure 4.24 movie:

https://github.com/Jamesafross/Thesis_Code/tree/main/Neural_Field_with_gaps/Movies/Figure_4.23.

APPENDIX C

SUPPLEMENTARY MATERIAL: COUPLING A NEURAL ACTIVITY MODEL TO EXTRACELLULAR SPACE

C.1 Turing Analysis in one spatial dimension

When $W(\mathbf{x}, \mathbf{x}') = W(|\mathbf{x} - \mathbf{x}'|)$ and $\int_\Omega W(x)\mathrm{d}x = 1$ a homogeneous steady state $(\bar{\psi}_{ab}, \bar{g}_{ab}, \bar{R}_a, \bar{V}_a, \bar{K}, \bar{\eta}_E, \bar{\eta}_I, \bar{\kappa}^v_{II})$ can be found as,

$$
\begin{aligned}
&\bar{\psi}_{ab} = \bar{R}_b, \\
&\bar{g}_{ab} = \kappa^s_{ab}\psi_{ab}, \\
&0 = -\bar{R}_E \sum_b (\bar{g}_{Eb}) + 2\bar{R}_E\bar{V}_E + \frac{\Delta_E}{\tau_E \pi}, \\
&0 = \sum_b \bar{g}_{Eb}(V^{Eb}_{syn} - \bar{V}_E) - \tau_E^2\pi^2\bar{R}_E^2 + \bar{V}_E^2 + \bar{\eta}_E, \\
&0 = -\bar{R}_I \sum_b (\bar{g}_{Ib})\bar{\kappa}^v_{II} + 2\bar{R}_I\bar{V}_I + \frac{\Delta_I}{\tau_I \pi}, \\
&0 = \sum_b \bar{g}_{Ib}(V^{Ib}_{syn} - \bar{V}_I) - \tau_I^2\pi^2\bar{R}_I^2 + \bar{V}_I^2 + \bar{\eta}_I, \\
&\bar{K} = \frac{1}{\delta} f_1(\bar{R}_E, \bar{R}_I), \\
&\bar{\eta}_E = f_2(\bar{K}), \\
&\bar{\eta}_I = f_3(\bar{K}), \\
&\bar{\kappa}^v_{II} = f_4(\bar{K}),
\end{aligned}
\tag{C.1}
$$

We then apply a perturbation to this steady state of the form:

$$\exp(-\lambda t)\exp(ikx)(\psi^0_{ab}, g^0_{ab}, R^0_a, V^0_a, K^0, \eta^0_E, \eta^0_I, \kappa^{v0}_{EE}, \kappa^{v0})$$

After linearising we find that,

$$\begin{aligned}
\left(1+\frac{\lambda}{\alpha_{ab}}\right)^2 g^0_{ab} &= \kappa^s_{ab}\psi^0_{ab},\\
\psi^0_{ab} &= \exp(-\lambda\tau^0_{ab})\int_{-\infty}^{\infty} w_{ab}(|y|)\exp(-iky)\exp(-\lambda|y|/c_{ab})R^0_b \mathrm{d}y,\\
\lambda\tau_E R^0_E &= 2\bar{V}_E R^0_E - R^0_E\sum_b \bar{g}_{Eb} + 2\bar{R}_E V^0_E - \bar{R}_E\sum_b g^0_{Eb},\\
\lambda\tau_I R^0_I &= 2\bar{V}_I R^0_I - R^0_I\sum_b \bar{g}_{Ib} - R^0_I\bar{\kappa}^v_{II} - \bar{R}_I\kappa^{v0}_{II} + 2\bar{R}_I V^0_I - \bar{R}_I\sum_b g^0_{Ib},\\
\lambda\tau_E V^0_E &= -2\pi^2\tau_E^2\bar{R}_E R^0_E + \bar{V}_E V^0_E - V^0_E\sum_b \bar{g}_{Eb} + \sum_b g^0_{Eb}(V^{Eb}_{syn} - \bar{V}_E) + \eta^0_E,\\
\lambda\tau_I V^0_I &= -2\pi^2\tau_I^2\bar{R}_I R^0_I + \bar{V}_I V^0_I - V^0_I\sum_b \bar{g}_{Ib} + \sum_b g^0_{Ib}(V^{Ib}_{syn} - \bar{V}_I) + \eta^0_I,\\
\lambda\beta_1 K^0 &= -\delta K^0 + \frac{\partial f_1(\bar{R}_E,\bar{R}_I)}{\partial R_E}R^0_E + \frac{\partial f_1(\bar{R}_E,\bar{R}_I)}{\partial R_I}R^0_I - A_3k^2K^0,\\
\lambda\beta_2\eta^0_E &= -\eta^0_E + \frac{\partial f_2(\bar{K})}{\partial K}K^0,\\
\lambda\beta_3\eta^0_I &= -\eta^0_I + \frac{\partial f_3(\bar{K})}{\partial K}K^0,\\
\lambda\beta_4\kappa^{v0}_{II} &= -\kappa^{v0}_{II} + \frac{\partial f^4(\bar{K})}{\partial K}K^0.
\end{aligned}$$

Note that $g^0_{ab} = \mathrm{e}^{-\lambda\tau^0_{ab}}\tilde{\eta}_{ab}(\lambda)\kappa^s_{ab}\hat{w}_{ab}(k,\lambda)R^0_b = F_{ab}(\lambda,k)R^0_b$ with $\hat{w}_{ab}(k,\lambda) = \int_{\mathbb{R}} w_{ab}(x)\exp(ikx)\exp(-\lambda|x|/c_{ab})\mathrm{d}x$ The spectral equation is therefore

found as: $0 = |M(\lambda, k)|$ where M is an 8×8 matrix and can be written as:

$$\begin{bmatrix} A - \underline{\tau}\lambda & B & & E \\ C & D - \underline{\tau}\lambda & & F \\ & & G - \underline{\beta}\lambda & \end{bmatrix}$$

Where

$$\underline{\tau} = \begin{bmatrix} \tau_E & 0 \\ 0 & \tau_I \end{bmatrix}$$

and

$$\underline{\beta} = \begin{bmatrix} 0 & 0 & 0 & 0 & \beta_1 & 0 & 0 & 0 \\ 0 & 0 & 0 & 0 & 0 & \beta_2 & 0 & 0 \\ 0 & 0 & 0 & 0 & 0 & 0 & \beta_3 & 0 \\ 0 & 0 & 0 & 0 & 0 & 0 & 0 & \beta_4 \end{bmatrix}$$

Where A, B, C, D are 2×2 matrices, E, F are 2×4 matrices and G is a 4×8 matrix

and

$$A = \begin{bmatrix} 2\bar{V}_E - \sum_b(\bar{g}_{Eb}) - \bar{R}_E F_{EE} & -\bar{R}_E F_{EI} \\ -\bar{R}_I F_{IE} & 2\bar{V}_I - \sum_b(\bar{g}_{Ib}) - \kappa_v^{II} - \bar{R}_I F_{II} \end{bmatrix},$$

$$B = \begin{bmatrix} PDf_1(\bar{R}_E, \bar{R}_I V_I 0 & 2\bar{R}_E \\ 0 & 2\bar{R}_I \end{bmatrix}, \quad E = \begin{bmatrix} 0 & 0 & 0 & -\bar{R}_E \\ 0 & 0 & 0 & -\bar{R}_I \end{bmatrix},$$

$$C = \begin{bmatrix} -2\pi^2\tau_E^2\bar{R}_E + F_{EE}(V_{syn}^{EE} - \bar{V}_E) & F_{EI}(V_{syn}^{EI} - \bar{V}_I) \\ F_{IE}(V_{syn}^{IE} - \bar{V}_E) & -2\pi^2\tau_I^2\bar{R}_I + F_{II}(V_{syn}^{II} - \bar{V}_I) \end{bmatrix},$$

$$D = \begin{bmatrix} \bar{V}_E - \sum_b \bar{g}_{Eb} & 0 \\ 0 & \bar{V}_I - \sum_b \bar{g}_{Ib} \end{bmatrix}, \quad F = \begin{bmatrix} 0 & 1 & 0 & 0 \\ 0 & 0 & 1 & 0 \end{bmatrix},$$

$$G = \begin{bmatrix} \frac{\partial f_1(\bar{R}_E,\bar{R}_I}{\partial R_E} & \frac{\partial f_1 \bar{R}_E,\bar{R}_I}{\partial R_I} & 0 & 0 & -\delta - A_3 k^2 & 0 & 0 \\ 0 & 0 & 0 & 0 & \frac{\partial f_2(\bar{K})}{\partial K} & -1 & 0 & 0 \\ 0 & 0 & 0 & 0 & \frac{\partial f_3(\bar{K})}{\partial K} & 0 & -1 & 0 \\ 0 & 0 & 0 & 0 & \frac{\partial f_4(\bar{K})}{\partial K} & 0 & 0 & -1 \end{bmatrix}.$$

In the case of two spatial dimensions we have

$$\hat{w}_{ab}(\mathbf{k}, \lambda) = \int_{\mathbb{R}^2} w_{ab}(\mathbf{x}) \exp(i\mathbf{k}\mathbf{x}) \exp(-\lambda|\mathbf{x}|/c_{ab}) \mathrm{d}\mathbf{x}, \tag{C.2}$$

with $\mathbf{k} \in \mathbb{R}^2$.

C.2 Movies

Movies related to Figure 6.8 (varying A_1) can be found at: https://github.com/Jamesafross/Thesis_Code/tree/main/Neural_Field_with_potassium/2D_Movies/

Movies related to Figure 6.10 (varying δ) can be found at: https://github.com/Jamesafross/Thesis_Code/tree/main/Neural_Field_with_potassium/2D_Movies/

Movies related to Figure 6.12 (varying A_4) can be found at: https://github.com/Jamesafross/Thesis_Code/tree/main/Neural_Field_with_potassium/2D_Movies/

Movies related to Figure 6.14 (travelling waves) can be found at: https://github.

com/Jamesafross/Thesis_Code/tree/main/Neural_Field_with_potassium/2D_Movies/

Parameter ranges for optimisation were informed by previous numerical investigations into the gap-junction model, i.e. in Chapter 4 where a discussion on the biophysical ranges of some parameters in the deterministic model can also be found. Below is a table with the ranges or values for each parameter in the model. The gap-junction strength parameters κ^v_{ab} were kept positive, but low, this is due to high gap-junction strengths leading to potentially highly synchronous states. The noise variance σ_a was kept low too so that the stochastic term did not dominate over the neural model dynamics. The synaptic strengths κ^s_{ab} were kept within positive and in a range that had been used in previous chapters. The synaptic time constants were kept within a biophysical range of 0.01-1ms^{-1}, similar to that of the numerical studies in Chapter 4.

Table C.1: Parameter List

Parameter	Optimised	Range/value	Description	Unit
α_{EE}	✓	0.1-1	Time constant for synapses $E \to E$	ms^{-1}
α_{EI}	✓	0.1-1	Time constant for synapses $I \to E$	ms^{-1}
α_{IE}	✓	0.01-1	Time constant for synapses $E \to I$	ms^{-1}
α_{II}	✓	0.01-1	Time constant for synapses $I \to I$	ms^{-1}
κ^s_{EE}	✓	0.1-5	$E \to E$ Synaptic strength	
κ^s_{EI}	✓	0.1-5	$I \to E$ Synaptic strength	
κ^s_{IE}	✓	0.1-5	$E \to I$ Synaptic strength	
κ^s_{II}	✓	0.1-5	$I \to I$ Synaptic strength	
κ^v_{EE}	✓	0-0.3	$E \to E$ Gap-junction coupling strength	
κ^v_{EI}	✓	0-0.3	$I \to E$ Gap-junction coupling strength	
κ^v_{IE}	✓	0-0.3	$E \to I$ Gap-junction coupling strength	
κ^v_{II}	✓	0-0.3	$I \to I$ Gap-junction coupling strength	
τ_E		12	Membrane time constant for population E	ms^{-1}

Continued on next page

Table C.1: Parameter List (Continued)

Parameter	Optimised	Range/value	Description	Unit
τ_I		15	Membrane time constant for population I	ms^{-1}
Δ_E		0.2	Coherence for underlying neuronal population E	
Δ_I		0.2	Coherence for underlying neuronal population I	
η_0^E		2.0	Drive for neuronal population E	
η_0^I		1.04	Drive for neuronal population I	
V_{syn}^{EE}		9	Voltage shunts for connection $E \to E$	
V_{syn}^{EI}		-10	Voltage shunts for connection $I \to E$	
V_{syn}^{IE}		9	Voltage shunts for connection $E \to I$	
V_{syn}^{II}		-10	Voltage shunts for connection $I \to I$	
τ_E^x	✓	40-100	Noise time-scale for population E	ms^{-1}
τ_I^x	✓	40-100	Noise time-scale for population I	ms^{-1}
σ_E	✓	0.001-0.1	Controls noise variance for population E	
σ_I	✓	0.001-0.1	Controls noise variance for population I	

BIBLIOGRAPHY

[1] J. Ross, M. Margetts, I. Bojak, R. Nicks, D. Avitabile, and S. Coombes, "Brain-wave equation incorporating axodendritic connectivity," *Physical Review E*, vol. 101, p. 022 411, 2 2020.

[2] Á. Byrne, J. Ross, R. Nicks, and S. Coombes, "Mean-Field Models for EEG/MEG: From Oscillations to Waves," *Brain Topography*, vol. 35, no. 1, pp. 36–53, 2022.

[3] E. Başar, C. Başar-Eroglu, S. Karakaş, and M. Schürmann, "Gamma, alpha, delta, and theta oscillations govern cognitive processes," *International journal of psychophysiology*, vol. 39, no. 2-3, pp. 241–248, 2001.

[4] S Ogawa, T. M. Lee, A. R. Kay, and D. W. Tank, "Brain magnetic resonance imaging with contrast dependent on blood oxygenation.," *Proceedings of the National Academy of Sciences*, vol. 87, no. 24, pp. 9868–9872, 1990.

[5] C. M. Michel and M. M. Murray, "Towards the utilization of EEG as a brain imaging tool," en, *Neuroimage*, vol. 61, no. 2, pp. 371–385, 2011.

[6] R. Hari and R. Salmelin, "Magnetoencephalography: From squids to neuroscience: Neuroimage 20th anniversary special edition," *NeuroImage*, vol. 61, no. 2, pp. 386–396, 2012, NEUROIMAGING: THEN, NOW AND THE FUTURE.

[7] A. L. Hodgkin and A. F. Huxley, "A quantitative description of membrane current and its application to conduction and excitation in nerve," *The Journal of physiology*, vol. 117, no. 4, p. 500, 1952.

[8] B. Ermentrout, "Type i membranes, phase resetting curves, and synchrony," *Neural Computation*, vol. 8, no. 5, pp. 979–1001, 1996.

[9] N. Fourcaud-Trocme, D. Hansel, C. van Vreeswijk, and N. Brunel, "How spike generation mechanisms determine the neuronal response to fluctuating inputs," en, *J Neurosci*, vol. 23, no. 37, pp. 11 628–11 640, 2003.

[10] M. Breakspear, "Dynamic models of large-scale brain activity," *Nature neuroscience*, vol. 20, no. 3, pp. 340–352, 2017.

[11] S. Coombes, "Large-scale neural dynamics: Simple and complex," *NeuroImage*, vol. 52, no. 3, pp. 731–739, 2010, Computational Models of the Brain.

[12] H. R. Wilson and J. D. Cowan, "Excitatory and Inhibitory Interactions in Localized Populations of Model Neurons," *Biophysical Journal*, vol. 12, no. 1, pp. 1–24, 1972.

[13] B. H. Jansen and V. G. Rit, "Electroencephalogram and visual evoked potential generation in a mathematical model of coupled cortical columns," *Biological Cybernetics volume*, 1995.

[14] A. Byrne, M. Brookes, and S. Coombes, "A mean field model for movement induced changes in the beta rhythm," *Journal of Computational Neuroscience*, vol. 43, 143–158, 2017.

[15] S. Coombes and A. Byrne, "Next Generation Neural Mass Models," in *Nonlinear Dynamics in Computational Neuroscience*. Springer International Publishing, 2019.

[16] A. Byrne, R. O. Dea, M Forrester, J Ross, and S Coombes, "Next generation neural mass and field modelling," *Journal of Neurophysiology*, vol. 123, pp. 726–742, 2020.

[17] G. B. Ermentrout, *Simulating, analyzing, and animating dynamical systems: A guide to XPPAUT for researchers and students*. SIAM Books, 2002.

[18] F. Wendling, J.-J. Bellanger, F. Bartolomei, and P. Chauvel, "Relevance of nonlinear lumped-parameter models in the analysis of depth-EEG epileptic signals," *Biological cybernetics*, vol. 83, no. 4, pp. 367–378, 2000.

[19] T. J, F. Wendling, P. Chauvel, and O. Faugeras, "Neural Mass Activity, Bifurcations, and Epilepsy," *Neural Computation*, 2011.

[20] C. R. Laing, "Derivation of a neural field model from a network of theta neurons," *Physical Review E*, vol. 90, 010901(R), 2014.

[21] E. Montbrió, D. Pazó, and A. Roxin, "Macroscopic Description for Networks of Spiking Neurons," *Physical Review X*, vol. 5, p. 021 028, 2015.

[22] A. Byrne, D Avitabile, and S Coombes, "A next generation neural field model: The evolution of synchrony within patterns and waves," *Physical Review E*, vol. 99, p. 012 313, 2019.

[23] C. R. Laing, "Exact neural fields incorporating gap junctions," *SIAM Journal on Applied Dynamical Systems*, vol. 14, pp. 1899–1929, 2015.

[24] H. Taher, A. Torcini, and S. Olmi, "Exact neural mass model for synaptic-based working memory," *PLOS Computational Biology*, vol. 16, no. 12, pp. 1–42, Dec. 2020.

[25] B. Pietras and E. Montbrió, "Heterogeneous populations of quadratic integrate-and-fire neurons: On the generality of lorentzian distributions," *arXiv preprint arXiv:2409.18278*, 2024.

[26] B. Gutkin, "Theta-neuron model," in *Encyclopedia of Computational Neuroscience*, D. Jaeger and R. Jung, Eds. New York, NY: Springer New York, 2013, pp. 1–9.

[27] S. Coombes, "Next generation neural population models," *Frontiers in Applied Mathematics and Statistics*, vol. 9, 2023.

[28] P. Sanz-Leon, S. A. Knock, A. Spiegler, and V. K. Jirsa, "Mathematical framework for large-scale brain network modeling in the virtual brain," *NeuroImage*, vol. 111, pp. 385–430, 2015.

[29] E. Giannakakis et al., "Computational modelling of the long-term effects of brain stimulation on the local and global structural connectivity of epileptic patients," *Plos one*, vol. 15, no. 2, e0221380, 2020.

[30] P. N. Taylor, M. Kaiser, and J. Dauwels, "Structural connectivity based whole brain modelling in epilepsy," *Journal of neuroscience methods*, vol. 236, pp. 51–57, 2014.

[31] M. Forrester et al., "Whole brain functional connectivity: Insights from next generation neural mass modelling incorporating electrical synapses," *PLOS Computational Biology*, vol. 20, no. 12, pp. 1–29, Dec. 2024.

[32] S. N. Sotiropoulos and A. Zalesky, "Building connectomes using diffusion mri: Why, how and but," *NMR in Biomedicine*, vol. 32, no. 4, e3752, 2019.

[33] P. Hagmann et al., "Mapping the structural core of human cerebral cortex," *PLOS Biology*, vol. 6, no. 7, pp. 1–15, Jul. 2008.

[34] K. J. Friston, "Functional and effective connectivity: A review," *Brain Connectivity*, vol. 1, no. 1, pp. 13–36, 2011, PMID: 22432952.

[35] J. Hlinka and S. Coombes, "Using computational models to relate structural and functional brain connectivity," *European Journal of Neuroscience*, vol. 36, no. 2, pp. 2137–2145, 2012.

[36] P. Tewarie et al., "Relationships Between Neuronal Oscillatory Amplitude and Dynamic Functional Connectivity," *Cerebral Cortex*, vol. 29, no. 6, pp. 2668–2681, 2018.

[37] M Forrester, S Coombes, J. J. Crofts, S. N. Sotiropoulos, and R. D. O'Dea, "The role of node dynamics in shaping emergent functional connectivity patterns in the brain," *Network Neuroscience*, vol. 4, pp. 467–483, 2020.

[38] R. G. Abeysuriya et al., "A biophysical model of dynamic balancing of excitation and inhibition in fast oscillatory large-scale networks," *PLOS Computational Biology*, vol. 14, no. 2, pp. 1–27, Feb. 2018.

[39] P. C. Bressloff and M. A. Webber, "Neural field model of binocular rivalry waves," *Journal of Computational Neuroscience*, vol. 32, pp. 233 –252, 2011.

[40] M. A. Webber and P. C. Bressloff, "The effects of noise on binocular rivalry waves: A stochastic neural field model," *Journal of Statistical Mechanics: Theory and Experiment*, vol. 2013, no. 03, P03001, 2013.

[41] B. Ermentrout, "Neural networks as spatio-temporal pattern-forming systems," *Reports on progress in physics*, vol. 61, no. 4, p. 353, 1998.

[42] V. Jirsa, K. Jantzen, A. Fuchs, and J. Kelso, "Spatiotemporal forward solution of the eeg and meg using network modeling," *IEEE Transactions on Medical Imaging*, vol. 21, no. 5, pp. 493–504, 2002.

[43] S. Coombes, P. Graben, and R. Potthast, "Neural Fields," in S. Coombes, P. Graben, R. Potthast, and J Wright, Eds. Springer, 2014, ch. 1.

[44] S. Amari, "Dynamics of Pattern Formation in Lateral-Inhibition Type Neural Fields," *Biological Cybernetics*, vol. 27, no. 2, 77–87, 1977.

[45] P. Bressloff, "Spatiotemporal dynamics of continuum neural fields," *Journal of Physics A: Mathematical and Theoretical*, 2012.

[46] S. Coombes, "Waves, bumps, and patterns in neural field theories," *Biological Cybernetics*, 2005.

[47] R. L. Beurle, "Properties of a Mass of Cells Capable of Regenerating Pulses," *Philosophical Transactions of the Royal Society of London. Series B, Biological Sciences*, vol. 240, no. 669, pp. 55–94, 1956.

[48] S. Amari, "Homogeneous nets of neuron-like elements," *Biological Cybernetics*, vol. 17, 211–220, 1975.

[49] G. B. Ermentrout, S. E. Folias, and Z. P. Kilpatrick, *Neural Fields*, S. Coombes, P. Graben, R. Potthast, and J Wright, Eds. Springer, 2014.

[50] P. L. Nunez, "The brain wave equation: a model for the EEG," *Mathematical Biosciences*, vol. 21, no. 3, pp. 279–297, 1974.

[51] Jirsa and Haken, "Field Theory of Electromagnetic Brain Activity.," *Physical review letters*, vol. 77 5, pp. 960–963, 1996.

[52] G. B. Ermentrout, S. E. Folias, and Z. P. Kilpatrick, "Neural Fields," in S. Coombes, P. Graben, R. Potthast, and J Wright, Eds. Springer, 2014, ch. 4.

[53] M. V. L. Bennet and R. S. Zukin, "Electrical coupling and neuronal synchronization in the mammalian brain," *Neuron*, vol. 41, pp. 495–511, 2004.

[54] M. L. Steyn-Ross, D. A. Steyn-Ross, M. T. Wilson, and J. W. Sleigh, "Gap junctions mediate large-scale turing structures in a mean-field cortex driven by subcortical noise," *Phys. Rev. E*, vol. 76, p. 011 916, 1 2007.

[55] G. Sypert and A. Ward, "Changes in extracellular potassium activity during neocortical propagated seizures," *Experimental Neurology*, vol. 45, no. 1, pp. 19–41, 1974.

[56] L.-E. Martinet et al., "Human seizures couple across spatial scales through travelling wave dynamics," *Nature Communications*, vol. 8, p. 14 896, 2017.

[57] W. Rall, "Core conductor theory and cable properties of neurons," in *Comprehensive Physiology*. John Wiley & Sons, Ltd, 2011, pp. 39–97.

[58] P. L. Nunez, "The brain wave equation: a model for the EEG," *Mathematical Biosciences*, vol. 21, pp. 279–297, 1974.

[59] B. W. Mel, "Information Processing in Dendritic Trees," *Neural Computation*, vol. 6, no. 6, pp. 1031–1085, 1994.

[60] W. Rall, "Theory of Physiological Properties of Dendrites," *Annals of the New York Academy of Sciences*, vol. 96, pp. 1071–1092, 1962.

[61] W. Rall, "Theoretical significance of dendritic trees for neuronal input-output relations," *Neural Theory and Modeling*, pp. 73–97, 1964.

[62] H. C. Tuckwell, *Introduction to Theoretical Neurobiology* (Cambridge Studies in Mathematical Biology). Cambridge University Press, 1988, vol. 1.

[63] D. Johnston and S. M.-S. Wu, *Foundations of cellular neurophysiology*. MIT press, 1994.

[64] L. F. Abbott, E. Farhi, and S. Gutmann, "The path integral for dendritic trees," *Biological Cybernetics*, vol. 66, no. 1, pp. 49–60, 1991.

[65] P. Bressloff and B. De Souza, "Neural pattern formation in networks with dendritic structure," *Physica D: Nonlinear Phenomena*, vol. 115, no. 1, pp. 124–144, 1998.

[66] G. M. Shepherd, *The Synaptic Organization of the Brain*. Oxford University Press, Jan. 2004.

[67] J Bezanson, A Edelman, S Karpinski, and V Shah, "Julia: A Fresh Approach to Numerical Computing," *SIAM Review*, vol. 59, pp. 65–98, 2017.

[68] C. Rackauckas and Q. Nie, "Differentialequations. jl–a performant and feature-rich ecosystem for solving differential equations in julia," *Journal of open research software*, vol. 5, no. 1, 2017.

[69] B. Ermentrout and D. H. Terman, *Mathematical foundations of neuroscience*. Springer, 2010, vol. 35.

[70] G. T. Einevoll, C. Kayser, N. K. Logothetis, and S. Panzeri, "Modelling and analysis of local field potentials for studying the function of cortical circuits," *Nature Reviews Neuroscience*, vol. 14, no. 11, pp. 770–785, 2013.

[71] K. H. Pettersen and G. T. Einevoll, "Amplitude variability and extracellular low-pass filtering of neuronal spikes," *Biophysical Journal*, vol. 94, no. 3, pp. 784–802, 2008.

[72] A. V. Alvarez, C. C. Chow, E. J. V. Bockstaele, and J. T. Williams, "Frequency-dependent synchrony in locus ceruleus: Role of electrotonic coupling," *Proceedings of the National Academy of Sciences*, vol. 99, pp. 4032–4036, 2002.

[73] J. L. P. Velazquez and P. L. Carlen, "Gap junctions, synchrony and seizures," *Trends in Neurosciences*, vol. 23, pp. 68–74, 2000.

[74] G. Pernelle, W. Nicola, and C. Clopath, "Gap junction plasticity as a mechanism to regulate network-wide oscillations," en, *PLoS Comput Biol*, vol. 14, no. 3, e1006025, Mar. 2018.

[75] B. Pietras, F. Devalle, A. Roxin, A. Daffertshofer, and E. Montbrió, "Exact firing rate model reveals the differential effects of chemical versus electrical synapses in spiking networks," *Physical Review E*, vol. 100, no. 4, p. 042 412, 2019.

[76] M. L. Steyn-Ross, D. A. Steyn-Ross, M. T. Wilson, and J. W. Sleigh, "Gap junctions mediate large-scale Turing structures in a mean-field cortex driven by subcortical noise.," *Physical Review E*, vol. 76, p. 011 916, 2007.

[77] B. W. Connors and M. A. Long, "Electrical synapses in the mammalian brain," *Annual Review of Neuroscience*, vol. 27, pp. 393–418, 2004.

[78] K. Dharani, "Chapter 8 - memory, intelligence and molecular grid," in *The Biology of Thought*, K. Dharani, Ed., San Diego: Academic Press, 2015, pp. 143–161.

[79] G. P. Krishnan, G Filatov, and M Bazhenov, "Dynamics of high-frequency synchronization during seizures," *Journal of Neurophysiology*, vol. 109, pp. 2423–2437, 2013.

[80] N. T. Markov et al., "Weight Consistency Specifies Regularities of Macaque Cortical Networks," *Cerebral Cortex*, vol. 21, pp. 1254–1272, 2010.

[81] I. Omelchenko, Y. Maistrenko, P. Hövel, and E. Schöll, "Loss of Coherence in Dynamical Networks: Spatial Chaos and Chimera States," *Physical Review Letters*, vol. 106, p. 234 102, 2011.

[82] D. M. Abrams and S. H. Strogatz, "Chimera States for Coupled Oscillators," *Physical Review Letters*, vol. 93, p. 174 102, 2004.

[83] C. R. Laing, "Chimera states in heterogeneous networks," *Chaos: An Interdisciplinary Journal of Nonlinear Science*, vol. 19, no. 1, p. 013 113, 2009.

[84] P. L. Nunez and R. Srinivasan, "Neocortical dynamics due to axon propagation delays in cortico-cortical fibers: Eeg traveling and standing waves with implications for top-down influences on local networks and white matter disease," *Brain Research*, vol. 1542, pp. 138–166, 2014.

[85] M Bataille-Gonzalez, M. G. Clerc, E Knobloch, and O. E. Omel'chenko, "Traveling spiral wave chimeras in coupled oscillator systems: Emergence, dynamics, and transitions," *New Journal of Physics*, vol. 25, no. 10, p. 103 023, 2023.

[86] Ma, Rubao, Wang, Jianxiong, and Liu, Zonghua, "Robust features of chimera states and the implementation of alternating chimera states," *EPL*, vol. 91, no. 4, p. 40 006, 2010.

[87] E. Tognoli and J. Kelso, "The metastable brain," *Neuron*, vol. 81, no. 1, pp. 35–48, 2014.

[88] J.-Y. Liou et al., "A model for focal seizure onset, propagation, evolution, and progression," en, *Elife*, vol. 9, Mar. 2020.

[89] X. Huang, W. Xu, J. Liang, K. Takagaki, X. Gao, and J.-y. Wu, "Spiral wave dynamics in neocortex," *Neuron*, vol. 68, no. 5, pp. 978–990, 2010.

[90] M. V. L. Bennett, "Electrical Transmission: A Functional Analysis and Comparison to Chemical Transmission," in *Cellular Biology of Neurons, (Handbook of Physiology, Vol. 1)*, E. Kandel, Ed. American Physiological Society, 1977, pp. 357–416.

[91] V. Volman, M. Perc, and M. Bazhenov, "Gap Junctions and Epileptic Seizures – Two Sides of the Same Coin?" *PLOS ONE*, vol. 6, no. 5, pp. 1–11, 2011.

[92] Y. Wei, G. Ullah, and S. J. Schiff, "Unification of neuronal spikes, seizures, and spreading depression," *Journal of Neuroscience*, vol. 34, no. 35, pp. 11 733–11 743, 2014.

[93] D. H. Mathalon and V. S. Sohal, "Neural Oscillations and Synchrony in Brain Dysfunction and Neuropsychiatric Disorders: It's About Time," *JAMA Psychiatry*, vol. 72, no. 8, pp. 840–844, 2015.

[94] Z. A. Seedat et al., "The role of transient spectral 'bursts' in functional connectivity: A magnetoencephalography study," *Neuroimage*, vol. 209, p. 116 537, 2020.

[95] S. E. Robson et al., "Abnormal visuomotor processing in schizophrenia," *NeuroImage: Clinical*, vol. 12, pp. 869–878, 2016.

[96] J. Gross, J. Kujala, M. Hamalainen, L. Timmermann, A. Schnitzler, and R. Salmelin, "Dynamic imaging of coherent sources: Studying neural interactions in the human brain," *Proceedings of the National Academy of Sciences*, vol. 98, no. 2, pp. 694–699, 2001.

[97] M. T. Jurkiewicz, W. C. Gaetz, A. C. Bostan, and D. Cheyne, "Post-movement beta rebound is generated in motor cortex: Evidence from neuromagnetic recordings," *NeuroImage*, vol. 32, no. 3, pp. 1281–1289, 2006.

[98] F. van Ede, A. J. Quinn, M. W. Woolrich, and A. C. Nobre, "Neural Oscillations: Sustained Rhythms or Transient Burst-Events?" *Trends in Neurosciences*, vol. 41, no. 7, pp. 415–417, 2018.

[99] A. S. Powanwe and A. Longtin, "Determinants of Brain Rhythm Burst Statistics," *Scientific Reports*, vol. 9, no. 1, p. 18 335, 2019.

[100] G. E. Uhlenbeck and L. S. Ornstein, "On the Theory of the Brownian Motion," *Physical Review*, vol. 36, pp. 823–841, 5 1930.

[101] E. Bibbona, G. Panfilo, and P. Tavella, "The Ornstein–Uhlenbeck process as a model of a low pass filtered white noise," *Metrologia*, vol. 45, no. 6, S117–S126, 2008.

[102] M. A. Sherman et al., "Neural mechanisms of transient neocortical beta rhythms: Converging evidence from humans, computational modeling, monkeys, and mice," *Proceedings of the National Academy of Sciences*, vol. 113, no. 33, E4885–E4894, 2016.

[103] B. A. E. Hunt et al., "Attenuated post-movement beta rebound associated with schizotypal features in healthy people," *Schizophrenia Bulletin*, vol. 45, no. 4, pp. 883–891, Sep. 2018.

[104] N Tzourio-Mazoyer et al., "Automated anatomical labeling of activations in SPM using a macroscopic anatomical parcellation of the MNI MRI single-subject brain," en, *Neuroimage*, vol. 15, no. 1, pp. 273–289, Jan. 2002.

[105] S. Katoch, S. S. Chauhan, and V. Kumar, "A review on genetic algorithm: Past, present, and future," *Multimedia Tools and Applications*, vol. 80, no. 5, pp. 8091–8126, 2021.

[106] E. Giannakakis et al., "Computational modelling of the long-term effects of brain stimulation on the local and global structural connectivity of epileptic patients," *PLOS ONE*, vol. 15, no. 2, pp. 1–21, Feb. 2020.

[107] P. Hagmann et al., "Mapping human whole-brain structural networks with diffusion mri," *PLOS ONE*, vol. 2, no. 7, pp. 1–9, Jul. 2007.

[108] M. P. van den Heuvel et al., "Comparison of diffusion tractography and tract-tracing measures of connectivity strength in rhesus macaque connectome," *Human Brain Mapping*, vol. 36, no. 8, pp. 3064–3075, 2015.

[109] S. Jbabdi and H. Johansen-Berg, "Tractography: Where do we go from here?" en, *Brain Connect*, vol. 1, no. 3, pp. 169–183, Aug. 2011.

[110] S. N. Sotiropoulos et al., "Advances in diffusion MRI acquisition and processing in the Human Connectome Project," *NeuroImage*, vol. 80, pp. 125–143, 2013, Mapping the Connectome.

[111] D. C. Van Essen et al., "The human connectome project: A data acquisition perspective," en, *NeuroImage*, vol. 62, no. 4, pp. 2222–2231, 2012.

[112] A. T. L. Leong et al., "Long-range projections coordinate distributed brain-wide neural activity with a specific spatiotemporal profile," *Proceedings of the National Academy of Sciences*, vol. 113, no. 51, E8306–E8315, 2016.

[113] C. Rackauckas and Q. Nie, "Adaptive methods for stochastic differential equations via natural embeddings and rejection sampling with memory," *Discrete and continuous dynamical systems. Series B*, vol. 22, no. 7, p. 2731, 2017.

[114] H. T. Sykora, C. V. Rackauckas, D. Widmann, and D. Bachrathy, "StochasticDelayDiffEq. jl-An Integrator Interface for Stochastic Delay Differential Equations in Julia," 2020.

[115] P. M. Briley et al., "Regional brain correlates of beta bursts in health and psychosis: A concurrent electroencephalography and functional magnetic resonance imaging study," en, *Biological Psychiatry: Cognitive Neuroscience and Neuroimaging*, vol. 6, no. 12, pp. 1145–1156, 2020.

[116] B. Rajakumar, "Impact of static and adaptive mutation techniques on the performance of genetic algorithm," *International Journal of Hybrid Intelligent Systems*, vol. 10, no. 1, pp. 11–22, 2013.

[117] Y. Rubner, C. Tomasi, and L. J. Guibas, "The earth mover's distance as a metric for image retrieval," *International Journal of Computer Vision*, vol. 40, no. 2, pp. 99–121, 2000.

[118] S. L. Moshé, E. Perucca, P. Ryvlin, and T. Tomson, "Epilepsy: new advances," *The Lancet*, vol. 385, no. 9971, pp. 884–898, 2015.

[119] P. Bazzigaluppi, I. Weisspapir, B. Stefanovic, L. Leybaert, and P. L. Carlen, "Astrocytic gap junction blockade markedly increases extracellular potassium without causing seizures in the mouse neocortex," *Neurobiology of Disease*, vol. 101, pp. 1–7, 2017.

[120] G. Somjen, "Ion regulation in the brain: implications for pathophysiology," *Neuroscientist*, vol. 8, pp. 254–27, 2002.

[121] B. H. Jansen and V. G. Rit, "Electroencephalogram and visual evoked potential generation in a mathematical model of coupled cortical columns," *Biological Cybernetics*, vol. 73, pp. 357–366, 1995.

[122] S. Ahmadizadeh et al., "Bifurcation analysis of two coupled Jansen-Rit neural mass models," *PLOS ONE*, vol. 13, no. 3, pp. 1–51, 2018.

[123] H. S. Haghighi and A. H. D. Markazi, "Control of epileptic seizures by electrical stimulation: a model-based study," *Biomedical Physics and Engineering Express*, vol. 7, no. 6, p. 065 009, 2021.

[124] J. V. Raimondo, R. J. Burman, A. A. Katz, and C. J. Akerman, "Ion dynamics during seizures," *Frontiers in cellular neuroscience*, vol. 9, p. 419, 2015.

[125] G. Rabuffo et al., "Biophysically inspired mean-field model of neuronal populations driven by ion exchange mechanisms," Feb. 2025.

[126] J. Bezanson, S. Karpinski, V. Shah, and A. Edelman, "Julia: A Fast Dynamic Language for Technical Computing," *MIT*, 2012.

[127] M. L. Steyn-Ross, D. A. Steyn-Ross, and J. W. Sleigh, "Gap junctions modulate seizures in a mean-field model of general anesthesia for the cortex," *Cognitive Neurodynamics*, vol. 6, no. 3, pp. 215–225, 2012.

[128] M. L. Steyn-Ross, D. A. Steyn-Ross, and J. W. Sleigh, "Interacting Turing-Hopf Instabilities Drive Symmetry-Breaking Transitions in a Mean-Field Model of the Cortex: A Mechanism for the Slow Oscillation," *Physical Review X*, vol. 3, p. 021 005, 2013.

[129] G. A. Worrell, L. Parish, S. D. Cranstoun, R. Jonas, G. Baltuch, and B. Litt, "High-frequency oscillations and seizure generation in neocortical epilepsy," *Brain*, vol. 127, no. 7, pp. 1496–1506, Jul. 2004.

[130] L. Ren et al., "Gamma oscillations precede interictal epileptiform spikes in the seizure onset zone," *Neurology*, vol. 84, no. 6, pp. 602–608, 2015.

[131] D. Wilson and B. Ermentrout, "Phase models beyond weak coupling," *Phys. Rev. Lett.*, vol. 123, p. 164 101, 16 2019.

[132] M. J. Panaggio and D. M. Abrams, "Chimera states: Coexistence of coherence and incoherence in networks of coupled oscillators," *Nonlinearity*, vol. 28, no. 3, R67, 2015.

[133] J. Hlinka and S. Coombes, "Using computational models to relate structural and functional brain connectivity," *European Journal of Neuroscience*, vol. 36, no. 2, pp. 2137–2145, 2012.

[134] V. K. Jirsa and H Haken, "A derivation of a macroscopic field theory of the brain from the quasi-microscopic neural dynamics," *Physica D*, vol. 99, pp. 503–526, 1997.

[135] N. A. Venkov, S Coombes, and P. C. Matthews, "Dynamic instabilities in scalar neural field equations with space-dependent delays," *Physica D*, vol. 232, pp. 1–15, 2007.